



HAL
open science

2D/3D lensless imaging: prototype and applications

Ramona Corman

► **To cite this version:**

Ramona Corman. 2D/3D lensless imaging: prototype and applications. Optics [physics.optics].
Université Paris-Saclay, 2020. English. NNT: 2020UPASS042 . tel-02944689

HAL Id: tel-02944689

<https://theses.hal.science/tel-02944689>

Submitted on 21 Sep 2020

HAL is a multi-disciplinary open access archive for the deposit and dissemination of scientific research documents, whether they are published or not. The documents may come from teaching and research institutions in France or abroad, or from public or private research centers.

L'archive ouverte pluridisciplinaire **HAL**, est destinée au dépôt et à la diffusion de documents scientifiques de niveau recherche, publiés ou non, émanant des établissements d'enseignement et de recherche français ou étrangers, des laboratoires publics ou privés.

2D/3D lensless imaging: Prototype and applications

Thèse de doctorat de l'université Paris-Saclay

École doctorale n° 572 Ondes et Matière (EDOM)
Spécialité de doctorat: optique et photonique
Unité de recherche : Université Paris-Saclay, CEA,
CNRS, LIDYL, 91191, Gif-sur-Yvette, France.
Réfèrent : Faculté des Sciences d'Orsay

**Thèse présentée et soutenue à Gif-sur-Yvette,
le 13 Mars 2020, par**

Ramona CORMAN

Composition du Jury

Thomas GUSTAVSSON

Directeur de recherche, Université Paris-Saclay, CNRS

Président

Olivier HAEBERLE

Professeur, Université de Haute-Alsace

Rapporteur & Examineur

Mona MIHAILESCU

Professeure, Politehnica University of Bucharest

Rapporteur & Examinatrice

Mathieu DUCOUSSO

Ingénieur de recherche, Safran - Paris

Examineur

Oana NEDELCU

Ingénieure de recherche, IMT- Bucharest

Examinatrice

Willem BOUTU

Ingénieur de recherche, Université Paris-Saclay, CEA

Directeur de thèse

Guillaume DOVILLAIRE

Ingénieur de recherche, Imagine Optic - Orsay

Invité

Université Paris-Saclay

Espace Technologique / Immeuble Discovery

Route de l'Orme aux Merisiers RD 128 / 91190 Saint-Aubin, France

“The woman who follows the crowd will usually go no further than the crowd. The woman who walks alone is likely to find herself in places no one has ever been before.”

— Albert Einstein

Dedication

This dissertation is dedicated to the memory of my grandfather. He was my inspiration to achieve a doctorate degree. This work is also dedicated to my parents who always believed in my ambitions and thought me to work hard for the things that I aspire to achieve. A special feeling of gratitude to my soulmate. He has been a constant source of support and encouragement during the challenges of PhD graduation and life.

Abstract

Biological imaging has made tremendous progresses these last decades. The latest developments concern manipulating and imaging single cells with nanometre spatial resolutions. A recent category of imaging techniques, called lensless microscopy, is very promising because they combine very good spatial resolutions in a large field-of-view, with simplicity of use and low cost, while operating on label free samples. In this thesis, two different lensless approaches are considered: digital in-line holography (DILH) and Fourier transform holography (FTH). In lensless imaging, the usual optical systems used to form the sample's image are removed and replaced by numerical algorithms using the light spatial coherence properties.

Two imaging prototypes, built on these principles, are presented. They offer (sub-) micrometer scale resolutions, and offer the possibility to retrieve both spatial amplitude and phase information of the optical field. This allows for achieving pseudo-3D reconstructions of volumetric objects from a single 2D hologram. Both devices were first characterized with reference samples. In a second step, real applications, relevant to selected biological problems, were performed to assess the device's performances towards high resolution, real time imaging and 3D.

This thesis objective is also to develop a new platform directly integrating in a single chip a microfluidics system for biological cell handling by dielectrophoresis and an optical mask for cell visualization by lensless microscopy. Its working principle is based on cell transport in a liquid media by microfluidics, cell separation in the microscope field of view by the electric field induced by specific electrodes, and simultaneous cell imaging by Fourier Transform Holography. The main advantage of such coupled electro-optical system for cell imaging and analysis are the improved control, the precision and sensitivity regarding cell morphology all together merged in a compact imaging platform. The capability of the platform can be extended to analysis of cells' behaviour and morphologic deviation during the electrochemical processes of DEP.

A major challenge in microscopy field is to reduce the production costs. The two types of lensless microscopy presented in this thesis aims to introduce new imaging tools that allows scientists to obtain low-cost high-resolution images in label-free conditions. Additionally, the microfluidics chip is a first demonstration of a new integrated platform for cell live analysis into a single Lab-on-a-chip device.

Résumé

L'imagerie biologique a réalisé des progrès significatifs durant les dernières décennies. Les récentes innovations portent sur la manipulation et la visualisation de cellules uniques avec une résolution spatiale de l'ordre du nanomètre. Une technologie d'imagerie récente, l'imagerie «sans lentille», est particulièrement prometteuse car elle combine une bonne résolution spatiale, un champ de vision étendu, une simplicité d'utilisation, un coût abordable et la possibilité de travailler sur des échantillons exempts de marqueurs spécifiques. En imagerie sans lentille, le système optique classiquement utilisé pour constituer l'image de l'échantillon est remplacé par des algorithmes informatiques qui s'appuient sur les propriétés de cohérence spatiale de la lumière. Dans cette thèse, deux approches différentes de microscopie sans lentille sont considérées : l'holographie numérique en ligne et l'holographie par transformée de Fourier.

Deux prototypes d'imagerie, construits selon ces principes, sont présentés. Ils offrent une résolution de l'ordre du micron, ainsi que la possibilité de retrouver les informations relatives à l'amplitude spatiale et à la phase du champ optique. Cela permet la réalisation de reconstructions pseudo-3D d'objets volumétriques à partir d'un unique hologramme. Les deux dispositifs ont d'abord été caractérisés avec des échantillons de référence. Par la suite, des expériences d'applications ont été testées pour estimer la capacité des dispositifs à répondre à des problématiques concrètes dans le domaine de la biologie, grâce à la haute résolution, l'imagerie en temps réel et la reconstruction 3D.

L'objectif de cette thèse est également de développer une nouvelle plateforme qui intègre, dans une puce microfluidique, d'une part un système permettant la manipulation de cellules par diélectrophorèse, et d'autre part un masque optique pour la visualisation des cellules par imagerie sans lentille. Le principe de fonctionnement est basé sur le déplacement des cellules en milieu liquide et la séparation des cellules dans le champ de vision du microscope en utilisant un champ électrique induit par des électrodes spécifiques. Le masque optique permet de définir le champ de vision du microscope et de créer les faisceaux de référence nécessaires pour l'imagerie par holographie par transformée de Fourier. Le principal avantage de ce système électro-optique pour l'imagerie cellulaire réside dans sa capacité à fournir une plateforme d'imagerie compacte qui regroupe précision et sensibilité. Les champs d'applications de cette plateforme sont variés. Une application concrète qui découle immédiatement des premières expériences présentées dans ce manuscrit serait l'analyse du comportement des cellules et de leurs modifications morphologiques lors d'un processus électrochimique de diélectrophorèse.

L'un des challenges majeurs dans le domaine de la microscopie est de réduire les coûts de fabrication. Les deux types de microscopes sans lentille présentés dans cette thèse visent à introduire dans le monde scientifique des outils d'imagerie permettant d'obtenir une haute résolution à un faible coût et sans marquage. Par ailleurs, la puce microfluidique est une première démonstration de plateforme intégrée pour l'analyse des cellules en temps réel dans un dispositif de type « Lab-on-a-chip ».

Author Contributions

Digital in-line holography for bio-applications

The acquisition and image reconstruction codes were taken over the previous PhD's work and upgraded with the twin image correction algorithm by Joana Duarte (she summarized in her PhD manuscript the code). The demand of live experimental acquisition needs a user-friendly GUI interface that was developed with the help of W. Boutu. I adapted the setup for each experiments. I performed all the experiments and data analysis having in mind the biological requirements, using the in-line configuration (helpful discussions with H. Merdji, W. Boutu). The biological samples used were provided by several collaborators (see below). I proposed the collaboration with Fernando Muzzoppapa from CEA/I2BC for cyanobacteria motility analysis, topic that later drew Prof. Franck Chauvat's interest after a project review at CEA where H. Merdji presented the results of my research. I build the setup necessary for the motility study with the help of H. Merdji.

I followed the sample protocol and prepared the samples in the following experiments: zebrafish embryos, cyanobacteria and some of U2OS cells (most of the samples received were already fixed in medium and there was no need of preparation).

A novel FTH microfluidic microscope for applications in biology

The concept of integrating FTH imaging with microfluidics came up as an answer of DILH limitations plus a strong background in microfluidics accumulated during my previous career. I proposed the collaboration with IMT Bucharest, with Oana Nedelcu who was in charge with the development of the device. The design for the chip was the result of numerous discussions with H. Merdji and W. Boutu for the optical part and O. Nedelcu for the microfluidics and electronics parts, while the final electrodes dimensioning resulted from simulations performed by IMT Bucharest. The fabrication was realized by IMT Bucharest. I modified the setup (helpful discussions with H. Merdji, W. Boutu) and adapted the in-line holography GUI to FTH with the help of W. Boutu. I performed the experiments assisted by O. Nedelcu. I analysed the data and I used a post-processing MATLAB code develop by Julien Samaan.

Together with H. Merdji, I summed up the whole idea in a proposal that was accepted in July 2019 (DIM ELICIT Ile-de-France IMAChip).

Collaboration with biological Institutes

Cell culture of U2OS and HeLa

Pablo Radicella and Anna Campalans, *Laboratoire de Recherche sur l'Instabilité du Génome (LRIG) and Light Microscopy Platform, Institute of Molecular and Cellular Radiobiology*

Zebrafish embryos

Prof. Laure Bally-Cuif and Nicolas Dray, *Institut Pasteur Dept. Developmental and Stem Cell Biology*

Cyanobacteria

Fernando Muzzoppapa, *Institut de Biologie Intégrative de la Cellule (I2BC)*

Prof. Franck Chauvat, *Laboratory Biology & Biotechnology of Cyanobacteria (LBBC)*

Table of Contents

DEDICATION	III
ABSTRACT	V
RESUME	VII
AUTHOR CONTRIBUTIONS	IX
LIST OF FIGURES	- 6 -
LIST OF TABLES	- 12 -
MOTIVATION	- 14 -
1. INTRODUCTION	- 16 -
1.1. REVIEW OF ESTABLISHED MICROSCOPY TECHNIQUES.....	- 16 -
1.1.1 Florescent microscopy	- 17 -
1.1.2. Wide field microscopy	- 18 -
1.1.3. Confocal microscopy.....	- 19 -
1.1.4 Super-resolution microscopy	- 21 -
1.2. X-RAY IMAGING	- 22 -
1.2.1 Coherent diffractive imaging (CDI)	- 23 -
1.2.2. X-ray Holography.....	- 27 -
1.3. LENSLESS IMAGING IN VISIBLE DOMAIN	- 28 -
1.4. CONCLUSION.....	- 30 -
2. DIGITAL IN-LINE HOLOGRAPHY: PRINCIPLES AND SETUP	- 33 -
2.1 DIGITAL HOLOGRAPHY (DH)	- 33 -
2.1.1 Configurations	- 34 -
2.1.2 Digital In-line Holography, general concept.....	- 35 -
2.1.3 DH solutions in the industry.....	- 36 -
2.2 PRINCIPLE AND THEORY	- 36 -
2.2.1 Experimental setup.....	- 36 -
2.2.2 Back-propagation and reconstruction.....	- 38 -
2.2.3 Resolution and depth of field.....	- 40 -
2.3 ALGORITHMS	- 41 -
2.4 DEVELOPMENT OF THE MICROSCOPE PROTOTYPE.....	- 44 -
2.4.1 Presentation of the prototype	- 44 -
2.4.2 Calibration of the spatial resolution	- 45 -
2.5. CONCLUSION.....	- 53 -
3. BIOMEDICAL APPLICATIONS	- 55 -
3.1. IMAGING OF ZEBRAFISH EMBRYOS.....	- 55 -
3.1.1. Sample preparation protocol.....	- 56 -
3.1.2. Zebrafish embryo imaging – configuration 1	- 56 -
3.1.3. Zebrafish embryo imaging – configuration 2	- 57 -
3.2. LABEL-FREE CANCER CELL IMAGING (U2OS CELL)	- 58 -
3.2.1. Cell culture protocol.....	- 60 -
3.2.2. Image acquisition and processing: high NA using lens.....	- 60 -
3.2.3. Image acquisition and processing: high NA using pinhole	- 62 -
3.3. IN-VIVO ANALYSIS OF CYANOBACTERIA MOTILITY (SYNECHOCYSTIS PCC 6803)	- 65 -
3.3.1. Sample preparation	- 66 -
3.3.2. Synechocystis motility in water	- 67 -

3.3.3. <i>Synechocystis motility fixed in gelatine</i>	- 69 -
3.4. EXTENSION DIH TO 3D VIEW.....	- 70 -
3.4.1. <i>Theoretical aspects</i>	- 71 -
3.4.2. <i>Calibration and results using a 3D calibration sample</i>	- 73 -
3.4.3. <i>3D reconstruction of a bio-sample</i>	- 77 -
3.5. CONCLUSION	- 80 -
4. A NOVEL FTH MICROFLUIDIC MICROSCOPE AND APPLICATIONS IN BIOLOGY	- 83 -
4.1. FOURIER TRANSFORM HOLOGRAPHY PRINCIPLES AND THEORY	- 83 -
4.1.1 <i>General principle</i>	- 83 -
4.1.2 <i>Principle of image reconstruction</i>	- 85 -
4.1.3 <i>Resolution</i>	- 86 -
4.2. MICROFLUIDICS HOLOGRAPHIC CONFIGURATION.....	- 87 -
4.2.1 <i>Cell handling in a non-uniform field: DEP and EP effects</i>	- 88 -
4.2.2. <i>Microfluidics in the context of FTH imaging</i>	- 92 -
4.3 DESIGN AND FABRICATION OF MICROFLUIDIC CHIPS FOR LENSLESS MICROSCOPY	- 92 -
4.3.1 <i>Pupil and nanoholes constrains</i>	- 93 -
4.3.2 <i>Design and simulation of the microfluidic part</i>	- 94 -
4.3.3 <i>Electrodes Design</i>	- 95 -
4.3.4 <i>Microfabrication procedure and assembly</i>	- 100 -
4.4. FOURIER TRANSFORM HOLOGRAPHY CALIBRATION AND TESTS.....	- 102 -
4.4.1 <i>Image reconstruction</i>	- 104 -
4.4.2 <i>Resolution</i>	- 105 -
4.5. INTEGRATION AND TESTING THE ELECTRO-OPTO-FLUIDIC PLATFORM	- 106 -
4.5.1. <i>Preparation protocol</i>	- 107 -
4.5.2. <i>DEP experiment</i>	- 108 -
4.5.3. <i>Microfluidic FTH imaging</i>	- 112 -
4.6. CONCLUSIONS	- 115 -
5. CONCLUSIONS.....	- 119 -
ANNEX A	- 123 -
A.1.1 INTERFERENCE	- 124 -
A.1.2 COHERENCE	- 125 -
A.1.3 DIFFRACTION	- 126 -
ANNEX B	- 129 -
ANNEX C	- 131 -
ANNEX D	- 135 -
ANNEX E	- 137 -
ANNEX F	- 139 -
ANNEX G	- 143 -
ARTICLES.....	- 145 -
BIBLIOGRAPHY.....	- 147 -

List of Figures

FIG. 1. 1. JELLY FISH AEQUOREA VICTORIA AND THE GFP PROTEIN, ADAPTED FROM NOBLE PRIZE IN CHEMISTRY 2008.....	17 -
FIG. 1. 2. ILLUSTRATION OF THE RESOLUTION RAYLEIGH CRITERION IN FLUORESCENCE MICROSCOPY ADAPTED FROM CHRISTOPH CREMER AND BARRY R. MASTERS.	18 -
FIG. 1. 3. (A) WIDE-FIELD EXCITES A COLUMN OF THE SAMPLE SECTION, WHICH CAUSES EMISSION FLUORESCENCE FROM BOTH INSIDE AND OUTSIDE THE FOCAL PLANE. OUT-OF-FOCUS FLUORESCENCE CONTRIBUTES TO DETAIL OBSCURITY, LIMITING THE DEPTH OF TISSUE THAT CAN BE IMAGED. (B) IN CONFOCAL MICROSCOPY, A PINHOLE PLACED JUST PROXIMALLY TO THE DETECTOR BLOCKS ALL OUT-OF-FOCUS LIGHT, ALLOWING FOR IN-FOCUS FLUORESCENCE TO BE COLLECTED FROM THE SAMPLE AND DRAMATICALLY IMPROVES VISUAL DETAIL. ADAPTED FROM KIM ET AL.....	19 -
FIG. 1. 4. IMAGES OF 15 μ M THICK MOUSE TISSUE REALIZED WITH 63X/1.4NA OIL OBJECTIVE IN BOTH A) WIDE FIELD AND B) A LASER SCANNING CONFOCAL MICROSCOPE.	20 -
FIG. 1. 5. STIMULATED EMISSION DEPLETION (STED) ADAPTED FROM L. SCHERMELLEH ET AL, JCB.	21 -
FIG. 1. 6. COMPARISON BETWEEN CONFOCAL RESOLUTION AND STED.	22 -
FIG. 1. 7. SCHEMATIC PRINCIPLE OF CDI PRINCIPLE, REPRODUCED FROM.....	24 -
FIG. 1. 8. EXAMPLE OF EXPERIMENTAL SETUP OF PTYCHOGRAPHY.	24 -
FIG. 1. 9. COHERENT DIFFRACTIVE IMAGING (CDI) EXAMPLE OF WHOLE ESCHERICHIA COLI BACTERIA: A) DIFFRACTION PATTERN OF PLANE-WAVE CDI; B) CORRESPONDING IMAGE RECONSTRUCTION, REPRODUCED FROM SCHERMELLEH, AND PTYCHO-TOMOGRAPHYGRAPHY (C) 3D RENDERING OF MEASURED FROZEN-HYDRATED CHLAMYDOMONASCELLS CONFINED IN A GLASS MICROCAPILLARY, REPRODUCE FROM.	25 -
FIG. 1. 10. ILLUSTRATION OF THE PRINCIPLE OF COHERENT DIFFRACTIVE IMAGING (CDI) WITH SINGLE SHOT DATA FROM THE CEA HHG SOURCE. A COHERENT BEAM IS ILLUMINATING AN ISOLATED SAMPLE. A CCD DETECTOR RECORDS THE FAR FIELD DIFFRACTION PATTERN. AN ALGORITHM IS THEN USED TO RECONSTRUCT THE IMAGE OF THE SAMPLE, HERE WITH SUB-100 NM SPATIAL RESOLUTION ²⁷	26 -
FIG. 1. 11. 3D DENSITY OF D. RADIODURANS. (A) DIRECT VOLUME RENDERING OF THE 3D EFFECTIVE MASS DENSITY OF FREEZE-DRIED D. RADIODURANS CELLS. (B) THE CELLS ARE SHOWN FROM ABOVE AND TURNED UPSIDE-DOWN. (C) COMBINED DIRECT VOLUME RENDERING AND SURFACE RENDERING.	27 -
FIG. 1. 12. LENSLESS IMAGING SET-UPS. (A) GENERAL LENSLESS IMAGING EXPERIMENTAL SETUP BASED ON LINE-HOLOGRAPHY (B) EXAMPLE OF A LARGE FIELD OF VIEW (FOV) AND A RESOLUTION COMPARABLE TO THAT OF HIGH-MAGNIFICATION OBJECTIVE LENSES. (C) LENSLESS IMAGING IMPLEMENTED IN A COMPACT DEVICE (D) LENSLESS IMAGING INCORPORATED INTO A CAMERA PHONE HANDSET. MODIFIED FROM REFERENCE ³⁸	29 -
FIG. 1. 13. LIVE CELL HOLOGRAPHIC TOMOGRAPHY-BASED ILLUSTRATION OF LIPID DROPLETS IN A) NON-INFECTED AND B) B. BESNOITI-INFECTED BUVEC. ADAPTED FROM REFERENCE.	30 -
FIG. 2. 1. THE HOLOGRAPHIC PRINCIPLE OF GABOR'S IN NATURE ⁴⁷	34 -
FIG. 2. 2. DIGITAL HOLOGRAPHIC MICROSCOPY: IN-LINE AND OFF-AXIS CONFIGURATION. THE SAMPLE IS REPRESENTED AS A YELLOW SPHERE.....	34 -
FIG. 2. 3. SCHEMA OF DIGITAL IN-LINE HOLOGRAPHY. 1 REPRESENTS THE ILLUMINATION SOURCE, 2 THE PINHOLE OR ASPHERICAL LENS TO INCREASE OF THE NUMERICAL APERTURE AND THE SPATIAL RESOLUTION, 3 THE SAMPLE THAT CAN BE MOVE USING NANOMETRIC STAGES AND 4 THE IMAGE SENSOR.	37 -

FIG. 2. 4. GUI INTERFACE PLATFORM (LABVIEW): THE INTERFACE PERMITS TO CONTROL (LIVE) THE SAMPLE POSITION (1); THE BACK-PROPAGATION FUNCTION TOOLS OR FOCUSES OF THE SAMPLE (2); BOTH AMPLITUDE (3) AND PHASE (4) CAN BE RECONSTRUCTED; THE IMAGES CAN BE SAVE FOR POST-PROCESSING USING THE PANEL IN (5)..... - 38 -

FIG. 2. 5. BLOCK DIAGRAM OF THE RECONSTRUCTION ALGORITHM FOR IN-LINE HOLOGRAPHY (ADAPTED FROM *SAMAAN*). - 43 -

FIG. 2. 6. PICTURE OF THE LENSLESS MICROSCOPE PROTOTYPE. - 45 -

FIG. 2. 7. OPTICAL IMAGE WITH THE RULER. - 46 -

FIG. 2. 8. HOLOGRAM AND AMPLITUDE RECONSTRUCTION OF THE OPTICAL RULER IN THE CASE OF MAGNIFICATION M_1 . THE RECONSTRUCTION WITH TWIN IMAGE CORRECTION WAS OBTAINED AFTER $N = 30$ ITERATIONS. - 47 -

FIG. 2. 9. PLOT PROFILE FOR THE RED LINE IN B WHICH REPRESENTS THE AMPLITUDE RECONSTRUCTION, AFTER TWIN IMAGE CORRECTION, IN THE CASE M_1 WITH $\lambda_1 = 405$ NM AND PIXEL SIZE $\Delta_{\text{PIXEL}} = 0.5 \mu\text{M}$ - 48 -

FIG. 2. 10. PLOT PROFILE FOR THE RED LINE IN B WHICH REPRESENTS THE AMPLITUDE RECONSTRUCTION, AFTER TWIN IMAGE CORRECTION, IN THE CASE M_1 WITH $\lambda_2 = 637$ NM AND PIXEL SIZE $\Delta_{\text{PIXEL}} = 0.7 \mu\text{M}$ - 48 -

FIG. 2. 11. HOLOGRAM AND AMPLITUDE RECONSTRUCTION OF THE OPTICAL RULER IN THE CASE OF MAGNIFICATION M_2 . THE RECONSTRUCTION WITH TWIN IMAGE CORRECTION WAS OBTAINED AFTER $N = 30$ ITERATIONS. - 49 -

FIG. 2. 12. PLOT PROFILE FOR THE RED LINE IN B WHICH REPRESENTS THE AMPLITUDE RECONSTRUCTION, AFTER TWIN IMAGE CORRECTION, IN THE CASE M_2 WITH $\lambda_1 = 405$ NM AND PIXEL SIZE $\Delta_{\text{PIXEL}} = 0.48 \mu\text{M}$ - 49 -

FIG. 2. 13. PLOT PROFILE FOR THE RED LINE IN B WHICH REPRESENTS THE AMPLITUDE RECONSTRUCTION, AFTER TWIN IMAGE CORRECTION, IN THE CASE M_2 WITH $\lambda_2 = 637$ NM AND PIXEL SIZE $\Delta_{\text{PIXEL}} = 0.7 \mu\text{M}$ - 50 -

FIG. 2. 14. HOLOGRAM AND AMPLITUDE RECONSTRUCTION OF THE OPTICAL RULER IN THE CASE OF MAGNIFICATION M_1 . THE RECONSTRUCTION WITH TWIN IMAGE CORRECTION WAS OBTAINED AFTER $N = 30$ ITERATIONS. - 51 -

FIG. 2. 15. PLOT PROFILE FOR THE RED LINE IN B WHICH REPRESENTS THE AMPLITUDE RECONSTRUCTION, AFTER TWIN IMAGE CORRECTION, IN THE CASE M_2 WITH $\lambda_1 = 405$ NM AND PIXEL SIZE $\Delta_{\text{PIXEL}} = 0.6 \mu\text{M}$ - 51 -

FIG. 2. 16. HOLOGRAM AND AMPLITUDE RECONSTRUCTION OF THE OPTICAL RULER IN THE CASE OF MAGNIFICATION M_2 . THE RECONSTRUCTION WITH TWIN IMAGE CORRECTION WAS SIMULATED UNDER $N = 30$ ITERATIONS..... - 52 -

FIG. 2. 17. PLOT PROFILE FOR THE RED LINE IN B WHICH REPRESENTS THE AMPLITUDE RECONSTRUCTION, AFTER TWIN IMAGE CORRECTION, IN THE CASE M_2 WITH $\lambda = 405$ NM AND PIXEL SIZE $\Delta_{\text{PIXEL}} = 0.7 \mu\text{M}$ - 52 -

FIG. 3. 1. ZEBRAFISH STAGE SEQUENCES ADAPTED FROM. - 56 -

FIG. 3. 2. A) 6 HPF FULL ZEBRAFISH EMBRYO, B) DETAIL OF A 24 HPF ZEBRAFISH EMBRYO, C) DETAIL OF A 48 HPF DECHORIONATED EMBRYO, H) RECONSTRUCTED AMPLITUDE IMAGE OF A DECHORIONATED 48 HPF ZEBRAFISH EMBRYO AND CORRESPONDING ZOOMS OF DIFFERENT DETAILS: D) RELATIVE POSITION $Z = 0 \mu\text{M}$, THE RED ARROW IS A BONE STRUCTURE LINE, E) $Z_1 = 250 \mu\text{M}$ THE ARROW INDICATES THE CAUDAL FIN; F) $Z_2 = 500 \mu\text{M}$ THE RED LINE POINTS THE VEIN AND ARTERY WHILE IN G) AT SAME DISTANCE $Z_2 = 500 \mu\text{M}$ THE RED LINES ARE FOLLOWING THE DIRECTION OF INTERSEGMENTAL BLOOD VESSELS. THE GIVEN VALUES OF Z_i CORRESPOND TO THE RELATIVE BACK-PROPAGATION DISTANCE, I.E. TO THE RELATIVE DISTANCE BETWEEN THE TRANSVERSE SLICES. - 58 -

-
- FIG. 3. 3. CELL CULTURE: A) IMAGE ACHIEVED WITH A 20X OPTICAL MICROSCOPE B) RECONSTRUCTED AMPLITUDE IMAGE OF A CELL CULTURE. THE FULL FIELD-OF-VIEW IS PRESENTED WITH THE CORRESPONDENT ZOOM INTO THE RED SQUARES IN THE CELLS REGION. - 60 -
- FIG. 3. 4. RECONSTRUCTED AMPLITUDE IMAGE OF A CELL CULTURE A) WITHOUT TWIN IMAGE CORRECTION B) WITH TWIN IMAGE CORRECTION AND THE CORRESPONDING PHASE IMAGES IN C. THE BOTTOM LINE IMAGES CORRESPOND TO ZOOMS INTO THE RED SQUARES OF A), B) AND C). THE SCALE BAR IS 50 μM - 61 -
- FIG. 3. 5. A), B), C) HOLOGRAM, D), E), F) RECONSTRUCTED AMPLITUDE IMAGE OF CELL CULTURE WITH ACQUISITION SOFTWARE AND NO TWIN IMAGE CORRECTION G), H), I) RECONSTRUCTED AMPLITUDE IMAGE USING POST-PROCESSING DATA WITH TWIN IMAGE CORRECTION; H) IS A ZOOM INTO THE BLUE SQUARE REPRESENTED IN I). THE CAPITAL LETTERS CORRESPONDS TO CYTOPLASM (A), NUCLEAR ENVELOPE (B), AND THE NUCLEOLUS (C). - 63 -
- FIG. 3. 6. ESTIMATION OF THE RESOLUTION ON THE NUCLEAR ENVELOPE: A) THE SAMPLE AND THE REGION CHOSEN FOR CALCULATION TAKEN FROM FIG. 3. 5G THE CAPITAL LETTERS CORRESPONDS TO CYTOPLASM (A), NUCLEAR ENVELOPE (B), AND THE NUCLEOLUS (C); B) PROFILE PLOTS OF THE REGION MARKED IN A. - 64 -
- FIG. 3. 7. LEFT: OPTICAL IMAGE WITH SYNECHOCYSTIS SP. PCC 6803, ADAPTED FROM RIGHT: SCHEMATIC REPRESENTATION OF CYANOBACTERIA' STRUCTURE..... - 65 -
- FIG. 3. 8. SAMPLE PREPARATION FOLLOWING THE PROTOCOL OF CYANOBACTERIA FIXED IN GELATIN. - 66 -
- FIG. 3. 9. CONFIGURATION USE FOR CYANOBACTERIA EXPERIMENT AND THEIR INTERACTION WITH THE LIGHT. . - 67 -
- FIG. 3. 10. RECONSTRUCTED HOLOGRAM FROM CYANOBACTERIA, IN A) AMPLITUDE AND B) PHASE; C) SCREENSHOTS AT DIFFERENT TIMES THAT SHOW THE MOVEMENT OF THE CELLS IN THE FLUID IN THE DIRECTION OF THE SOURCE OF LIGHT (THE RED STAR)..... - 68 -
- FIG. 3. 11. A) HOLOGRAM, RECONSTRUCTED HOLOGRAM FROM CYANOBACTERIA, IN B) AMPLITUDE AND C) PHASE; D) SCREENSHOTS AT DIFFERENT TIMES THAT SHOW THE MOVEMENT OF THE CELLS IN THE GELATIN IN THE DIRECTION OF THE SOURCE OF LIGHT (THE RED STAR). THE TRACKING OF THE MOTION OF BACTERIA CAN ALSO BE VIEWED IN THE VIDEO, SEE LINK. - 69 -
- FIG. 3. 12. PRINCIPLE OF BACK-PROPAGATION SLICING. THE HOLOGRAM IS BACK-PROPAGATED IN THE OBJECT PLANE AND DEPENDING ON THE NUMERICAL APERTURE OF THE COLLECTED PATTERN ON THE DETECTOR THE DEPTH OF FOCUS WILL VARY INVERSELY PROPORTIONAL TO IT. A HIGH NA WILL CREATE A THIN DOF (OR 2D SLICE) AND A LOW NA WILL ELONGATE THE DOF. - 72 -
- FIG. 3. 13. ILLUSTRATION OF THE 3D CALIBRATION TARGET. TO BE MORE REPRESENTATIVE WE DEFINE EACH PLAN WITH A DIFFERENT COLOR. IN INSET, AN IMAGE OF THE POLYMERIC MICROSPHERES (IMAGE FROM THE MANUFACTURER). - 73 -
- FIG. 3. 14. ILLUSTRATION OF THE FREE SPACE PROPAGATOR IN DIFFERENT PLANES USING ONE HOLOGRAM. 1- THE SAMPLE IS LOCATED UNDER A COHERENT ILLUMINATION. 2- ONE HOLOGRAM IS ACQUIRED. 3- BY USING THE SLICING FUNCTION BASED ON FRESNEL PROPAGATION (H_z) WE CAN EXTRACT IMAGES FOR EACH PLAN Δz_i - 74 -
- FIG. 3. 15. THE EXPERIMENTAL HOLOGRAM FROM THE 3D CALIBRATION TARGET (LEFT), AND THE REFERENCE SIGNAL WITHOUT THE SAMPLE (RIGHT). THE ACQUISITION TIME IS 100MS..... - 75 -
- FIG. 3. 16. DEMONSTRATION OF 3D IMAGING WITH DIH. A) THE HOLOGRAM IN FULL FIELD OF VIEW. THE WHITE SQUARE REPRESENTS THE AREA SHOWN IN B; B) THE RECONSTRUCTION OBTAINED FROM HOLOGRAM A) IN THE THREE SUCCESSIVE PLANES. - 75 -
- FIG. 3. 17. A) ZOOM INTO EACH MICROSPHERE MARKED FIG. 3. 16 -B WHEN ON FOCUS (I.E. AT THE APPROPRIATE PROPAGATION DISTANCE). B) THE SAME MICROSPHERES, BUT AS RECONSTRUCTED FOR THE PROPAGATION
-

DISTANCE THAT PUT PARTICLE 1 INTO FOCUS. THE ZOOM FACTOR WAS REDUCED IN ORDER TO SEE THE INTERFERENCE RINGS AROUND THE OUT OF FOCUS MICROSPHERES. - 76 -

FIG. 3. 18. OPTICAL IMAGE OF 10 μ M DIAMETER MICROSPHERES, OBJECTIVE 20X. - 76 -

FIG. 3. 19. U2OS CELLS OBSERVED WITH AN OPTICAL MICROSCOPE. THE FIRST IMAGE REPRESENTS THE SAMPLE THAT WILL BE IMAGED WITH OUR DIH MICROSCOPE. IN THE SECOND IMAGE, WE CAN SEE AN AREA WITH A GROUP OF CELLS. - 77 -

FIG. 3. 20. A) THE EXPERIMENTAL HOLOGRAM OF THE DIH; B) THE AMPLITUDE RECONSTRUCTION WITH TWIN IMAGE CORRECTION, AFTER N = 10 ITERATION, RESPECTIVELY C) THE PHASE RECONSTRUCTION - 78 -

FIG. 3. 21. SLICING OF THE RECONSTRUCTED AMPLITUDE OF THE CELL DISPLAYED IN FIG. 3. 20-B. SLICES ARE RECOVERED AT DIFFERENT FOCAL POINTS Δz_i (μ M) RANGING FROM 0 TO 8 μ M. - 79 -

FIG. 3. 22. 3D RECONSTRUCTION OF U2OS CELLS USING SLICING FUNCTION LEFT: THE SLICES USED FOR RECONSTRUCTION; RIGHT: THE 3D VIEW OF THE SAMPLE (SEE VIDEO *LINK*). - 79 -

FIG. 3. 23. A) CONFOCAL IMAGE OF U2OS CELLS TRANSFECTED WITH GFP-FUSIONS AND LABELED WITH MITOTRACKER, RESPECTIVELY B) TRANSMISSION REPRESENTATION OF THE SAME SAMPLE. BOTH WITH A MAGNIFICATION FACTOR 60X. - 80 -

FIG. 4. 1 ILLUSTRATION OF THE HOLOGRAPHIC SEPARATION IN FOURIER TRANSFORM HOLOGRAPHY. - 87 -

FIG. 4. 2. A SCHEME OF THE WORKING PRINCIPLE OF OUR EXPERIMENTAL PROTOTYPE OF LAB-ON-A-CHIP FTH MICROSCOPE. - 88 -

FIG. 4. 3. EXAMPLE OF UNIFORM (A) AND NON-UNIFORM (B) ELECTRIC FIELD EFFECT ON ELECTRICALLY CHARGED PARTICLES AND ON NEUTRAL POLARIZED PARTICLES (POSITIVE DEP), RESPECTIVELY⁹⁷. - 89 -

FIG. 4. 4. POSITIVE DEP OF 557 NM DIAMETER FLUORESCENT LATEX SPHERES ON CASTELLATED ELECTRODES WITH AN APPLIED SIGNAL OF 8 VOLTS PEAK-TO-PEAK AT 700 KHZ. THE SPHERES COLLECT AT THE HIGH FIELD REGIONS MARKED B, C. - 90 -

FIG. 4. 5 SCHEMATIC REPRESENTATION OF THE PHENOMENON OF ELECTROPORATION, ADAPTED FROM LAKSHMANAN ET AL. - 91 -

FIG. 4. 6 OPTICAL IMAGE OF A MICROFLUIDIC ELECTROPORATION DEVICE. - 91 -

FIG. 4. 7 SCHEMATIC REPRESENTATION OF THE MICROFLUIDIC CHIP. - 93 -

FIG. 4. 8. BOTTOM VIEW OF THE GLASS LAYER WITH THE PATTERN OF THE FOV PUPIL AND NANOHOLES (THEIR POSITION IS REPRESENTED BY THE SQUARES), REPRESENTED IN TRANSMISSION (PINK COLOUR MEANS FULL TRANSMISSION, WHITE MEANS NO TRANSMISSION). - 94 -

FIG. 4. 9. GENERAL PRINCIPLES DESIGN: A) 2-LAYER CHIP; B) DETAIL OF THE CENTRAL AREA; C) DETAIL OF THE CHAMBER AND VISUALIZATION AREA. BLUE - FLUIDIC LAYER (IN Si); RED: FIELD OF VIEW AND NANOHOLES (IN GLASS); CYAN: ELECTRODES (METAL ON GLASS). NOTES: I) THE LINKS TO PADS ARE NOT REPRESENTED; II) THE DIMENSION OF THE NANOHOLES ARE CONVENTIONALLY EXAGGERATED; III) LIGHT CAN ONLY GO THROUGH THE RED PARTS; IV) THE SEMICIRCLE AROUND THE NANOHOLES REPRESENT OPENINGS BY ETCHING IN SILICON LAYER THAT ALLOWS THE LIGHT TO PASS THROUGH AND REACH THE DETECTOR. - 94 -

FIG. 4. 10. CM FACTOR AS FUNCTION OF FREQUENCY. - 95 -

FIG. 4. 11. FIRST DESIGN OF PLANAR ELECTRODES CONFIGURED ON A GLASS SUBSTRATE. - 96 -

FIG. 4. 12 F_{DEP} (Z COMPONENT MAGNITUDE). CROSS-SECTION VIEW ALONG (LEFT) AND ACROSS (RIGHT) THE INPUT-OUTPUT CHANNEL..... - 97 -

FIG. 4. 13 VECTOR REPRESENTATION OF THE DEP FORCES. CROSS-SECTION ALONG (LEFT) AND ACROSS (RIGHT) THE INPUT-OUTPUT CHANNELS ASSOCIATED TO FIG. 4. 11 FIELD REPRESENTATION RESPECTIVELY (ARROW LENGTH IN LOGARITHMIC SCALE)..... - 97 -

FIG. 4. 14 CELLS TRAJECTORIES IN THE NEGATIVE DEP REGIME. POSITIONS REACHED AFTER 300 SECONDS. INSET: INITIAL POSITIONS OF THE CELLS. - 97 -

FIG. 4. 15 OPTIMIZED DESIGN OF PLANAR ELECTRODES CONFIGURED ON A GLASS SUBSTRATE..... - 98 -

FIG. 4. 16 CELLS TRAJECTORIES IN C1 CONFIGURATION IN NEGATIVE (LEFT) AND POSITIVE (RIGHT) DEP REGIMES. POSITIONS REACHED AFTER 300 SECONDS AND AFTER 30 SECONDS, RESPECTIVELY. - 99 -

FIG. 4. 17 CELLS TRAJECTORIES IN C2 CONFIGURATION IN NEGATIVE (LEFT) AND POSITIVE (RIGHT) DEP REGIMES. POSITIONS REACHED AFTER 300 SECONDS AND AFTER 30 SECONDS, RESPECTIVELY. - 100 -

FIG. 4. 18 CELLS TRAJECTORIES IN C4 CONFIGURATION IN NEGATIVE (LEFT) AND POSITIVE (RIGHT) DEP REGIMES. POSITIONS REACHED AFTER 300 SECONDS AND AFTER 30 SECONDS, RESPECTIVELY. - 100 -

FIG. 4. 19. A) OPTICAL IMAGE OF THE ELECTRODES AND THE CHAMBER AND B-C) SEM IMAGES OF THE NANOHOLE, WITH A DIAMETER OF C) 490 NM AND B) 1400 NM. IN D) A PICTURE OF THE FINAL DEVICE. THE TWO LARGE HOLES VISIBLE ON THE TOP SIDE ARE USED TO FILL THE CHAMBER WITH FLUID AND CELLS. ELECTRICAL WIRES (YELLOW AND BLACK) ARE CONNECTED TO THE PADS. NOTE: THE THREE ELECTRODES ARE NUMBERED A, B1, B2. - 101 -

FIG. 4. 20. THE EXPERIMENTAL DEMONSTRATION FOR THE TWO CASES: A. THE BEAM IS CENTRED WITH THE PUPIL: A) THE RECORDED HOLOGRAM AND B) THE HOLOGRAPHIC RECONSTRUCTION OF A. ; B. THE BEAM IS CENTRED BETWEEN THE PUPIL AND ONE NANOHOLE: C) THE RECORDED HOLOGRAM AND D) THE HOLOGRAPHIC RECONSTRUCTION OF THE SIGNAL IN C. NOTE: THE RED AND YELLOW CIRCLES IN B SURROUNDS THE HOLOGRAMS (SOLID LINE) AND THEIR CONJUGATES (DASH LINE) FOR TWO DIFFERENT NANOHOLE. - 103 -

FIG. 4. 21. FINAL OBJECT RECONSTRUCTION: A) ZOOM INTO THE SAMPLE EXIT FIELD RECONSTRUCTED IN THE PUPIL PLANE, CORRESPONDING TO $z = 0 \mu\text{m}$. HERE, WE SELECTED THE TOP RECONSTRUCTION FROM IMAGE 4.19-D. B) MODULUS OF THE SAMPLE RECONSTRUCTION IN THE SAMPLE PLANE, I.E. AT $z = 400 \text{ nm}$; C) MODULUS OF THE SAMPLE EXIT WAVE AFTER BACK-PROPAGATION AT $z = 600 \text{ nm}$. THE TRANSVERSE SAMPLING STEP IS $0.5 \mu\text{m}$ - 105 -

FIG. 4. 22 THE INITIAL WAVEFRONT (LEFT) USED FOR THE RECONSTRUCTION AND THE WAVEFRONT IN THE PLANE SAMPLE (RIGHT). - 105 -

FIG. 4. 23. RESOLUTION TEST OF THE SAMPLE (ELECTRODES). THE GRAPH IS A LINEOUT ALONG THE RED LINE ON THE GREY SCALE IMAGE, REPRESENTING THE HOLOGRAPHIC RECONSTRUCTION OF THE SAMPLE..... - 106 -

FIG. 4. 24. OPTICAL IMAGE OF HE^LA CELLS AFTER TRYPSINISATION, OBTAINED WITH A 40X MAGNIFICATION. THE CELL'S DIMENSION, MARKED BY THE BLACK LINE, IS $15 \mu\text{m}$ - 108 -

FIG. 4. 25 ELECTRODES CONNECTION: C1- BETWEEN A AND B1+B2 (B1 AND B2 CONNECTED TOGETHER).- 109 -

FIG. 4. 26. MICROFLUIDIC CHIP FOR CELLS SEPARATION IN THE CIRCULAR REGION FOR HOLOGRAPHIC IMAGING. THE CELL ISOLATED UNDER A POSITIVE DEP IS HIGHLIGHTED BY A RED CIRCLE. FOUR PHASES OF DISPLACEMENT ARE PRESENTED IN: **A**: $t=0\text{s}$, **B**: $t=4\text{s}$, **C**: $t=8\text{s}$, **D**: $t=18\text{s}$. THE CELL IS ISOLATED AT $t=14\text{s}$. THOSE IMAGES WERE OBTAINED WITH AN OPTICAL MICROSCOPE WITH A 20X OBJECTIVE. - 110 -

FIG. 4. 27. OPTICAL MICROSCOPE IMAGE OF A N-DEP EXPERIMENT (20X OBJECTIVE). THE WHITE DOTTED CIRCLE EMPHASIZES THE TENDENCY OF THE CELLS TO FORM GROUPS IN THE PRESENCE OF AN ELECTRIC FIELD.- 111 -

- FIG. 4. 28. CELL HANDLING WITH P-DEP FOR 10VPP AND 20MHZ. THE CELL OF INTEREST IS MARKED WITH A RED SQUARE IN A TRANSMISSION IMAGE OBTAINED WITH A MICROSCOPE OBJECTIVE OF 10X. IN B), A MAGNIFIED IMAGE OF THE RED SQUARE, WITH A 40X MICROSCOPE OBJECTIVE. - 112 -
- FIG. 4. 29. EXPERIMENTAL RESULTS OF HE^LA CELL IMAGING WITH THE FTH MICROSCOPE. - 113 -
- FIG. 4. 30. CELLS HANDLING WITH P-DEP FOR 10VPP AND 20MHZ. A) OPTICAL MICROSCOPE IMAGE, IN TRANSMISSION AND 20X OBJECTIVE, WITH ABOUT 20 CELLS IN THE FIELD OF VIEW; B) HOLOGRAPHIC RECONSTRUCTION TAKEN ABOUT 10 MIN AFTER THE OPTICAL IMAGE, $Z=450\mu\text{M}$ - 114 -
- FIG. 4. 31. EXPERIMENTAL RESULTS OF HE^LA CELLS IMAGING WITH THE FTH MICROSCOPE. A) THE HOLOGRAM DETECTED IN THE FAR FIELD BY THE CAMERA; B) AMPLITUDE OF THE FOURIER TRANSFORM OF A), WITH BOTH THE OBJECT AND ITS MIRROR CONJUGATE VISIBLE. C) ZOOM FROM IMAGE B) INTO THE RECONSTRUCTED FIELD IN THE PUPIL PLANE ($Z=0\mu\text{M}$). D) THE RECONSTRUCTION OF THE MODULUS IN THE SAMPLE PLANE: $Z = 450\text{MM}$ - 115 -
- FIG. 4. 32. A) SIMULATIONS OF A MASK WITH FOV OF $150\mu\text{M}$ IN THE ELECTRODES REGION, RESPECTIVELY A MASK OF $20\mu\text{M}$ WIDTH IN THE CHANNELS REGION. TWO NANOHOLES OF $1\mu\text{M}$ DIAMETER WERE CONSIDERED AS FTH REFERENCES (THE POSITION OF THE NANOHOLES IS SURROUNDED BY THE RED CIRCLE); B) THE SIMULATION SHOWS THE HOLOGRAMS RECONSTRUCTION AND THEIR CONJUGATE. NOTE: IN THE FOV REGION A REPRESENTATION OF A CELL OF $15\mu\text{M}$ DIAMETER WAS CONSIDER AS AN ARTIFICIAL OBJECT FOR A SIZE REFERENCE. - 116 -

List of Tables

TABLE 3. 1. TYPICAL REFRACTIVE INDEX VALUES FOR VARIOUS ORGANELLES IN A CELL ^{73,74,75}	- 59 -
TABLE 4. 1 DIMENSIONS OF THE NANOHOLES (NHs) ON 5 VERSIONS OF THE CHIP.	- 102 -
TABLE 4. 2. ELECTRICAL PROPERTIES OF THE CELLS AND BUFFER ^{39,40}	- 108 -
TABLE 4. 3 APPLIED VOLTAGE IN C1 CONFIGURATION: BETWEEN A AND B1+B2 (B1 AND B2 CONNECTED TOGETHER).....	- 111 -

Motivation

The microscope's historical progress reveals a revolution in science and medicine and illustrates how it has become one of the most vital tools in medicine today. For a long time the sub millimetric world of microorganisms was inaccessible to humans and limited the medical progress and diagnosis. Only after the invention and refinement of the microscope did scientists manage to decipher many of the mysteries of this unknown micro universe. One such landmark was the first observation and drawing of bacteria realized by Anton von Leeuwenhoek in the early 1670s. Today's microscopes produce striking images that impress with their forms and, apart from the esthetic aspect, offer invaluable information for many fields of application.

Microscopes are usually built around a common process: one or more lenses deflect the trajectory of the light rays coming from the object to be observed in order to create a magnified image, visible to the naked eye or on a detector. After the first demonstrations in the 17th century, other methods to increase the resolution and contrast were developed. New improvements are still proposed nowadays. One such direction is to extend its use out of the limits of the visible part of the electromagnetic spectrum of light, towards the X-ray domain. However, although extraordinary progresses have been made, modern versions of those microscopes still use the same operating principle as the original ones.

Nevertheless, new operating principles have been proposed over the years in order to obtain ever better spatial resolutions, leading to major breakthroughs, such as fluorescence microscopy and super-resolution microscopy. X-ray microscopy, on the other hand, prompted the development of diffraction based imaging techniques that are at the heart of this work. However, as I saw during the formation that I attended during my PhD (FEBS Advanced Course Functional imaging of nuclear organization & signaling, advance microscopy - <http://intranet.lcam-fnwi.nl/>), not all biological problems can be addressed based on the distribution of fluorescence markers, for example. The objective of **Chapter 1** is to give a brief overview about the evolution of the most used microscopy techniques from optical to the ones based on diffractive physics.

Diffraction based modern techniques, often called through the generic name of lensless microscopy, are the new hot topic of microscopy research. First developed for X-ray and electron imaging, the techniques suppress the objective optics to remove aberration sources and reach resolutions closer to the Abbe limits. Building up on those successes, lensless imaging is now being transposed back to the visible range. Emerging from the initial idea of Denis Gabor, holography represents one basis of these new microscopy approaches. Digital holography is based on the diffraction and interference phenomena. The light scattered by the sample is directly recorded by a spatial detector. Using this so-called hologram, a numerical algorithm then reconstructs the sample image with a resolution that is not any more limited by the objective quality. The main advantages of lensless techniques are their ability to reach nanometric spatial resolutions with label-free samples. Additionally, as the complete diffracted field is reconstructed, they can emulate many different types

of visible microscopy in a single acquisition (dark and bright field, phase contrast...). Moreover, they allow pseudo-3D reconstructions of the samples without requiring destructive and time-consuming acquisition procedures.

This thesis aims to merge two major fields, lensless microscopy and biology, into a new ‘microscopy know-how’. The idea started in the LIDYL research laboratory in 2014 in the context of an ANR Project called « Nano-Imagine » (‘2D Nanoscale Lensless Imaging and wave front correction in imaging’), built around a strong collaboration between LIDYL (CEA Saclay) and the SME Company Imagine Optic (<https://www.imagine-optic.com/>). At that time, a first PhD student posed the basis of the apparatus. However, real applications relevant to bio-related problems were not yet addressed.

During this thesis, I improved the technology and tested its impact on cell imaging and analysis. I developed the instrument further on, with applications relevant to biologists in mind. Based on these preliminary studies, I could select digital in-line holography (DIH) as the lensless technique best fitted for most bio-related problems. Its main advantages are the large field of view for imaging which permits to test a wide range of samples (from single cell to embryos or tissue); the low dose of radiation that allows an in-vivo analysis and 3D image acquisition in single shot. The simplicity of digital in-line holography configuration brings easy handling, portability (easy to transport from one place to another) and low manufacturing costs. The technique, the microscope and its applicability are presented **Chapter 2 and 3**. Additionally in **Chapter 3**, I assess non-invasive 3D in-line holographic imaging and its impact on imaging reconstruction and cell analysis.

One key advantage of lensless microscopy is the ability for live imaging at high speed. This is of crucial importance for point of care applications, where speed and statistics are mandatory. However, in line holography presents drawbacks that could prevent those high profile applications. Therefore, in the last experiment of my PhD, I switched to Fourier Transform Holography (FTH), which the aim of integrating a microfluidics device to manipulate the samples directly in the prototype. This proposal uses the expertise in microfluidics that I accumulated during my master thesis. The concept is based on single cell analysis by coupling electric handling and measurements with digital holography, thus allowing imaging single cells with nanoscale resolutions. Compared to DIH, where the resolution is limited by various parameters (sensor pixel size, sample transparency, temporal and spatial resolution...), in the case of FTH microscopy the resolution is given by the holographic references necessary in the image reconstruction. The development of Lab-on-a-chip (LOC) systems allows the optimization of the production costs which contributes to cost-effective image tool and data analysis. With the help of LOC a low number of cells or molecules can be manipulated, detected or/and analysed which further leads to truly single-cell studies.

The successive steps of development and implementation of the microfluidic chip, together with the first preliminary imaging results, are presented **Chapter 4**.

1. INTRODUCTION

The microscopy evolution opened a large field of applications especially in biology. Major breakthroughs have been realized targeting better and better spatio-temporal performance of various microscopy modalities, such as classical optical microscopy and fluorescence microscopy. In the latter case, only selected biological problems can be addressed based on the compatibility and distribution of fluorescence markers. In many instances additional and complementary contrast properties are needed. Thanks to the large availability of lower cost, megapixel detectors and the progress in computing speed in the 2000s years, digital lensless imaging has emerged. This technique has the advantage, by definition, of being free of optical components, avoiding the drawbacks of aberrations which systematically deteriorate the final image.

Imaging by lensless technique is non-invasive and capable of operating on label free samples in a large field-of-view (FOV). A single acquisition is enough to record the amplitude and phase of the sample, which further allows real-time filming of biological processes when a sequence of image can be recorded using fast cameras. Another significant advantage of lensless imaging is the possibility to achieve 3D reconstruction of volume objects from a 2D image-hologram and to retrieve both amplitude and phase information of the optical field.

Here, we review some biological context and their standard imaging tools. I also introduce the development of lensless imaging and its 3D applications.

1.1. Review of established microscopy techniques

The discovery of the cell as the basic unit of life in the 17th century¹ opened for scientists an important field of investigation. Two major issues made the progress of their exploration harder: the dimension of the cells and their transparency. During the next centuries, these two difficulties led the researchers to build machines based on bulky lenses. Complex optical systems with aberration correction have been invented. By varying the type of lenses and light sources, five types of light microscopy can be defined: bright-field, dark-field, phase-contrast, differential interference, and fluorescence. In the late 20th century, fluorescent microscopy has been demonstrated expanding optical microscopy to fluorescence spectroscopy and fluorescent probes. Fluorescence or STED microscopy has been awarded. Fluorescence microscopy has allowed to image objects much smaller than the diffraction limit. Other techniques have allowed to break the diffraction limit such as multiphoton microscopy (or second harmonic generation imaging), confocal microscopy, super-resolution imaging, wide field, spin disk to cite a few.

In the next section we will present some of the currently most used techniques, their limitations and the importance of investigating new microscopy tools, such as lensless imaging.

1.1.1 Florescent microscopy

Florescent microscopy remains one of the most important standard technique applied in biological imaging, especially 3D cell imaging. The principle of fluorescence imaging is based on different molecules with fluorescent properties, so called fluorophores that are attached to the cell component that we aim to image. One of the most used fluorophore is Green Fluorescent Protein (GFP), which is a fluorescent protein from the Pacific jelly fish *Aequorea Victoria*, discovery that received Nobel Prize in Chemistry in 2008². From this basis many fluorescent proteins were developed to cover the full visible spectrum of emissions³.

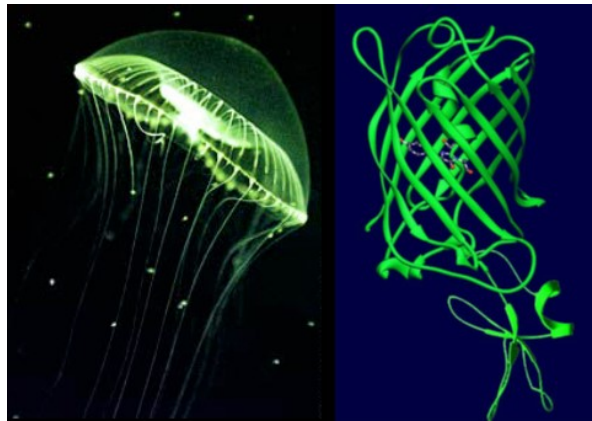


FIG.1. 1. JELLY FISH AEQUOREA VICTORIA AND THE GFP PROTEIN, ADAPTED FROM NOBLE PRIZE IN CHEMISTRY 2008.

These fluorescent proteins can for instance be fixed on microbeads or antibodies or can be directly expressed by genetically modified cells. Illuminated with a specific exciting wavelength λ_a , a fluorophore absorbs the light and re-emits at a longer wavelength λ_e . Using a filter, this light can be selected and re-imaged by standard microscopy to give a repartition map of the fluorophores. Each fluorophore emission is detected as a point source which creates the shape of the object or more precisely the intensity distribution. These shapes are called the point spread distribution. The smoother the shape, the more details can be identified in the image.

In Fig.1. 2 is illustrated the resolution given by the Rayleigh criterion. In the top images the diffraction pattern resulted from the emission of one single fluorescent molecule is represented, while in the bottom parte is shown an overlap of two adjacent point sources.

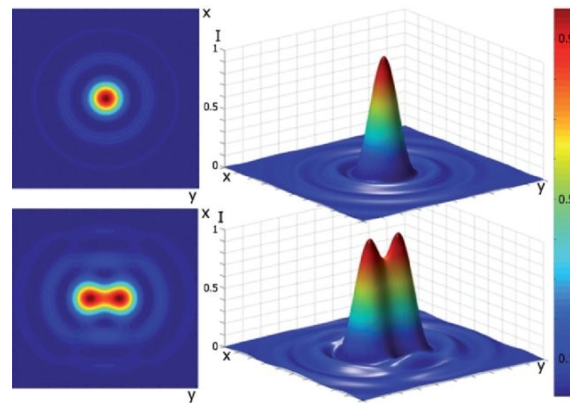


FIG.1. 2. ILLUSTRATION OF THE RESOLUTION RAYLEIGH CRITERION IN FLUORESCENCE MICROSCOPY ADAPTED FROM CHRISTOPH CREMER AND BARRY R. MASTERS⁴.

Imaging systems resolution in fluorescence microscopy are usually based on the Rayleigh criterion⁵, which marks the well know “diffraction limit resolution”. The formula that defines this principle is:

$$\sin\theta = 1.22 \frac{\lambda}{NA} \quad (1.1)$$

where λ is the wavelength of light and NA the numerical aperture of the optical system. The diffraction limit of the system represents the resolving distance between two points that are separated by the angle θ . For instance, if we consider $\lambda = 550\text{nm}$, and the $NA = 1.5$ (corresponding to medium based on oil), the maximum resolution in this case is approximately 440 nm.

The principal advantage of this technique is its high signal to noise ratio. However, there are still lot of problems that results due to the fluorophores that causes damage in the image visualization. The three main techniques based on fluorescent emission are *the wide-field microscopy*, *the confocal microscopy* and *the super-resolution microscopy* and their derivatives. We present them below, with their main characteristics.

1.1.2. Wide field microscopy

Wide field microscopy refers to a basic concept of illumination in microscopy. The whole sample is illuminate with a specific wavelength that excites the fluorescent molecules in the bio-sample. This is a good advantage for producing 2D images of the specimen as the entire field can be captured at once. The typical setup uses two filters, one for excitation and one for emission, and a dichroic mirror. By only allowing light of specific wavelengths to pass, the filter cube reduces the ‘noise’

from the sample, ensuring a clear image is produced which only shows the fluorescence of specific fluorophores. In the Fig.1. 3A a schematic configuration of the optical part is presented.

However, the wide field and linear excitation implies that the fluorescent molecules that are out of focus will also be excited. Therefore, the out of focus emission represents a factor that reduces the resolution, and makes the production of 3D images sometimes unsuitable for this type of microscopy. Additionally, a post-processing step can be realized with deconvolution programs to improve the quality of the image by removing part of the blur.

1.1.3. Confocal microscopy

The most important advantage of this microscope is the ability to produce thin optically section, removing unwanted light above and below the focal plane. It can provide better contrast and allows 3D reconstruction by combining the data from a stack of images. Confocal scanning microscopy is the most common optical sectioning technique used for fluorescence imaging⁶. The configuration scheme of the apparatus is presented in Fig.1. 3B.

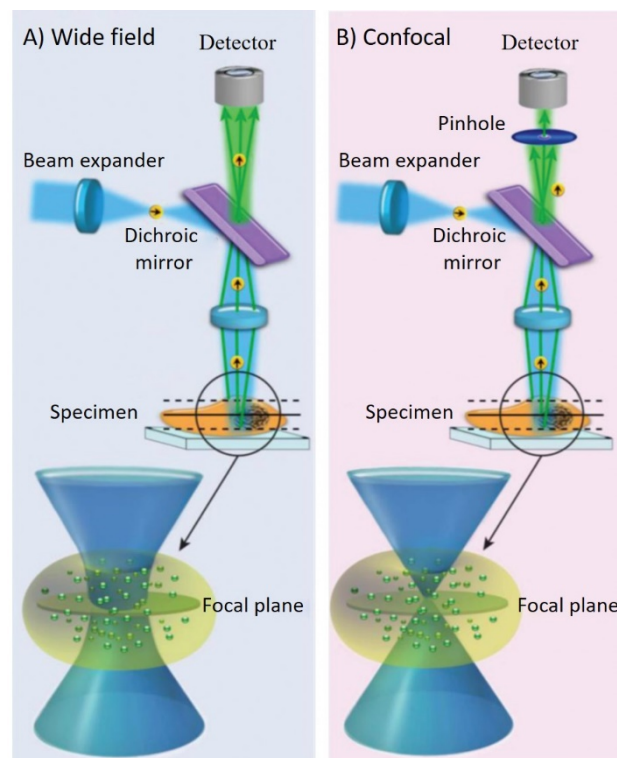


FIG.1. 3. (A) WIDE-FIELD EXCITES A COLUMN OF THE SAMPLE SECTION, WHICH CAUSES EMISSION FLUORESCENCE FROM BOTH INSIDE AND OUTSIDE THE FOCAL PLANE. OUT-OF-FOCUS FLUORESCENCE CONTRIBUTES TO DETAIL OBSCURITY, LIMITING THE DEPTH OF TISSUE THAT CAN BE IMAGED. (B) IN CONFOCAL MICROSCOPY, A PINHOLE PLACED JUST PROXIMALLY TO THE DETECTOR BLOCKS ALL OUT-OF-FOCUS LIGHT, ALLOWING FOR IN-FOCUS FLUORESCENCE TO BE COLLECTED FROM THE SAMPLE AND DRAMATICALLY IMPROVES VISUAL DETAIL. ADAPTED FROM KIM ET AL7.

The basic concept behind the confocal approach is that spatial filtering techniques are used to remove the light that is out of focus, by placing a pinhole as shown in Fig.1. 3B. The emitted light is detected by a photomultiplier tube (PMT) or an avalanche photodiode (APD) and the image is then constructed by mapping the detected light in dependence of the position of the scanning spot. The 3D volume is scanned by translating either the sample or the optical parts along the three directions. This modality of acquisition presents an important photo-toxicity for the sample since at each acquisition of a point in the volume, the exciting light passes through the whole culture.

One important problem of confocal is photobleaching, especially for sample with low signal. Photobleaching is a photochemical process which defines the alteration of the fluorophores, in other words the fluorophores are no longer able to fluoresce. This effect disturbs the correct observation of fluorescent molecules that are basically destroyed by the light exposure necessary to stimulate them. However, this effect has other applications such as study the motion of diffusion of molecules, but adapted microscopy techniques are needed. These techniques include FRAP (Fluorescence recovery after photobleaching) where observing the recovery after photobleaching can confirm the movements of certain molecules. FRET (Foster Resonance Energy Transfer) is another technique where the energy transfer between the two light-sensitive molecules can be used to determine the distance between two molecules.

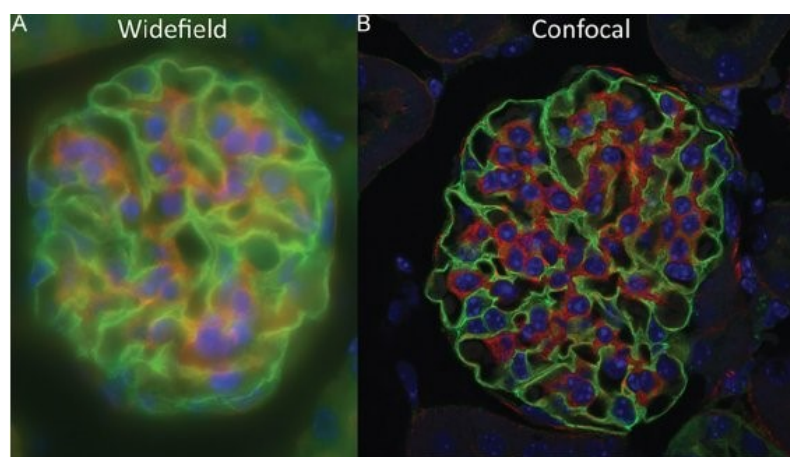


FIG.1. 4. IMAGES OF 15 μ m THICK MOUSE TISSUE REALIZED WITH 63X/1.4NA OIL OBJECTIVE IN BOTH A) WIDE FIELD AND B) A LASER SCANNING CONFOCAL MICROSCOPE⁸.

The confocal has better resolution in comparison with the wide field technique, but it has the disadvantage of the harmful nature of high-intensity laser irradiation to living cells and tissues.

1.1.4 Super-resolution microscopy

Wide-field deconvolution and confocal microscopes are widely used in optical bio imaging, but recently several new technologies, collectively named super-resolution microscopy, have been developed. Super-resolution microscopy breaks the classical diffraction limit and shift the optical resolution down to macromolecular or even molecular levels⁹. Among those different techniques one can cite PALM (PhotoActivation Localization Microscopy), STORM (Stochastic Optical Reconstruction Microscopy) or STED (Stimulated-Emission-Depletion fluorescence microscopy) for example.

I propose here to detail the STED method. STED microscope is a modified confocal laser microscope that uses a second laser¹⁰. The second laser has a longer wavelength and the beam has a donut shaped (in Fig.1. 5 it is called STED pulse PSF). In the process of image acquisition the donut beam follow the excitation beam. Its role is to filter the excited fluorophores used for the final image¹¹. Therefore, all the excited fluorophores that are in the centre of the donut beam (the hole in donut) are able to emit fluorescence, while the others are ‘bleached’ back to the ground state.

The resolution in this case is given by the hole in the centre of the donut, and can go beyond the diffraction limit.

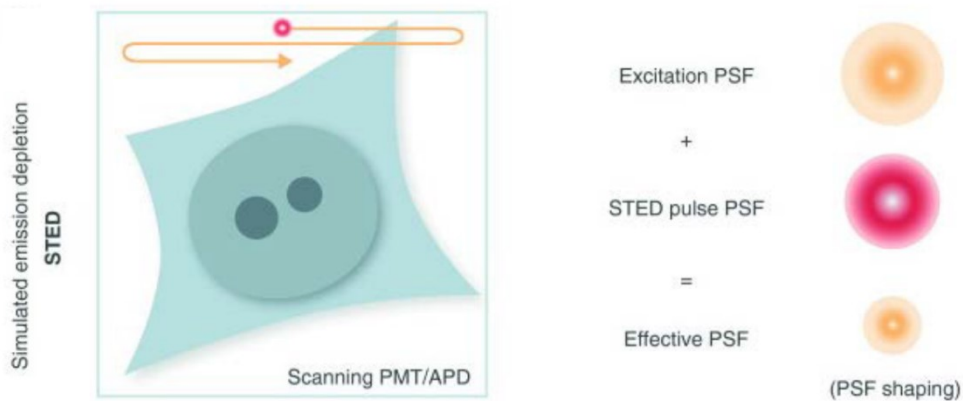


FIG.1. 5. STIMULATED EMISSION DEPLETION (STED) ADAPTED FROM L. SCHERMELLEH ET AL, JCB¹².

In the Fig.1. 6 a comparison between the two powerful microscopic tools is presented. In the STED image the lateral resolution is much higher whereas the longitudinal resolution (z) is just slightly improved. However the damage of the sample is larger. This leads to the disadvantage that in-vivo imaging possibilities are limited.

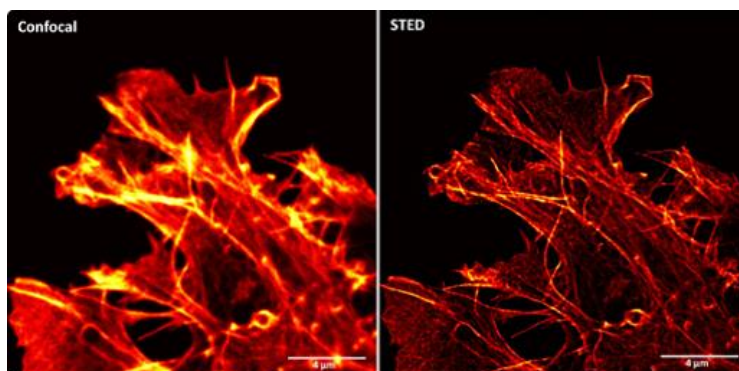


FIG.1. 6. COMPARISON BETWEEN CONFOCAL RESOLUTION AND STED.

Super-resolution microscopy allows discrimination of single features at high spatial densities. STED microscopy is clearly suitable for the investigation of rapid dynamic processes beyond the diffraction limit. A potential drawback in STED is the very high intensity of the laser that could produce photobleaching or phototoxicity. If we compare with a conventional laser scanning confocal the power used is much higher.

1.2. X-ray imaging

Beside the compact imaging tools that are able to resolve most of the elements of a cell, X-ray microscopy has the power to look into the nanoscale domain and understand the functions of the organelles and proteins, thanks to X-rays short wavelengths. Additionally, the use of X-rays leads to chemical specificity, and the short pulse duration has already allowed time resolved studies of dynamics. X-ray microscopes are typically based on synchrotron-radiation sources, which makes them hard to access to. Nowadays many X-ray microscopes are available worldwide, such as the ones at Berkeley's Advanced Light Source¹³ or the HERMES beamline at SOLEIL¹⁴. However, while spatial resolutions of 1nm have been demonstrated, the resolution is typically around 25nm, limited by the signal to noise ratio¹⁵ and the performance of the X-ray lenses. An additional constraint is the fact that for soft X-ray radiation, especially for the so-called water window range, especially useful for bio-imaging, vacuum experimental conditions are needed, which restricts a lot its applicability.

Moreover, the contrast in X-ray imaging is given by the interaction of the X-rays with the electron clouds. The larger the element atomic number, the higher the contrast. Since the biological samples are mostly constituted of low atomic number elements, a high flux of photons is necessary. This dramatically increases the dose received by the sample. Consequently, as biological matter is highly radiation sensitive, severe radiation damage may be induced¹⁶. To summarize, the limitation of the X-ray "traditional" microscopy techniques are mostly given by the high energy used that

produces radiation damage in most of the wet samples, and the difficulty to manufacture optics in the X-ray domain for high spatial resolution. A potential solution for these drawbacks is to remove the objective optics, and to replace them by numerical algorithms acting as virtual lenses. This is the basic idea behind the family of lensless imaging techniques called coherent diffraction imaging.

In the next section, we present a short overview and history of the lensless approach, starting from the X-ray techniques now largely in used for biological imaging to some derivatives that are developed nowadays in the visible regime (see section 1.3. Lensless imaging in visible domain).

1.2.1 Coherent diffractive imaging (CDI)

In coherent diffraction imaging (CDI), **no lens is needed**. One only needs to record the intensity of the diffraction pattern that emerges in the far field after the interaction of a spatially coherent light beam with an isolated object on a high-resolution high-dynamic range pixelated detector as shown Fig.1. 7. The sample and the image sensor are positioned in the same axis perpendicular to the beam. A highly coherent illumination source is required since the techniques is based on the interferences of the diffracted waves on the detector. A general explanation for readers that are not familiar with the phenomena could be find in *Annex A*. In no way does the diffraction pattern resemble the object itself but, given specific experimental conditions, a computer can convert this digitized image using a phase-retrieval approach. In this way, it is possible to create much better images than with conventional lens-based systems. No aberration lens distorts the magnified image, therefore the spatial resolution, limited only the highest frequencies recorded on the CCD, i.e. by the CCD numerical aperture, can be pushed down close to the diffraction-limit given by the source wavelength. CDI has some advantages compare to super-resolution microscopy. The final image is aberration-free (no lens is used to obtain it). Most importantly, the large penetration depth of X-rays makes the reconstruction of whole cells possible without the need of sectioning. Finally, CDI can lead to quantitative 3D imaging of the entire content of cells and cellular organelles.

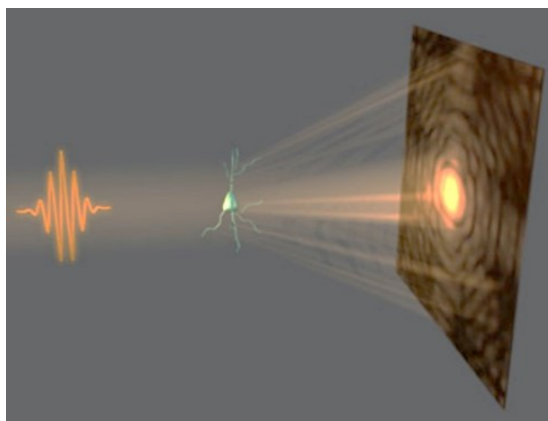


FIG.1. 7. SCHEMATIC PRINCIPLE OF CDI PRINCIPLE, REPRODUCED FROM¹⁷.

Several variants of CDI have been proposed, the more common ones for biological imaging being ptychography¹⁸ and plane-wave CDI.

Ptychography is a derivative approach of coherent diffractive image to overcome the limitation of the finite size of the sample. The X-ray beam is scanned over the sample with a spatial overlap between consecutive positions, while a diffraction pattern is recorded for every position (see Fig.1. 8). Ptychography extension to tomography, the so-called ptycho-tomography, is already available at some synchrotron beamlines. While this kind of experiment is highly demanding (in term of experimental stability, total acquisition time and computational power), it has led to impressive 3D resolutions (Fig.1. 9c).

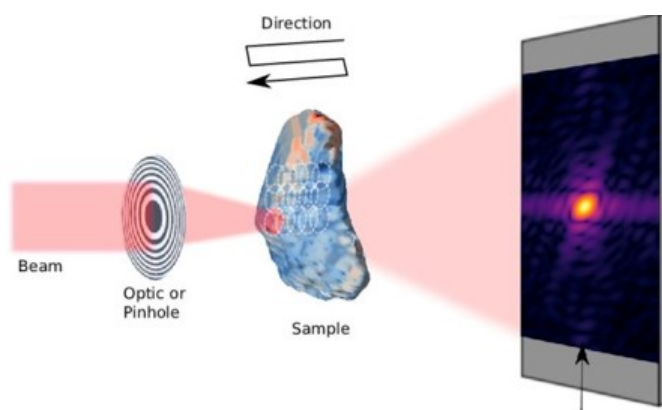


FIG.1. 8. EXAMPLE OF EXPERIMENTAL SETUP OF PTYCHOGRAPHY¹⁹.

Plane wave CDI simply follows the experimental scheme described before, and has already led to impressive results (Fig. 1.9 a, b illustrates one such use in bio-imaging). Collecting several 2D diffraction patterns at different angles of a single sample can lead to a tomographic reconstruction of the 3D image of the sample. However, this induces additional experimental constraints, the major one being linked to radiation induced damages. Nevertheless, this capability is already available in various synchrotron beamlines.

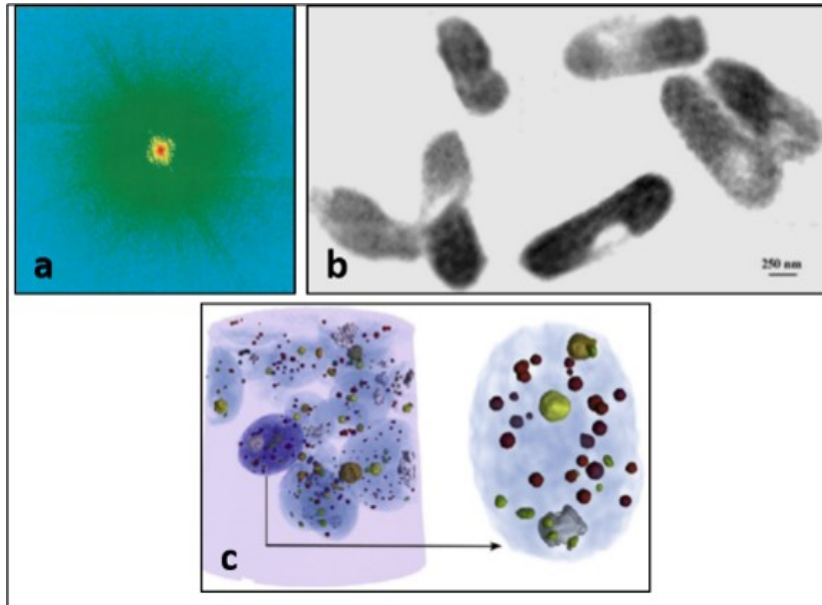


FIG.1. 9. COHERENT DIFFRACTIVE IMAGING (CDI) EXAMPLE OF WHOLE ESCHERICHIA COLI BACTERIA: A) DIFFRACTION PATTERN OF PLANE-WAVE CDI; B) CORRESPONDING IMAGE RECONSTRUCTION, REPRODUCED FROM SCHERMELLEH²⁰, AND PTYCHOTOMOGRAPHY (C) 3D RENDERING OF MEASURED FROZEN-HYDRATED CHLAMYDOMONAS CELLS CONFINED IN A GLASS MICROCAPILLARY, REPRODUCE FROM²¹.

CDI with short wavelength laser based sources: Since the first demonstration of CDI²², many researchers have taken a large step in this direction using synchrotron radiation, free electron lasers (FEL) and laser high harmonic generation (HHG). Ultrafast lensless imaging has first been demonstrated using the FLASH FEL facility in Hamburg (Germany)²³. In 2007, the group of *Kapteyn* and *Murnane* in Boulder Colorado (USA) has demonstrated a similar capability but in multi-shot using high harmonic generation from a 0.8- μm wavelength femtosecond table-top Ti:Sa laser system at a repetition rate of 1 kHz²⁴. Using their powerful μJ yield harmonic source, driven by an 800 nm high power terawatt laser system, the CEA group proved that single shot femtosecond studies were possible. They are one of the world leaders in this domain^{25 26 27}. Experiments on ultrafast nanoscale characterization of magnetic samples have also been performed. More recently^{28 29 30}. Following these results, CDI using HHG driven by new fibre laser sources has been demonstrated but at a relatively long XUV wavelength ($\lambda=33\text{nm}$)³¹. Future prospects focus on pushing nanoscale imaging applications down to the nanolithography (13.5 nm) and the water window (2-4 nm) spectral ranges.

Attosecond coherent diffractive imaging: Imaging methods that combine attosecond temporal with nanometre spatial resolution are currently out of reach. Coherent diffractive imaging is based on the diffraction by a sample of a quasi-monochromatic illumination with a coherence time that exceeds the duration of an attosecond pulse. Because of the extremely broad nature of attosecond spectra, novel imaging techniques are required. Attosecond nanoscale lensless imaging has been

demonstrated by CEA and collaborators using a discrete HHG spectral produced by a train of attosecond pulses³². To generalize the approach to broadband isolated attosecond sources a novel method has been proposed by CEA. It is based on a numerical monochromatisation of the broadband diffraction pattern by the regularised inversion of a matrix, which depends only on the spectrum of the diffracted radiation. Experimental validations in the visible and hard X-rays has already validated the applicability of the method (Huijts et al, submitted to Nature Photonics, in review, <https://arxiv.org/abs/1909.11345v1>)³³. Because of its generality and ease of implementation for single attosecond pulses, we expect this method to find widespread applications in future attosecond technologies such as petahertz electronics, attosecond nanomagnetism or attosecond energy transfer.

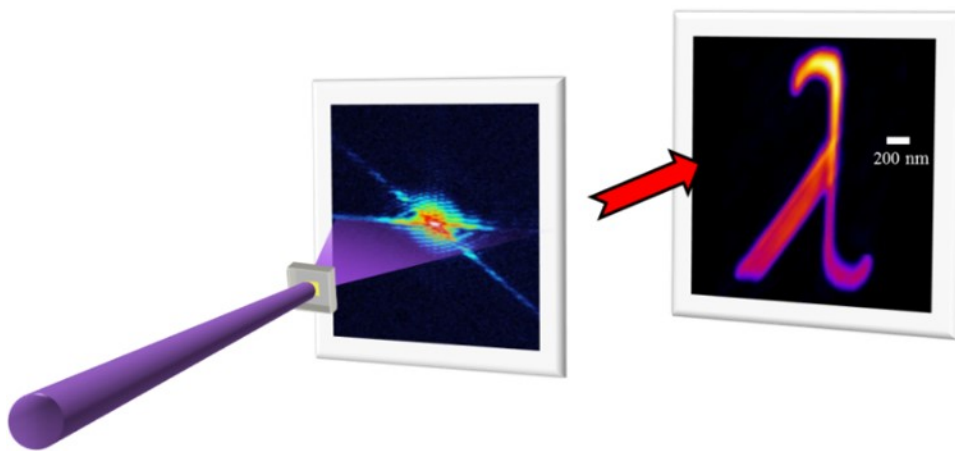


FIG.1. 10. ILLUSTRATION OF THE PRINCIPLE OF COHERENT DIFFRACTIVE IMAGING (CDI) WITH SINGLE SHOT DATA FROM THE CEA HHG SOURCE. A COHERENT BEAM IS ILLUMINATING AN ISOLATED SAMPLE. A CCD DETECTOR RECORDS THE FAR FIELD DIFFRACTION PATTERN. AN ALGORITHM IS THEN USED TO RECONSTRUCT THE IMAGE OF THE SAMPLE, HERE WITH SUB-100 nm SPATIAL RESOLUTION²⁹.

Computer stereo lensless imaging: At a nanometre scale, the ability to gain insights into the 3D properties of artificial or biological systems is often critical. This information is, however, difficult to retrieve as most techniques provide only two-dimensional projections along the imaging axis. Nowadays, intense ultrashort XUV and X-ray pulses allow realizing nanometre scale studies and ultrafast time-resolved 2D movies. Unfortunately, these existing methods are not easily extended to single shot 3D images. As a rule, a three-dimensional image of an object is generated mathematically from hundreds of individual images. This means a high expenditure of time, large amounts of data and high radiation sums. Our group at CEA has now succeeded in significantly accelerating this process by developing a method in which two twin images of an object can be taken with a single ultrafast acquisition from two different viewing directions, which are then combined to form a spatial image - similar to how the human brain forms a stereo image from the two slightly

different images of the two eyes. Computer-aided spatial vision is already established in the field of machine vision and robotics and is now demonstrated in the XUV and hard X-ray spectral ranges³⁴.

1.2.2. X-ray Holography

In 1948 the Nobel Prize Laureate *Denis Gabor* proposed his famous “method of wave-front reconstruction” which opened the era of holography. The holography technique is presented in details in **Chapter 2**. The development of optical lasers enabled *E. N. Leith and J. Upatnieks*³⁵ to demonstrate the first wave-front reconstruction of a hologram with a reference beam. Since this first successful demonstration, the method of holographic reconstruction has found applications in many different fields of arts, science and technology. Holographic optical elements were used in laser design and investigations of optical semiconductor laser light properties. The full illumination of the specimen makes possible the 3D reconstruction of it recording several projection of the sample from different angles. Using X-ray illumination, holography can be a favourable technique due to the high resolution imaging. As in the case of CDI the sample is isolated. However, the sample may also suffer changes or damage during an experiment when positioned on a surface. There are only a few examples of holographic hard X-ray imaging applied to biological cells.

In the paper of *M. Bartels et al*³⁶ present the 3D image reconstruction of unstained and unsliced, freeze-dried cells of the gram-positive bacterium *Deinococcus radiodurans* (see Fig.1. 10) by tomographic X-ray propagation microscopy, i.e. projection tomography with phase contrast formation by free space propagation.

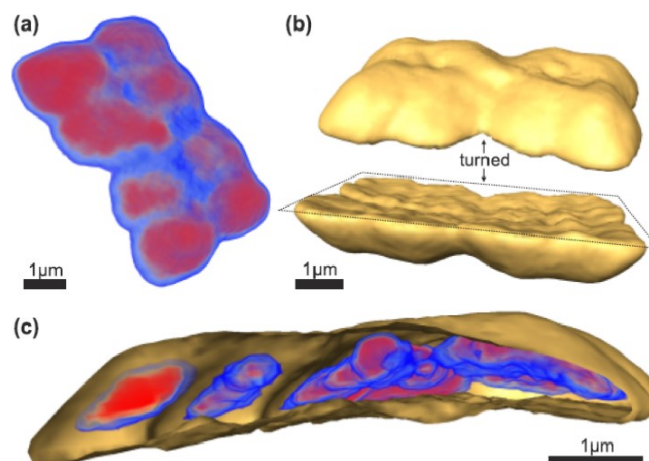


FIG.1. 11. 3D DENSITY OF *D. RADIODURANS*. (A) DIRECT VOLUME RENDERING OF THE 3D EFFECTIVE MASS DENSITY OF FREEZE-DRIED *D. RADIODURANS* CELLS. (B) THE CELLS ARE SHOWN FROM ABOVE AND TURNED UPSIDE-DOWN. (C) COMBINED DIRECT VOLUME RENDERING AND SURFACE RENDERING.

However, instead of ptychography tomography which involves scanning two translations and one rotation with correspondingly large overhead time, they used X-ray propagation microscopy, based on projection imaging with contrast formation by free space propagation. For the 3D imaging the advantages is the uses of the scanning based on only one degree of freedom (rotation axis). This produces less overhead time in data acquisition and imposes less restrictive requirements on mechanical accuracy and long-term vibrational stability.

In a recent study *T. Gorkhover et al*³⁷ developed a new holographic method called in-flight holography. With this method, they were able to demonstrate the first X-ray holograms of nano-sized viruses that were not attached to any surface. In the new study, the authors superimposed scattered X-ray light from the virus with scattered X-ray light from a reference nano-sized sphere. The curvature in the superimposed images from the two objects provided depth information and details about the shape of the 450-nanometer-wide virus, the mimivirus. This technique greatly simplified the interpretation of the data. However, their large and expensive setups constitute a huge drawback, which limits their use to only a few X-ray free electron laser facilities in the world.

1.3. Lensless imaging in visible domain

In the 90s, Lensless imaging based on coherent diffraction was initially developed for application in the X-ray and UV spectral ranges because of the difficulty to produce lenses in these wavelength domains. In the beginning of 2000s years we have seen a rapid progress of processing computer clocks and faster graphic processor units. This has allowed to develop digital image processing and made possible to have an-all computed based microscope. After 2010 we have seen the emergence of the technique in the visible range and company have started to exploit the technique for microscopy. The advantage is that this lensless technique is label free and can provide high resolution (sub-micrometer) with a large field of view (FOV) equal to the size of the camera chip (~several mm²).

Lensless microscopy often utilizes an on-chip imaging geometry in which a transparent sample is placed on an image sensor array. This systems are based inexpensive high-resolution CMOS image sensors, combine with the computational power of laptops, tablets, smartphones, and other mobile devices³⁸.

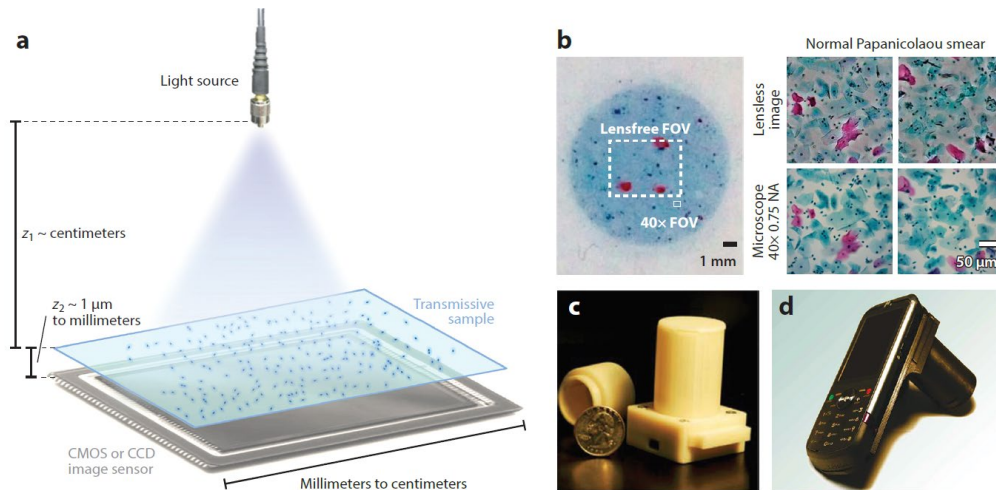


FIG.1. 12. LENSLESS IMAGING SET-UPS. (A) GENERAL LENSLESS IMAGING EXPERIMENTAL SETUP BASED ON IN-LINE-HOLOGRAPHY (B) EXAMPLE OF A LARGE FIELD OF VIEW (FOV) AND A RESOLUTION COMPARABLE TO THAT OF HIGH-MAGNIFICATION OBJECTIVE LENSES. (C) LENSLESS IMAGING IMPLEMENTED IN A COMPACT DEVICE (D) LENSLESS IMAGING INCORPORATED INTO A CAMERA PHONE HANDSET. MODIFIED FROM REFERENCE³⁸.

During the last decade, lens-free microscopy has been developed in a variety of systems and found lots of applications^{39 40 41 42}. Most of the applications have been targeting biological applications. The demand of miniaturization and portability made lensless microscopy attractive. It proposes also to overcome some of the limitations of fluorescence microscopy. Indeed, the resulting image depends on the optical path through the sample rays and allow to retrieve its local complex refractive index. The technique is label-free which opens a large variety of samples compared to fluorescent microscopy.

Although nanometric imaging techniques without 2D lenses are now under control, 3D imaging requires new developments. Digital in-line holography microscopy, Optical coherence tomography, Optical diffractive tomography are few methods that can perform 3D imaging.

For instance, one of the most recent device is created by Nanolive (<https://nanolive.ch/>). Their image techniques is based on light interference (holography) and for a higher magnification additionally they use an objective (dry objective, magnification x60, NA = 0.8). They had developed an innovative technology that allows living cells to be examined in a three-dimensional space without damaging them. This device extends the exploration of living cells from single cells to cell populations. It enables to investigate macro cellular dynamics like cell health, proliferation, movement and function. At micro level micro organelle dynamics and interactions such as mitochondrial network characterization could be monitored. Several application could be found for instance in the following references^{43 44 45}.

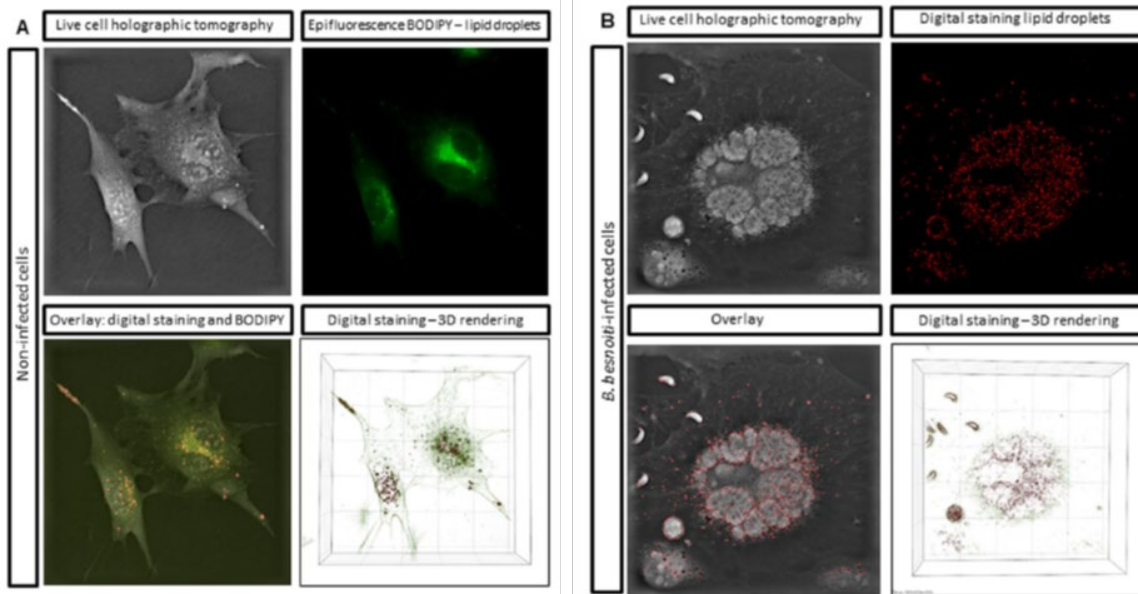


FIG.1. 13. LIVE CELL HOLOGRAPHIC TOMOGRAPHY-BASED ILLUSTRATION OF LIPID DROPLETS IN A) NON-INFECTED AND B) *B. BESNOITI*-INFECTED BUVEC. ADAPTED FROM REFERENCE⁴⁶.

In the classic microscopy tools, all dynamic studies of the intracellular content is made with the aid of fluorescent markers. That means that an additional step before imaging is made, the preparation of the sample. In lensless imaging, “virtual” colours can encode the spatial detail of a sample based only on the refractive index of the intracellular structure.

Such a compact and simple technology leads to numerous advantages in the microscopy applications:

- The absence of lenses or additional parts means robustness and ease of use.
- Such a device can handle incubator conditions, while being user-friendly for the experimenter;
- The absence of labels can remove the toxicity induce by these molecules; moreover a longer time of investigation could be proceed.
- The possibility to achieve 3D reconstructions from a simple hologram by numerically retrieving 2D slices.

1.4. Conclusion

In this chapter the most significant points in the microscope evolution were outlined. The importance of microscopy is crucial in the analysis and diagnosis of human diseases. We saw that the progression of these imaging apparatuses was focused on increasing the spatial resolution, which lead to machines based on bulky lenses. The optimization came with the discovery of the fluorescent

molecules that permits the enhancement of the resolution up to molecular level. However, we so that this invasive methods presents limitations and new strategies were proposed. X-ray imaging opened the field of lensless imaging as the optics needed for this configuration are hard to be produced and very expensive.

Lensless imaging experiments in the X-ray domain make it easy to achieve nanoscale resolutions. Nevertheless, they are highly constraining experimentally, thus limiting their exploitation beyond the academic domain: synchrotron facilities needed. To overcome these limitations, new techniques based on coherent illuminations begin to emerge and provide complementary tool to study 3D bio-samples.

Based on these general introduction we would like to highlight the importance of the development of new microscopes configuration. The portability and easy to use could be an alternative for the very expensive tools. Basic diagnostics such as identification of the cancer cells or cell motility analysis, can be successfully realize with the resolution of these apparatus.

2. DIGITAL IN-LINE HOLOGRAPHY: PRINCIPLES AND SETUP

Holography was discovered in 1947. While the scientist Dennis Gabor⁴⁷ was aiming to improve the power of the electron microscope to image single atoms, he fortuitously came upon his theory of wavefront reconstruction, which later he named it *holography* based on the Greek words '*holos*' for *whole* and '*graphie*' for *message*. During the next decade, the development in the field was difficult because the light sources available at the time were not intrinsically spatially coherent. Spatial coherence was built over light beam propagation. The basic principle introduced by Gabor is elegant. The waves weakly scattered by the object interferes with an unscattered wave (the reference wave) on a photographic film to form an interference pattern, which was then recorded. Gabor showed how it was possible to restore the original object wavefield by illuminating the recorded film with the original reference wave. However, an inherent artefact of the method is that the resultant image of the reconstructed object is impaired by the presence of a twin-image. The twin-image problem was first addressed by Leith and Upatnieks^{35 48} who developed an off-axis configuration which produced reconstructions free of the twin-image.

2.1 Digital holography (DH)

Digital holography (DH)^{49 50 51} uses the same principle as the one initially developed by Gabor. This technology has been made possible thanks to the development of digital detectors and the increase of computational speeds and memories. Instead of using photographic films, a digital support such as charged coupled devices (CCDs) or Complementary Metal Oxide Semiconductor (CMOSs) is used to record the hologram. DH uses numerical algorithm to simulate the image formation, simulating the reference wave illumination proposed by Gabor. CCD and CMOS detectors have nowadays multi-megapixels CCD sensors with high spatial resolution and high dynamic range that allow encoding the hologram with accurate information. The amplitude and phase image of the scene can then be processed through numerical reconstruction. The image is reconstructed based on Fourier Transforms and back-propagation functions. Algorithms have been developed to correct the holograms from the twin image superposition, aberrations, broadband nature of the illumination, to cite few examples.

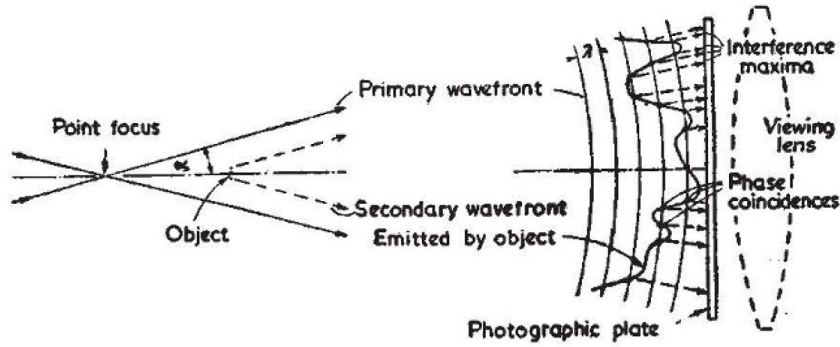


FIG. 2. 1. THE HOLOGRAPHIC PRINCIPLE OF GABOR'S IN NATURE⁴⁷.

2.1.1 Configurations

There are two forms of digital holographic configurations: in-line and off-axis. In this chapter we focus on in-line digital holography. In in-line holography (see Fig. 2. 1), the reference beam and the diffracted object beam both share the same optical axis. In the off-axis scheme (Fig. 2. 2), the reference beam propagates along another axis than the diffracted beam, usually parallel. The off-axis holography is computationally advantageous as it removes traditional limitation of in-line digital holography errors (i.e. twin image and phase sensitivity)^{52 53 54 55}. However, the in-line setup has many advantages over an off-axis setup including a less developed speckle noise, a more efficient use of the CCD bandwidth⁵⁶, a stable design and an easier sample implementation. This explains why this configuration was initially chosen for development in the LIDYL Ultrafast Nanophotonics group. Later, in **Chapter 4** we introduce a modified version of the off-axis configuration, that brings several advantages in terms of resolution and sample manipulation.

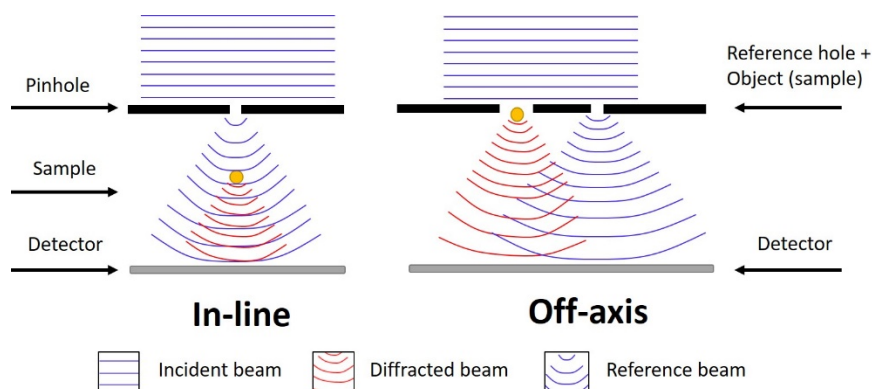


FIG. 2. 2. DIGITAL HOLOGRAPHIC MICROSCOPY: IN-LINE AND OFF-AXIS CONFIGURATION. THE SAMPLE IS REPRESENTED AS A YELLOW SPHERE.

In both configurations an incident beam illuminates the sample. In the case of in-line experiment, after the sample the undisturbed beam and disturbed beam interfere on the camera, and an in-line hologram is then recorded. For the off-axis configuration, the reference beam unperturbed by the sample, interferes with the object beam on the camera and then an off-axis hologram is recorded.

2.1.2 Digital In-line Holography, general concept

As mentioned in **Chapter 1**, digital in-line holography (DIH) involves no lenses between object and detector. It only requires the reference wavefield to be traveling in the same axis as the object wavefield at the plane of the detector. The light is divided into two components: the scattered light that has interacted with the sample, and the unscattered light that goes through undisturbed. These two components, coherent between them, will interfere on the image sensor forming the so called hologram. The holographic information is then sent to a computer where, through numerical methods, the spatial details of the sample are obtained. In other words no optics are used to form the image of the object that we want to observe.

Amongst the advantages of DIH one can find its simplicity: the setup required is usually only a coherent source, a pinhole, and an image sensor; the speed: intrinsic changes in the object can be followed at the capture video rate of the sensor; high resolution: optimal resolutions, of the order of the wavelength of the laser, can be easily achieved; and, finally, the simplicity of sample preparations: no sectioning or staining is required - feature valued specially in the imaging of biological samples, where living specimens can be viewed. One of the most amazing advantages of DIH is the fact that a single 2D hologram can lead to a 3D image of the object without loss of resolution. This is in strong contrast to standard optical microscopy, where depth of field sharply reduces when one improves the resolution, requiring to mechanically refocus to be able to map out a larger volume. We illustrated this advantage in **Chapter 3** using a numerical reconstruction in several focal plane of Z-test samples and a biological cell.

As drawbacks, the main ones are the requirement of a high numerical aperture since it limits the achievable resolution and the superposition on the reconstruction of a twin image created by an out-of-focus virtual image of the object due to the symmetry of the in-line scheme.

2.1.3 DH solutions in the industry

In the industrial field, commercial solutions have been developed in recent years. Holography is now emerging in the industry with projects benefiting from several million euros in budget. As an example, the Swiss Company NanoLive (<https://nanolive.ch/>) has opened new markets in biology, and medicine (cells interaction, diagnosis cancer cells, and intracellular dynamics). South Korea has just followed with the creation of the Tomocube Company (<http://www.tomocube.com/>) in 2016. These apparatus are extremely novel and are starting to be spread over the world. The resolution of such devices is sufficient (i.e. Nanolive microscope CX-A model can obtain a lateral resolution $x, y = 200$ and an axial resolution $z = 400\text{nm}$) to diagnose, for example, cancer cells. However, most solutions are based on off-axis holography.

In the same line, we have developed a low-cost, long-term industrializable, lensless microscope using the in-line holography principle, called the NanoXim. These developments were undertaken in strong collaboration with the SME Company Imagine Optic (<https://www.imagine-optic.com/>) and started during a previous PhD thesis ⁵⁷ which posed the basis of the apparatus. I developed the instrument further on, with applications relevant to biologists in mind. Using the previous work, I choose an in-line configuration as fitting for most experimental needs. However, in the last experiment of my PhD, I switched to Fourier Transform Holography in order to be able to use microfluidics to manipulate the samples.

2.2 Principle and theory

2.2.1 Experimental setup

In DIH, the object is located nearly in a central position related to the beam illumination. Part of the wave is scattered by the object, thus creating the object wave I_{scat} , and the unscattered part of the wave forms the reference wave I_{ref} . The interference of this two waves is captured by a detector, located perpendicularly to the optical axis at a distance Z from the object. The amplitude at the detector is given by

$$I^* = I_{\text{ref}}^* + I_{\text{scat}}^* \Rightarrow |I^*| = |I_{\text{ref}}^*| + |I_{\text{scat}}^*| + |I_{\text{ref}}^* I_{\text{scat}}^*| + |I_{\text{ref}} I_{\text{scat}}^*| \quad (2.1)$$

In the equation 2.1 the third term represent the hologram, while the fourth term, its complex conjugate, or as we will see in the next sections, the twin image. In our case, the experiments were

performed using a divergent illumination source. We therefore work with a Gaussian mode of numerical aperture $NA = 0.12$ (Annex B and C). We spatially filter the beam using a pinhole of $1 \mu\text{m}$ diameter. The CCD camera is located downstream, after the sample, and records the hologram (see Fig. 2. 3). The CCD (Annex D) has a pixel size $5.5 \mu\text{m}$ and $3296(\text{H}) \times 2472(\text{V})$ active pixels allowing a maximum of 6.6 fps (frame per second). DIH with spherical reference wave⁵⁸ produces a magnified hologram at the recording screen. This implies that the number of fringes captured, and hence the resolution, depends on the object–screen distance as well⁵⁹. The smallest measurable separation of two scattering points increases nearly linearly with source – object distance. The uses of the pinhole and the distance source – screen gives a new $NA = 0.33$ (in fig. 2.3 θ is defined in equation 1.1). To push the resolution we thus locate the object close to the point source. Noting z_1 the distance between the diode and the object, z_2 the distance between the object and the CCD, and $Z = z_1 + z_2$ the diode-camera distance, we can write the magnification in the following form:

$$M = 1 + \frac{z_2}{z_1} = \frac{Z}{z_1} \quad (2.2)$$

The hologram recorded with spherical waves corresponds to the size of the object area, and multiplied by the magnification factor M . Besides, the reconstruction of the object is equal to the size of the hologram, divided by the magnification factor M .

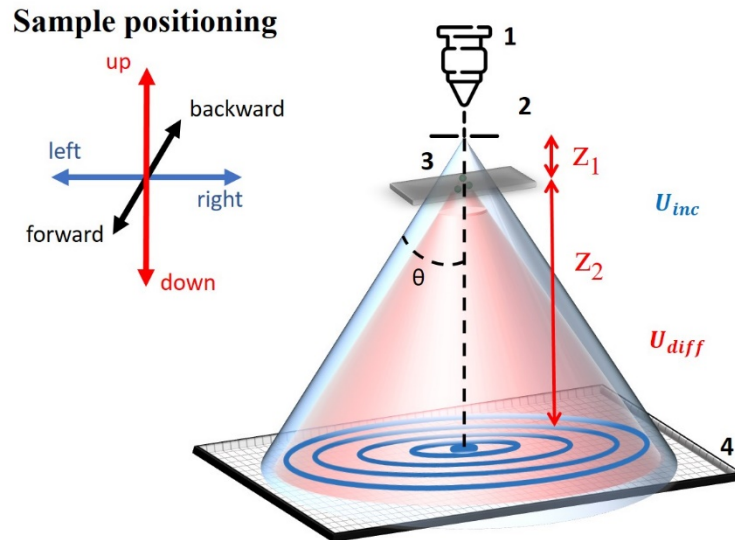


FIG. 2. 3. SCHEMA OF DIGITAL IN-LINE HOLOGRAPHY. **1** REPRESENTS THE ILLUMINATION SOURCE, **2** THE PINHOLE OR ASPHERICAL LENS TO INCREASE OF THE NUMERICAL APERTURE AND THE SPATIAL RESOLUTION, **3** THE SAMPLE THAT CAN BE MOVE USING NANOMETRIC STAGES AND **4** THE IMAGE SENSOR.

2.2.2 Back-propagation and reconstruction

A "user friendly" interface has been developed during the thesis of Julien Samaan and updated during my PhD (see Fig. 2. 4). The dedicated graphical interface that allows the control of the sample position, the control over the magnification factor and the visualization of the reconstruction in real time. The numerical computation replaces the role of the lenses from classical microscope, by back-propagating the recorded hologram using model of light propagation.

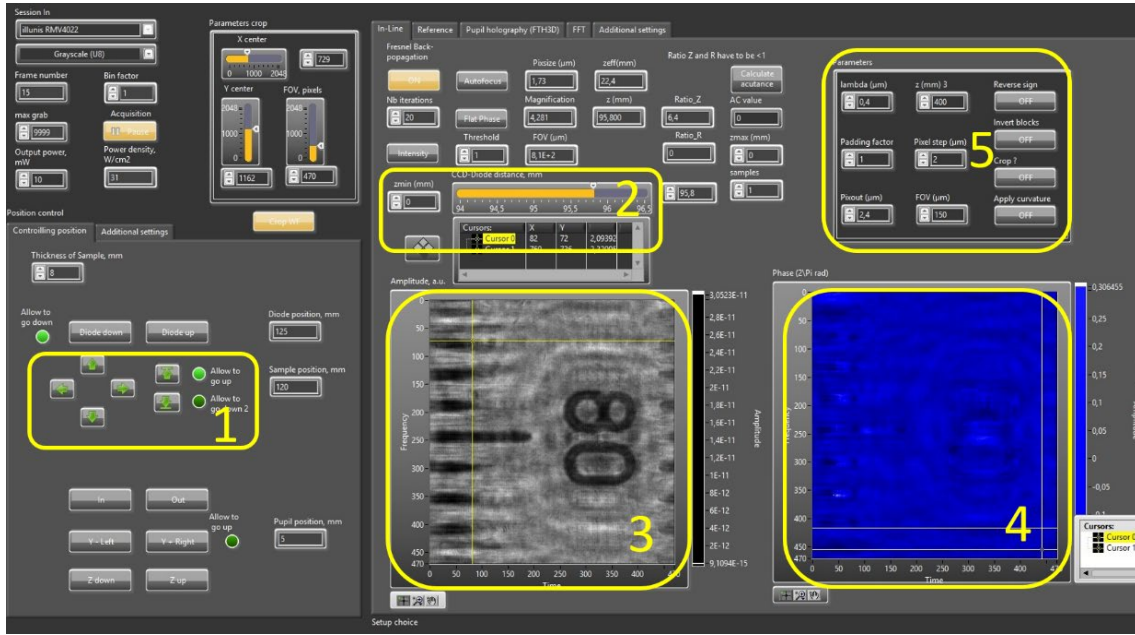


FIG. 2. 4. GUI INTERFACE PLATFORM (LABVIEW): THE INTERFACE PERMITS TO CONTROL (LIVE) THE SAMPLE POSITION (1); THE BACK-PROPAGATION FUNCTION TOOLS OR FOCUSES OF THE SAMPLE (2); BOTH AMPLITUDE (3) AND PHASE (4) CAN BE RECONSTRUCTED; THE IMAGES CAN BE SAVE FOR POST-PROCESSING USING THE PANEL IN (5).

Lensless microscopy is based on the model of Rayleigh-Sommerfeld diffraction formula⁶⁰. Following the notation of Fig. 2. 3, it shows that for a monochromatic incident wave U_{inc} in the free space, $\vec{r}_0 = (\xi, \eta, z_0)$ and wavelength λ , the diffracted wave U_{diff} by a 2D transparent sample t_{2D} at $z=0$ is given at a specific point $\vec{r} = (x, y, z > 0)$ as follow:

$$U_{diff}(\vec{r}) = \frac{z}{i\lambda} \iint t_{2D}(\vec{r}_0) U_{inc}(\vec{r}_0) \frac{e^{ik\|\vec{r}-\vec{r}_0\|}}{\|\vec{r}-\vec{r}_0\|^2} d^2 \vec{r}_0 \quad (2.3)$$

where $k = 2\pi/\lambda$ is the wave number of the field in the free space \mathcal{O} for the 2D objects. Applying the convolution operator \otimes , the equation 2.3 becomes:

$$U_{diff}(\vec{r}) = (U_{inc}t_{2D}) \otimes \left(\frac{ze^{ikr}}{i\lambda r^2} \right) \quad (2.4)$$

The kernel convolution $\frac{ze^{ikr}}{i\lambda r^2}$ is represented by the equation of propagating spherical complex wave $\frac{e^{ikr}}{r}$, normalized by a factor $\frac{z}{i\lambda r}$. The angle formed by the term $z/r = \cos\theta$, gives the angle between the normal directions to the diffracting plane. The equation 2.4 introduces the mathematical formulation of the well-known Huygens-Fresnel principle: each point \vec{r}_O of the sample produces spherical waves, and the total sum of them is the diffracted wave. This equation is an important mathematical tool to propagate a complex field from the object at distance z to the sensor plane at z_s , using a convolution.

In addition, adding the Fresnel formulation we could say that the illumination is normal to the sample and the sensor. It is therefore considered that the diffracting object is small compared to the propagation distance, so $z_s \gg (x, y; \xi, \eta)$ we obtain:

$$\vec{r} - \vec{r}_O = \sqrt{(x - \xi)^2 + (y - \eta)^2 + z_s^2} \cong z_s + \frac{(x-\xi)^2 + (y-\eta)^2}{2z_s} \quad (2.5)$$

and 2.4 becomes:

$$U_{diff}(\vec{r}) = (U_{inc}t_{2D}) \otimes \left(\frac{e^{ikrz_s}}{i\lambda z_s} e^{\frac{ik}{2} \frac{r_{2D}^2}{z_s}} \right) = (U_{inc}t_{2D}) \otimes (h_{z_s}^\lambda) \quad (2.6)$$

Where $h_{z_s}^\lambda = \frac{e^{ikrz_s}}{i\lambda z_s} e^{\frac{ik}{2} \frac{r_{2D}^2}{z_s}}$ represents the Fresnel propagator. The Fourier transform of $h_{z_s}^\lambda$ gives the free space transfer function. So equation 2.6 becomes:

$$U_{diff} = \mathfrak{F}^{-1}[\mathfrak{F}[U_{inc}]H_{z_s}^\lambda] \quad (2.7)$$

In most of algorithms used for lensless imaging, this equation is preferred due to its rapidity and simplicity.

Finally, the hologram recorded represents the intensity of the field in the image sensor plane.

$$I_{CCD} = |U_{diff}|^2 = |U_{inc}(t_{2D}) \otimes (h_{z_s}^\lambda)|^2 \quad (2.8)$$

This diffracted wave can be written as the square module of the field:

$$|U_{diff}| = \sqrt{I_{CCD}} \quad (2.9)$$

During the detection the phase is lost since the detector used is sensible only to the intensity detection (equation 2.9). Thus, we miss information on the complex field detected. Without the phase, we have the appearance of a virtual object in the reconstruction, which is the symmetrical of the real object

with respect to the CCD camera, the so called twin image. In the section 2.3 Algorithms we recalled the principle of the algorithm used for the twin image correction.

2.2.3 Resolution and depth of field

In digital in-line holography, the spatial resolution is limited by the wavelength, the numerical aperture but also by the detection of the finest interference fringes in the hologram. Since the reference illumination is passing through the object, the smallest fringes, in this case, are formed by the interference between references and object waves, scattered at large diffraction angles. In the case of in-line holography with plane waves, these fringes are sampled by the detector, with the same pixel size as if we discretized the object plane in the same size, by $N \times N$ pixels ($\Delta_{\text{pixel}} = \Delta_{\text{obj}}$, as there is no magnification). However, for a good quality reconstruction, all fringes should be collected in the field of view of the detector, which should be extended enough to reach high spatial resolution. The latter can be increased by a high sampling of the fringes, which means a smaller pixel size of the detector. In all imaging techniques one of the most important parameters that defines the resolution of the system is the numerical aperture (NA). The numerical aperture number is directly related to the angle of diffraction of the light from the specimen. A higher NA will give a better resolution.

The achievable resolution in the case of in-line holography is subject of many studies and detailed explanation can be found, in several references⁶¹. The theoretical lateral resolution follows:

$$\delta_{\text{lat}} = \frac{\lambda}{2NA} \quad (2.10)$$

With NA the numerical aperture of the beam. In in-line holography, the NA is defined as:

$$NA = \frac{D}{Z} \quad (2.11)$$

where Z is the source-detector distance and D the beam diameter at the detector. In the original configuration with $\lambda = 405 \text{ nm}$ and $NA = 0.12$ we obtained $\delta = 1.7 \text{ }\mu\text{m}$. The addition of the pinhole has several purpose, first it “cleans” the beam from aberrations and increases the coherence of the beam, and second it increases the effective NA of the system (the diffraction angle of the beam that passes through the pinhole increases as well the information collected by the image sensor). In our setup, the use of a $1 \text{ }\mu\text{m}$ diameter pinhole allows in principle to reach a theoretical resolution of $\delta = 1 \text{ }\mu\text{m}$.

The axial resolution (in z-direction) can be defined as a depth of focus distance^{62 63}:

$$\delta_{axial} = \frac{\lambda}{2NA^2} \quad (2.12)$$

The pinhole geometry generates spherical waves which introduces a magnification factor. In fact, the pixel size in the hologram recorded with spherical waves, Δ_{pixel} , corresponds to the pixel size of the plane wave illumination case, multiplied by the magnification factor M . We have $\Delta_{\text{pixel}} = \Delta_{\text{obj}}M$, with Δ_{obj} the pixel size in the object planes.

Other limitation of the technique: Like any imaging technique, online holography faces intrinsic limitations in terms of resolution as explained above. However, the resolution can be affected by experimental and algorithmic issues such as:

- The signal-to-noise ratio, which depends on the sample size, the diffracted intensity, and the detectability of the interference fringes formed at the detector plane;
- Spatial aliasing, occurring when the intensity fringes are under-sampled by the sensor. Reconstructed images exhibit distortions and fake features, not present in the object.
- Limited spatial and temporal coherence of the source, limiting the maximum observable fringe frequency, limiting the maximum system resolution.

2.3 Algorithms

As already mentioned this thesis was focused on calibration and tests concerning biological applications. The microscope platform follows a numerical reconstruction based on a previous doctoral research in the lab. In the in-line configuration a simple back-propagation function is not enough to obtain a reconstructed image due to the loss of phase. This was the subject of many studies as^{64 65}. Here, the algorithm was adapted by Joana Duarte in the group (Thesis 18/10/2019, LIDYL) from a research work by T. Latychevskaia and Fink⁶³. We can recall a short description of the program. It consists in an iterative method as follows:

-the hologram is divided by the intensity of the reference beam ($I_{\text{CCD}}/I_{\text{ref}}$), then the square root of this quantity is taken; a normalized hologram is obtained, equal to 1 at all points in the absence of a sample.

- then the following loop is applied:

1. The Fresnel propagator is applied at the distance z_2 : we obtain a first image of our object. The resulting field contains the physical parameters of our sample, due to the normalization of the hologram. More precisely, the field can be written:

$$U_{diff}(\xi, \eta) = (1 - a(\xi, \eta)) \times \exp(-j\Phi(\xi, \eta)) \quad (2.13)$$

Where $a(\xi, \eta)$ is the real absorption of the sample, and $\Phi(\xi, \eta)$ is the phase shift due to the reference wave.

2. If the object is perfectly opaque, then it is possible to delete the phase term to accelerate the convergence. We are getting: $U_{diff}(\xi, \eta) = (1 - a(\xi, \eta))$

-In case the object is partially absorbing, we keep the phase term.

-If the object is opaque or not, a constraint on $t(\xi; \eta)$ is applied in order to eliminate the twin image. This function represents the complex contribution of the object.

3. The Fresnel propagator (in the opposite direction) is applied to this new field.

4. In the camera plane the modulus of the propagated field must be equal to the initially calculated experimental hologram. An error function calculates the deviation of the new hologram from the experimental hologram.

The iteration of this loop will result in the elimination of the twin image contribution and the reconstruction of the object in phase and amplitude. The block diagram of this algorithm is presented in Fig. 2. 5.

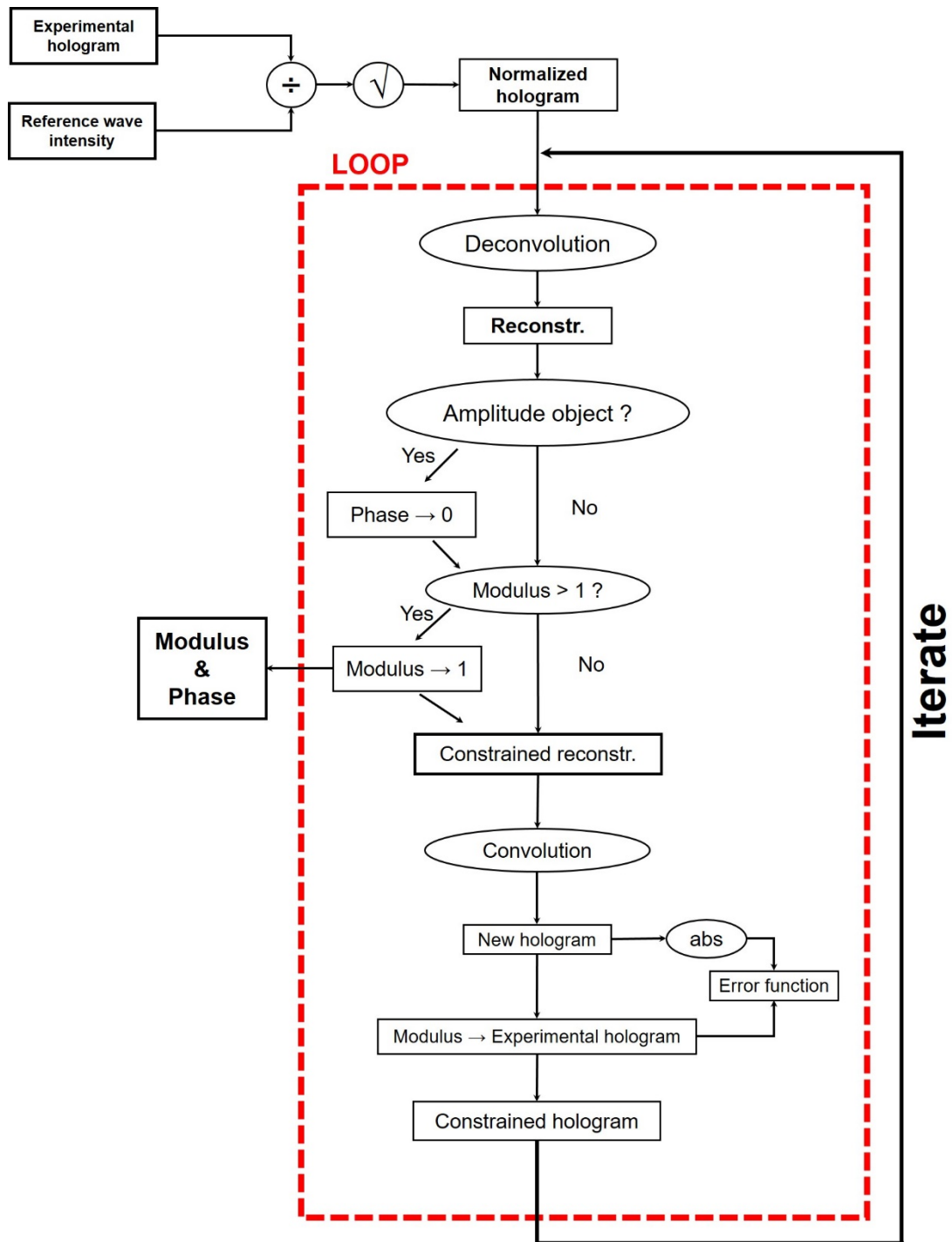


FIG. 2. 5. BLOCK DIAGRAM OF THE RECONSTRUCTION ALGORITHM FOR IN-LINE HOLOGRAPHY (ADAPTED FROM SAMAN).

2.4 Development of the microscope prototype

2.4.1 Presentation of the prototype

This microscopy approach is defined by two main characteristics: on the one hand, it uses the principle of lensless imaging. On the other hand, it is extremely compact. It consists of a laser diode, a pinhole, nano-positioners used for the sample holder motion, and a CCD camera connected to a computer for processing the signal. It is easy to build, align and use, and has a very low cost (a few 10k€). An image of the prototype is presented Fig. 2. 4.

The total dimension of the microscope is about 20 cm. For the sample motion control we use stages with nanometric resolution which give as a better control of the sample position. The illumination source, the sample motion control and the CDD are connected through a GUI interface. The GUI interface is addressed using a LabVIEW base software. The LabVIEW interface allows to realize a live analysis of the holograms, including zooming and back-propagation, and/or to save the data for post-processing treatment using more powerful algorithms.

In this configuration we have used two different wavelengths $\lambda_1 = 405$ nm with adjustable power $PW = 0 \rightarrow 60$ mW and $\lambda_2 = 637$ nm with adjustable power $PW = 0 \rightarrow 120$ mW. Here we wanted to test two different wavelengths to see if the absorption of light might be a problem for imaging or if it could give us different information about the sample. Indeed, the absorption of light differs from one type of cell due for example to an excess of lipids which have a strong absorption.

The NA of the illumination source is an important parameter for image resolution. We tested two conditions: high NA given by an aspherical lens added at the exit of the fibre laser, and a pinhole of 1 μ m diameter. Both cases are presented in the next sections.

The distance between the point source and CCD camera, with a 5.5 μ m pixel size (p_{CCD}) and 3296x2472 pixels, is $Z = 40$ mm. The position of the sample was located in different z_2 in order to test the magnification factor, and possible errors.

In the case of a pinhole of 1 μ m diameter and distances mentioned above the necessary power it is about 50 mW (405 nm), respectively 70 mW (637 nm), according with the acquisition time of 50 ms. The total power received by the sample is 0.25nW for a distance fibre-pinhole of 2 mm.

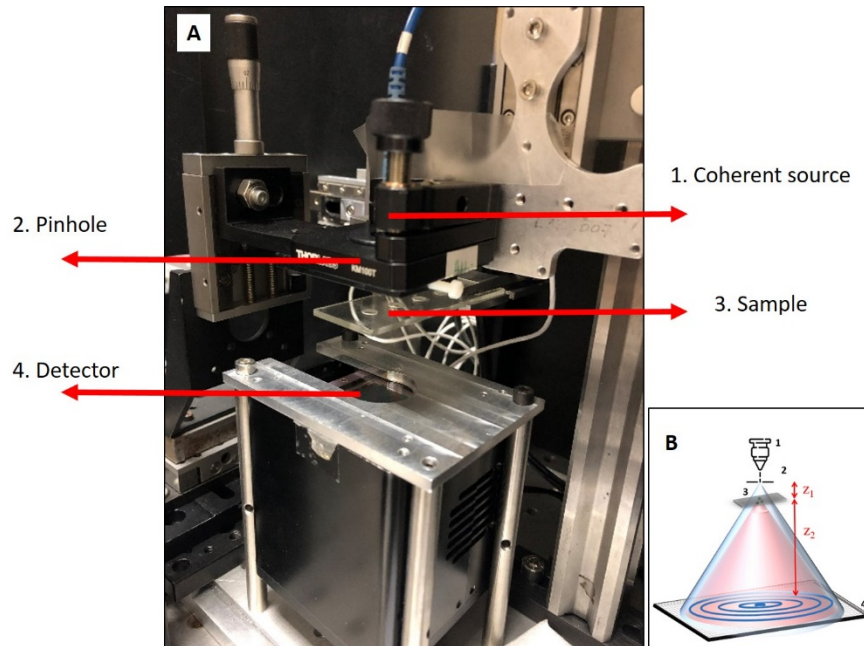


FIG. 2. 6. PICTURE OF THE LENSLESS MICROSCOPE PROTOTYPE.

2.4.2 Calibration of the spatial resolution

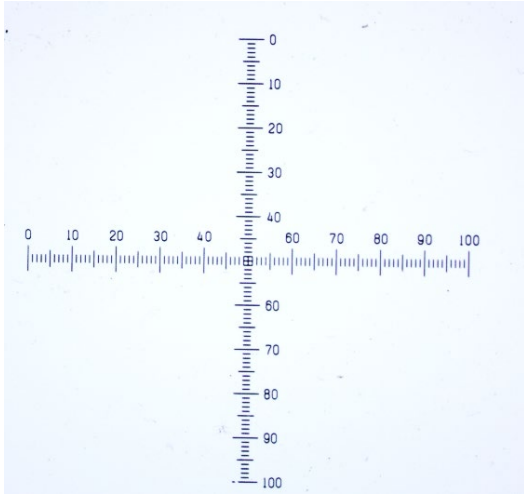
2.4.2.1 Optical reference

In this section we present the characterization of the spatial resolution using an optical reference. As already mentioned, the resolution in DIH depends on several factors: pinhole size, the numerical aperture, the spatial coherence and the illumination cone; numerical aperture, given also by the size and position of the recording image detector; pixel size and dynamic range, controlling fringe resolution and noise level in the hologram; wavelength. Evaluating a microscope spatial resolution is always partly subjective, as the definition of resolution varies from publication to publication. Here, we used the Rayleigh criterion (estimation of the resolution for our experimental data) which defines the spatial resolution R as the shortest distance required to distinguish two point sources⁶⁶. It can be expressed as:

$$R = n_{10\%-90\%} \times \Delta_{pixel} \quad (2.15)$$

with $n_{10\%-90\%}$ the number of pixels that constitute the 10% - to - 90% rising (or falling) edge, in intensity, and Δ_{pixel} the image pixel size. Additionally, the result of this measurement is very

dependent on where the profile is extracted from. Therefore, we always calculate a mean value over several cut on the sample reconstruction.

We start the first tests using an object of pure amplitude based on a positive test pattern, i.e. a ruler for microscope calibration. The vertical and horizontal graduations are laid out in the shape of a cross, the spacing of each line is 100 microns over 1 cm. The transmission profile of this is shown in  Fig. 2. 7. The image was recorded with an optical microscope of magnification 20x.

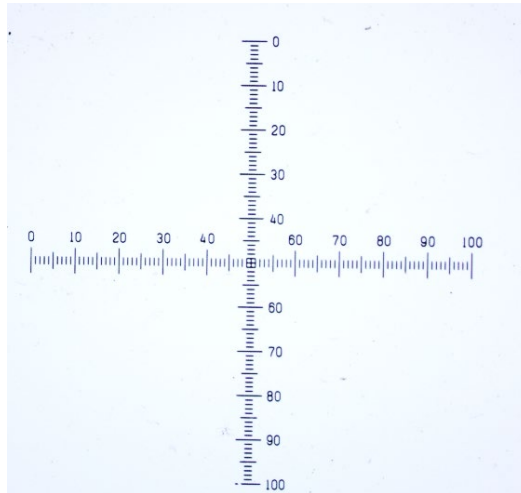


FIG. 2. 7. OPTICAL IMAGE WITH THE RULER.

Thanks to its simplicity (it does not present any variation of the refractive index and transmit either the full light or nothing) and because it is perfectly known, this sample is a perfect candidate to calibrate and check the performance of our reconstruction algorithm. In order to prove the efficiency of the algorithm, we will compare the reconstruction from a simple Fresnel back-propagation (thus containing the contribution of the twin image), with the reconstruction resulting from several iterations of our algorithm, including twin image correction.

2.4.2.2 Pinhole configuration

In the configuration we used the most, the continuous laser source is spatially filtered using a pinhole with a diameter $d = 1 \mu\text{m}$ in order to create a clean spherical wave. The use of a pinhole allows creating a well-defined mode which improves the spatial coherence, improves the wavefront of the illumination and increases the $\text{NA} = 0.33$.

The diode-to-camera Z distance allows performing the calibration on the reconstructions, namely, to determine the sampling step. Indeed, the actual propagation distance can be retrieved looking at the calibration target reconstruction. For this, the sample is located at a distance of 31 mm, respectively 36 mm, from the CDD, which gives us a magnification of $M_1 = 5$, respectively $M_2 = 10$, so a sampling step of $p_1 = \frac{p_{\text{CCD}}}{M} = 1.1 \mu\text{m}$ and $p_2 = 0.55 \mu\text{m}$. The experimental data are presented in Fig. 2. 8 to Fig. 2. 13. Note that I display here only an example of plot profile. Other profiles have been realized and show similar behaviour and values. For each configuration, only one hologram is needed, and was subsequently inverted with our back-propagation algorithm to analyse the quality of the data. In the case of the pure amplitude sample the two wavelengths have the purpose of calibration and validation of our set-up.

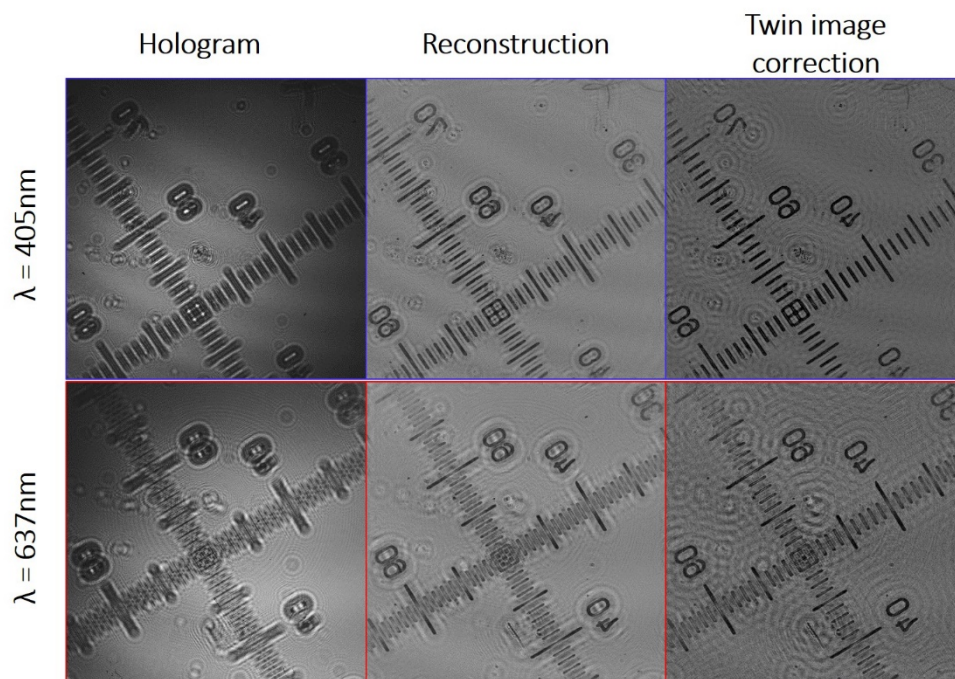


FIG. 2. 8. HOLOGRAM AND AMPLITUDE RECONSTRUCTION OF THE OPTICAL RULER IN THE CASE OF MAGNIFICATION M_1 . THE RECONSTRUCTION WITH TWIN IMAGE CORRECTION WAS OBTAINED AFTER $N = 30$ ITERATIONS.

Fig. 2. 8 presents the calibration steps for the first magnification $M_1 = 5$. The uses of the optical ruler help us to define a first experimental resolution using the two wavelengths. The elimination of the twin image is clearly highlighted by the improvement of the contrast and removal of many artefacts from the image (for instance, the rings around each pattern). To estimate the resolution in this configuration, we apply the “10-90%” criterion: I define a line that crosses the patterns (see Fig. 2. 9-Fig. 2. 10) to get the resolution. The experimental resolution resulted for $\lambda_1 = 405\text{nm}$ is $\delta_{\text{exp}} = 2.77 \mu\text{m}$ while the theoretical resolution is $\delta_t = 1.24 \mu\text{m}$. For the second wavelength $\lambda_2 = 637 \text{ nm}$, the experimental resolution is $\delta_{\text{exp}} = 3.59 \mu\text{m}$, respectively theoretical value $\delta_t = 1.95 \mu\text{m}$. We can observe that two results are coherent with the change of wavelength.

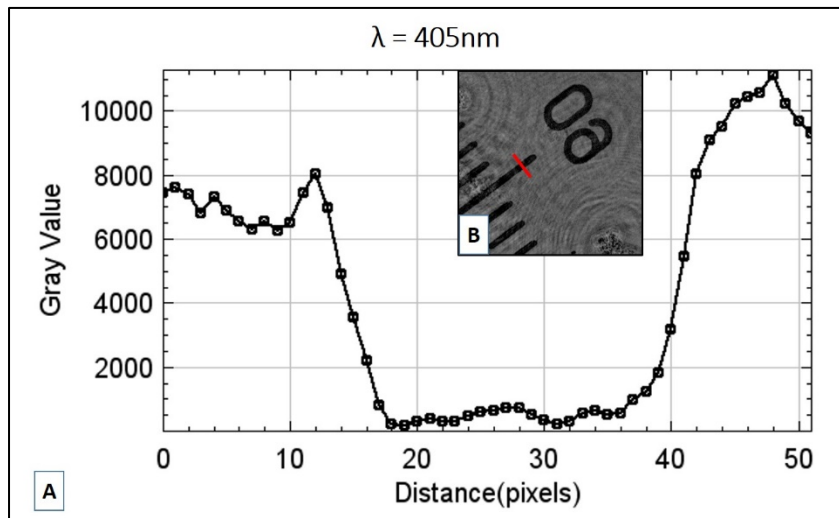


FIG. 2. 9. PLOT PROFILE FOR THE RED LINE IN B WHICH REPRESENTS THE AMPLITUDE RECONSTRUCTION, AFTER TWIN IMAGE CORRECTION, IN THE CASE M_1 WITH $\lambda_1 = 405$ nm AND PIXEL SIZE $\Delta_{\text{PIXEL}} = 0.5 \mu\text{m}$.

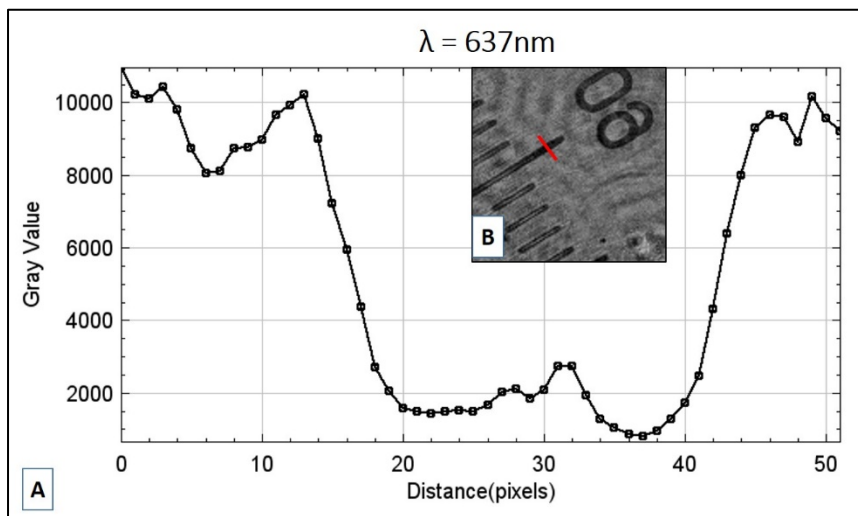


FIG. 2. 10. PLOT PROFILE FOR THE RED LINE IN B WHICH REPRESENTS THE AMPLITUDE RECONSTRUCTION, AFTER TWIN IMAGE CORRECTION, IN THE CASE M_1 WITH $\lambda_2 = 637$ nm AND PIXEL SIZE $\Delta_{\text{PIXEL}} = 0.7 \mu\text{m}$.

In this configuration it is possible to play with the field of view. In the previous results we have seen a larger part of the ruler, increasing the magnification factor we will reduce the field of view so we will limit our reconstruction to a restricted part of the object. The results are present in the Fig. 2. 11.

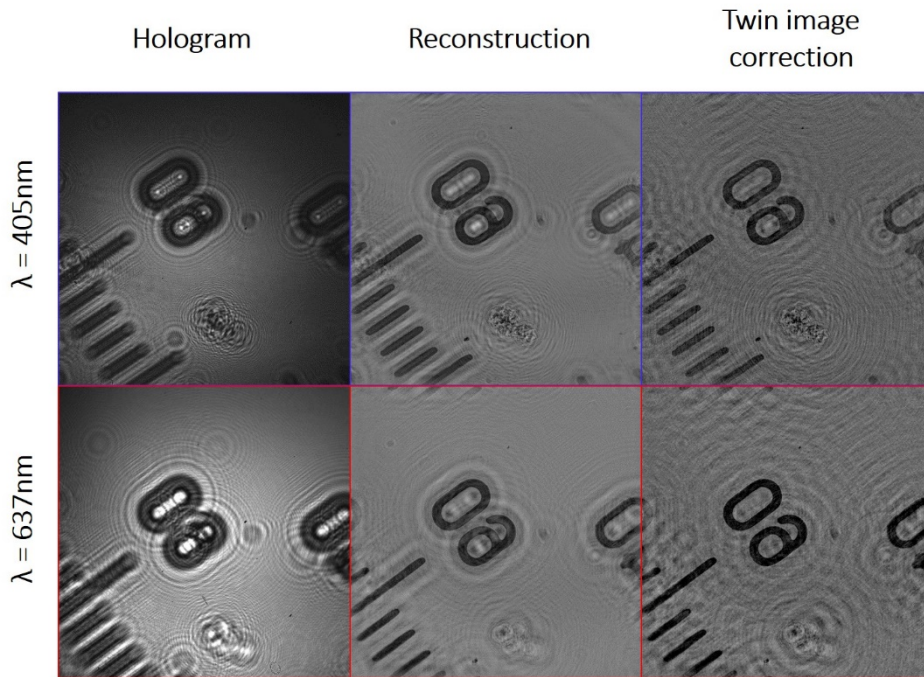


FIG. 2. 11. HOLOGRAM AND AMPLITUDE RECONSTRUCTION OF THE OPTICAL RULER IN THE CASE OF MAGNIFICATION M_2 . THE RECONSTRUCTION WITH TWIN IMAGE CORRECTION WAS OBTAINED AFTER $N = 30$ ITERATIONS.

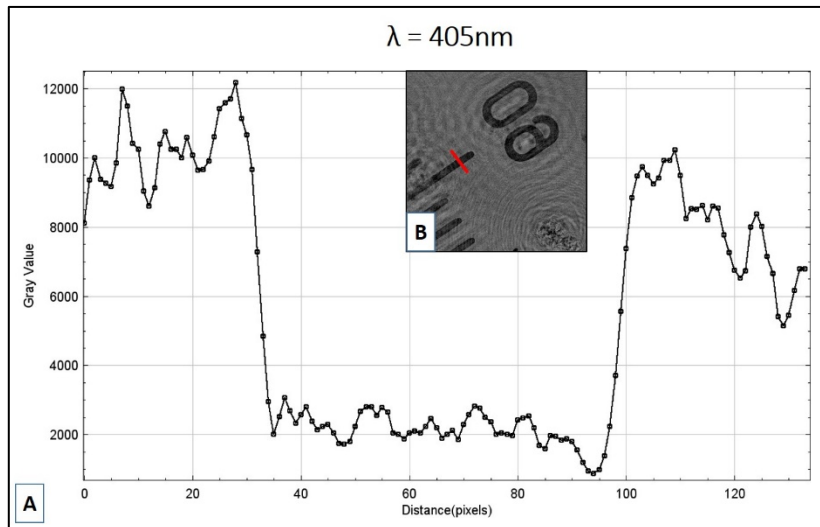


FIG. 2. 12. PLOT PROFILE FOR THE RED LINE IN B WHICH REPRESENTS THE AMPLITUDE RECONSTRUCTION, AFTER TWIN IMAGE CORRECTION, IN THE CASE M_2 WITH $\lambda_1 = 405$ nm AND PIXEL SIZE $\Delta_{\text{PIXEL}} = 0.48 \mu\text{m}$.

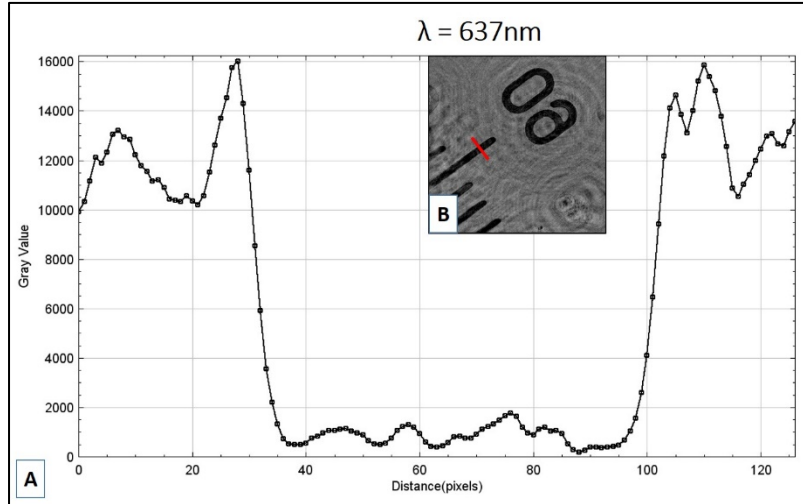


FIG. 2. 13. PLOT PROFILE FOR THE RED LINE IN B WHICH REPRESENTS THE AMPLITUDE RECONSTRUCTION, AFTER TWIN IMAGE CORRECTION, IN THE CASE M_2 WITH $\lambda_2 = 637$ nm AND PIXEL SIZE $\Delta_{\text{PIXEL}} = 0.7 \mu\text{m}$.

The above experimental results give an estimation of the spatial resolution in the case with magnification $M_2 = 10$ and two wavelengths. As in the previous case, the elimination of the twin image is clearly highlighted by the improvement of the contrast and removal of many artefacts from the image (for instance, the rings around each pattern). The resolution was estimated based on the same principle as in the previous set of experiments (see Fig. 2. 13). The experimental resolution resulted for $\lambda_1 = 405$ nm is $\delta_{\text{exp}} = 1.87 \mu\text{m}$ while the theoretical resolution is $\delta_t = 1.24 \mu\text{m}$. For the second wavelength $\lambda_2 = 637$ nm, the experimental resolution is $\delta_{\text{exp}} = 3.8 \mu\text{m}$, respectively theoretical value $\delta_t = 1.95 \mu\text{m}$.

We can observe that the resolution is improved in the case of $\lambda_1 = 405$ nm, which can be explained by increased of magnification factor. In the case of $\lambda_2 = 637$ nm the resolution is deteriorated compared to the previous case, but the result could be influenced by errors due to external factors such as alignment.

Among the measurements carried out, we obtain "clean" reconstructions confirmed by the effectiveness of the algorithm of the twin image elimination. In this case the object was of pure amplitude, so there is no phase shift, and the algorithm converged efficient. We can estimate that the quality of the image given by the "cleaning" program does not imply a better resolution but a better contrast. According to the magnification chosen, we could define an ultimate utile resolution of $1.87 \mu\text{m}$.

2.4.2.3 High NA using aspheric lens

As the resolution is limited by the numerical aperture, I tried different strategies to increase this value as much as possible. Apart from the approach relying on a micrometric pinhole we used an aspheric lens compatible with the 405 nm source, presented a theoretical NA of 0.53, which is 1.6 time higher than the NA given by the 1 μ m pinhole. Calibration tests with the optical ruler are presented Fig. 2. 14 and Fig. 2. 17. Note that I display here only an example of plot profile. Other profiles have been realized and show similar behaviour and values. Two different magnification factors were analysed. The total working distance is $Z = 35$ mm, and the sample was located at a distance $z_2 = 25$ mm from the detector, and $z_2 = 30$ mm respectively. In the first case the magnification factor is $M_1 = 3.5$, so a sampling step of $p_1 = \frac{p_{CCD}}{M} = 1.57 \mu\text{m}$, while in the second case is $M_2 = 7$ and $p_2 = 0.79 \mu\text{m}$.

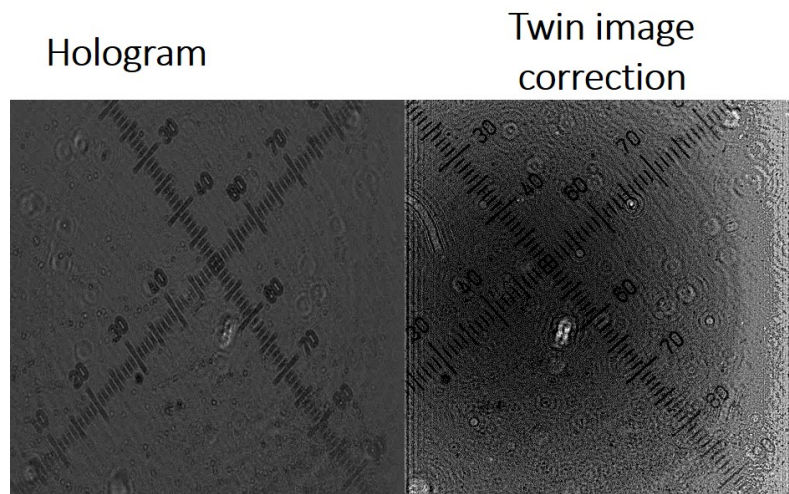


FIG. 2. 14. HOLOGRAM AND AMPLITUDE RECONSTRUCTION OF THE OPTICAL RULER IN THE CASE OF MAGNIFICATION M_1 . THE RECONSTRUCTION WITH TWIN IMAGE CORRECTION WAS OBTAINED AFTER $N = 30$ ITERATIONS.

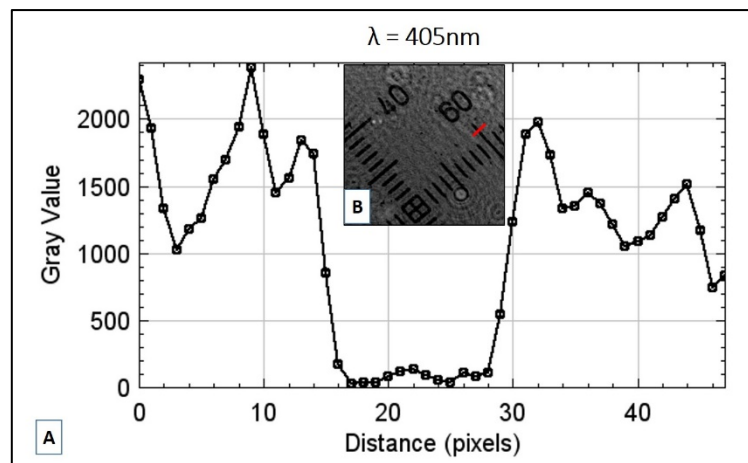


FIG. 2. 15. PLOT PROFILE FOR THE RED LINE IN B WHICH REPRESENTS THE AMPLITUDE RECONSTRUCTION, AFTER TWIN IMAGE CORRECTION, IN THE CASE M_2 WITH $\lambda_1 = 405$ nm AND PIXEL SIZE $\Delta_{\text{PIXEL}} = 0.6 \mu\text{m}$.

Fig. 2. 14 presents the calibration steps for the first magnification $M_1 = 3.5$. The uses of the optical ruler help us to define a first experimental resolution using a lens with $NA = 0.53$. The twin image correction is clearly highlight by removal of many artefacts from the image, but new artefacts are presented in the reconstruction due to aberration introduced by the high NA lens. To estimate the resolution in this configuration, we apply the “10-90%” criterion: I defined a line that crosses the patterns (see Fig. 2. 15). The experimental resolution resulted for $\lambda = 405$ nm is $\delta_{exp} = 4.2$ μm while the theoretical resolution is $\delta_t = 0.9$ μm .

For the second experiment with $M_2 = 7$, I followed the same experimental conditions as in case of $M_1 = 3.5$. Fig. 2. 16 presents the hologram and the reconstruction with the twin image corrections.

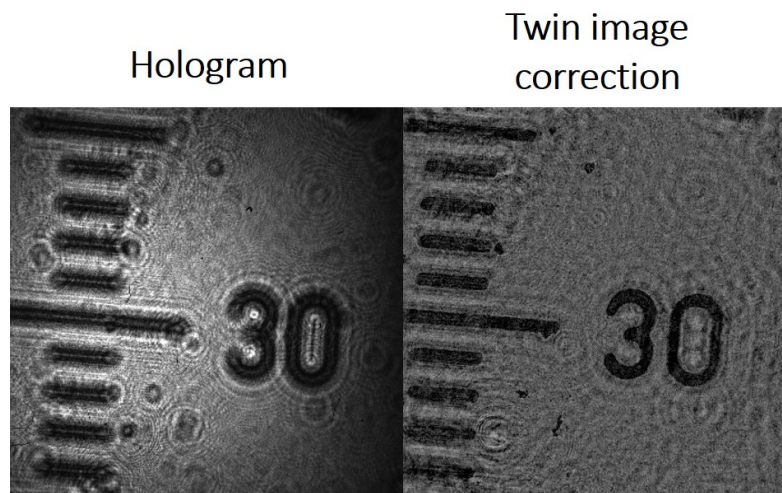


FIG. 2. 16. HOLOGRAM AND AMPLITUDE RECONSTRUCTION OF THE OPTICAL RULER IN THE CASE OF MAGNIFICATION M_2 . THE RECONSTRUCTION WITH TWIN IMAGE CORRECTION WAS SIMULATED UNDER $N = 30$ ITERATIONS.

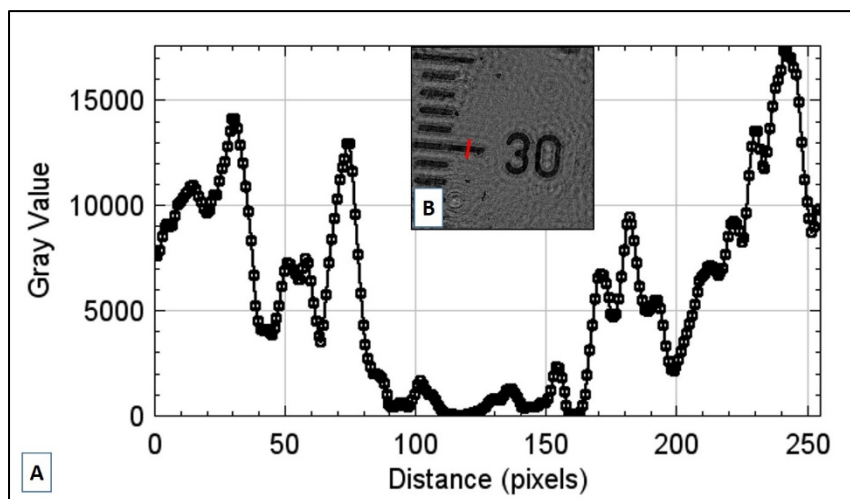


FIG. 2. 17. PLOT PROFILE FOR THE RED LINE IN B WHICH REPRESENTS THE AMPLITUDE RECONSTRUCTION, AFTER TWIN IMAGE CORRECTION, IN THE CASE M_2 WITH $\lambda = 405$ nm AND PIXEL SIZE $\Delta_{PIXEL} = 0.7$ μm .

As in the previous case, the elimination of the twin image is clearly visible. The resolution was estimated based on the same principle of “10-90%” criterion (see Fig. 2. 17). The experimental resolution resulted for $\lambda = 405$ nm is $\delta_{\text{exp}} = 6.9$ μm while the theoretical resolution is $\delta_t = 0.9$ μm . As in the previous case the quality of the image is distorted by the optical lens used to increase the NA which is the principal cause of resolution loss. An algorithm is under development (Thesis Joana Duarte) in our group to correct for optical aberration and source wave front distortion. Unfortunately, it was not finished but will be implemented in the next software upgrade.

The actual status is that the pinhole gives us the best resolution of $\delta_{\text{exp}} = 2.77$ μm for a magnification factor $M_1 = 5$, while for a similar arrangement but using the aspheric lens the resolution is $\delta_{\text{exp}} = 4.2$ μm ($M_1 = 3.5$).

2.5. Conclusion

In this chapter the principles of digital in-line holography were presented. Based on theoretical points a new prototype was developed and tested. The configuration was calibrated using a test pattern for measuring the parameters of the image reproduction system and test the efficiency of the algorithm. The characterization of the spatial resolution was completed using an optical reference. Two different configuration were tested to increase the NA: one based on aspheric lens and the other one using 1 μm diameter pinhole. In the case of high NA using the optical lens the quality of the image it was found to be distorted by the optical aberration induced by lens which is the principal cause of resolution loss. Further on, in the next chapter, we present the first bio-demonstrations using our microscopy technique based on the in-line configuration.

3. BIOMEDICAL APPLICATIONS

In this chapter we will introduce the first experimental results obtained considering biological application. Several types of sample were tried: thick sample (zebrafish embryos), thin sample (cell culture) and test the motility of single cells (cyanobacteria). The chapter will conclude with a 3D demonstration, obtained with a z-stack based on the back-propagation function.

3.1. Imaging of Zebrafish Embryos

In the neuroscience research many questions are still open. A main part of neuroscience focuses on cell lineages and cell behaviour in the zebrafish embryo. The main reasons of using this species in biomedicine include: high physiological and genetic homology to mammals, external fertilization, rapid development (cost-effectiveness), transparency of embryos and larvae, ease of genetic and other experimental manipulations. Most of these studies include work on stem cells with a potential for tissue regeneration, and the creation of a number of animal models for developmental defects and human disease, in a variety of model systems.

For the biological content we used the help of our collaborator from Institut Pasteur - Laboratory of Zebrafish neurogenetics in Dept. of Developmental & Stem Cell Biology group led by Prof. Laure Bally-Cuif. The main activity of the group focuses on the mechanisms regulating the spatiotemporal dynamic of adult neural stem cells activation in the telencephalon. They perform their studies using as instrument a standard fluorescence microscope. A potential drawback for them is the step of transgenically labelled tissues, which means that they genetically include fluorescent markers in to the animal for the future imaging step. A label-free approach could facilitate their research. With this perspective, we tested our label-free instrument with in-vivo test samples.

Zebrafish embryo is a complex and thick sample. In the first hours of embryo' development the majority of the medium is formed of proteins. It is well known that each cell organelle has its own influence in the scattered light direction^{67 68}. That means that the refraction indices of the proteins are dominating and a high degree of scattering is produced. This 'background' noise may have influence in the image reconstruction. To reduce this side effect as much as possible, we modified slightly the microscope, introducing a polarizer in the set-up. The role of the polarizer will be to reduce the multiple scattering effect. I present here a chronological set of experiments, while I was performing the experiments in the configuration with the lens for high NA. Later I performed the resolution tests (presented in the previous section) in the case of high NA with pinhole or lens. In order to define the efficiency of the system several tests on zebrafish embryos were carried on two different configurations.

3.1.1. Sample preparation protocol

Zebrafishes (*Danio rerio*), AB wild type were maintained in accordance with the institutional guidelines. Embryos were obtained from natural spawning of wild type. At some desired stages (between 24-48 hpf), embryos are collected and dechorionated for in-vivo imaging. Before imaging, the embryos are anesthetized to prevent them from moving and then located in the well of a glass-bottom microfluidic chip. 24 hours post fertilization (hpf) embryos were anesthetized tricaine (Sigma) at 0.2 mg/ml and located on the imaging holder. The same protocol was followed for the imaging of 48 hpf embryos. Fig. 3. 1 present a set of optical microscope images with the zebrafish stages of development which give us a useful reference to follow in our image reconstruction.

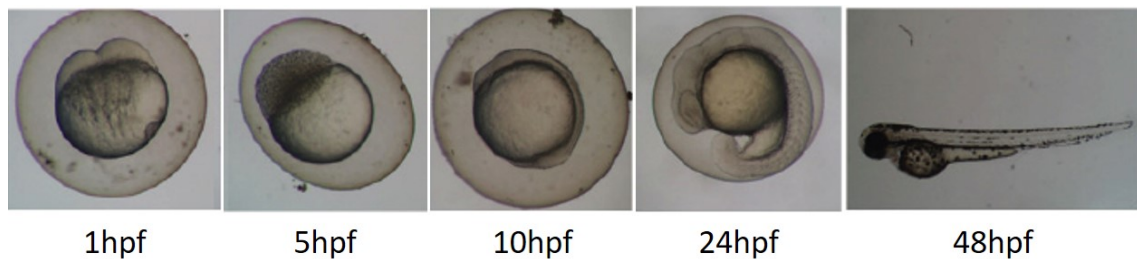


FIG. 3. 1. ZEBRAFISH STAGE SEQUENCES ADAPTED FROM⁶⁹.

3.1.2. Zebrafish embryo imaging – configuration 1

A coherent light source (405 nm) illuminates the sample from the top, the NA of the illumination source is increased using the aspheric lens. The commercial value NA of the lens is 0.48, while the experimental value of NA for our working distance is 0.3. The total working distance is $Z = 37\text{mm}$ while the sample was located at different distance z_2 from the CCD as follows: 31 mm with $M = 8.75$ (Fig. 3. 2A), 33.5 mm with $M = 23.5$ (Fig. 3. 2B) and 3 mm with $M = 7$ (Fig. 3. 2-C). In order to improve the hologram signal to noise ratio, we used a polarizer in the front of the CCD to reduce the scattered light contribution. The maximum power used for this experiment is 18 mW. The reconstructed amplitude are presented in the Fig. 3. 2-A, B, C.

If we compare with the optical microscope images from Fig. 3. 1 we do not have lot of resolution to define the stage of development by counting the number of cells. But for instance we can estimate by comparison with the optical microscope that the stage of development is around 5hps in the case of Fig. 3. 2-A. However, the large number of proteins implies a large index of refraction

(see section 3.2. Label-free cancer cell imaging (U2OS cell)) so that a lot of light will be either scattered or absorbed before it can reach the detector.

3.1.3. Zebrafish embryo imaging – configuration 2

In the previous configuration, we installed a polarizer after the sample in order to reduce the background scattering and improve the quality of the image. However, the complexity of the sample and the random refractive index variations within the sample scatter the photons and distort the optical wavefront. All these effects induce an increase of the background noise and reduce the quality of the image for large tissue thicknesses. To this goal, the polarizer was located before the sample. As well a new aspheric lens of commercial value $NA = 0.60$ was used so that we can increase the resolution. The effective experimental NA is 0.35. The working distance is $Z = 35$ mm and the object was located at a distance $z_1 = 5$ mm from the source. If we compare with the experiments from section 3.1.2 we can observe that the quality of the images is better and several embryos components could be defined. The high NA and the new position of the polarizer are the main factors that are responsible for the new quality of these images. Several focused planes are presented in the Fig. 3. 2 images D-G.

The image reconstructions were performed similarly to the procedures presented in the sections above. A zebrafish embryo is a three-dimensional object, thus reconstructions at different depths using our microscope allow recovering z-slices of the sample (see **Chapter 3** for details of z-slices), in order to focus on different part components or to follow the 3D structure (see Fig. 3. 2). As an illustration, the morphology of a blood vessel superimposed with bone structure (Fig. 3. 2-G, F) within the tail fin (Fig. 3. 2-A, C, D) and the shape of the caudal fin are presented. In Fig. 3. 2-D we choose to define a relative position $\Delta z = 0$ μm where the red arrow indicates a bone structure line; for Fig. 3. 2-E the new distance from the relative position is $\Delta z_1 = 250$ μm and the arrow indicates the caudal fin; in F at $\Delta z_2 = 500$ μm two main blood vessels are indicated by the red line vein and artery while for G at same distance $\Delta z_2 = 500$ μm the red lines are following the direction of intersegmental blood vessels.

The new optimizations of the NanoXim using higher power and larger NA reveal fine structures with microns resolution. Nevertheless, several approaches have been proposed for cleaning noise, aberrations, that could achieve better results for zebrafish analysis³⁹. Another solution would be to use digital holography in an off-axis configuration, in which the reference wave does not propagate inside the sample medium⁷⁰.

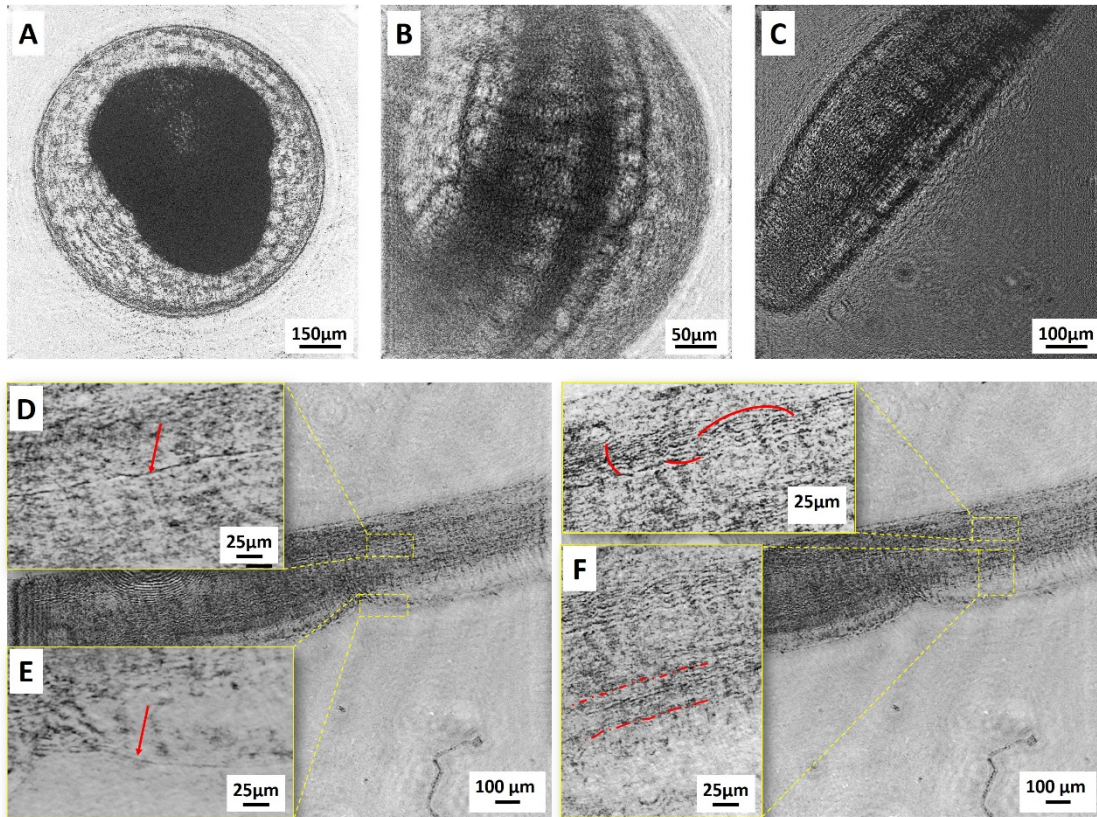


FIG. 3. 2. A) 6 HPF FULL ZEBRAFISH EMBRYO, B) DETAIL OF A 24 HPF ZEBRAFISH EMBRYO, C) DETAIL OF A 48 HPF DECHORIONATED EMBRYO, H) RECONSTRUCTED AMPLITUDE IMAGE OF A DECHORIONATED 48 HPF ZEBRAFISH EMBRYO AND CORRESPONDING ZOOMS OF DIFFERENT DETAILS: D) RELATIVE POSITION $Z = 0 \mu\text{m}$, THE RED ARROW IS A BONE STRUCTURE LINE, E) $Z_1 = 250 \mu\text{m}$ THE ARROW INDICATES THE CAUDAL FIN; F) $Z_2 = 500 \mu\text{m}$ THE RED LINE POINTS THE VEIN AND ARTERY WHILE IN G) AT SAME DISTANCE $Z_2 = 500 \mu\text{m}$ THE RED LINES ARE FOLLOWING THE DIRECTION OF INTERSEGMENTAL BLOOD VESSELS. THE GIVEN VALUES OF Z_1 CORRESPOND TO THE RELATIVE BACK-PROPAGATION DISTANCE, I.E. TO THE RELATIVE DISTANCE BETWEEN THE TRANSVERSE SLICES.

3.2. Label-free cancer cell imaging (U2OS cell)

In most of the experiments in a high resolution context the bio-samples are tagged using fluorescent markers. These nano-markers are monitored in order to record in-situ high-resolution data. The post-processing steps are crucial for biological samples because of the transparency of the cells. Indeed, the transparency of each cell's component is given by its index of refraction (n). Any living cell is a complex structure and contains numerous organelles with different refractive index. However, the difference between these n values is very small^{71 72 73}, making very difficult to distinguish between them using the classical imaging tools without the use of the markers (see table 3.1). One way around this limit could be to combine different wavelengths.

Organelles/intracellular matter	Refractive index
Cytosol	1.360 – 1.390
Nucleus	1.355 – 1.365
Nucleolus	1.375 – 1.385
Mitochondria	1.400 – 1.420
Lysosome	1.600

TABLE 3. 1. TYPICAL REFRACTIVE INDEX VALUES FOR VARIOUS ORGANELLES IN A CELL^{73,74,75}.

The knowledge about the refraction index can be exploited as environmental monitoring and/or disease diagnosis such as the identification of cancers cells. Indeed, the protein concentration within the cell components mainly determines the effective refractive index. Proteins presents a high refractive index of 1.50–1.58^{74 75}. Compared to normal cells, cancer cells have more proteins mostly in the nucleus in order to make the cell division faster⁷⁶. The presence of a large amount of protein makes cancer cells to have a relatively larger refractive index than normal cells. Therefore, some cancers probably can be diagnosed by the effective refractive index of the cell as an indicator, maybe before it becomes invasive in the beginning of the disease.

We tested the instrument using a specific class of cell with the aid of our collaborators at Laboratoire de Recherche sur l'Instabilité Génétique – LRIG (CEA Fontenay-aux-Roses) lead by Pablo Radicella. We imaged and characterized the cancer cell line U2OS (Human Osteosarcoma Cell Line). One main activity of the group is focused on the cells response to stress. When cells are exposed to oxidative stress, many lesions are induced in DNA. Complex repair mechanisms can be used to detect and repair injuries. Mitochondria are cell organelles that produce high levels of reactive oxygen species and therefore play a vital role in the response of cells to stress. A challenge is to visualize cellular organelles without the use of fluorescent markers and with a good spatial resolution in both x y and z that are the main limitations with the use of confocal microscopes. However, when observing the dynamics of organelles or DNA repair proteins in response to oxidative stress, it is important to minimize the impact of the imaging, making the development of less invasive techniques crucial.

Currently, LRIG uses confocal microscopes to monitor mitochondrial dynamics using fluorescent markers. This imaging system proves to be quite toxic to cells because of the point by point laser scan and the use of markers. This toxicity imposes a reduction in the number of frames that can be obtained, thus limiting both the spatial and temporal resolutions. The advantage of the lensless microscope is obviously its capacity to follow dynamics by using a sequence of single acquisition obtained in a very short time frame. Thus, this technology could significantly reduce the toxicity of the imaging protocol while increasing the temporal resolution. Furthermore, the lensless

approach can provide complementary information, i.e. phase contrast, related to the optical index of the specimen.

We analysed the cells in the two configurations of high NA, pinhole and lens, and the results are presented below.

3.2.1. Cell culture protocol

U2OS cells were cultured in Dulbecco's modified Eagle's medium (DMEM, ThermoFisher, 31966021), supplemented with 10% fetal bovine serum (FBS) (Sigma, F7524) and 5% penicillin/streptomycin (Gibco, 15140122) at 37°C and 5% CO₂. For microscopy, cells were grown on 12 mm round coverslips N°1,5H (Marienfeld, 900532), fixed in 2% formaldehyde (Thermo Scientific™, 28908) for 20min at 37°C and rinsed with PBS before mounting in DAKO Fluorescence mounting medium (S3023).

3.2.2. Image acquisition and processing: high NA using lens

The first set of data were obtained using the following configuration: illumination source $\lambda = 405$ nm and aspheric lens with NA = 0.63. The polarizer was not necessary in this configuration. The source-CCD distance is $Z = 44$ mm while the sample was located at a distance $z_2 = 35$ mm from the detector, giving a factor of magnification $M = 5$ and a sampling step of $p = p_{\text{ccd}}/M = 1.1\mu\text{m}$. For this experiment, normal cells (no fluorescent tags) were used. The acquisition time was 100 ms. The experimental data are presented in Fig. 3. 3.

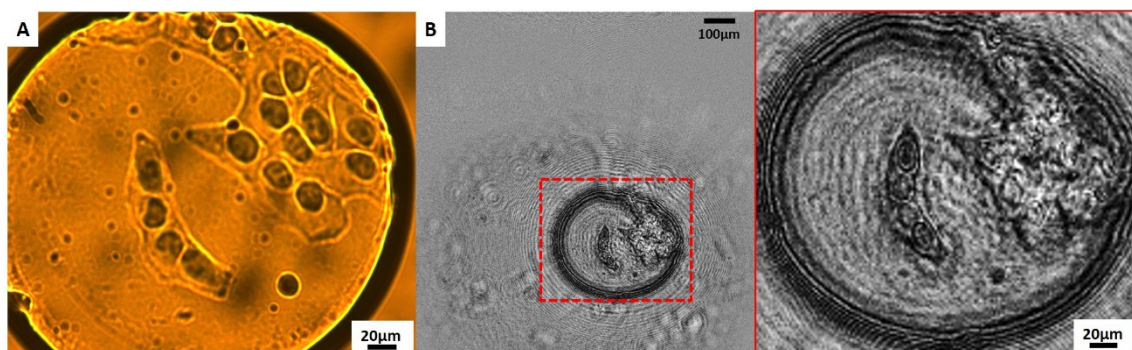


FIG. 3. 3. CELL CULTURE: A) IMAGE ACHIEVED WITH A 20X OPTICAL MICROSCOPE B) RECONSTRUCTED AMPLITUDE IMAGE OF A CELL CULTURE. THE FULL FIELD-OF-VIEW IS PRESENTED WITH THE CORRESPONDENT ZOOM INTO THE RED SQUARES IN THE CELLS REGION.

In Fig. 3. 3-B we can observe several dark rings around the sample, which can be identified in the optical image (Fig. 3. 3-A) as a dark circle. The cells are fixed in a mounting medium that is changing its texture in time. The mounting medium dries, and produces distortions in the final diffraction pattern. The contrast of the optical image seems good but there is not enough resolution for a detailed analysis of the sample. In the image produced with the in-line configuration the high resolution allows us to observe several details as: nucleolus or nuclear membrane. The nuclear envelop is more contrasted and we can make differentiation between the transition from the nucleus to the cytoplasm. However, this configuration can be improved by first: reducing optical aberrations (sample mounting medium and lens setup can be improved (see 2.4.2.3)) and second by performing a twin image correction.

An interesting evolution of the setup would be to be able to compare holographic images with fluorescent techniques on the same cells. Data fusion of the fluorescence and phase images would give access to new information, as the unambiguous knowledge on which organelle the fluorophores belong to. A first necessary trial before reaching this goal is to make sure that our microscope is compatible with cell cultures fluorescently labelled (DAPI for DNA). We were expecting artefacts produced by the florescent nanoparticles, inducing additional noise in the holograms. The results are present in Fig. 3. 4.

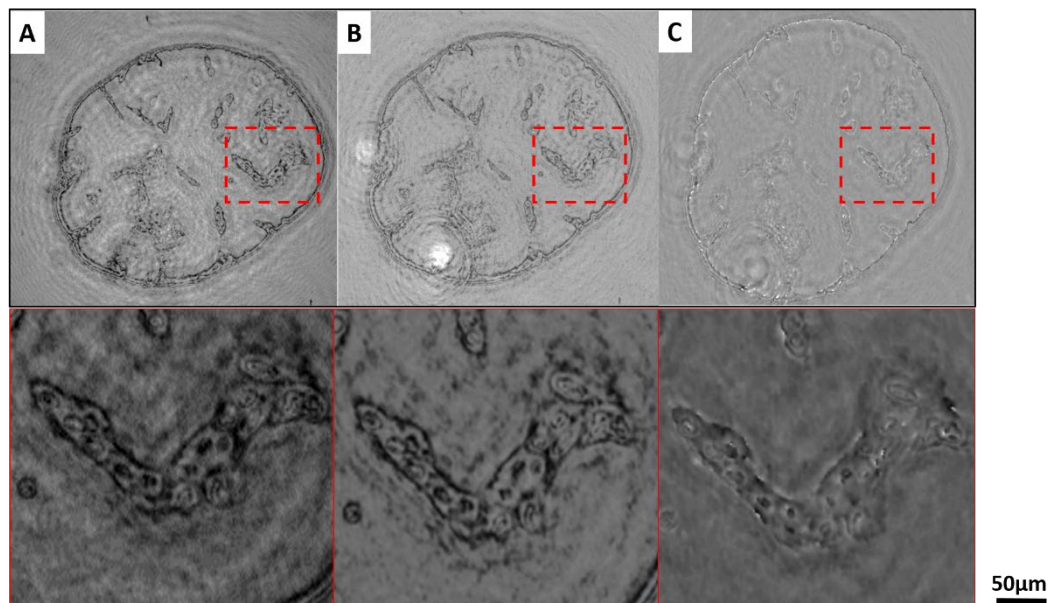


FIG. 3. 4. RECONSTRUCTED AMPLITUDE IMAGE OF A CELL CULTURE A) WITHOUT TWIN IMAGE CORRECTION B) WITH TWIN IMAGE CORRECTION AND THE CORRESPONDING PHASE IMAGES IN C. THE BOTTOM LINE IMAGES CORRESPOND TO ZOOMS INTO THE RED SQUARES OF A), B) AND C). THE SCALE BAR IS 50 μm .

Fig. 3. 4 presents the reconstruction amplitude and phase of our object. A group of cells were targeted for imaging in order to see the effects of labelling for future data fusion. Fig. 3. 4-A presents the amplitude reconstruction without the twin image correction. The twin image correction is presented in Fig. 3. 4-B, and we can observe an improvement of image quality thanks to the cleaning of artefacts. In **Chapter 2** (section 2.3 Algorithms) we presented a potential solution for phase recovering which gives us access to more information about our sample. The phase image is presented in Fig. 3. 4-C.

In our first trial, we could not identify an effect of the label emission, neither in the holograms nor in the reconstructions. Each fluorescent dye has its excitation wavelength. In this case the fluorescent marker used is DAPI that can be excited with λ around 400-600 nm, with a maximum emission around 470 nm, while our illumination source is only 405 nm. The emission is not strong enough to be detected by our CCD which make the technique compatible for data fusion with fluorescent images. Indeed, a strong emission of the fluorescent could interfere with the fringes from the hologram and affect the final image reconstruction. We can conclude by saying that these results are similar with the one obtained for cells without labelling and thanks, to the strong absorption of 405 nm important parts of the cells were distinguished.

3.2.3. Image acquisition and processing: high NA using pinhole

Using our lensless microscope, we collected holograms of U2OS cells at various distances between source and image sensor and various magnification factors, and processed them as described above. To try to increase the image quality, we replace the high NA lens by a 1 μ m diameter pinhole. The total working distance is $Z = 40$ mm. The reconstruction steps are presented in Fig. 3. 5: from hologram to standard reconstruction and twin image corrected reconstruction. All images were acquired in a single 100 ms acquisition time. The reconstruction time could vary from few seconds to several minutes depending of the number of successive plans required and the size of the selected hologram area.

In Fig. 3. 5-b the full FOV (80 mm²) of the mounted sample is presented. Two regions of interest were selected for this study (Fig. 3. 5-a, c). The first region (Fig. 3. 5-a, d, g) presents an area with a single cell. In this reconstruction the magnification factor is about $M_1 = 36$. Fig. 3. 5-c, f, i, h report a larger FOV containing several cells and a factor $M_2 = 40$. The sampling step it is $p_1 = 0.152$ μ m, respectively $p_2 = 0.137$ μ m.

In both region of analysis, we distinguish several areas of the cell, e.g. (Fig. 3. 5-g): cytoplasm (A), nuclear envelope (C), and the nucleolus (B). The size of the reconstructed cells, as well as their nuclear dimensions, are consistent with the sizes of freely growing U2OS cells reported in the

literature⁷⁷. Additionally, the images are well contrasted and contain both the amplitude and the phase of the exit wave. We have to mention that the magnification factor is changed both through numerical and physical manipulation (changing the position of the sample by changing the distance z_1).

In this scheme, the resolving power (resolution) δ_{exp} increases with the magnification factor M . For example, Fig. 3. 5-e shows a large FOV with $M = 2$ and $\delta_{\text{exp}} = 24 \mu\text{m}$. Our device allows to easily zoom in a given area, as reported in Fig. 3. 5-d, simply by tuning the vertical sample position. As an illustration, Fig. 3. 5 represents a zoom into the red square (Fig. 3. 5-b) with a magnification factor $M = 36$ and a resolving power $\delta_{\text{exp}} = 0.8 \mu\text{m}$. The calculation of the effective spatial resolution is illustrated in Fig. 3. 6, applying the Rayleigh criterion. Several points were chosen, and the final value was estimated as an average of the measured values. We obtain for the nuclear envelope a resolution of $0.6 \mu\text{m}$ with a pixel size of $\Delta_{\text{pixel}} = 0.15 \mu\text{m}$.

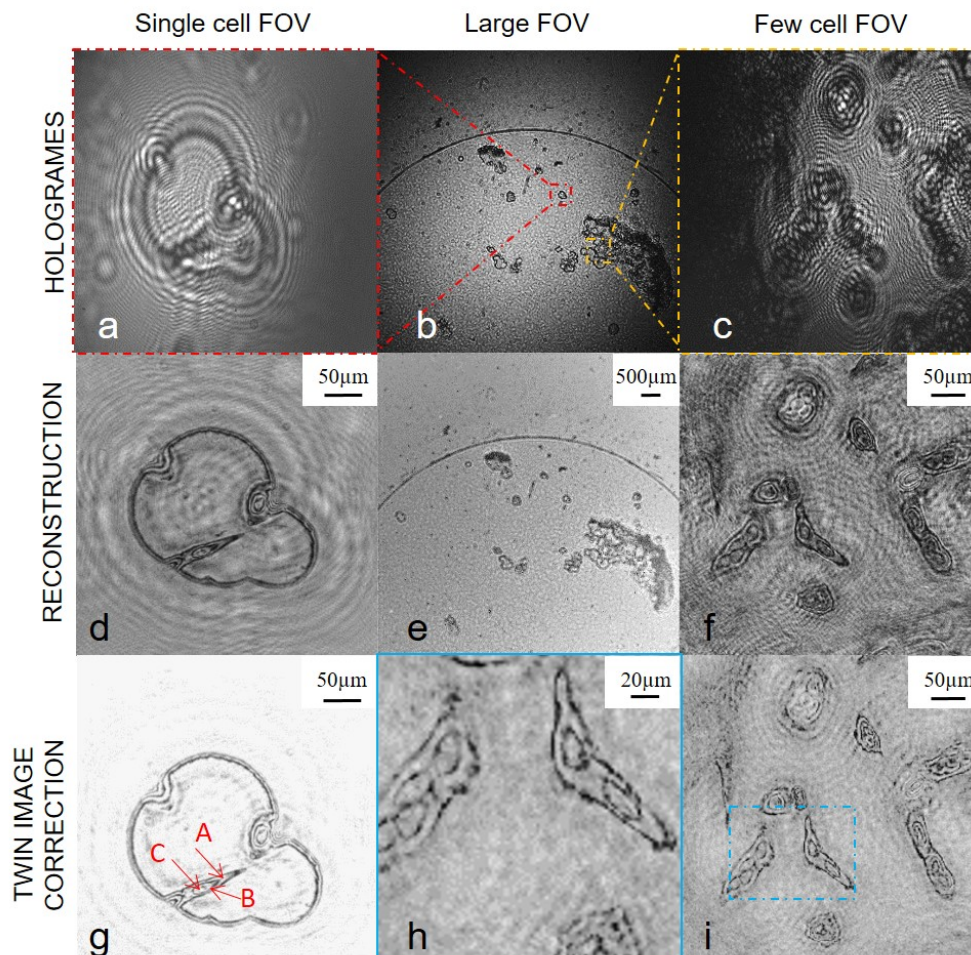


FIG. 3. 5. A), B), C) HOLOGRAM, D), E), F) RECONSTRUCTED AMPLITUDE IMAGE OF CELL CULTURE WITH ACQUISITION SOFTWARE AND NO TWIN IMAGE CORRECTION G), H), I) RECONSTRUCTED AMPLITUDE IMAGE USING POST-PROCESSING DATA WITH TWIN IMAGE CORRECTION; H) IS A ZOOM INTO THE BLUE SQUARE REPRESENTED IN I). THE CAPITAL LETTERS CORRESPONDS TO CYTOPLASM (A), NUCLEAR ENVELOPE (B), AND THE NUCLEOLUS (C).

Fig. 3. 5-d, f presents the amplitude reconstruction without the twin image correction, while the twin image correction is presented in Fig. 3. 5-g, i respectively the zoom of i in h. The images quality is improved (better contrast) thanks to the removal of artefacts. In both regions of analysis, several components of the cells can be observed, like (Fig. 3. 5-g): cytoplasm (A), nuclear envelope (C), and in the single cell case also the nucleoid (B). According to literature, the average nuclear dimensions of the freely growing U2OS cells is around $16 \pm 2 \mu\text{m}$ in width, $23 \pm 3 \mu\text{m}$ in length, and $4 \pm 1 \mu\text{m}$ in height. Those values are compatible with what we retrieve with our system and the calibration we made.

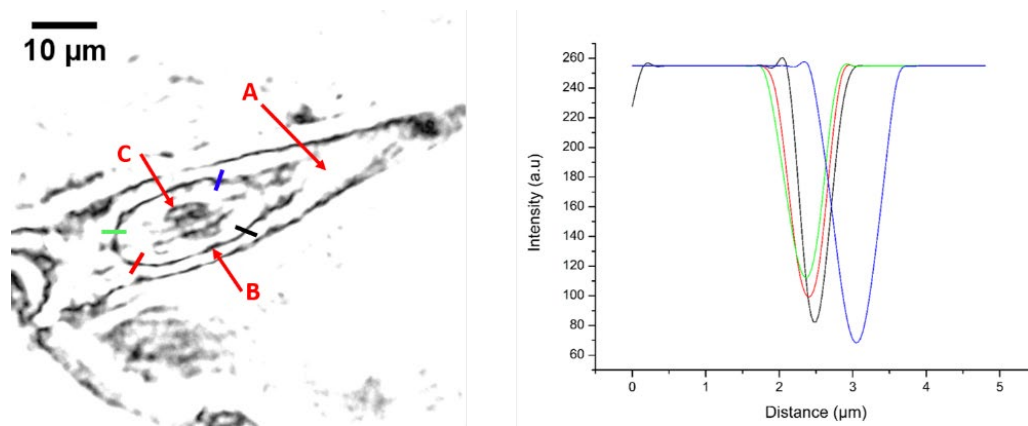


FIG. 3. 6. ESTIMATION OF THE RESOLUTION ON THE NUCLEAR ENVELOPE: A) THE SAMPLE AND THE REGION CHOSEN FOR CALCULATION TAKEN FROM FIG. 3. 5G THE CAPITAL LETTERS CORRESPONDS TO CYTOPLASM (A), NUCLEAR ENVELOPE (B), AND THE NUCLEOLUS (C); B) PROFILE PLOTS OF THE REGION MARKED IN A.

The estimation of the image transverse spatial resolution is shown in Fig. 3. 6, applying Rayleigh criterion. Several lineouts were chosen for the calculation, in order to reduce any ambiguity, and the final value was estimated as an average of the values obtained. The average value for the nuclear envelope thickness (which are the thinner structures we can see) is about $0.6 \mu\text{m}$, which gives an upper value of the resolution.

Between the two types of experiments using cell culture, we can conclude that the best case is the one with high NA using the pinhole ($1 \mu\text{m}$) that creates a clean spherical wave. It can be clearly observed if we compare the images from Fig. 3. 3-B with Fig. 3. 5-g.

Mitochondria is a cell' organelle with a spatial resolution of few hundreds nanometers. The resolution of our system is now limited to $0.6 \mu\text{m}$, which is not enough to analyse them. Thus we could not make a characterization of this cell' component but we could obviously see that the label-free approach is efficient: the nuclear envelope is usually observed and measured only if there is a labelling, with our system it was seen without any labelling. However, the spatial resolution can be improved, for instance, by increasing the resolution in the sensor plane with a sensor with smaller pixel size.

3.3. In-vivo analysis of Cyanobacteria motility (*Synechocystis* PCC 6803)

In this section, we focus our lensless microscope on cyanobacteria cells (*Synechocystis*), a high-aimed type of cells studied by at the *Laboratoire de biologie et biotechnologie des Cyanobactéries* led by our collaborator Prof. Franck Chauvat. Studying this kind of cell is challenging due to their fast motility and strong interaction with light. The accessibility of a large FOV at high resolution allowed us to analyse the cells behaviour and their interaction with a probe light. This micro-organism, according to several studies, uses micro-optics to sense light direction⁷⁸. Similarly to the human eye, they can focus light to the rear side of the cell which appears the brightest. The motility is ensured by pili that are photo-activated only in the regions where light is concentrated⁷⁹. The ability to move help cyanobacteria to orientate and move favourably to light and environment. The motility of these cells could be the answer of a recent concern: the decline in fossil energy reserves. The answer is found in the uses of micro-algae, such as cyanobacteria, for sustainable production of biofuels. Using a multidisciplinary approach, they investigate the metabolism and stress responses of cyanobacteria (the most abundant photosynthetic organisms) with the prospect of using them for the sustainable production of biofuels, as well as the biodetection and/or bioremediation of pollutants. These two objectives are intrinsically related as the metabolism uses a wealth of metallo-enzymes.

An example of cyanobacteria is *Synechocystis* sp. PCC 6803, an optical image is presented in Fig. 3. 7 as well as a schematic representation of its structures.

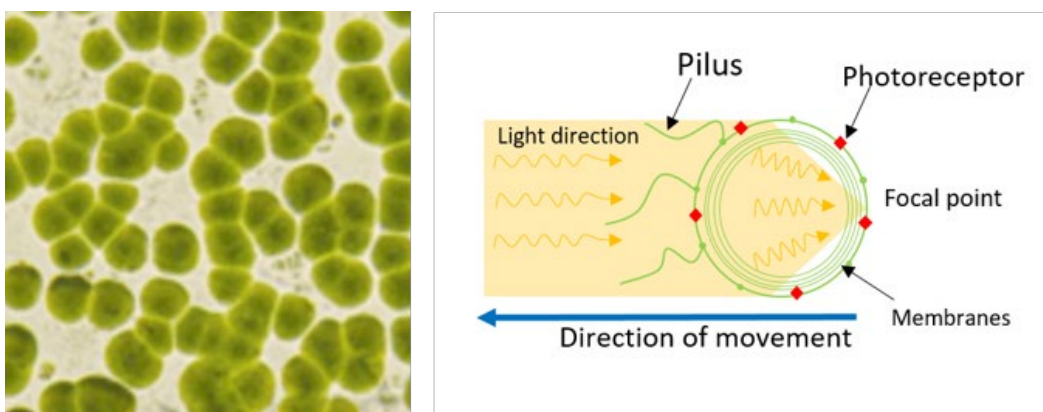


FIG. 3. 7. LEFT: OPTICAL IMAGE WITH SYNECHOCYSTIS SP. PCC 6803, ADAPTED FROM⁸⁰
RIGHT: SCHEMATIC REPRESENTATION OF CYANOBACTERIA' STRUCTURE.

3.3.1. Sample preparation

The freshwater cyanobacterium *Synechocystis* sp. PCC 6803 wild type were grown photoautotrophically in a modified BG11 medium (Herdman et al., 1973), containing twice the same amount of sodium nitrate. The cells were kept in a rotary shaker (120 rpm) at 30°C and illuminated by fluorescent white lamps giving a total intensity of about 50 to 60 $\text{mmol} \cdot \text{Photons} \cdot \text{m}^{-2} \cdot \text{s}^{-1}$ under a CO_2 atmosphere. The cells were maintained in the logarithmic phase of growth and were collected at an optical density at 800 nm of 0.6 to 0.8⁸¹.

Another protocol was followed, using gelatine to prevent Brownian motion and increase the viscosity of the medium, and is described below:

- 0.2% of gelatine (agar-agar) was diluted in 50 ml of deionized water;
- One droplet of gelation with the diameter of approximately 2 cm was set on a microscopic glass, and let few seconds to dry;
- On top of the gelatine we add a droplet of sample with cells *Synechocystis* PCC 6803. Some images with the sample used are presented in Fig. 3. 8.

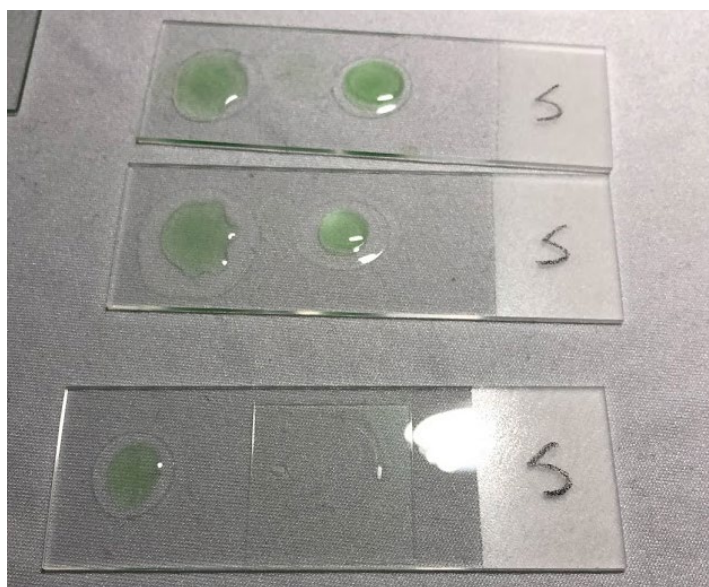


FIG. 3. 8. SAMPLE PREPARATION FOLLOWING THE PROTOCOL OF CYANOBACTERIA FIXED IN GELATIN.

3.3.2. *Synechocystis motility in water*

Using our prototype with fast acquisition time and low laser power, live imaging of the cyanobacteria was achieved. This cell category is usually challenging to analyse due to their fast motility and interaction with the light. The accessibility of a large field of view allowed us to analyse the cells' behaviour when subjected to an external light source. It was found out that these cells presents three ways of response to the light as follow: phototaxis, photokinesis and photophobic⁸². In order to study the cell motility with a controllable light source, we inserted a second diode of 637 nm (see Fig. 3. 9) in the system, with an estimated power of 1-2 mW. The light was coming from left side, and the illumination covered the whole sample holder. The coherent illumination used for imaging was filtered with 1 μ m pinhole to create a clean spherical wave and a higher NA = 0.33. In addition, we inserted a bandpass filter with CWL = 405 \pm 2 nm, that will protect the CCD from the scattering of 637 nm.

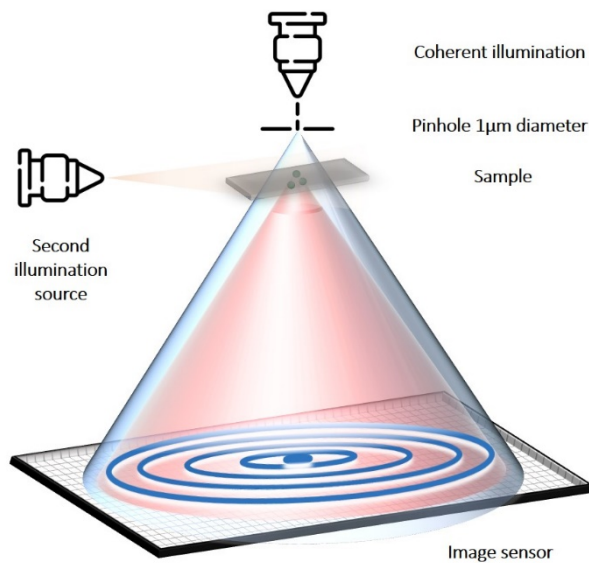


FIG. 3. 9. CONFIGURATION USE FOR CYANOBACTERIA EXPERIMENT AND THEIR INTERACTION WITH THE LIGHT.

The total working distance is $Z = 40$ mm, and the sample was located at a distance $z_2 = 38.5$ mm from the detector, which gives a magnification $M = 27$ and a sampling step $p = 0.205$ μ m.

Fig. 3. 10 present's amplitude and phase reconstructions of living cyanobacteria. In this case we are not interested in recovering high resolution images but mostly to track the position of the cells. Within each cell, the bright point (visible in both amplitude and phase maps) is associated to a

self-focusing effect of the light propagating through the cell. The cyanobacteria used in our experiment are spherically shaped.

From Fig. 3. 10-c, we can follow the motion of single cells. Some particular cells are labelled with arrows for illustration. The cells are moving towards the illumination source. Indeed, the bacteria respond to the light stimuli moving away from that side and advancing towards the light.

From Fig. 3. 10, we can calculate the motility of a single cell. We found a motility ranging between 0.03 and 0.07 $\mu\text{m/s}$, in good agreement with previous studies⁸³. We observed that the majority of the cells (70%) moved towards the light (for example see the yellow trajectory in Fig. 3. 10). The rest (30%) displayed a stationary behaviour followed by a circular rotation (red arrow from Fig. 3. 10). Dead cells were not considered and the motility estimation was made for a total of 40 cells that are present in the screen captures in Fig. 3. 10. The acquisition time for individual frames was 100 ms.

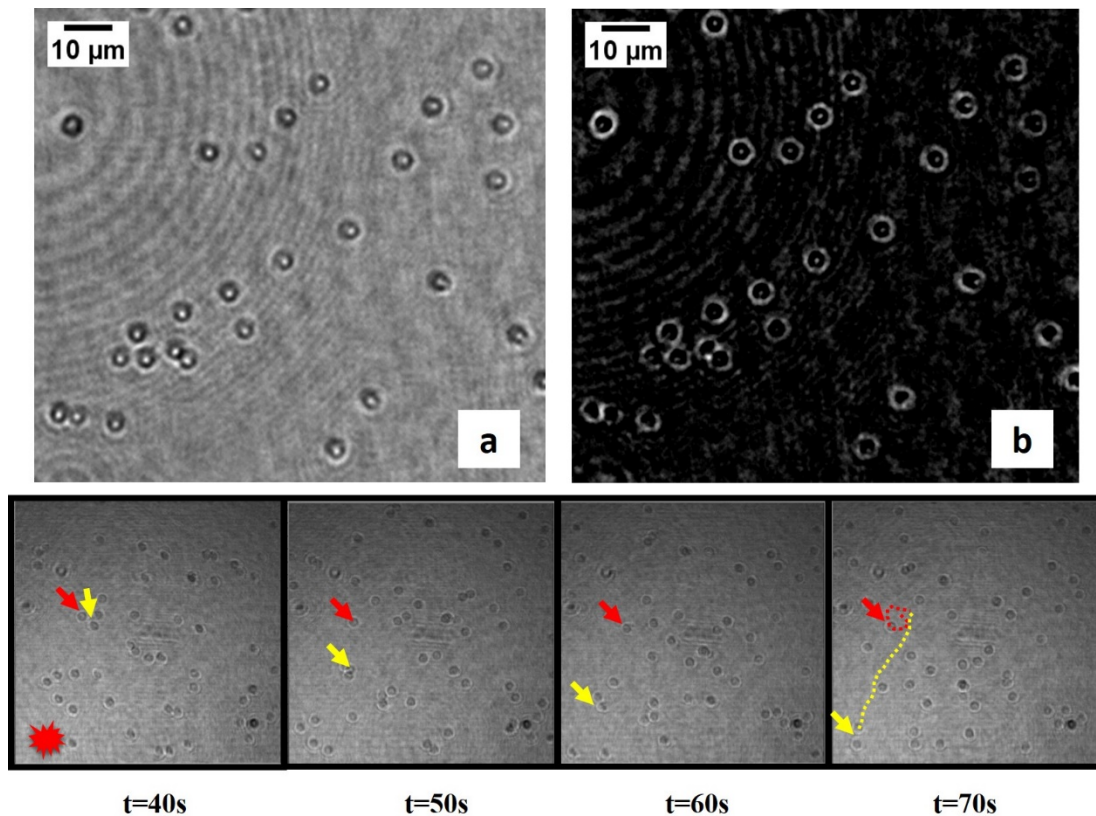


FIG. 3. 10. RECONSTRUCTED HOLOGRAM FROM CYANOBACTERIA, IN A) AMPLITUDE AND B) PHASE; C) SCREENSHOTS AT DIFFERENT TIMES THAT SHOW THE MOVEMENT OF THE CELLS IN THE FLUID IN THE DIRECTION OF THE SOURCE OF LIGHT (THE RED STAR).

3.3.3. *Synechocystis motility fixed in gelatine*

The natural fluid motion complicates the motility analysis. Moreover, in our experimental configuration, the transfer of heat from the laser beam to the sample produces a thermic effect that increases the fluid convection. For example in the previous experiment, we cannot confirm that we have recover the real motility of the cells due to the fluid agitation. To prevent this parasitic motion, I modified the sample preparation using the second protocol (see section 3.3.1. Sample preparation) based on a gelation medium.

I analysed the sample in the same experimental configuration used before with the following parameters: the sample was located at a distance $z_2 = 38\text{mm}$ from the detector, while the total working distance Z is 40 mm, which gives a magnification $M = 20$ and a sampling step $p = 0.275\ \mu\text{m}$. First, I tested the quality of the sample. Several holograms were saved and analysed in terms of image quality that could be influenced by the presence of the gelatine as medium support.

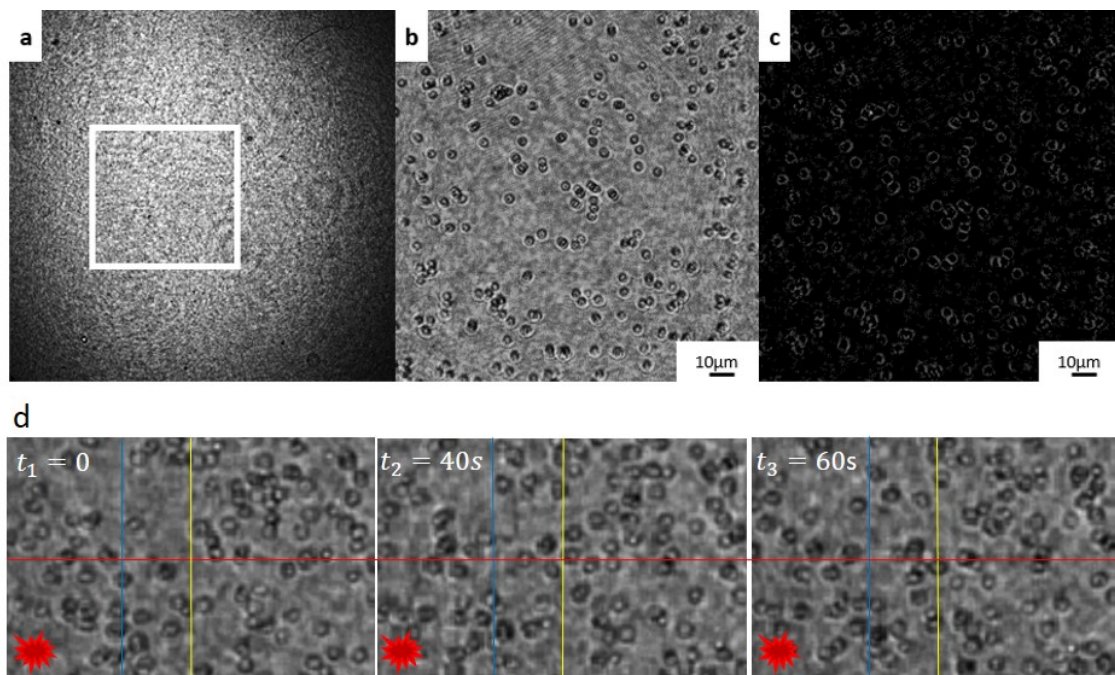


FIG. 3. 11. A) HOLOGRAM, RECONSTRUCTED HOLOGRAM FROM CYANOBACTERIA, IN B) AMPLITUDE AND C) PHASE; D) SCREENSHOTS AT DIFFERENT TIMES THAT SHOW THE MOVEMENT OF THE CELLS IN THE GELATIN IN THE DIRECTION OF THE SOURCE OF LIGHT (THE RED STAR). THE TRACKING OF THE MOTION OF BACTERIA CAN ALSO BE VIEWED IN THE VIDEO, SEE [LINK](#).

Fig. 3. 11 presents the hologram with its amplitude and phase reconstructions of living cyanobacteria. The same type of cell is used. As in the previous experiment (cyanobacteria in water) the bright point (visible in both amplitude and phase maps) is presented. It is associated to a self-focusing effect of the light propagating through the cell.

From Fig. 3. 11-d, we can follow the motion of single cells. In this case the concentration of the cell was high so it is difficult to track individual cells without special tools (cytometry programs). To simplify the tracking, we used vertical and horizontal lines (red, blue, yellow) in the same position for the three screen captures at different times. We present a zoom in the centre of each image for illustration of some particular cells. We can clearly see the displacement of the cells from one image to another, if we follow the guideline. The cells are moving towards the illumination source. Indeed, the bacteria respond to the light stimuli moving away from that side and advancing towards the light. The acquisition time for individual frames was 100ms.

The simplicity of in-line holography makes possible the tracking of cells without the need of expensive apparatus. An adapted program for cytometry could help for a faster analysis. In the cyanobacteria case we could tracked bacteria moving vertically, this point can also help for non-spherical bacteria. The cyanobacteria investigation will continue in the framework of a new project in the group, as well as the other experiments presented before, in a new configuration presented in **Chapter 4**.

3.4. Extension DIH to 3D view

Today, 3D imaging techniques are emerging, not only as a new tool in early drug discovery but also for the development of potential therapeutics to treat disease. Particular efforts are directed towards in vivo physiology to avoid perturbing the system under study.

As we saw in the **Chapter 1**, optical tomography techniques were initially developed in the standpoint of X-Ray imaging⁸⁴. The sample position was fixed or the sample was immobilized using methods of crystallography or cryogenesis. The position of the sample is changed using an automatic rotation. The rays are passing through the sample and 2D projections at different angles are extracted and merged in a 3D volume. The sample structure has to remain the same in order to obtain the right reconstruction. This is why the object is immobilized from the beginning, and why the dose received by the sample needs to be controlled, least it induces damages that modify the sample during the acquisition.

In classic microscopic techniques, a 3D image of a sample can easily be achieved. Several methods were presented in the beginning of **Chapter 1**. However, they usually require the sample to be labelled with fluorescent dyes and the geometry of the sample container is constrained.

In this chapter I present a 3D reconstruction based on back-propagation function using as demonstration a 3D synthetic sample. The chapter ends with a first demonstration of a 3D biological application.

3.4.1. Theoretical aspects

We saw in **Chapter 2** (section 2.2.2 Back-propagation and reconstruction) that the field at the detector position could be written as:

$$U_{diff}(\vec{r}) = (U_{inc}t_{2D}) \circledast (h_{z_s}^\lambda) \quad (3.1)$$

With $h_{z_s}^\lambda$ the Fresnel propagator to a distance z_s . Using the algorithm previously described (**Chapter 2**, section 2.3), we can retrieve the complete exit wave after a 2D sample at a distance z_s from the detector. The method consist in:

- 1- Perform the Fourier transform of the complex field (hologram);
- 2- Multiply by the free space propagator;
- 3- Perform the inverse Fourier transform.

In these conditions, the propagated field is sampled at the same step as the initial field which allows to control the phase jumps that can occur. The adjustment of the curvature consists in adding a parabolic curvature to the initial field ($z = 0$) in order to be able to control and set the magnification in the image plane. This will allow to control continuously the phase jump and to calculate the propagated field at any distance with a final correction of the sampling in the final plane. The detailed mathematical approach has been fully treated in the thesis of Julien Samaan who has developed the software suite exploited in this thesis.

In the case of a 3D sample, the diffracted field recorded in the hologram contains the contributions from the field diffracted by all the successive planes. Therefore, by back-propagating the field to different planes we can obtain a 2D slices of the sample that can be merged in a 3D representation. As drawbacks, at every in-focus plane you also get the out of focus contributions from the other planes. Therefore, this can be quite challenging for very complex samples. Algorithms exists to “clean” the slices by removing out of focus contribution, using for instance the acutance function. I have not implemented such algorithms but we will see that for “simple” sample this gives already good results. Second, the DOF is directly proportional to the object distance and its size. As the wavelength of the laser increases, the DOF decreases. The DOF is inversely proportional to the pixel size and to the number of pixels in detector⁸⁵. DOF can could be defined as:

$$DOF = \frac{\Delta_{pixel}^2}{\lambda} \quad (3.2)$$

where Δ_{pixel} represents the pixel size of the detector, and λ the wavelength of the illumination source. Axial resolution (in z-direction) is defined as we already describe in **Chapter 2** (section 2.2.3 Resolution and depth of field) by equation:

$$\delta_{axial} = \frac{\lambda}{2NA^2} \quad (3.3)$$

We clearly see that the lateral and axial resolution are coupled. For a low DOF, the variation of the field with z will be more stringent and the various reconstructed slices will have a weak superposition. Inversely, with a large DOF, the reconstruction will vary slowly with z and the slices will be integrated over the axial path with a lower visibility of fine details, thus decreasing the resolution. This is schematized in Fig. 3. 12.

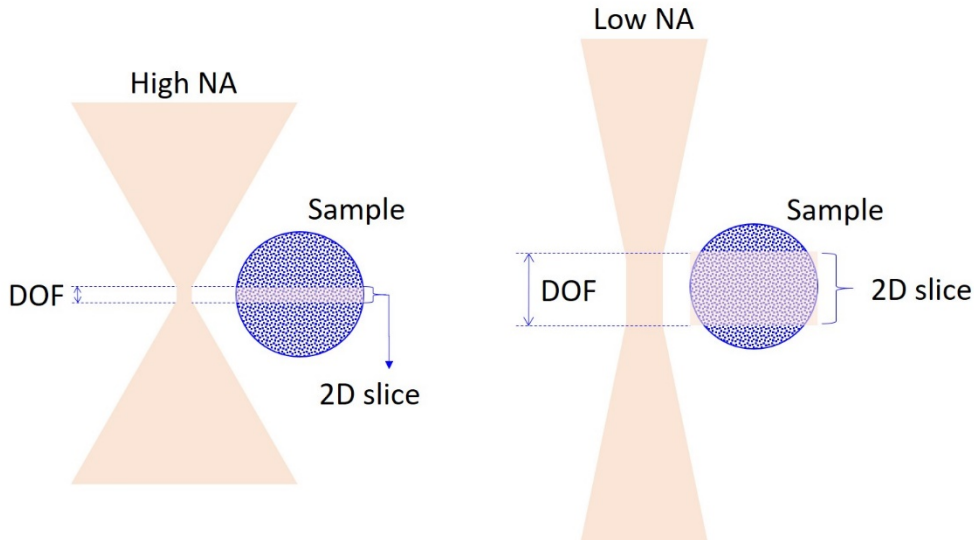


FIG. 3. 12. PRINCIPLE OF BACK-PROPAGATION SLICING. THE HOLOGRAM IS BACK-PROPAGATED IN THE OBJECT PLANE AND DEPENDING ON THE NUMERICAL APERTURE OF THE COLLECTED PATTERN ON THE DETECTOR THE DEPTH OF FOCUS WILL VARY INVERSELY PROPORTIONAL TO IT. A HIGH NA WILL CREATE A THIN DOF (OR 2D SLICE) AND A LOW NA WILL ELONGATE THE DOF.

In summary, the 3D configuration requires a high numerical aperture, which will limit the out of focus contribution of a selected z -slice. We also need to achieve an almost perfect wavefront to keep the validity of the curvature adjustment. Indeed, aberrations will distort the image formation during the back-propagation process. In our case, both conditions are fulfilled by using the $1 \mu\text{m}$ pinhole.

Acutance function: the sharpness of a feature in a specific plane is quite difficult to define precisely because it's based on subjective evaluations. This can be numerically estimated by computing the acutance function which corresponds to the gradient of the modulus of the reconstruction. In case of a 2D sample, only one local minimal is retrieved. For a 3D sample, we will observe multiple local minima. For very complex 3D samples, this function will be smoothen and it will be difficult to identify in-focus features.

3.4.2. Calibration and results using a 3D calibration sample

3.4.2.1. Description of the 3D calibration target

In a first step, in order to evaluate the performance of the instrument for 3D imaging, I designed a 3D calibration target based on polymeric microspheres. It is made of 3 microscopic slides with a thickness of approximately $170\ \mu\text{m}$ each, stacked one on top of the other. Between each one, we distributed a solution of deionized water with a concentration of $0.06\ \mu\text{L}$ of polymeric microspheres with a diameter $d = 10\ \mu\text{m}$ (see Fig. 3. 13).

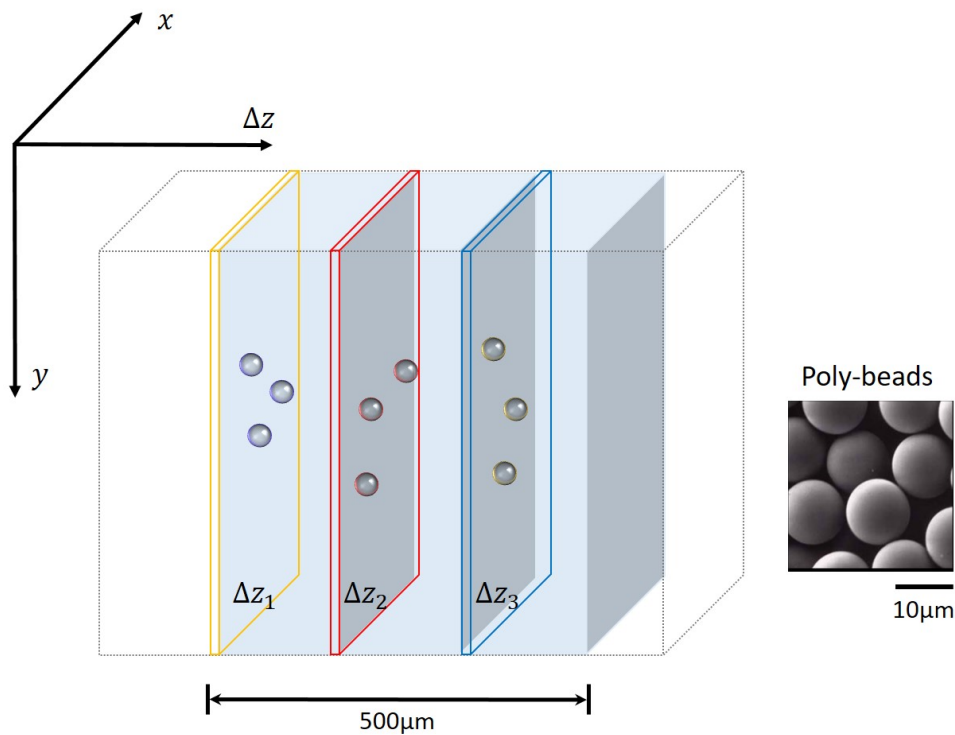


FIG. 3. 13. ILLUSTRATION OF THE 3D CALIBRATION TARGET. TO BE MORE REPRESENTATIVE WE DEFINE EACH PLAN WITH A DIFFERENT COLOR. IN INSET, AN IMAGE OF THE POLYMERIC MICROSPHERES (IMAGE FROM THE MANUFACTURER).

The total working distance is $Z = 40\ \text{mm}$ and the sample was positioned at $z_1 = 3\ \text{mm}$ far from the illumination source of wavelength $\lambda = 405\ \text{nm}$, while the sensor is being located at $z_2 = 37\ \text{mm}$ from the sample. That means that the magnification is $M = 20$, and a sampling step $p = 0.275\ \mu\text{m}$. Using the digital interface, one hologram was saved, and later on post-processed using the improved algorithm that removes the twin image contribution. The propagation distance can be adjusted numerically and we will effectively scan in the $\Delta z = 500\ \mu\text{m}$ region. Fig. 3. 14 summarizes the whole process.

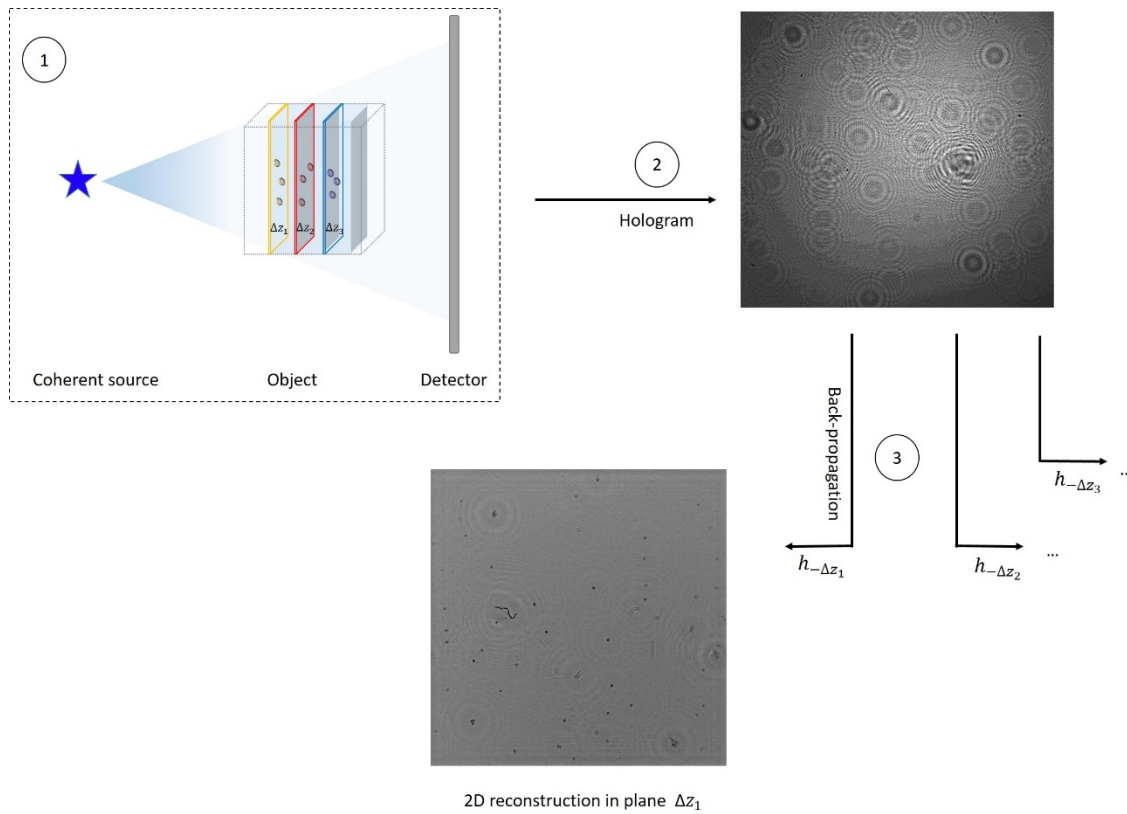


FIG. 3. 14. ILLUSTRATION OF THE FREE SPACE PROPAGATOR IN DIFFERENT PLANES USING ONE HOLOGRAM. 1-THE SAMPLE IS LOCATED UNDER A COHERENT ILLUMINATION. 2- ONE HOLOGRAM IS ACQUIRED. 3- BY USING THE SLICING FUNCTION BASED ON FRESNEL PROPAGATION (H_z) WE CAN EXTRACT IMAGES FOR EACH PLAN Δz_i .

3.4.2.2. Experimental calibration

From this single hologram, the reconstruction is carried out in three successive planes. As we already mentioned on the calibration procedure, the knowledge of the source-to-camera Z distance is necessary and sufficient to perform the calibration on the reconstructions, namely, to determine the sampling step. Indeed, the actual propagation distance can be retrieved looking at the calibration target reconstruction. The experimental hologram and the reference signal are presented Fig. 3. 15.

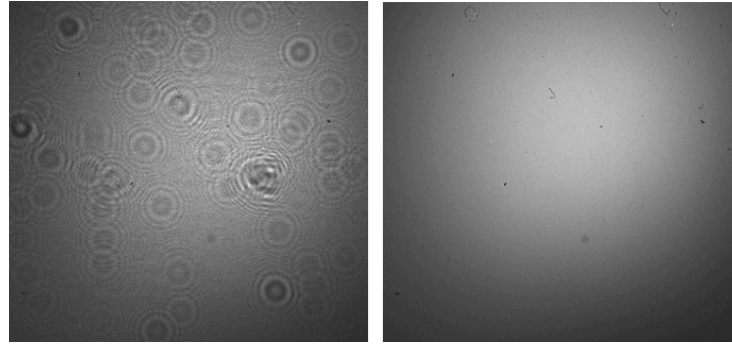


FIG. 3. 15. THE EXPERIMENTAL HOLOGRAM FROM THE 3D CALIBRATION TARGET (LEFT), AND THE REFERENCE SIGNAL WITHOUT THE SAMPLE (RIGHT). THE ACQUISITION TIME IS 100ms.

Fig. 3. 16 presents the reconstruction based on the Fresnel propagator. Three holographic reconstructions are therefore made, one for each planes presenting a focused image. The three planes of focus were found by looking at the reconstruction slice by slice. The corresponding results are shown in Fig. 3. 16-b. We selected an area from the full-field-of-view and we present the back-propagated images for the three planes.

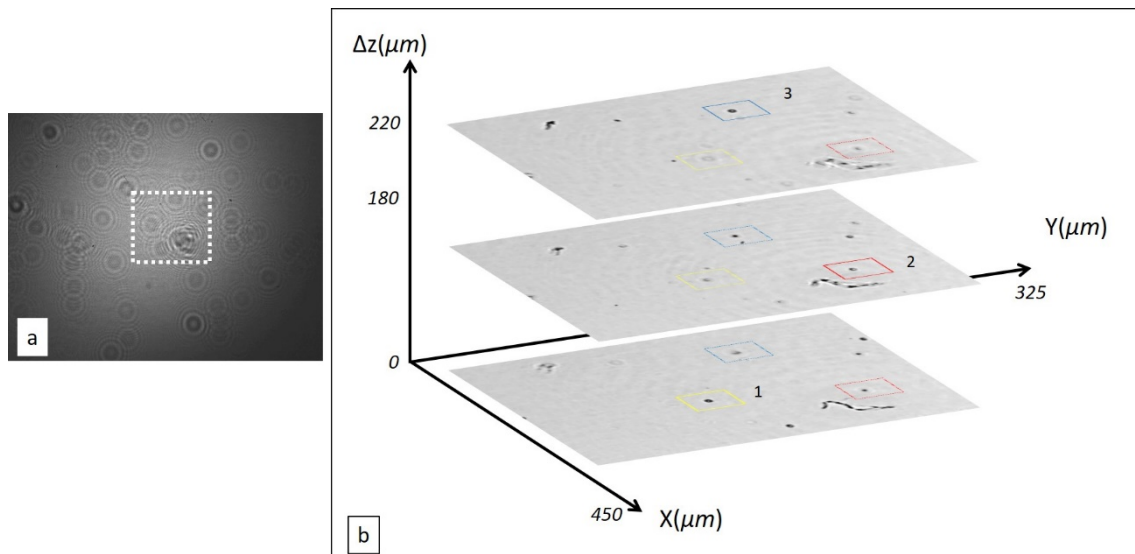


FIG. 3. 16. DEMONSTRATION OF 3D IMAGING WITH DIH. A) THE HOLOGRAM IN FULL FIELD OF VIEW. THE WHITE SQUARE REPRESENTS THE AREA SHOWN IN B; B) THE RECONSTRUCTION OBTAINED FROM HOLOGRAM A) IN THE THREE SUCCESSIVE PLANES.

Fig. 3. 17 represents close-ups on each particle's reconstruction. For each plane we chose one given microsphere that is in-focus. Fig. 3. 17-a shows in-focus images of those 3 microspheres, obtained for a different propagation distance. They all look similar, and have a diameter of $10 \mu\text{m} \pm 1 \mu\text{m}$.

In Fig. 3. 17-b, we present the reconstruction of each of these microspheres but with a propagation distance corresponding to plane 1. It appears clearly that once we change the distance of the back-propagation function the microsphere starts to be defocused. As a side note, the white spot in at the centre of each microsphere is due to their spherical shape. Indeed, the microspheres are behaving as lenses, and focus the light from one side

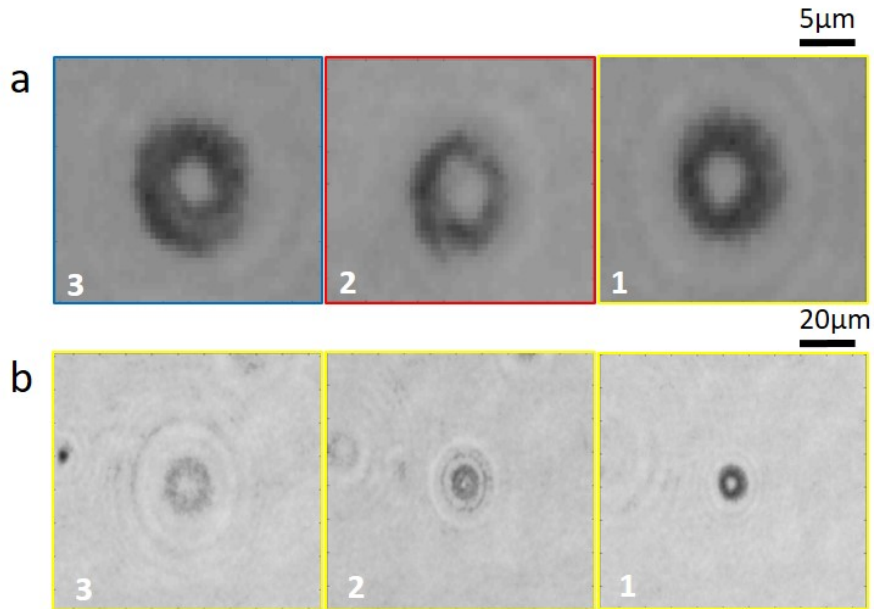


FIG. 3. 17. A) ZOOM INTO EACH MICROSPHERE MARKED FIG. 3. 16 -B WHEN ON FOCUS (I.E. AT THE APPROPRIATE PROPAGATION DISTANCE). B) THE SAME MICROSPHERES, BUT AS RECONSTRUCTED FOR THE PROPAGATION DISTANCE THAT PUT PARTICLE 1 INTO FOCUS. THE ZOOM FACTOR WAS REDUCED IN ORDER TO SEE THE INTERFERENCE RINGS AROUND THE OUT OF FOCUS MICROSPHERES.

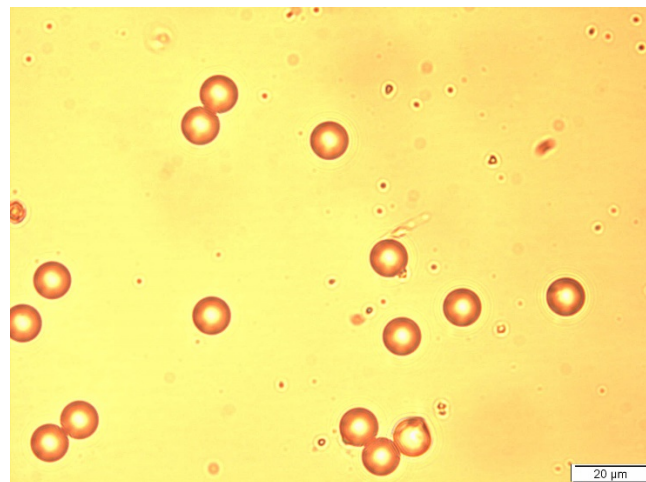


FIG. 3. 18. OPTICAL IMAGE OF 10µM DIAMETER MICROSPHERES, OBJECTIVE 20X.

3.4.2.3. Discussion

In the calibration step we used the sample as a reference to confirm the extension of the depth-of-field (DOF) by using sample up to 250 μm thickness. As clearly visible in Fig. 3. 17-a, the different microspheres in the colour frames are in-focus for different values of Δz , reflecting their vertical position in the multi-layer slices. Typically, in classical microscopy the DOF is inversely proportional to the numerical aperture and magnification of the objective⁸⁶. The limitation is less stringent in in-line holography; however, the complexity of the sample is an important parameter. Indeed, a thick and complex sample limits the DOF due to the high scattering and absorption of the sample that cause losses of information. Several methods have been developed to improve the optical quality of some biological targets that could advantageously be applied to in-line holography^{87 88}.

3.4.3. 3D reconstruction of a bio-sample

In the first demonstration, we used a simple sample that was composed of the microsphere presenting a unique refraction index (n) inside a homogeneous medium. As we already discussed (see 2.5.2), in biological samples all the components possess relatively similar refraction indices n_i , making them hard to distinguish with optical microscopy. Additionally, this is even more complicated for a three-dimensional biological sample.

We are interested here in an U2OS cell culture, with nuclear dimensions to be $16 \pm 2 \mu\text{m}$ in width, $23 \pm 3 \mu\text{m}$ in length, and $4 \pm 1 \mu\text{m}$ in height, while the cell volume including cytoplasm arrives at approximatively $4,000 \mu\text{m}^3$ (see 2.5.2). Fig. 3. 19 presents two examples of such a type of sample, observed under an optical microscope.

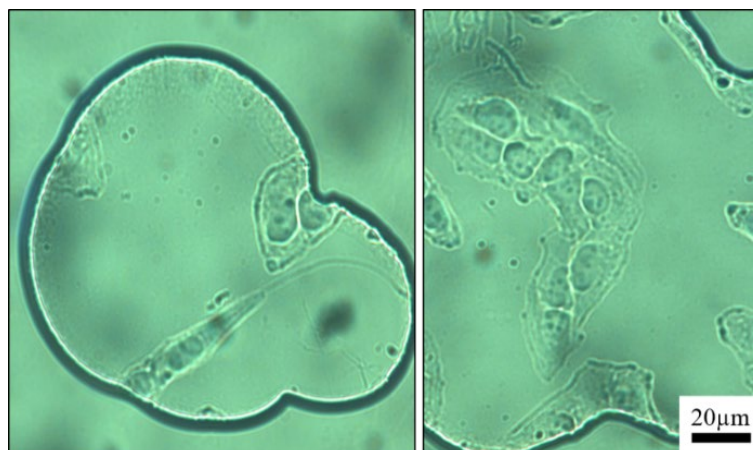


FIG. 3. 19. U2OS CELLS OBSERVED WITH AN OPTICAL MICROSCOPE. THE FIRST IMAGE REPRESENTS THE SAMPLE THAT WILL BE IMAGED WITH OUR DIH MICROSCOPE. IN THE SECOND IMAGE, WE CAN SEE AN AREA WITH A GROUP OF CELLS.

The total working distance in our experiment is $Z = 40$ mm. The object is located approximately $z_2 = 37$ mm from the camera (the in-focus plane is at $z_2 = 38.5$ mm from the back-propagation), giving a magnification $M = 27$, and a sampling step of $0.2 \mu\text{m}$. The experimental hologram is presented in Fig. 3. 20-a, and the corresponding reconstruction in Fig. 3. 20-b, and c respectively.

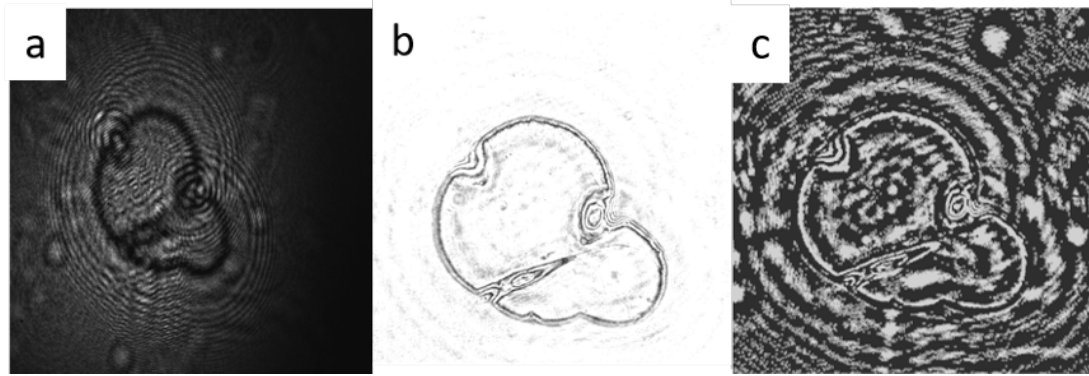


FIG. 3. 20. A) THE EXPERIMENTAL HOLOGRAM OF THE DIH; B) THE AMPLITUDE RECONSTRUCTION WITH TWIN IMAGE CORRECTION, AFTER $N = 10$ ITERATION, RESPECTIVELY C) THE PHASE RECONSTRUCTION

Using the free space propagation function, we can give an estimate of the thickness of the sample (Fig. 3. 21). Here, we named $z_2 = \Delta z = 0$, an arbitrary starting position for the fine z_2 numerical scanning over several transverse planes. For this step, we used the algorithm with the implementation of the twin image correction, with 10 iterations. We clearly observe that the nucleus shape evolves over $8 \mu\text{m}$ propagation distance, as seen in the example that emphasizes the variation of the nucleus width, from 8 to $11 \mu\text{m}$.

Additionally, using a 3D slicing package from the Image J software suiteⁱ, we have compiled the displayed slices to achieve a 3D representation of the sample.

In Fig. 3. 22 we represent the process of slice stacking, as well as the 3D reconstruction of the single U2OS cell. We can observe a lack of contrast in the reconstructions. It could be explained by the Signal to Noise Ratio (SNR) affected by the scattered of the cell, the hologram of the cell differs from the one of the solid microspheres used in the calibration test (see Fig. 3. 16-a, and Fig. 3. 20-a, hologram comparison).

The 3D is satisfying but we notice that the depth resolution (theoretically of 700 nm, calculated from equation 3.3) limits the quality of the Z perception.

ⁱ <https://imagej.net/Welcome>

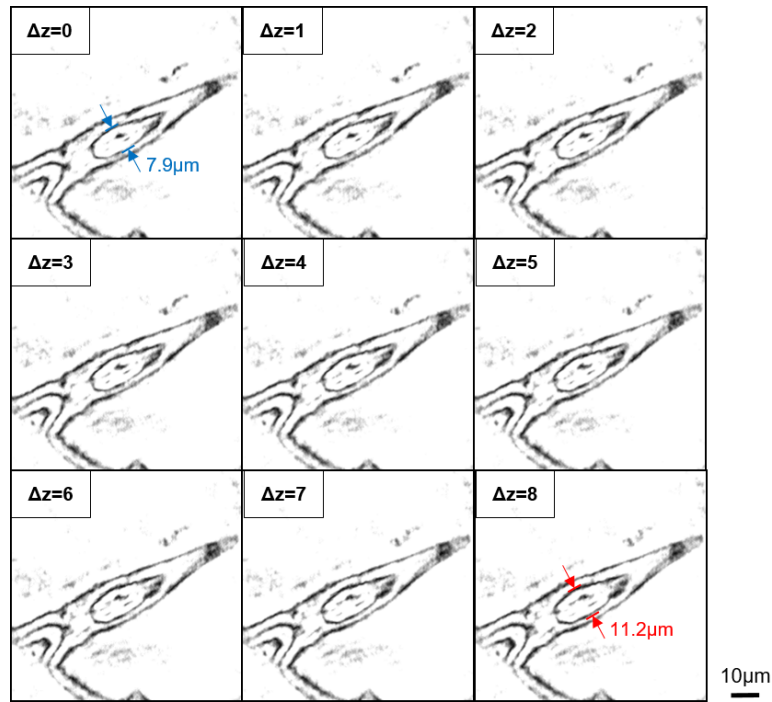


FIG. 3. 21. SLICING OF THE RECONSTRUCTED AMPLITUDE OF THE CELL DISPLAYED IN FIG. 3. 20-B. SLICES ARE RECOVERED AT DIFFERENT FOCAL POINTS Δz_i (μm) RANGING FROM 0 TO 8 μm .

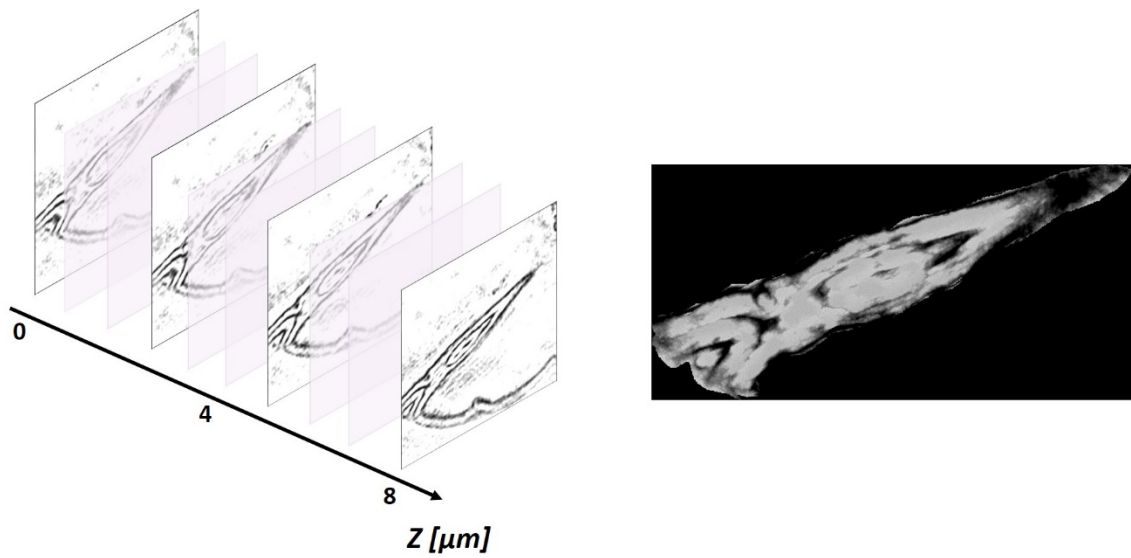


FIG. 3. 22. 3D RECONSTRUCTION OF U2OS CELLS USING SLICING FUNCTION LEFT: THE SLICES USED FOR RECONSTRUCTION; RIGHT: THE 3D VIEW OF THE SAMPLE (SEE VIDEO [LINK](#)).

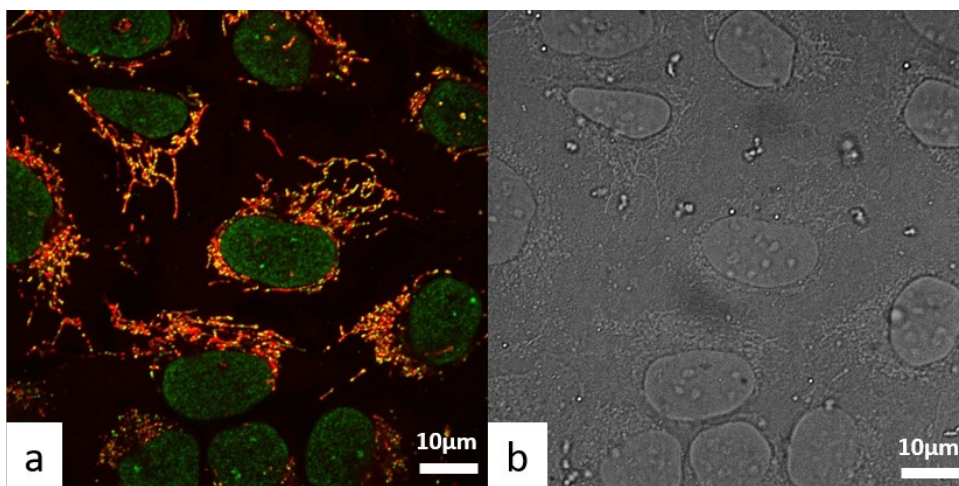


FIG. 3. 23. A) CONFOCAL IMAGE OF U2OS CELLS TRANSFECTED WITH GFP-FUSIONS AND LABELED WITH MITOTRACKER, RESPECTIVELY B) TRANSMISSION REPRESENTATION OF THE SAME SAMPLE. BOTH WITH A MAGNIFICATION FACTOR 60X.

In classic microscopy techniques, as confocal used by our collaborator LGRI, the 3D rendering of the sample can be easily retrieved as there is a labelling (Fig. 3. 23-a). The confocal microscope realizes 3D images by producing serial sections in the labelled sample. The problem is that the fluorophores are excited in the same time in the whole thickness of the sample. That means that the sample is excessively exposed to the light source, in the need to collect several Z-planes for each time-point. This leads to problems such as photobleaching of fluorophores, phototoxicity, and slow 3D frame rate as we have seen in **Chapter 1**. The label free approach is an alternative solution for a 3D bio-reconstruction in a single acquisition.

3.5. Conclusion

Lensless imaging based on in-line holography is an appealing solution for biomedical investigations due to its portability and in-vivo capability. We imaged and analysed biological samples in different working conditions, pointing out the ease of use of our platform for real time in vivo studies. This non-invasive tool provides a wide range of applications from single cell to population of cells and tissue imaging. Another remarkable advantage is the low level of radiation that is needed, as the illumination is spread over the full FOV and the laser power is low. In the first configuration, the total power received by the sample is 0.25 nW for a distance fibre-pinhole of 2 mm.

The instrument is compact, cost-effective and allows sub-micrometer spatial resolution associated to a wide FOV. A major advantage of in-line holography is that it is label free. Moreover, after eliminating the twin image, it provides the exit field complete information, i.e. amplitude and

phase. Consequently, it is possible to observe 3D samples with phase contrast. Our in-line configuration allows for the observation of larger features (FOV between 15 mm and 400 μm), at a variable resolution (24 μm to 0.8 μm). The calibration steps were made using two wavelengths (405 and 637 nm) in order to reduce the external errors as alignment, test the pinhole shape and optimize the distances sample-detector, source-detector. Moreover, two different possibilities of high numerical aperture were considered in the calibration stage: pinhole and high NA lens.

In the case of zebrafish embryo (thick sample), the complex refractive index variations within the sample scatter the photons and distort the optical wavefront, resulting in an increased background noise and a reduced quality of the images. However, the technique could be useful to make distinction between several stages of development, using a portable and less expensive microscopy alternative.

Thin sample proved to be compatible with our in-line configuration, and a lateral resolution of 0.6 μm was demonstrated for cell culture (U2OS). The label free asset made it possible for visualizing different cell component such as nuclear membrane, nucleus and cytoplasm. Moreover, the fast acquisition time (100 ms) allows to study dynamical properties of the cells. As an illustration, we reported the monitoring of the motility of cyanobacteria excited by light. The simplicity of the setup allowed us to integrate a second wavelength necessary for the study of cyanobacteria motility. We could observe the motion of very fast features, thanks to the high speed of the process (based on Fast Fourier Transform and Fresnel propagation).

We have also shown that we reconstruct amplitude and phase that would in principle give access to the complex index of refraction of the cells. Using the phase as a map we could calculate the phase difference between different cells regions. This can be a future perspective of the evolution of the instrument.

Compared with an off-axis digital holography microscopy, in-line holography is very stable against vibration of the optical system, sharing the advantages of portability allowing this system to be brought out of the laboratory without requiring any isolation system. A forthcoming and more sophisticated setup aims at integrating single cell manipulation.

Extension to 3D

The 3D reconstruction of the sample was achieved from a single hologram by back-propagation function and inverse Fourier transform. In the context of in-line configuration, it is a considerable challenge because, the different slices can coexist and the whole sample is difficult to visualize. We have shown that very simple 3D samples, like the poly-beads embedded in various Z-plane, provide an accurate 3D slicing as the DOF is much lower than the size of individual microsphere. In the case of a biological sample, the example of the U2OS shows the limitation as the DOF is close the size of the features we would like to isolate. However, the reconstruction is satisfying and some details of the cell can be followed in 3D.

Our analysis of 3D reconstruction using back-propagation function demonstrated its functionality. The effect of the depth of field, however, induces “gaps” in the structure of the object: at the moment when the contributions of a slice in z appear, those of the previous slice are always present if the NA is low. In this case, a speckle noise analysis would improve the axial resolution, thus a better 3D reconstruction could be obtained. Iterative algorithm exists to clean slices from out of focus but I didn’t work on this implementation.

4. A NOVEL FTH MICROFLUIDIC MICROSCOPE AND APPLICATIONS IN BIOLOGY

Biological imaging has made tremendous progresses these last decades. The latest developments concern manipulating and imaging single cells with nanometre spatial resolution. This chapter aims at introducing the development of a platform for single biological cell handling by dielectrophoresis (DEP) in a microfluidic system and cell visualization by lensless microscopy. The working principle is based on: i) cell transport in liquid media by microfluidics, ii) cell separation in the field of view by an electric field induced by microelectrodes, iii) optical imaging of transparent samples in the range of visible/UV light by holography. The main advantages of such coupled electro-optical method for cell analysis are the improved control, precision and sensitivity regarding cell morphology and behaviour analysis during the electrochemical processes.

This chapter introduces the successive steps of design, fabrication and testing of an electrofluidic system compatible with lensless imaging and its integration in an experimental platform for nanoscale holography. Various materials and processing methods were considered for the electric and microfluidic components in relation to optimal specifications and transparency of the pupil (field-of-view) and reference areas, in order to obtain a configuration that allows single cell imaging. I then performed the first tests of the platform in terms of electrodes efficiency via cell response to electric field, quality of the recorded images and correlation of electrical and holographic acquisition data.

The chapter begins with a general introduction of the developed imaging technique, i.e. Fourier Transform Holography. Then in the second part I present the principle of the microfluidics part and detail its main characteristics and operations. I then conclude with the preliminary validation and the experimental results.

4.1. Fourier transform holography principles and theory

4.1.1 General principle

In this section, we introduce a specific experimental configuration, which allows combining lensless imaging techniques with the observation of objects in a microfluidic chip. This opens the way to the observation of large and three-dimensional samples in an artificial environment, and contributes to the versatility of the microscope. The 2D and 3D samples (e.g. biological cells) will be observed through a holographic pupil, integrated in a microfluidic chip, used to reconstruct the sample exit

wave in a simple and deterministic way, using a holographic imaging technique called Fourier Transform Holography (FTH). The choice of using an off-axis reference has been also driven by the difficulty of the in-line scheme to ensure a “clean” reference. The off-axis scheme generates an unperturbed reference. Therefore, the spatial resolution is in principle limited by the laser wavelength and the size and quality of the reference pupil.

The experimental configuration presented in this chapter uses the principles of direct Fourier Transform holography: the sample is illuminated by the spatially coherent source, the diffraction pattern is detected by the CCD camera, and the signal can be directly processed using a Fourier Transform to achieve the reconstruction. Two major modifications are made here compared to the previous chapters: the object to be observed is located near a holographic pupil to "isolate" the field of view and to observe the diffracted field under the usual over-sampling conditions. Additionally, circular references are etched around this pupil to perform FTH reconstructions. A previous version of our microscope, developed by Julien Samaan during his PhD research⁵⁷, has introduced a holographic configuration that uses a mask in a transmission geometry with a UV illumination ($\lambda = 400$ nm). Building on his development, we propose the integration of the holographic mask in a microfluidic device.

The FTH technique is very simple to implement experimentally. It consists of engraving one or more circular references around the object. By interfering with the field diffracted by object, the field diffracted by these references will create an interference pattern in the hologram that encodes the field spatial phase. The reconstruction step is then reduced to a simple Fourier transform of the hologram. The theory is detailed for example in Samaan's PhD manuscript.

In order to perform an experimental imaging acquisition the following steps have to be completed:

1. Illuminate the sample with a spatially coherent beam, with a flat phase on the object. In our case, we use a collimated beam, created by inserting an adjustable collimator after the illumination source;
2. The light propagates through the sample, then through the pupil and reference holes (set in a plane very close to the plane of the sample);
3. The diffracted field propagates towards the CCD camera, which records the hologram, i.e. the modulus square of the field;
4. The FTH algorithm (a simple Fourier transform, plus some image processing steps) inverts the hologram in the pupil plane;
5. The retrieved field (amplitude and phase) is propagated via the free space transfer function (see section 2.2.2 Back-propagation and reconstruction), in order to focus on the object.

The reconstruction steps are detailed in the following section.

4.1.2 Principle of image reconstruction

It is easy to demonstrate that the field diffracted by a sample is equal in the far field to the Fourier transform of the sample exit wave. The far field approximation is valid when the Fresnel number is smaller than one, with the Fresnel number equal to

$$F = \frac{\phi^2}{\lambda z} \ll 1 \quad (4.1)$$

with ϕ the object diameter, z the distance to the camera plane and λ the illumination wavelength. Since the camera is sensitive to the field intensity only, i.e. to the square modulus of the field, we can represent the diffracted signal $I(X, Y)$ by:

$$I(X, Y) = |\mathcal{F}\{t(x, y)\}|^2 \quad (4.2)$$

with $t(x, y)$ the 2D sample transmission. Applying the inverse Fourier transform to the signal $I(X, Y)$, we obtain:

$$\mathcal{F}^{-1}\{I\} = \mathcal{F}^{-1}\{|\mathcal{F}\{t\}|^2\} = t \otimes t = o \otimes o + h \otimes h + o \otimes h + h \otimes o \quad (4.3)$$

Where \otimes is the correlation operation and the sample transmission t is written as $t=o+h$, with o the component of the field going through the pupil (the object) and r the one through the reference(s). In equation (4.3), each term can be explained as:

- $t \otimes t \rightarrow$ Autocorrelation of the entire sample consisting of the object and the reference
- $o \otimes o \rightarrow$ Autocorrelation of the object
- $h \otimes h \rightarrow$ Autocorrelation of the reference
- $h \otimes o \rightarrow$ Cross-correlation of the reference and the complex conjugate of the object
- $o \otimes h \rightarrow$ Cross-correlation of the object and the complex conjugate of the reference

The first two terms are centred and overlap in the centre of the Fourier transform, while the other two represent the object reconstruction and its twin image, centred at the reference position. In the holographic case with several references, the inverse Fourier transform of the signal can be written as:

$$\mathcal{F}^{-1}\{I\} = t \otimes t = o \otimes o + \sum_{k=1}^n [o \otimes h_k + h_k \otimes o] + \sum_{i,j=1}^n h_i \otimes h_j \quad (4.4)$$

The first term in equation 4.4 is the autocorrelation of the pupil. The second term represents the correlations between the object and each reference. The third term represents the correlations between the references - including their autocorrelations. In both cases, if the size of the reference(s) is small enough to be assimilated after Fourier transform to a Dirac function, the inverse Fourier

transform of the hologram then directly reveals the object reconstruction. In our specific case, the exit field is reconstructed in the pupil plane. As this plane is distinct from the proper sample plane, an additional numerical back-propagation step is needed, using the tools presented for DIHL, as the sample is in the near field to the pupil.

4.1.3 Resolution

In FTH, provided the numerical aperture of the detector is large enough, equation (4.3) shows that the resolution is limited by the diameter of the reference. In principle, smaller diameters will offer better resolutions. However, the reconstruction quality is also sensitive to other parameters such as signal strength. Indeed, if the field coming out of the holes is not strong enough, the hologram's contrast will be limited, effectively reducing the resolution. It is therefore necessary to make a compromise between resolution and signal-to-noise ratio. This is why in the present design we have chosen to make several circular references with different diameters, rather than just one. The influence of the dimension and number of the reference nanoholes was the work of several studies, but a good explanation could be found for instance in the dissertation of W.F. Schlotter⁸⁹. We get as many independent reconstructions as there are references, with different limits of resolution according to the hole diameter.

Moreover, there is an additional difficulty in the design on the holographic pupil. Indeed, the so-called holographic separation must be respected in order to avoid that the reconstructions overlap with each other and with the central term (see Fig. 4. 1). The circular references must be at least three times the radius of the object away from the centre of the object in order to avoid superposition with the central term. Because of this constraint, the illumination diameter has to be very large, hence reducing the power available for the sample itself, which in turn may decrease the signal to noise ratio of the hologram.

Additionally, because of several factors as alignment on the sample, collimator or lens misalignment or imperfection, the reconstructed phase in the pupil plane might be affected by optical aberrations, which could be responsible for distortions of the final image. Algorithms exist to correct for such aberrations and improve the quality of the reconstructions but are not yet implemented in the software. Finally, if we consider a 3D imaging approach consisting in summing the successive slices along the z axis (see **Chapter 3**), the presence of a 2D phase gradient in the reconstructed spatial phase will result in a gradual lateral shift of the image. This non-physical effect will deteriorate the final result, preventing the final 3D assembly. In order to avoid all these aberrations, a phase unfolding algorithm is applied to our data. The algorithm is presented in detail in Julien Samaan's manuscript⁵⁷.

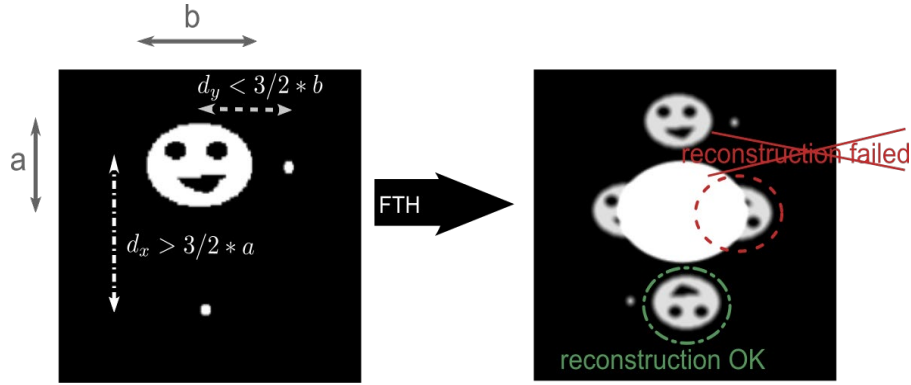


FIG. 4. 1 ILLUSTRATION OF THE HOLOGRAPHIC SEPARATION IN FOURIER TRANSFORM HOLOGRAPHY.

In the following experiments, we will estimate the 2D spatial resolution using the “10-90” criterion, as presented in 2.4.2. As a short reminder, it can be described by the following relation:

$$R = n_{10\%-90\%} \times \Delta_{pixel} \quad (4.5)$$

with $n_{10\%-90\%}$ the number of pixels that constitute the 10% - to - 90% rising (or falling) edge, in intensity, of a given feature in the sample image, and Δ_{pixel} the image pixel size.

Similarly to DIH, the FTH configuration can be used to perform quasi 3D reconstruction, using back-propagation functions to move the focus to successive planes. It is therefore important to consider the available depth of focus, i.e. the sample thickness covered by the field. The depth of field, noted DOF (Depth of Focus), is written as:

$$DOF = \frac{2R^2}{\lambda} \quad (4.6)$$

where R is the system transverse resolution.

We will present the variation of the back-propagation function and the effect of the pupil on depth of field in section 4.4. Fourier transform holography calibration and tests.

4.2. Microfluidics holographic configuration

Our novel holographic experimental scheme, coupling the imaging part to a microfluidic and single cell manipulation device, is presented in Fig. 4. 2. Microfluidic technology allows handling, separating and mixing samples and fluids in large area, or for instance chemical reaction initiation. The advantages of microfluidic-based devices over classical alternatives are the reduced consumption of reactants, the reduced processing time, the low costs, as well as the increased

capability of controlling the reaction parameters. The ability to manipulate bioparticles is added to the microfluidic chip by applying an intense electric field using microelectrodes. The electric field creates temporary pores in the cell membrane, phenomenon called electroporation or electropermeabilization⁹⁰. Reversible electroporation allows loading of different substances (molecular probes, drugs or DNA) into the cells, while irreversible electroporation is used to release cellular content for further analysis. As an illustration, the technique has been used for the detection of abnormal genes or proteins and offers invaluable information for early diagnosis of various diseases^{91 92 93}. Furthermore, the electric field is used to control the fluid flow by electro-osmosis and the particles movement through the fluids by electrophoresis (for electrical charged particles) or DEP (for neutral particles)⁹⁴.

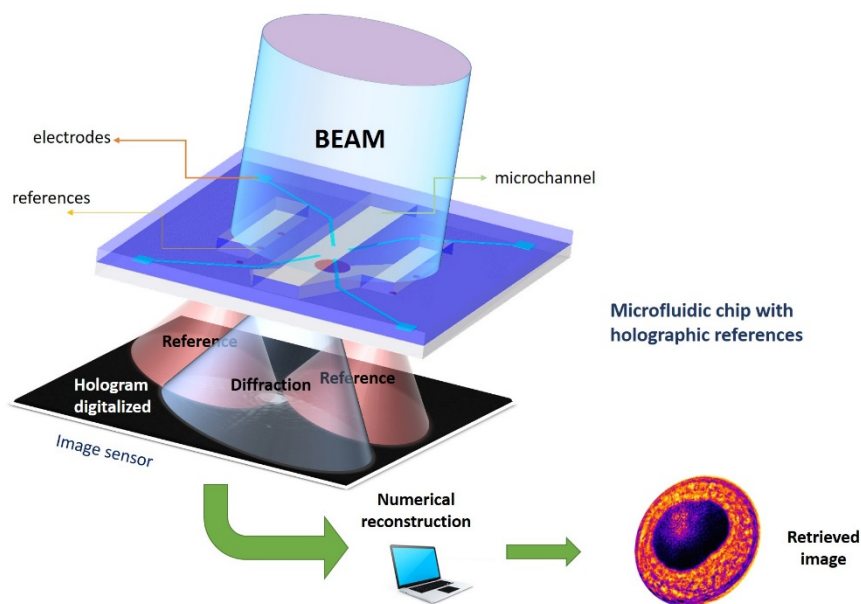


FIG. 4. 2. A SCHEME OF THE WORKING PRINCIPLE OF OUR EXPERIMENTAL PROTOTYPE OF LAB-ON-A-CHIP FTH MICROSCOPE.

4.2.1 Cell handling in a non-uniform field: DEP and EP effects

Manipulation of bioparticles by DEP is a particular effect of electric fields, used for bioparticles detection and separation (biological cells, micro-organisms, bacteria, viruses)⁹⁵. When located in a non-uniform electric field, the particles are electrically polarized and experience a translational force (Fig. 4. 3). This force depends on the electrical properties of the particles and fluid, as well on the intensity and frequency of the applied electric field⁹⁶. The frequency is an essential parameter in DEP because the particle's polarization depends on its value. At frequencies below the so-called crossover frequency,

the bioparticles migrate to the regions where the field intensity is maximum (positive DEP); while above this value, they migrate to the regions of minimum field intensity (negative DEP). Therefore, the system of electrodes that generates the electric field is of crucial importance and has to be designed carefully. The electrodes have to produce high field gradients at lower voltages, in order to increase the dielectrophoretic forces and to lower the thermal effects.

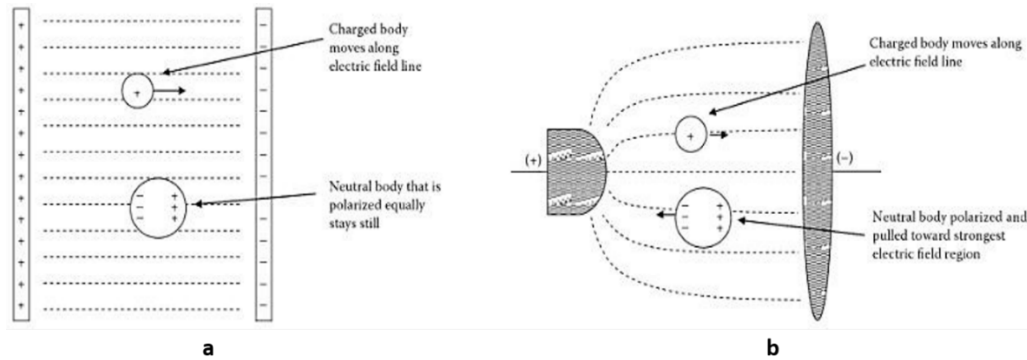


FIG. 4. 3. EXAMPLE OF UNIFORM (A) AND NON-UNIFORM (B) ELECTRIC FIELD EFFECT ON ELECTRICALLY CHARGED PARTICLES AND ON NEUTRAL POLARIZED PARTICLES (POSITIVE DEP), RESPECTIVELY⁹⁵.

In the last decade, this method has spread thanks to the new fabrication techniques of micro-electrodes and integration of the microfluidic devices into lab-on-a-chip systems⁹⁷. Most of the results regarding the separation effect are based on experimental studies (see Fig. 4. 4 for one such example among many). Dielectrophoretic effects can be used in microfilters to separate the bioparticles in a specific region of interest (for example a detection surface or chamber), or in selective separation of different populations of bioparticles, based on their different behaviours in relation to a given field frequency (at which some are subject to positive electrophoresis and others to negative electrophoresis); in this way they can be separated in distinct regions. The sizes of the separate particles vary from 0.01 to 15 μm , and the separation fluids consist in aqueous solutions with different electric conductivities⁹⁸. Interdigitated⁹⁹ ¹⁰⁰, castellated⁹⁹, polynomial¹⁰⁰ shaped electrodes are usually used, as well as 3D electrodes¹⁰¹ ¹⁰². The electrodes are all located on the same side of the fluidic channel, and usually they are in contact with the fluid because in the presence of a dielectric layer the dielectrophoretic force decreases by almost 80%. The lengths of the electrodes may reach several millimetres, and the gap between electrodes varies from 1 to 500 μm ¹⁰³, compatible with current fabrication technologies, as lift-off or electron beam lithography (EBL). Microsystems are fabricated in silicon¹⁰⁴, glass¹⁰⁵, PDMS¹⁰⁶, PMMA¹⁰⁷, and the electrodes are made from platinum, gold, silver, titanium or combined titanium-gold or platinum-chromium¹⁰⁴. The applied voltages vary from 1 to 20 V, and the frequency from 100 Hz to 100 MHz.

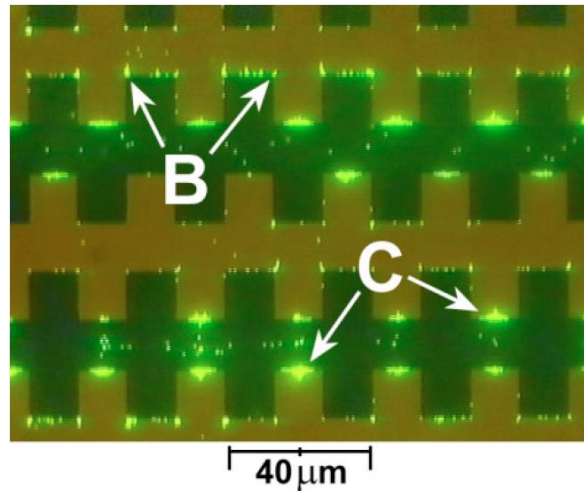


FIG. 4. 4. POSITIVE DEP OF 557 NM DIAMETER FLUORESCENT LATEX SPHERES ON CASTELLATED ELECTRODES WITH AN APPLIED SIGNAL OF 8 VOLTS PEAK-TO-PEAK AT 700 KHZ. THE SPHERES COLLECT AT THE HIGH FIELD REGIONS MARKED B, C¹⁰⁸.

One of the most interesting application of the electric field on cells is the electroporation effect (EP). When an intense electric field is applied, the membrane acts as a capacitor due to the difference between intra- and extra-cellular conductivities, and an electric potential discontinuity occurs across the membrane. The potential drop, called transmembrane potential, depends on the electric field and the cell's size, and creates nanopores through the cell's membrane. Depending on the intensity and duration of the applied electric pulses, the created pores can be temporarily (reversible) or permanently (irreversible) opened pores. Electroporation devices use the reversible electroporation effect for transfection (introducing DNA or other specific molecules inside a cell, (see Fig. 4. 5)¹⁰⁹¹¹⁰, and the irreversible electroporation effect for cell properties or cell content analysis, cell inactivation or sterilization¹¹¹. Experimental studies have been performed on various cells, e.g. human prostate adenocarcinoma¹¹² human colon carcinoma¹¹³, mouse tumoral and blood cells¹¹⁴, mammalian cells¹¹⁵ or *E. coli*¹⁰⁶. In other experiments, impedance measurements have been performed on electroporated cells¹¹⁶, and indirect methods have been used to determine the conductivity variation of the cytosol (or intracellular fluid) by determining the frequency threshold (the frequency value at which the cells change direction due to the variation of the dielectrophoretic force). An increase of the threshold frequency has also been reported for electroporated cells¹¹⁷.

Most of the electroporation systems include microchannels through which the cells are transported by controlling the carrying fluid. The dimensions of these channels vary from 1.5 times the cell's diameter (for a single cell electroporation)¹¹² up to several hundreds of micrometers¹¹⁸. To induce the electrical field, planar electrodes with rectangular geometries¹¹², or castellated electrodes¹¹³, are used.

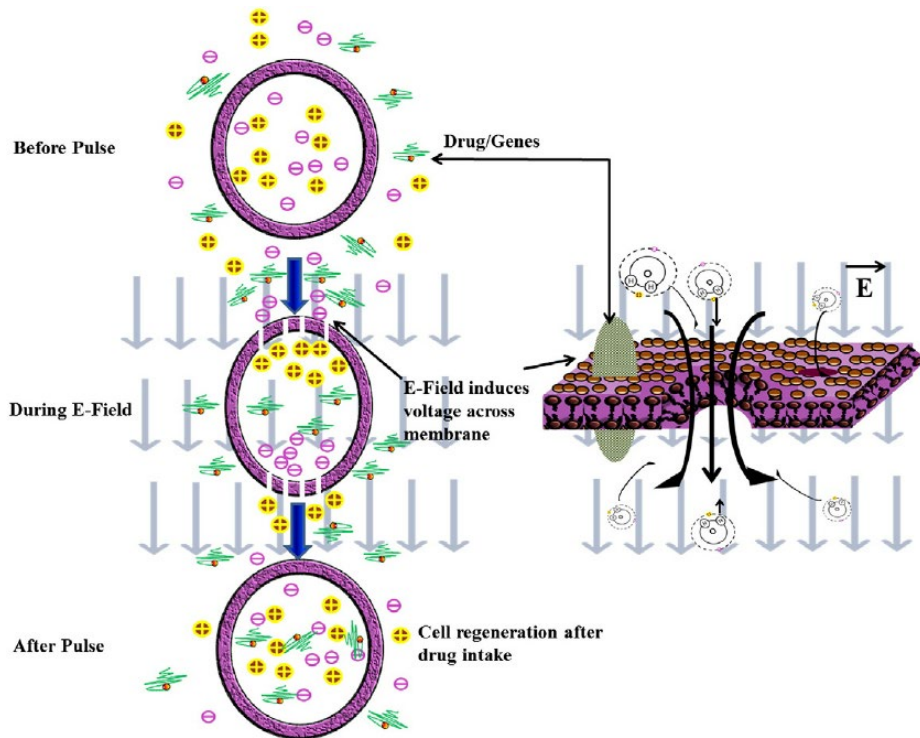


FIG. 4. 5 SCHEMATIC REPRESENTATION OF THE PHENOMENON OF ELECTROPORATION, ADAPTED FROM LAKSHMANAN ET AL¹¹⁹.

Microfluidic systems that use both techniques - DEP and electroporation – are not so common in practice because of the need of multiple electrodes with separate functions for flow paths, separation and permeabilization (Fig. 4. 6). This leads to complex and expensive technologies for fabrication, poor control on cells, high risk of overheating due to Joule effect, risk of degradation of the cell viability (that needs to be avoided in reversible electroporation) and high power consumption.

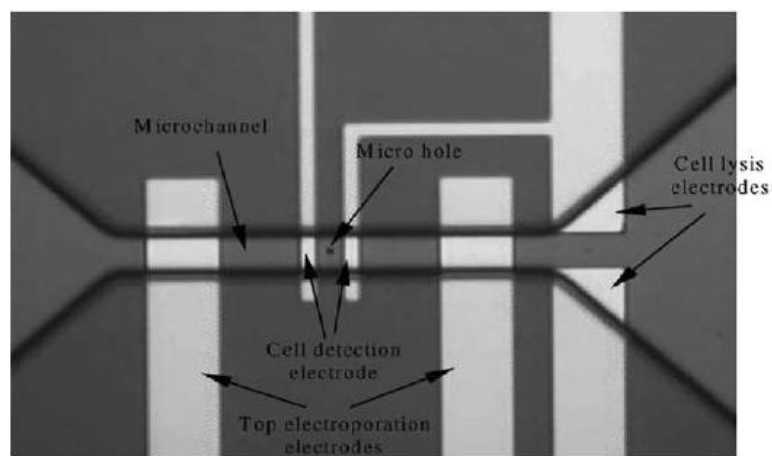


FIG. 4. 6 OPTICAL IMAGE OF A MICROFLUIDIC ELECTROPORATION DEVICE¹²⁰.

4.2.2. Microfluidics in the context of FTH imaging

Studies regarding electro-optical detection for biology and medicine applications have been reported over a recent period, mostly over the last 8 years, but their operating principles differ from the approach proposed in this manuscript^{121 122 123 124}. Thanks to revolutionary advances in microfabrication technologies, remarkable miniaturization of the imaging systems has opened up a wide variety of innovative applications to point of care analysis and controlled environment for fundamental research. The development of advanced microscopic imaging, combining the ‘point and click microscopy’ with ‘smart microscopy’, will rely heavily on an improved understanding of the behaviour of biological samples. Indeed, combining the two advantages, i.e. large FOV and microfluidics, could represent a major tool for future diagnosis. The approach we proposed combines cell analysis by coupling electric handling and high resolution imaging using Fourier transform holography. Our goal is to reach single cell manipulation and imaging with nanoscale resolution. Conceiving and integration of microfluidics for transport, electrodes to perform multiple electric functions (as cell separation in the holographic field of view and/or electric monitoring) together with the multiple apertures with the nano/micrometer scale dimensions needed for FTH, while respecting the holographic separation conditions, is an innovative approach by comparison to current devices.

4.3 Design and fabrication of microfluidic chips for lensless microscopy

This section presents the design and the optimization of specific parameters (electrodes geometry, channels configuration, applied voltage and frequency) by modelling and coupled simulations of the electro-fluidic system response. Several types of materials, microfabrication processes and assembly techniques will be taken into account in order to ensure compliance with our set of constraints. The platform will be tested in terms of electrodes efficiency via cell response to electric field, quality of optical recordings and complementary interpretation of electrical and optical acquisition data. The main advantages of such coupled electro-optical method for cell analysis are the improved control, precision and sensitivity regarding cell behaviour analysis.

The final device is composed of three parts as is represented in Fig. 4. 7: the first part is the microfluidic channel, the second consists in the electrodes used for cells handling and the third is the lensless imaging mask based on FTH pupil and reference apertures. The high quality of the reference, unaffected by the fluid that flows in the pupil imaging area, will provide a high phase contrast and a high resolution of the holograms.

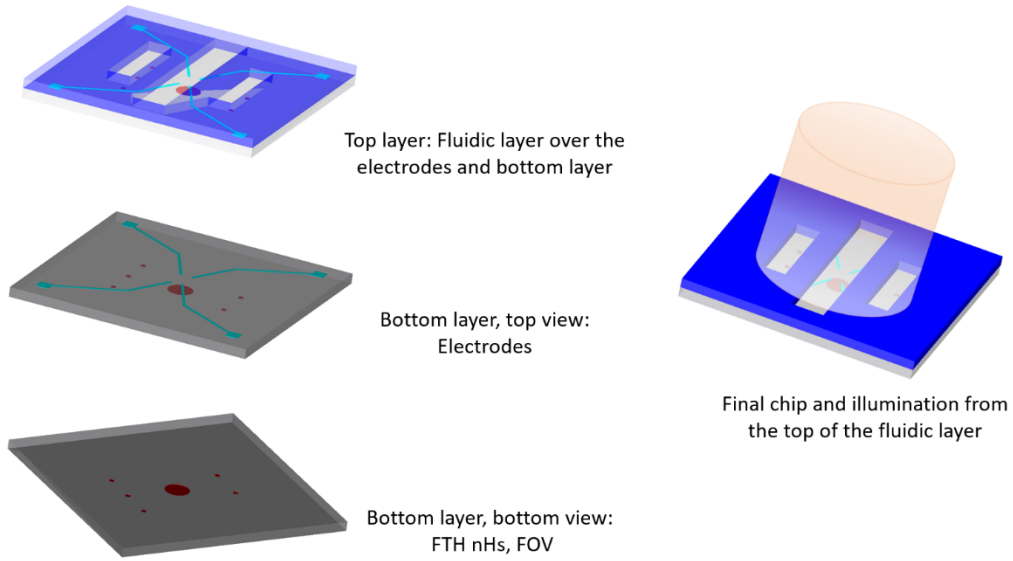


FIG. 4. 7 SCHEMATIC REPRESENTATION OF THE MICROFLUIDIC CHIP.

4.3.1 Pupil and nanoholes constrains

In this section we will present the solution we choose to satisfy the holographic imaging constrains. As mentioned in section 4.1.1 General principle, the FTH holographic mask is made of two parts. First, a large pupil is positioned at the centre of the chip, to define the actual field of view. Then one or several small aperture(s) are inserted around it, to serve as holographic reference(s) that will generate the spherical reference wave(s).

The pupil (FOV), serving as a support for the reconstructed field, is designed as a large circular hole drilled in an opaque silicon plate. In our setup, we defined a circular pupil with a $300\ \mu\text{m}$ diameter D and five circular references of diameters d ranging from $500\ \text{nm}$ to $1200\ \text{nm}$ (Fig. 4. 8). The references are etched around the pupil, at a distance of $2D_{\text{pupil}} = 600\ \mu\text{m}$, in order to respect the holographic separation. The holographic mask is then glued to a borosilicate glass slide. We chose this type of glass because of its good optical properties (90% transmission for a $1\ \text{mm}$ thickness and a wavelength of $405\ \text{nm}$).

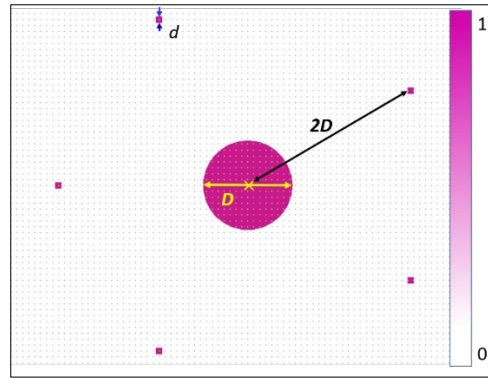


FIG. 4. 8. BOTTOM VIEW OF THE GLASS LAYER WITH THE PATTERN OF THE FOV PUPIL AND NANOHOLES (THEIR POSITION IS REPRESENTED BY THE SQUARES), REPRESENTED IN TRANSMISSION (PINK COLOUR MEANS FULL TRANSMISSION, WHITE MEANS NO TRANSMISSION).

4.3.2 Design and simulation of the microfluidic part

The microfluidic chip has the role of transporting and separating the samples (biological cells), inside a liquid medium, to the field of view defined by the holographic pupil. DEP using electrodes is used to control the cell with the goal to reach the level of single cell separation in the central area of the FOV.

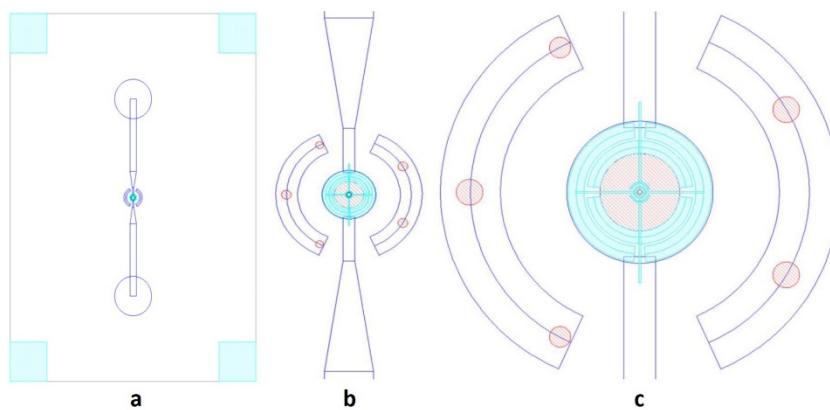


FIG. 4. 9. GENERAL PRINCIPLES DESIGN: A) 2-LAYER CHIP; B) DETAIL OF THE CENTRAL AREA; C) DETAIL OF THE CHAMBER AND VISUALIZATION AREA. BLUE - FLUIDIC LAYER (IN Si); RED: FIELD OF VIEW AND NANOHOLES (IN GLASS); CYAN: ELECTRODES (METAL ON GLASS). NOTES: I) THE LINKS TO PADS ARE NOT REPRESENTED; II) THE DIMENSION OF THE NANOHOLES ARE CONVENTIONALLY EXAGGERATED; III) LIGHT CAN ONLY GO THROUGH THE RED PARTS; IV) THE SEMICIRCLE AROUND THE NANOHOLES REPRESENT OPENINGS BY ETCHING IN SILICON LAYER THAT ALLOWS THE LIGHT TO PASS THROUGH AND REACH THE DETECTOR.

The DEP effect is defined by the dielectrophoretic force generated by the system, given by the relation¹²⁵:

$$F_{\text{DEP}} = 2\pi\epsilon_0\epsilon_m r^3 \text{Re}[K(\omega)] \nabla E^2 \quad (4.7)$$

where ϵ_0 represents the permittivity of free space, ϵ_m the environment permittivity, r is the particle radius, E electric field, $\text{Re}[K(\omega)]$ is the real part of Clausius-Mossotti (CM) factor, defined in equation 4.8.

$$K(\omega) = \frac{\epsilon_p^* - \epsilon_m^*}{\epsilon_p^* + \epsilon_m^*} \quad (4.8)$$

which depends on complex permittivity of medium (ϵ_m^*) and cell (ϵ_p^*).

$$\epsilon^* = \epsilon + \frac{\sigma}{i\omega} = \epsilon - \frac{i\sigma}{\omega} \quad (4.9)$$

Where ϵ is permittivity (with indices p for cell and m for medium), σ the conductivity, ω the angular frequency of the electric field. The following electrical properties of cells and medium were assumed: $\epsilon_{\text{cell}} = 10^4$, $\epsilon_{\text{medium}} = 80$, $\sigma_{\text{cell}} = 0.1 \text{ S/m}$, $\sigma_{\text{medium}} = 1.5 \text{ S/m}$ ^{126 127}. The cell diameter was considered to be of $20 \mu\text{m}$. First, using the above mentioned properties, we computed the Clausius-Mossotti factor as function of frequency in order to find out the ranges of negative and positive DEP. As one can see in Fig. 4. 10, the transition between the two regimes is around 3.5 MHz, therefore we set up a frequency of 100 kHz for n-DEP simulations, and a frequency of 100 MHz for p-DEP simulations.

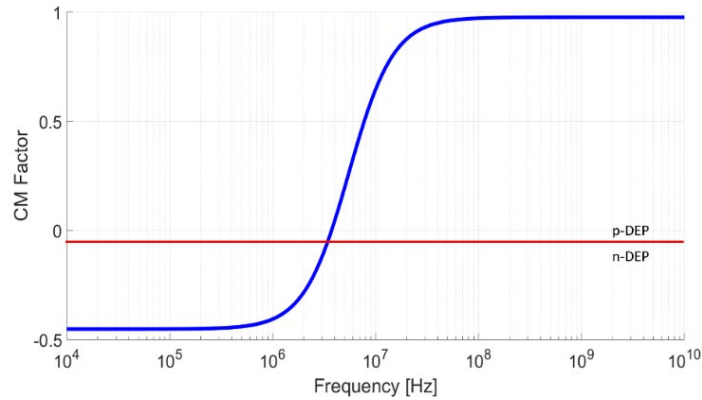


FIG. 4. 10. CM FACTOR AS FUNCTION OF FREQUENCY.

4.3.3 Electrodes Design

The electrodes configuration is important because it defines the electric field distribution inside the chamber and consequently defines the DEP force field acting on the cells depending on their position

at any moment. To assess the device's behaviour, numerical simulations were performed using the COMSOL Multiphysics software. To simulate the movement of the cells through the medium, the drag forces acting on the cells were also considered. Studies concerning the electrodes efficiency were performed by different research groups and it was found that their shape is essential for generation of an efficient electric field^{128 129}. In manipulation or trapping experiments, electrodes with circle and parallel geometry provide higher electric field strength compared to other configurations¹³⁰. In our case the design had to follow a circular geometry due to the FTH pupil symmetry.

4.3.3.1 First design

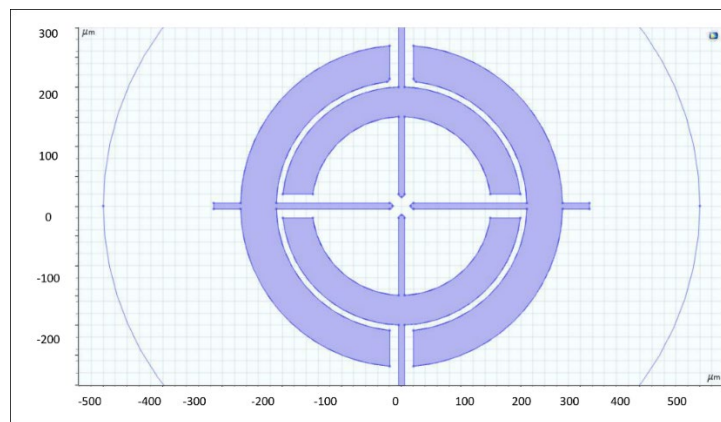


FIG. 4. 11. FIRST DESIGN OF PLANAR ELECTRODES CONFIGURED ON A GLASS SUBSTRATE.

Essentially, this is a two-electrode design because there are two un-connected metallic areas. Therefore, the AC excitation voltage will be applied on two terminals. Originally, this design was conceived to be used in negative DEP regime (in the low frequency domain). Fig. 4. 12- Fig. 4. 13 present the results of the DEP forces simulations. The distribution of the electric field is represented in volume for different sections along the X and Y axes. The difference of potential is applied in no-flow condition in order to avoid convection effects. In Fig. 4. 12, the blue areas represent narrow zones where the vertical forces are negative. In those areas, the cells are attracted towards the substrate. Additionally, a vector representation of the DEP forces is shown Fig. 4. 13. The numerical results predict that a cell should be trapped in the centre, slightly above the bottom of the chamber. To check that, a particle-tracing simulation was performed by our collaborators at IMT Bucharest using a home-made code under MATLAB environment. A number of 25 cells were uniformly distributed into a horizontal plane at a distance of 100 μm above the substrate, with their initial velocities set at zero, and an AC voltage of 10 V_{pp} (peak to peak voltage) at 100 kHz was applied.

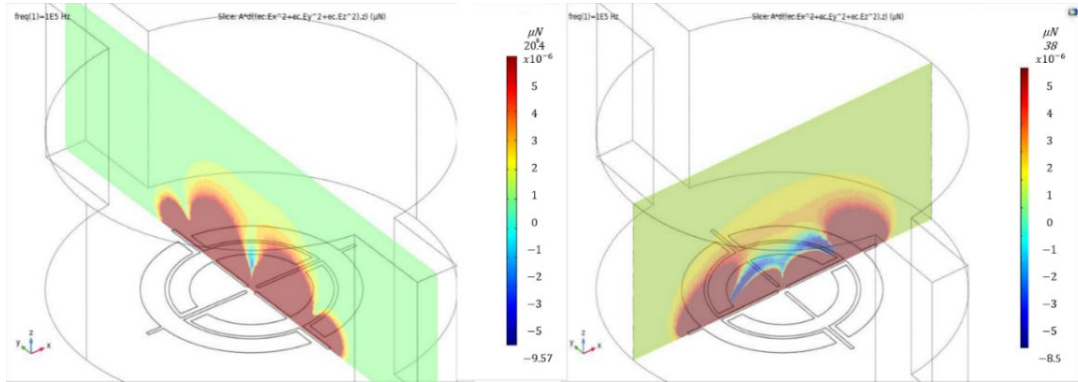


FIG. 4. 12 F_{DEP} (Z COMPONENT MAGNITUDE). CROSS-SECTION VIEW ALONG (LEFT) AND ACROSS (RIGHT) THE INPUT-OUTPUT CHANNEL.

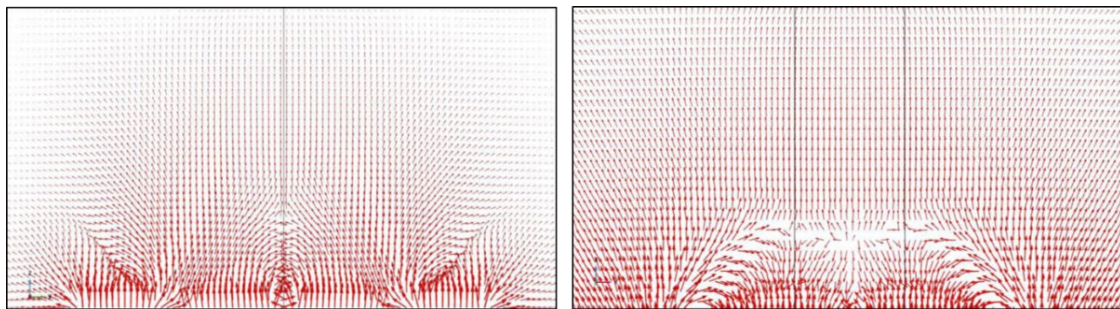


FIG. 4. 13 VECTOR REPRESENTATION OF THE DEP FORCES. CROSS-SECTION ALONG (LEFT) AND ACROSS (RIGHT) THE INPUT-OUTPUT CHANNELS ASSOCIATED TO FIG. 4. 11 FIELD REPRESENTATION RESPECTIVELY (ARROW LENGTH IN LOGARITHMIC SCALE).

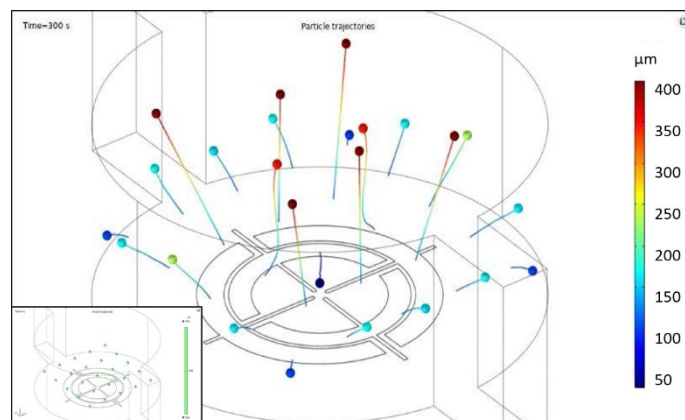


FIG. 4. 14 CELLS TRAJECTORIES IN THE NEGATIVE DEP REGIME. POSITIONS REACHED AFTER 300 SECONDS. INSET: INITIAL POSITIONS OF THE CELLS.

From Fig. 4. 14 we can see that one single cell moves towards the bottom plane where it is trapped into a central position (as desired) while all the others move away. The aim of the simulation is to define an optimum gradient of the electric field to optimize the separation or isolation process of cells in the centre region. In this first design we aimed to use an n-DEP effect that requires low tensions and frequency and to avoid that many cells will be in the region of observation (FOV). However, the first design intended to follow a simple configuration of electrodes in the region of FOV that would reduce potential obstruction of the light that pass through the FTH pupil region. In order to integrate both types of DEP effects, more flexibility and applications the next configuration follows a circle electrodes geometry. Therefore, an optimized geometry of the electrodes was simulated under similar conditions.

4.3.3.2 Optimized Design

As opposed to the first design, this second design is a three-electrode design, which means that three un-connected metallic areas exist. Thus, the excitation voltage can be applied in four different ways:

- C1. between A and B1+B2 (B1 and B2 connected together)
- C2. between A and B1 (B2 unconnected)
- C3. between A and B2 (B1 unconnected)
- C4. between B1 and B2 (A unconnected)

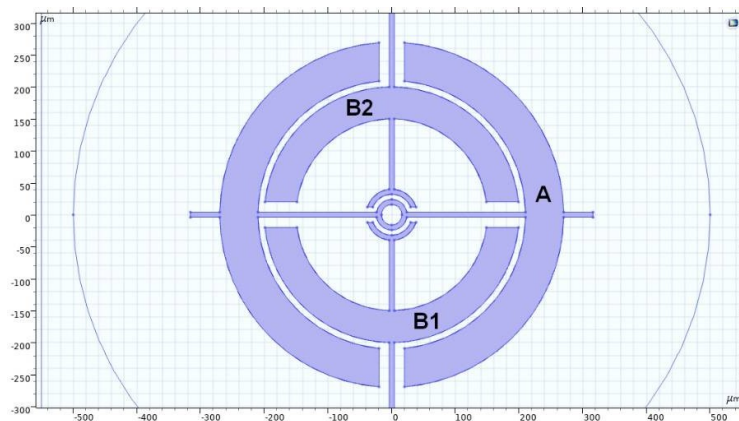


FIG. 4. 15 OPTIMIZED DESIGN OF PLANAR ELECTRODES CONFIGURED ON A GLASS SUBSTRATE.

Therefore, this design allows a more flexible control on the cell position thanks to the different possible configurations of electric field. Also, the particular design of the central area (ring and arc shapes) allows better trapping conditions of the cell in negative DEP regime. In addition, for this optimized design we will analyse the positive DEP regime as well. All the parameters describing the

cells and medium are similar as in the first design. For negative DEP simulations a frequency of 100 kHz and an AC voltage of 10 V_{pp} (peak to peak voltage) was set, while for positive DEP simulation a frequency of 100 MHz in order to ensure a maximum gain from Clausius-Mossotti factor. We performed simulations for excitation voltages applied in C1, C2 and C4 configurations (for both negative and positive DEP). The C3 configuration is similar to C2 since they mirror each other, and thus was not simulated. In the following, we present the final distribution of the cells for the three configurations and the two types of DEP effects. The simulated electric field distributions inside the chamber and the corresponding DEP forces are presented in **Annex F**.

As general rule, with our optimized electrodes design, in the negative DEP regime the cells move away from the bottom, while in the positive DEP one the cells are attracted to the electrodes in the region of intense electric field. However, in negative DEP also there is a narrow volume in the centre where a single cell can be trapped (see Fig. 4. 16 left panel). Increasing the voltage to 20V_{pp} will produce a faster separation of the cells in the case of n-DEP, but not faster than the p-DEP. Moreover, the high tension applied could induces thermic effects or electroporation and is not recommended for our purpose.

The proposed design favours the central trapping of a single cell in p-DEP (see Fig. 4. 16 - Fig. 4. 18, right panels), which depends nevertheless from the initial distribution of the cells in the chamber. Therefore, achieving a uniform initial distribution of cells in the chamber is recommended. Choosing the voltage configuration offers an additional control over the cells movement. For example, the C2 and C3 excitation configurations, due to their asymmetry, can be used to move the cells back and forth along a direction, creating a proper positioning before trapping (see Fig. 4. 17 left panel). Consequently, handling and trapping of cells through DEP methods will be an operator's task that requires an in-vivo imaging system (optical or digital microscope) and knowledge on how cells movements can be controlled.

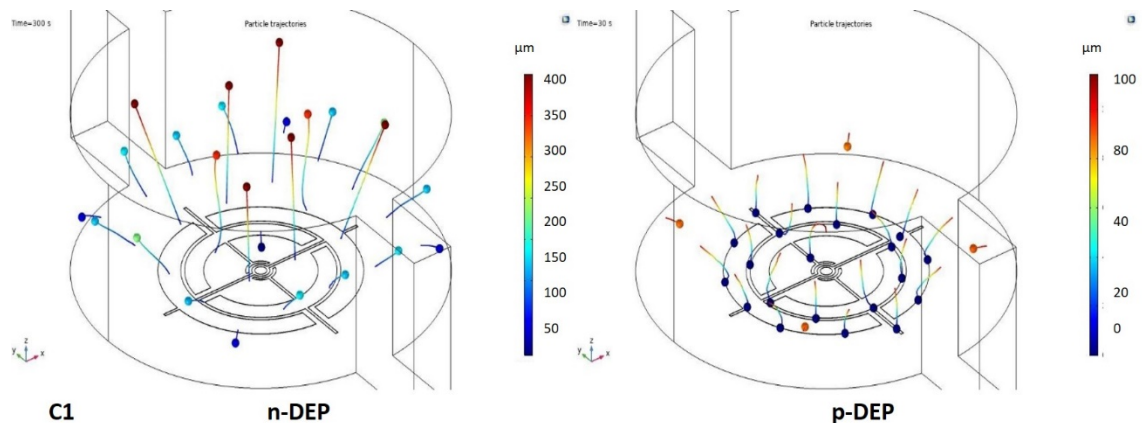


FIG. 4. 16 CELLS TRAJECTORIES IN C1 CONFIGURATION IN NEGATIVE (LEFT) AND POSITIVE (RIGHT) DEP REGIMES. POSITIONS REACHED AFTER 300 SECONDS AND AFTER 30 SECONDS, RESPECTIVELY.

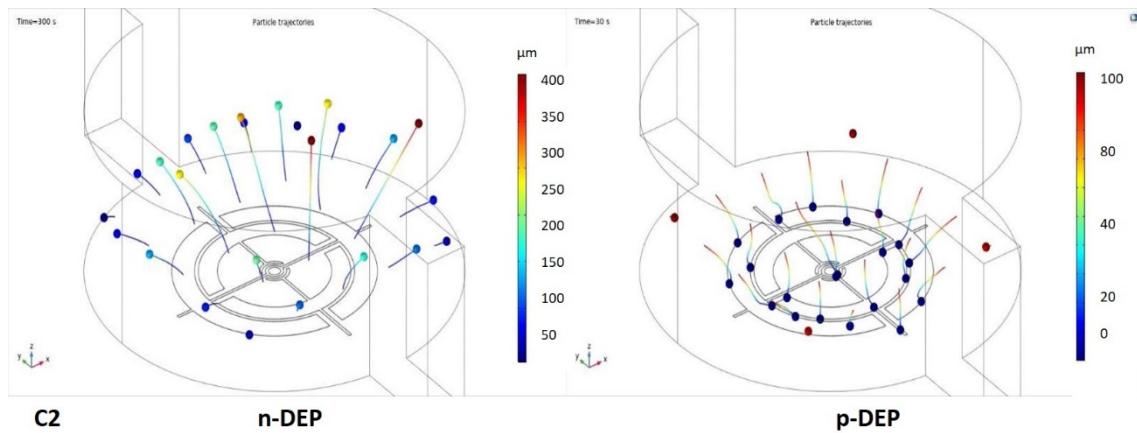


FIG. 4. 17 CELLS TRAJECTORIES IN C2 CONFIGURATION IN NEGATIVE (LEFT) AND POSITIVE (RIGHT) DEP REGIMES. POSITIONS REACHED AFTER 300 SECONDS AND AFTER 30 SECONDS, RESPECTIVELY.

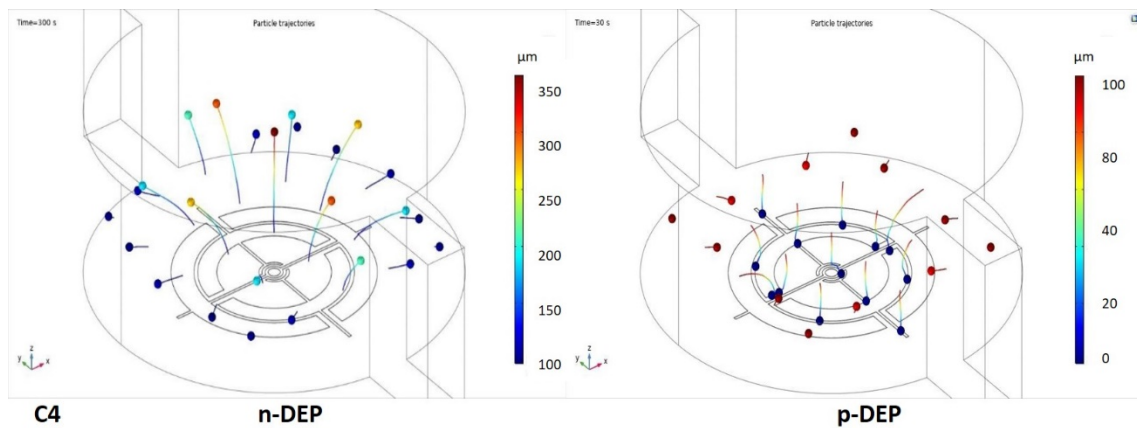


FIG. 4. 18 CELLS TRAJECTORIES IN C4 CONFIGURATION IN NEGATIVE (LEFT) AND POSITIVE (RIGHT) DEP REGIMES. POSITIONS REACHED AFTER 300 SECONDS AND AFTER 30 SECONDS, RESPECTIVELY.

4.3.4 Microfabrication procedure and assembly

After defining the electrode configuration through simulations, we present here the microfabrication process. The device is composed of three parts: the electrodes, the FTH mask (pupil with the holographic references) and the microfluidic channels. The electrodes and the FTH mask were realized on the same slide of borosilicate glass (400 μm thick): on the top side, we patterned the electrodes and on the bottom side, previously made opaque by a metallic deposition, we patterned

the pupil (FOV) and the nanoholes (nHs) as presented in 4.3.1. The metallic layer used to pattern the pupil is 150 nm thick, and the electrodes' thickness is about a few hundred nanometres. The electrodes are centred with the pupil on the opposite side of the glass (see Fig. 4. 19-a). The microfluidics channels were realized in a different layer of silicon (Si) approximately 450 μm thick. The microfluidic layer was realized by etching based on DRIE (Deep Reactive Ion Etching). The pattern of the pupil and electrodes was realized by lift-off, while the nanoholes were realized with EBL (Electron-Beam Lithography) process due to their small size. In Fig. 4. 19-a) an optical image with the electrodes is presented, as well as scanning electron microscope (SEM) images of the nanoholes in b) and c). The final device is presented in Fig. 4. 19-d. The image presents a top view of the silicon layer with the microfluidic channels. The two layers, glass and silicon, were attached with microscale alignment and bonding procedures at IMT Bucharest.

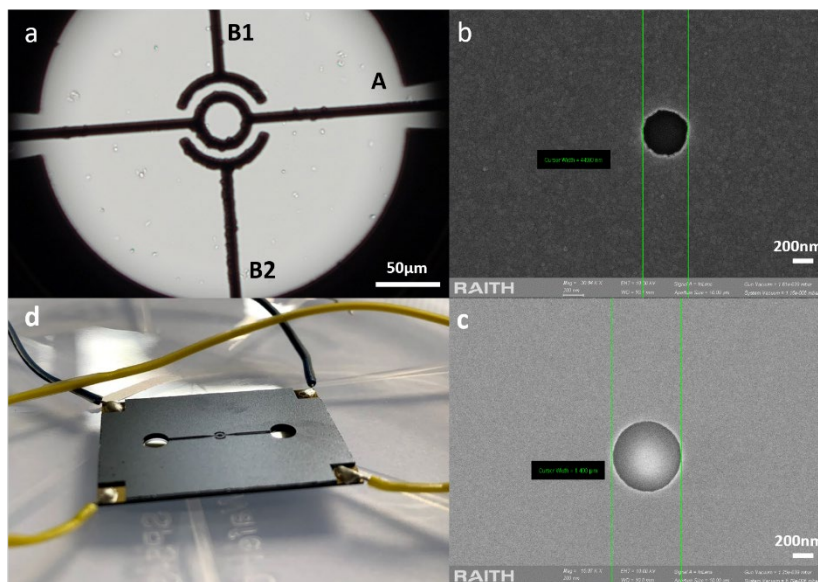


FIG. 4. 19. A) OPTICAL IMAGE OF THE ELECTRODES AND THE CHAMBER AND B-C) SEM IMAGES OF THE NANOHOLES, WITH A DIAMETER OF C) 490 nm AND B) 1400 nm. IN D) A PICTURE OF THE FINAL DEVICE. THE TWO LARGE HOLES VISIBLE ON THE TOP SIDE ARE USED TO FILL THE CHAMBER WITH FLUID AND CELLS. ELECTRICAL WIRES (YELLOW AND BLACK) ARE CONNECTED TO THE PADS. NOTE: THE THREE ELECTRODES ARE NUMBERED A, B1, B2.

Several microfluidic chips were designed and fabricated following the values presented in table 4. 1. We designed several nanohole references to obtain several images of the samples with various resolutions. Combining the images will enhance the reliability and functionality of the chip. The small dimensions of the references might be a problem in the fabrication operation. Imperfection of the nanoholes or impurities could affect the imaging process. To minimize the risk we chose to

engrave five nanoholes per chip: each chip has one reference nanohole of 1.2 μm and four nanoholes with dimension ranging from 500 to 1000 nm.

	Chip 1	Chip 2	Chip 3	Chip 4
nH 1	1200	1200	1200	1200
nH 2	500	800	1200	800
nH 3	500	800	1200	500
nH 4	500	800	1200	1200
nH 5	500	800	1200	1000

TABLE 4. 1 DIMENSIONS OF THE NANOHOLES (nHs) ON 5 VERSIONS OF THE CHIP.

4.4. Fourier transform holography calibration and tests

As a first step, we used as a static calibration sample: the electrodes that were deposited on the opposite side of the glass layer. The total thickness of the glass was about 400 μm , distance which respects the condition of imaging: the object to be observed is located in the near field of the holographic pupil. The calibration step includes optimization of the distances (light source-sample and sample-detector) and of the illumination of the holographic plate to minimize the loss of photons. Each nanohole is located at a distance $L = 2D$ from the centre, as explained in section 4.3.1 Pupil and nanoholes constrains, which means $L = 600 \mu\text{m}$. For imaging we used a collimated beam of diameter approximatively 700 μm . In these conditions, two illumination schemes were considered:

- In the first case we centred the beam with the pupil, in order to get a uniform distribution of the light through the pupil;
- In the second one, we centred the beam between one nanohole and the pupil, in order to maximize the photon flux through that reference.

This new setup uses similar functionalities as the one presented **Chapter 2** and developed for DIH: motorized system for sample motion (nanopositionning stages) and a similar GUI interface, which has been adapted for these experiments. The wavelength of the illumination source is $\lambda = 405 \text{ nm}$. The microfluidic chip was illuminated from the top side, i.e. the illumination was first propagating through the silicon layer (microfluidic channel) and then through the glass layer, with the electrodes on top and the FOV with nHs at the bottom. The CCD is a PROSILICA GT-6600 with pixel size $\Delta_{\text{pixel}} = 5.5 \mu\text{m}$ and dimension 6576 (H) \times 4384 (V) (Annex E). The illumination source is located at a distance $z_1 = 200 \text{ mm}$, while the microfluidic chip with holographic references is set at a distance $z_2 \cong 30 \text{ mm}$ from the image sensor. In FTH, the field must be recorded in the far field, i.e.

far enough from the sample. The far field condition can be expressed by calculating the Fresnel number, which is equal to 7.5 in our conditions. This does not correspond to the far field, for which F has to be smaller than one. One solution to reach $F < 1$ would be to increase the sample-to-CCD distance. However, this would decrease the spatial resolution. Instead, we inserted a lens between the sample and the image sensor, and installed the CCD at the lens focus position. While this solves the far field issue, this solution limits the actual resolution due to the reimaging lens NA (another solution to solve the far field issue can be to perform a numerical correction of the aberrations). Moreover, short focal length lenses often introduce optical aberrations, reducing even more the resolution. The experimental results for the two cases are presented Fig. 4. 20. The whole experiments of this chapter were performed with an acquisition time of 100ms.

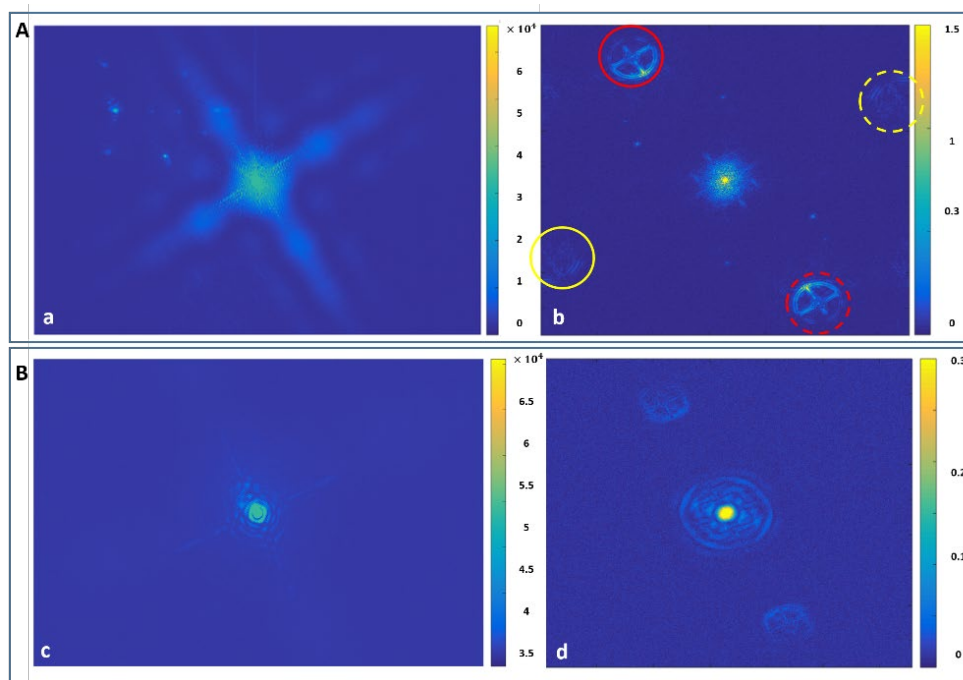


FIG. 4. 20. THE EXPERIMENTAL DEMONSTRATION FOR THE TWO CASES: A. THE BEAM IS CENTRED WITH THE PUPIL: A) THE RECORDED HOLOGRAM AND B) THE HOLOGRAPHIC RECONSTRUCTION OF A. ; B. THE BEAM IS CENTRED BETWEEN THE PUPIL AND ONE NANO HOLE: C) THE RECORDED HOLOGRAM AND D) THE HOLOGRAPHIC RECONSTRUCTION OF THE SIGNAL IN C. NOTE: THE RED AND YELLOW CIRCLES IN B SURROUNDS THE HOLOGRAMS (SOLID LINE) AND THEIR CONJUGATES (DASH LINE) FOR TWO DIFFERENT NANOHOLES.

When the incident beam is centred with the pupil (case A), several reference holes are illuminated. The inverted hologram thus shows more reconstructions (two are visible in Fig. 4. 20-b, with 2 twin images symmetric with respect to the centre of the image). However, the flux of photons through the pupil is larger than the one through the nanoholes, which seat at the edge of the Gaussian illumination because of the large separation distance between the pupil and the nanoholes. This

implies that the contrast of the hologram, and of the reconstructions, is lower. Additionally, the saturation of the signal due to the direct beam reduces the dynamics of the hologram (Fig. 4. 20-a), but also in the reconstruction (Fig. 4. 20-b). We do not get the 5 independent reconstruction in Fig. 4. 20. This is due to errors in the patterning of the FTH layer. Indeed, the diameter of the holes were too close from the EBL technical limit and were not completely drilled. In the second case (B), the beam is located between the pupil and one nanohole. The experimental results are presented in Fig. 4. 20-c and d. As expected, only one reconstruction (and its twin image) is visible. However, even if the saturation is removed the limited number of photons reduces the quality of the reconstruction, which influences the image contrast.

4.4.1 Image reconstruction

In this part, I present with more details the reconstruction principle. After the Fourier transform of the hologram (see Fig. 4. 20-d and Fig. 4. 21-a), the object's exit wave is reconstructed in the pupil plane. An extra numerical back-propagation step is needed to reach the object actual plane. Back propagating the whole image is too costly (and not useful). Therefore the following step consists in selecting a region of interest, centered on one of the holographic reconstruction. This field is then back propagated at different distances, using the numerical tools presented **Chapter 2** (Fig. 4. 21-b, c). In order to find the focus plane, we extracted images at different distances (having in mind the minimum and maximum distance of the object). The best focus position is then visually determined. This procedure could be made when out of focus, the reconstruction is clearly blurred (Fig. 4. 21-c). In Fig. 4. 22 we present the initial wavefront profile (at $z = 0 \mu\text{m}$) and the wavefront profile after the final reconstruction in the sample plan ($z = 400 \mu\text{m}$). Note that as this is an off-axis holographic scheme, the twin image is not superimposed with the actual image, and there is no need for an iterative algorithm to remove its contribution. The phase in the central area, where the cells will be located, appears to be almost perfectly flat, which will ensure a sample reconstruction with minimum artefacts. With this technique, we find that the object is $400 \mu\text{m}$ away from the pupil plane, which is consistent with the overall thickness of the glass plate used as support. This is consistent with the thickness of the glass plate that we used as support. The back-propagation to the focus leads to an image presenting sharp edges and good contrast.

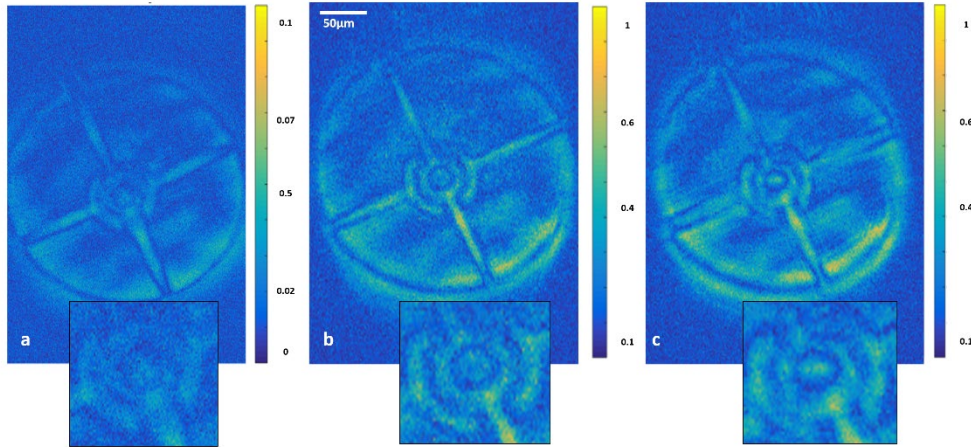


FIG. 4. 21. FINAL OBJECT RECONSTRUCTION: A) ZOOM INTO THE SAMPLE EXIT FIELD RECONSTRUCTED IN THE PUPIL PLANE, CORRESPONDING TO $z = 0 \mu\text{m}$. HERE, WE SELECTED THE TOP RECONSTRUCTION FROM IMAGE 4.19-D. B) MODULUS OF THE SAMPLE RECONSTRUCTION IN THE SAMPLE PLANE, I.E. AT $z = 400 \mu\text{m}$; C) MODULUS OF THE SAMPLE EXIT WAVE AFTER BACK-PROPAGATION AT $z = 600 \mu\text{m}$. THE TRANSVERSE SAMPLING STEP IS $0.5 \mu\text{m}$.

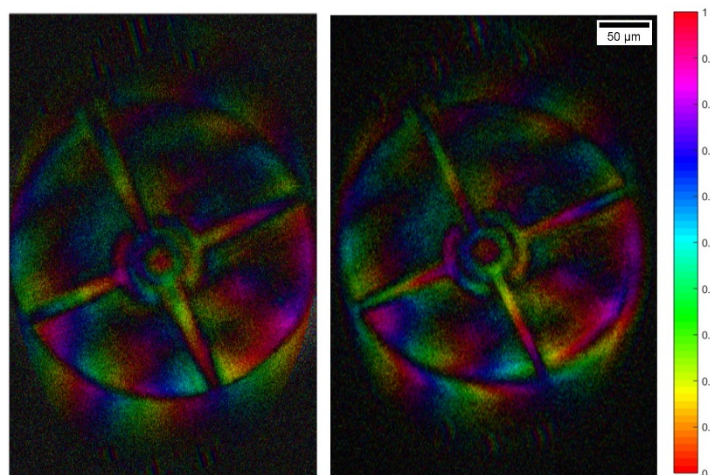


FIG. 4. 22 THE INITIAL WAVEFRONT (LEFT) USED FOR THE RECONSTRUCTION AND THE WAVEFRONT IN THE PLANE SAMPLE (RIGHT).

4.4.2 Resolution

To determine the spatial resolution we use the "10-90" criterion on the in-focus reconstruction of the electrodes, as defined in section 4.1.3 Resolution. Several lines, at different positions were used (see e.g. the red line Fig. 4. 23). Using the in-focus reconstruction of the electrodes (Fig. 4. 21-b), we obtain a resolution of $2.4 \mu\text{m}$. The theoretical resolution is given by the dimension of the circular nanohole of $1 \mu\text{m}$ diameter or in our case is calculated as a function of the focal length of the lens we

inserted to far field condition, as mentioned before (see equation 4.10). The theoretical resolution for a lens with focal length $f = 30\text{mm}$ is $2.2 \mu\text{m}$. The loss of resolution compared is explained by both the limited SNR as well as the reimaging lens which has a NA of 0.66.

$$\delta t = f\lambda/(N\Delta x) \quad (4.10)$$

where f is the focal length, N the number of pixels occupied by the hologram and Δx the pixel size of the CCD.

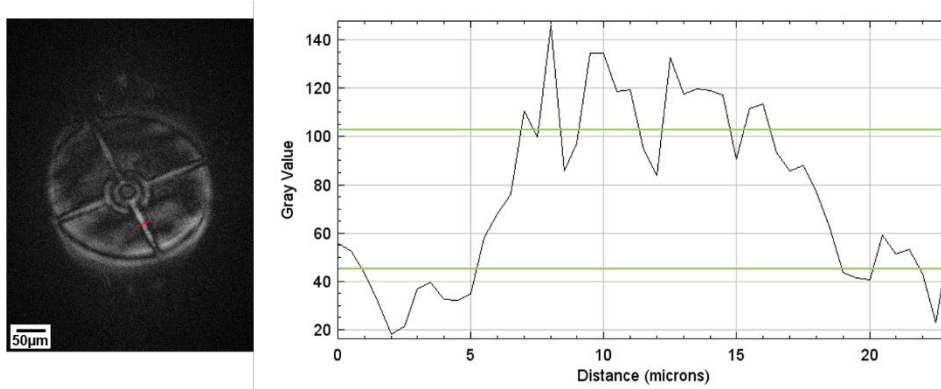


FIG. 4. 23. RESOLUTION TEST OF THE SAMPLE (ELECTRODES). THE GRAPH IS A LINEOUT ALONG THE RED LINE ON THE GREY SCALE IMAGE, REPRESENTING THE HOLOGRAPHIC RECONSTRUCTION OF THE SAMPLE.

The achievable resolution in this configuration is not enough for a detail analysis of a single cell, but is enough to characterise a real sample as the basic principle of the Fourier transform holography with holographic references is working.

4.5. Integration and testing the electro-opto-fluidic platform

In this section we will present the performance of the final system. In this context, biological samples (HeLa cells) are used to perform the experiment. The samples were provided by our collaborators from LRIG at CEA Fontenay aux Roses near Paris. Both parameters, i.e. electrical control and digital imaging, will be investigated. One key point of the experiment is the cell concentration: in order to enable the experiments in suitable conditions for the DEP effect, the cells should flow individually in the volume (clusters are not desired or high concentration of cells could block the channel and fluid flow). Therefore, we have to follow a specific protocol in order to perform our experiments.

4.5.1. Preparation protocol

In this section we will list the steps I followed to define a good protocol for our experiment. The use of biological samples involves good working conditions and clean equipment. The microfabrication procedures leave behind lot of dust and impurities. Special cleaning steps have to be followed to ensure good optical conditions for imaging. After this, electrical tests are performed to define the efficiency of the electrodes and the working conditions in different solutions.

Preparation steps:

1. Chip Cleaning: DI Water and Ethanol for sterilization.
2. Chip drying: drying with compressed air because natural drying leave shadows that affect the imaging.
3. Preliminary flow experiment: comparison between DI Water, ethanol and buffer (D-PBS - Dulbecco's Phosphate Buffered Saline). Three types of medium of different viscosity are tested in order to verify if the channels are well configured.
4. Initial electric measurements:
 - 4.1 On Empty Chip (necessary to test the continuity of the metal)
 - 4.2 On DI Water
 - 4.3 On Buffer (no Cell)
5. Chip cleaning and drying (step 1 and 2): prepare the chip for experiment
6. Supply cells by flow (prior we define the concentration of the cells according with the volume of the chamber)/ Optical monitoring (reflection or/and transmission optical microscope)
7. DEP: positive (p-DEP) / negative (n-DEP)

Sample protocol: The Hela cells were cultured in Dulbecco's modified Eagle's medium (DMEM, ThermoFisher). Cells were grown on 12 mm round coverslips N°1,5H (Marienfeld, 900532), at 37°C. Before trypsinisation, we rinsed with DMEM to remove the dead cells and incubated again for 5 min. 3ml of trypsin was added in order to detach adherent cells from the dish so we can transfer them. When the cells started to detach we removed the trypsin and added 2% formaldehyde for 10 min, followed by 5 min centrifugation and then washed with D-PBS. After this protocol the cells got a round shape and long life for experiments (Fig. 4. 24). The final concentration is $c = 2 \cdot 10^6$ cells/ml that were stored in D-PBS.

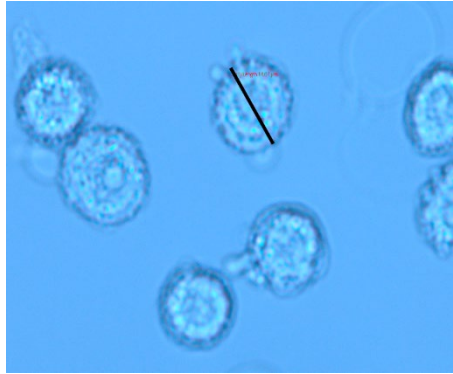


FIG. 4. 24. OPTICAL IMAGE OF HELa CELLS AFTER TRYPSINISATION, OBTAINED WITH A 40X MAGNIFICATION. THE CELL'S DIMENSION, MARKED BY THE BLACK LINE, IS 15 μ m.

4.5.2. DEP experiment

As already mentioned, the two key factors for DEP manipulation are the frequency and voltage. Here, we used the generator described in Annex G. The generator specifications are: Voltage: 2-30 V/ Signal type: Sinusoidal / Frequency: 100 kHz – 20 MHz. The electrical parameters defined in the simulations have to be followed in the experimental procedure in order to perform the DEP in the optimum conditions. The electrical properties of both cells and medium from literature are presented in Table 4. 2.

	Electrical parameters	
	Conductivity	Permittivity
HeLa	$\sigma_{\text{cell}} = 0.1 \text{ S/m}$	$\epsilon_{\text{cell}} = 10^4$
D-PBS	$\sigma_{\text{medium}} = 1.5 \text{ S/m}$	$\epsilon_{\text{medium}} = 80$

TABLE 4. 2. ELECTRICAL PROPERTIES OF THE CELLS AND BUFFER^{39 40}.

The electrical properties of the buffer depend on the concentration of the inorganic salts that are in its composition. We used D-PBS and more details could be found for instance in the following reference¹³¹. In the case of the cells, the impedance was taken from the literature^{132 133}. As a reminder, the Clausius-Mossotti factor vs frequency graph (Fig. 4. 10) shows that the range of negative DEP is in low frequency regime up to 3.5 MHz. Positive DEP is obtained for 3.5 – 100 MHz and higher. Maximum DEP forces are obtained above 50 MHz frequency, while for 20 MHz the velocity is 90% from the maximum value. Our optimized electrode design allows a more flexible control on the cells thanks to the different configurations of electric field that can be achieved. In this section we chose to present the results obtain in the case of only one electrodes connection scheme,

presented Fig. 4. 25. The other configurations already presented could be used with similar procedures.

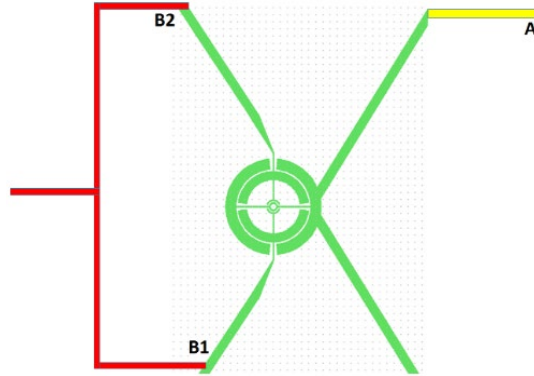


FIG. 4. 25 ELECTRODES CONNECTION: C1- BETWEEN A AND B1+B2 (B1 AND B2 CONNECTED TOGETHER).

One last pre-experiment important parameter is the maximum allowed cell concentration. It is an important aspect if we do not want the channels to be blocked because of a too high concentration of cells. Our chamber volume is $V = \pi r^2 h = 0.06 \mu\text{l}$, with r the base radius of the chamber and h the height. If we want to reproduce the simulated case (with 25 cells uniformly distributed in the chamber), we need a concentration of:

$$c = \frac{\text{number of cells}}{\text{unit volume}} = 253 \text{ cell}/\mu\text{l} \quad (4.11)$$

After the filling of the chamber with the buffer and cells, we waited a certain time until equilibrium, before applying the electric fields in order to perform the cells manipulation. The electric field for separation needs to be applied in non-flow conditions, after the channel is filled. In Fig. 4. 26 we present a screen capture of an experiment where we used positive DEP. We generated between the electrodes 10 Vpp and 20 MHz frequency. The total time for the cells to arrive at the equilibrium state was about 6 min and I present the last 18 seconds of the experiment. The red circle shows the trajectory of the cell that is attracted to the central area.

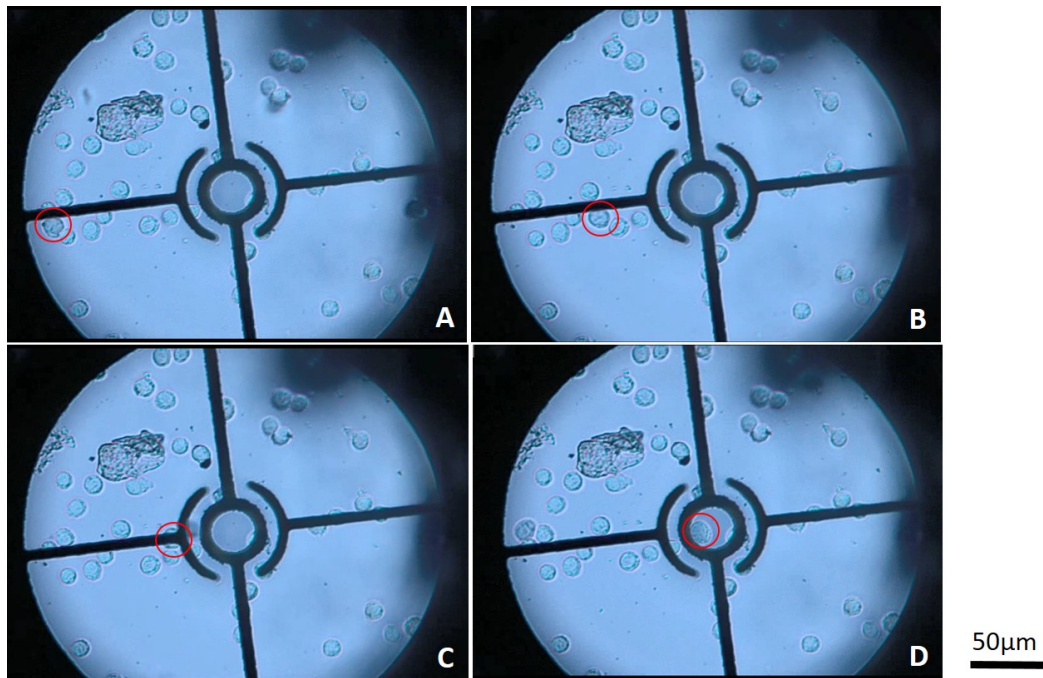


FIG. 4. 26. MICROFLUIDIC CHIP FOR CELLS SEPARATION IN THE CIRCULAR REGION FOR HOLOGRAPHIC IMAGING. THE CELL ISOLATED UNDER A POSITIVE DEP IS HIGHLIGHTED BY A RED CIRCLE. FOUR PHASES OF DISPLACEMENT ARE PRESENTED IN: **A**: $T=0s$, **B**: $T=4s$, **C**: $T=8s$, **D**: $T=18s$. THE CELL IS ISOLATED AT $T= 14s$. THOSE IMAGES WERE OBTAINED WITH AN OPTICAL MICROSCOPE WITH A 20X OBJECTIVE.

Both n-DEP and p-DEP can separate cells to single level in the field of view. One difference between the two cases lies in the vertical distance between the trapped cell and the bottom surface. In the case of the p-DEP, the cell is attracted to the maximal electric field region at the bottom side: in Fig. 2.26, the cells and the electrodes are all in focus in the same image plane. On the contrary, in the case of the n-DEP, the cell is repelled from the bottom to the minimal electric field upper region of the chamber. In Fig. 4. 27, the cells are in focus while the electrodes are not. Additionally, the cells distribution is affected by the electric field. Indeed, the cells are organized in groups of about 10-20 cells, in low field regions (see dotted circle). This tendency is not general and will depend on the concentration. At low concentration, the cells will start to behave individually.

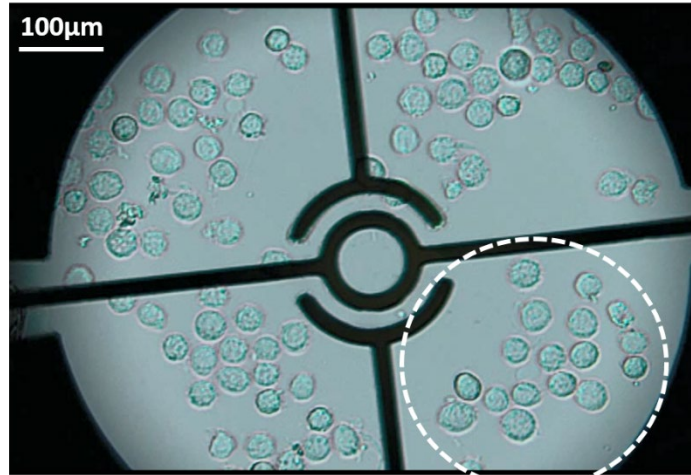


FIG. 4. 27. OPTICAL MICROSCOPE IMAGE OF A n-DEP EXPERIMENT (20X OBJECTIVE). THE WHITE DOTTED CIRCLE EMPHASIZES THE TENDENCY OF THE CELLS TO FORM GROUPS IN THE PRESENCE OF AN ELECTRIC FIELD.

In the following table we listed the experimental parameters used to characterize the chip in different working conditions. While the design of the central area (ring and arc shapes) allows for better trapping conditions of the cells in negative DEP regime, the positive DEP regime leads to a faster separation of the cells and would therefore allow for faster image acquisitions. Therefore, it allows reducing the risk of evaporating the buffer and of drying the sample. In the experiment number 4, a possible electroporation was noticed, but the available equipment did not allow to validate or invalidate this hypothesis. The assumption is made based on the experimentally applied parameters (signal type, intensity, frequency and duration) in correlation to other data presented in the literature¹³⁴.

No.	DEP	Signal	Applied Voltage	Frequency	Time*	Comments
1	n-DEP	Sine	5 Vpp	1 kHz	16 min	Slow time for separation
2	n-DEP	Sine	10 Vpp	1 kHz	12 min	Slow time for separation
3	p-DEP	Sine	10 Vpp	20 MHz	6 min	Ideal in our case
4	p-DEP	Sine	20 Vpp	20 MHz	4 min	Possible electroporation Not suitable if only input cell observation is needed

*To stationary / equilibrium state

TABLE 4. 3 APPLIED VOLTAGE IN C1 CONFIGURATION: BETWEEN A AND B1+B2 (B1 AND B2 CONNECTED TOGETHER).

4.5.3. Microfluidic FTH imaging

In this section, we present a comparison between the results achieved with an optical microscope and with our platform. Thanks to the real time graphic user interface, the FTH microscope is particularly useful for searching samples with a complex structure, such as biological samples which are usually randomly distributed on the coverslip. Moreover the integration of the electrodes helps us to isolate the sample for a faster identification.

4.5.3.1 Low cell concentration

We tried first to isolate only one cell in the whole FOV. We first verified the correct position with an optical microscope and the corresponding images are presented in Fig. 4. 28. The experimental protocol is the same as in section 4.5.1 but with a low concentration of cells. We first optimize the electric field using the optical microscope to isolate a single cell (or few of them) in the field of view of the chip. Then, the chip is transported (4-5 min transportation delay) to the holographic microscope to verify their position. During the transportation, the voltage is turned off. The whole process takes place in no flow conditions inside the channels. Theoretically, the cells keep their polarization, initially induced by the electric field, so that they can be again analysed in the holographic microscope. Indeed, we can see from the reconstructed images that the cell more or less kept its position and could easily be identified by comparing the optical image (Fig. 4. 28) and the FTH reconstruction (Fig. 4. 29). Let us remark here that this experimental procedure is not the normal one, but was imposed by the necessity to learn how exactly the microfluidic device was behaving. This was more easily done using the optical microscope. Moreover, the optical microscope was not in the same laboratory as the FTH microscope.

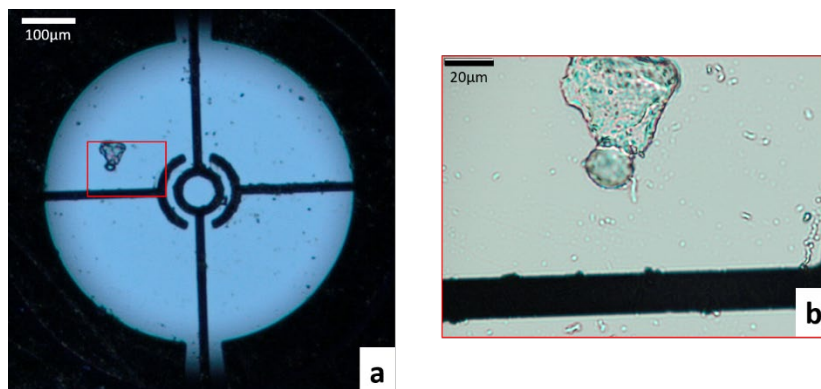


FIG. 4. 28. CELL HANDLING WITH P-DEP FOR 10VPP AND 20MHZ. THE CELL OF INTEREST IS MARKED WITH A RED SQUARE IN A TRANSMISSION IMAGE OBTAINED WITH A MICROSCOPE OBJECTIVE OF 10X. IN B), A MAGNIFIED IMAGE OF THE RED SQUARE, WITH A 40X MICROSCOPE OBJECTIVE.

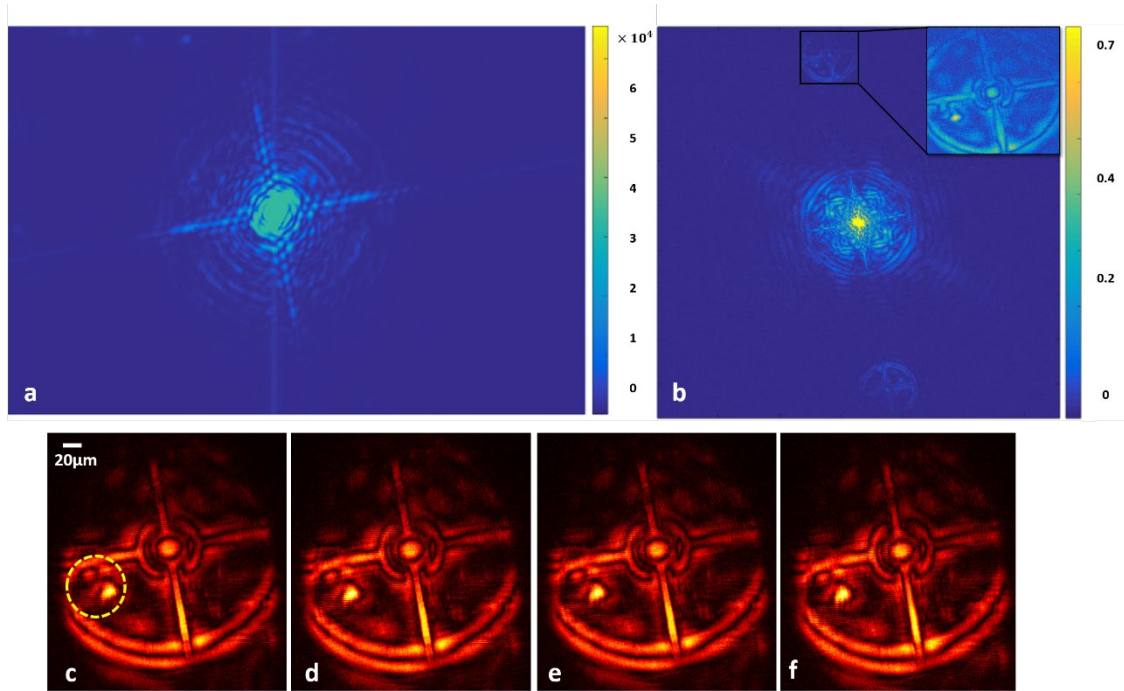


FIG. 4.29. EXPERIMENTAL RESULTS OF HELa CELL IMAGING WITH THE FTH MICROSCOPE.

A) THE HOLOGRAM DETECTED IN THE FAR FIELD BY THE CAMERA; B) AMPLITUDE OF THE FOURIER TRANSFORM OF A), WITH BOTH THE OBJECT AND ITS MIRROR CONJUGATE VISIBLE. IN INSET, A ZOOM INTO THE OBJECT FROM B), I.E. RECONSTRUCTED IN THE PUPIL PLANE ($z=0 \mu\text{m}$). **BOTTOM LINE:** BACK-PROPAGATION OF THE SAMPLE EXIT WAVE. MODULUS OF THE RECONSTRUCTED FIELD AFTER A BACK-PROPAGATION BY C) $z = 450 \mu\text{m}$, WHICH CORRESPONDS TO THE IN FOCUS PLANE, THE CELL CAN BE IDENTIFY IN THE YELLOW CIRCLE D) $z = 460 \mu\text{m}$, E) $z = 480 \mu\text{m}$, F) $z = 550 \mu\text{m}$. THE LATERAL SAMPLING STEP IS $0.5 \mu\text{m}$.

Using the FTH technique, the cell can clearly be distinguished from the electrodes. Determining the best-focused plane is not easy, as the variations of the amplitude of the field with the propagation distance are small. Additional modulations nevertheless appear for $z > 480 \mu\text{m}$. While in principle a pseudo 3D reconstruction of the cell is possible, similarly to what was obtained **Chapter 3**, the limited depth resolution prevents it here. In this case, the low cell concentration reduces the efficiency of the p-DEP handling to isolate a cell in the centre of interest: as the number of cells is very limited, the probability of having one cell in the initial conditions that allow trapping is small. Moreover, the transportation of the chip between the two imaging apparatus could have influenced the cell's position. Nevertheless, we demonstrated that our new scheme combining imaging pupil, DEP electrodes and microfluidics was performing well and that it could lead to real time imaging of the cells. Even if in this first demonstration the resolution of our set-up is not as good as expected, theoretically we should have seen cells with approximately 500nm resolution using a large FOV. This remarkable advantage could be used to investigate single cell or a large population of cells. In the conclusion I proposed a list of future improvements.

4.5.3.2 Large cell concentration

For this set of experiments we used the normal concentration of cells. As in the previous case, we first verified the position of the cells with an optical microscope. The corresponding image is presented Fig. 4. 30. We followed the same experimental procedure. We first optimized the electric field using the optical microscope to isolate a group of about 10-20 cells in the field of view of the chip. Then, the chip is transported, with the voltage turned off, to the holographic microscope (see Fig. 4. 30b) to verify their position. In this case, it is clear that the cells have moved during transportation. The motions of the chip disturb the fluid that shifted the cells position. However, some of them are still in the FOV and are clearly distinguished in the reconstruction. We present, in FIG. 4. 31, the results associated with the diffraction of the object of 4. 30-a.

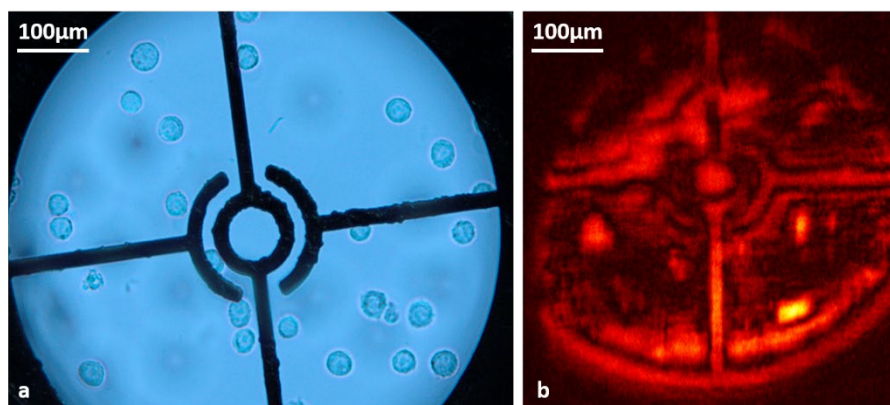


FIG. 4. 30. CELLS HANDLING WITH P-DEP FOR 10VPP AND 20MHZ. A) OPTICAL MICROSCOPE IMAGE, IN TRANSMISSION AND 20X OBJECTIVE, WITH ABOUT 20 CELLS IN THE FIELD OF VIEW; B) HOLOGRAPHIC RECONSTRUCTION TAKEN ABOUT 10 MIN AFTER THE OPTICAL IMAGE, $Z=450\mu\text{m}$.

As in the case with low concentration of cells, we can clearly distinguish the cells from the electrodes. However, the quality of the final reconstruction is limited. Though the reconstructed objects are visible, they do not show the level of details seen in Fig. 4. 30-a. The experiment can be further optimized in particular by enhancing the illumination of the reference while keeping the same intensity level at the sample. A discontinuity of the electrodes can be noticed in the FTH image reconstruction, which can be due to the peeling of the metal in the region of electrodes caused by the voltage or presence of cells clusters.

The limitation of lateral resolution has effects on the vertical resolution (z). As you could see in both type of experiments, low and high concentration of cells, the variation in the z plane does not give any deep information about the shape or position of the cells in volume.

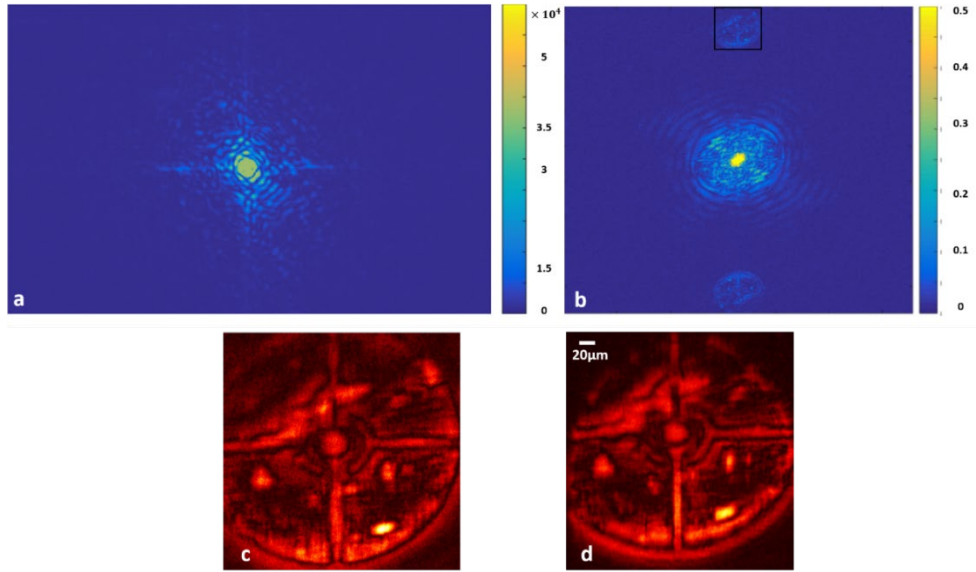


FIG. 4. 31. EXPERIMENTAL RESULTS OF HELa CELLS IMAGING WITH THE FTH MICROSCOPE. A) THE HOLOGRAM DETECTED IN THE FAR FIELD BY THE CAMERA; B) AMPLITUDE OF THE FOURIER TRANSFORM OF A), WITH BOTH THE OBJECT AND ITS MIRROR CONJUGATE VISIBLE. C) ZOOM FROM IMAGE B) INTO THE RECONSTRUCTED FIELD IN THE PUPIL PLANE ($z=0\mu\text{m}$). D) THE RECONSTRUCTION OF THE MODULUS IN THE SAMPLE PLANE: $z = 450\mu\text{m}$.

4.6. Conclusions

In this chapter we focused on the design, fabrication and testing of an electro-fluidic system compatible with lensless imaging and its integration in an experimental platform for nanoscale holography. We studied various samples, such as metallic electrodes and HeLa cells. We demonstrated the compatibility of holography with microfluidics technology. In this preliminary validation, we tested the efficiency of the DEP effect using an optical microscope. At this level, a full DEP experiment was not possible with the FTH, because a visual access to the microfluidic channels was mandatory to check the cells' movements towards the central pupil. However, we could test the technique by calibrating the experimental parameters with the optical microscope and then move the microfluidic chip to the FTH microscope. We have seen that while this additional transportation step may influence the position of the cells, we could nevertheless identify the cells in the FOV and image them by FTH microscopy. We explain the limited transverse resolution by the fact that we had to insert a lens between the sample and the CCD in order to reach the Fraunhofer far-field regime. Another drawback could be a possible leak of liquid between the silicon/glass layers, so that the liquid cover the nanohole used for the reconstruction.

This first set of experiments helps us determine the future parameters to improve the quality of the images. A smaller pupil will allow direct far field acquisition of the hologram, removing the

need for the extra lens after the sample. This will improve the spatial resolution, and will eliminate the optical aberrations induced by the lens. Regarding the resolution, the fabrication process could be improved by optimizing the parameters for the nanoholes patterning. Finally, we saw in section 4.5.2. DEP experiment that the optimal frequency (related to DEP force and velocity) for p-DEP separation is larger than 50 MHz. However, this high frequency could not be reached by the available pulse generator, limited to 20 MHz. A larger frequency would have allow a faster separation of the cells. In this case, drying of the sample because of the laser illumination would have been avoided, allowing for a better operation of the device. Nevertheless, this configuration presents lot of advantages. It is easy to develop thanks to the simple FTH implementation. With few additional improvements, the quality of our date can be significantly improved.

From the perspective of image reconstruction the first and main improvement of the device is to reduce the FOV size in order to reach the far-field conditions. A new design is necessary to proceed new experiments. This modification will remove the optical lens that we used in the first experiments and will help to increase the lateral resolution and at the same time vertical resolution, of the system. For instance reducing the FOV from 300 μm diameter to 150 μm diameter, the far-field condition can be reach as the Fresnel number become $F = 1.85$ (from equation 4.1). In this numerical example I supposed the distance sample-CDD equal to 30 mm, as in the experimental results presented in this chapter. To reach an F closer to 1, this distance can be reduced. Below I present a simulation with the image reconstruction with the additional modifications.

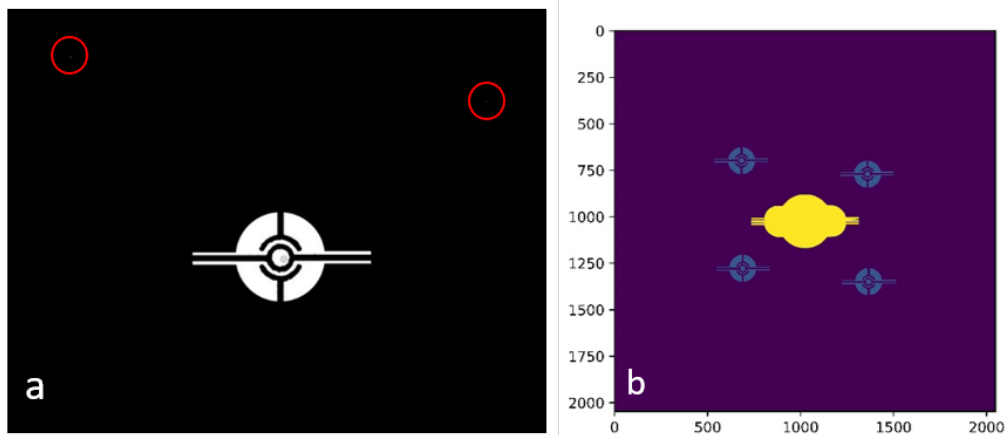


FIG. 4. 32. A) SIMULATIONS OF A MASK WITH FOV OF 150 μm IN THE ELECTRODES REGION, RESPECTIVELY A MASK OF 20 μm WIDTH IN THE CHANNELS REGION. TWO NANOHOLES OF 1 μm DIAMETER WHERE CONSIDERED AS FTH REFERENCES (THE POSITION OF THE NANOHOLES IS SURROUNDED BY THE RED CIRCLE); B) THE SIMULATION SHOWS THE HOLOGRAMS RECONSTRUCTION AND THEIR CONJUGATE. NOTE: IN THE FOV REGION A REPRESENTATION OF A CELL OF 15 μm DIAMETER WAS CONSIDER AS AN ARTIFICIAL OBJECT FOR A SIZE REFERENCE.

In the current version the microfluidic part brings some impediments due to the optical restrictions. The liquid flow and stabilization time of the cells in the channel cannot be visualized

with the FTH technique, but only with the conventional microscopy apparatus. Two additional openings in the channel region will leave enough space to visualize the liquid flow with the cells. The observation of the process could help to establish a faster and stricter protocol necessary for future industrializable products. This improvement could open a new direction of experiments analysing cells in flow conditions (i.e. bacteria sorting, different type of cells separation and trapping...). The possibility of fast acquisition image could track and monitor single cell analysis.

The two improvements proposed could conduct to an industrializable product. The lab-on-the-chip microscope has potential to cover a large field of application due to its simplicity and adaptability to different working conditions, such as: different type of cells and medium, flow or no-flow conditions (with simulations it can be defined a protocol with electrical parameters needed for DEP and EP effects for many type of cells). This platform opens a new research direction where the integration and compatibility of classical technologies for microfluidics with optics and electronics will have a direct impact on the methods and accuracy regarding separation, detection and analysis of bioparticles going through biophysical or biochemical processes. The platform is a step to new generation of devices used for cell research in bio-medicine. Moreover, the working principle could easily be extended to other type of biological samples.

5. CONCLUSIONS

In this thesis, I presented two techniques of coherent lensless microscopy, that both have the potential to solve the critical problem of fast, simple and low cost imaging for biological samples, while insuring an improved lateral spatial resolution.











The two concept proposed are complementary to each other. Both are based on holographic principle; however, one follows an in-line configuration and the other an on off-axis scheme.

The first, digital in-line holography microscope offers a very large field of view with a micrometer scale lateral resolution in a very simple optical setup. In the development step, I tried to find the best compromise between sample viability (that limits the laser fluency on the sample) and optical performances. I tested two different configurations in order to increase the lateral and axial resolutions by enlarging the numerical aperture. I found out that using high NA lenses can be a good solution, theoretically reaching sub-micron resolution. However, experimentally the resolution is limited by the optical aberrations introduced by the lens. Special algorithms should be adapted to the setup in order to remove their effects on the reconstruction. On the other hand, using a small diameter (1 μ m) pinhole does not introduce additional aberration, but leads to limited spatial resolutions which in this case the maximum experimental resolution was 600nm. In a first step, the experimental validation of the two schemes was carried out on synthetic polymeric microspheres and an optical ruler. I implemented an advanced iterative reconstruction algorithm to remove the out-of-focus twin-image contribution to the reconstruction, leading to an improved resolution and better contrast. Those results are presented in **Chapter 2**. In order to assess the applicability of the prototypes to real biological samples of interest, different objects with a range of optical properties (thick, thin and single cell) were tested, such as zebrafish embryo, cell cultures and cyanobacteria. The portability and ease of use of the in-line apparatus can be an alternative for the current very expensive tools. Basic diagnostics, such as identification of cancer cells (U2OS) or cell motility analysis (cyanobacteria), have been successfully achieved. Those results were presented in details **Chapter 3**. Additionally, DIH allows to reconstruct the full diffracted wave in both spatial amplitude and phase. It is therefore possible to obtain slices of the sample at different successive depth positions. This technique allowed me to obtain a pseudo-3D representation of a cell. This technique is a single shot label free concept, and as such a perfect solution for imaging 3D sensitive biological samples. However, the contribution of out of focus particles in each z-slice induces artefacts in the structure of the final 3D reconstructed object. A full-algorithm for speckle noise analysis on the hologram would improve the axial resolution (as M. Molaei presents in his research paper¹³⁵), thus a better 3D reconstruction could be obtained from for the slice extraction.

The second microscope I studied is based on off-axis holography. This second configuration is complementary from DIH, in the sense that it can give answers to specific needs that the former one does not meet.

This configuration uses one or more additional pinhole references on the side of a pupil that isolates the sample. This non-symmetric arrangement removes the twin image problem. Moreover, the reconstruction is mainly based on a simple Fourier transform, followed by a back-propagation step to focus the reconstruction of the wanted sample feature. Additionally, I integrated in the pupil and reference plane microfluidics components in order to electrically control and manipulate the samples. In a preliminary validation with HeLa cells, I demonstrated for the first time the compatibility of the two intricate devices, i.e. holographic mask and microfluidics technology. The first demonstration of these experiments with the analysis were presented in details in **Chapter 4**. While a complete DEP experiment was not possible using FTH imaging, this first set of experiments helped to determine the future parameters in order to improve the functionalized sample holder. For instance, using a smaller pupil will remove the need of a lens after the sample and direct observation of the hologram in the far field. This will improve the spatial resolution, and will eliminate the optical aberrations induced by the lens. Those results are presented **Chapter 4**.

Generally, lensless microscopy presents many advantages. The main ones in my view are listed in the following table, which compares the two platforms that I developed during this PhD. The in-line holography setup is very stable against vibrations. This insures its direct portability to field imaging out of the laboratory, without any additional isolation system. On the other hand, the FTH platform opens a new research direction where the integration and compatibility of classical technologies for microfluidics with optics and electronics will have a direct impact on the methods and accuracy regarding separation, detection and analysis of bioparticles going through biophysical or biochemical processes.

	Advantages	FOV	Single cell imaging	Resolution	3D reconstruction	Live imaging
Lensless microscopes	DIH					
	FTH					

Perspectives

Based on the experimental demonstration run in this PhD research I would like to highlight the importance of the development of new microscopy configurations. Lensless imaging proved a perfect solution for several types of biological analyses, and I think it is promising for an even larger field of applications. For instance, for biologists a new challenge lies in bacteria antibiotic resistance. Some pathogenic bacteria become insensitive to the usual antibiotics and can even inactivate them.

A screening of bacteria resistance requires very large statistics, hence the need to image in parallel with large fields of view to analyse myriad of bacteria's reaction to the antibiotic. Classical microscopy has a limitation of its field of view, and implies large apparatus, which complicates this kind of analysis. Some features could be easily adapted to the devices I developed. Cell tracking algorithms could allow automatic motility studies, helping screening sane or cancerous cells for instance. Also, depending of the type of cells, pattern and shape recognition algorithms based on artificial intelligence could be developed.

Along similar lines of development, the advantages of the microfluidic-based devices integrated in the FTH microscope allow medical diagnosis for biological cells and microorganisms. Furthermore, chemical analysis of the cellular content can be performed and offers a special interest for bio-chemistry and molecular biology medicine and pharmaceuticals. These studies reduce the consumption of reactants and the processing times, and are available at low costs, while offering an enhanced capability of controlling the reaction parameters through specific design of the microfluidics part.

However, biologist are often reluctant to turn towards new types of imaging tools, as living organisms are complex systems with numerous components that one needs training to recognize. An ideal evolution of our GUI would for instance be to use artificial colours based on refraction index that would mimic current microscopy solution. We are not yet at the level of integration of lensless microscopes in most bio labs (although several companies already sell products based on another off-axis configuration), but in my opinion this technology opens very interesting routes towards always more beautiful, resolved and informative images.

Annex A

A.1 Fourier optics

The Fourier transform is one important physical tool used in mathematics, engineering, and the physical sciences. Its discrete correspondent, the Discrete Fourier Transform (DFT), which is normally computed using the so-called Fast Fourier Transform (FFT), has revolutionized modern society, as it is omnipresent in digital electronics and signal processing. Nowadays, this modern tool is not only an interesting concept but it can be applied in a very efficient way, so it is useful.

A huge proportion of the formalism underlying diffraction, and consequently holography, rely on the application of Fourier transformations. For numerical computations the functions used in our experiments were developed during a previous doctoral research focused on software development⁵⁷.

We can restrict the mathematical explanation (**Annex A**) to a visual representation (see Fig. A. 1-Fig. A. 2) and say that the real space has its equivalent in the reciprocal space (FT) as a function of low and high frequency.

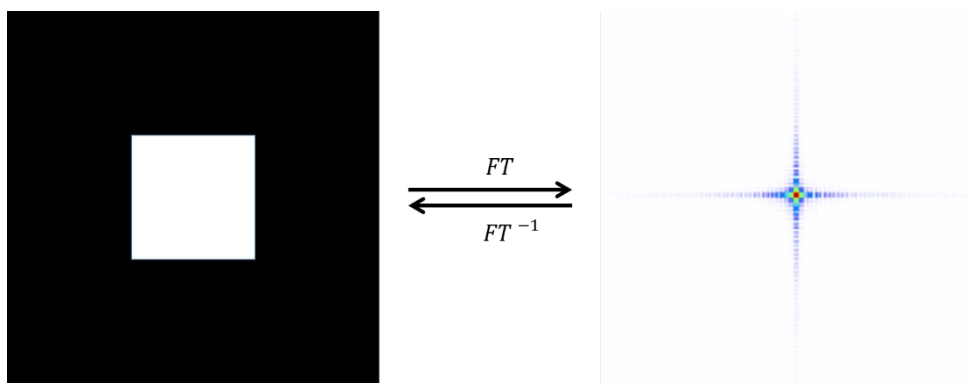


Fig. A. 1. Real space and equivalent in the reciprocal space (FT) at low frequencies

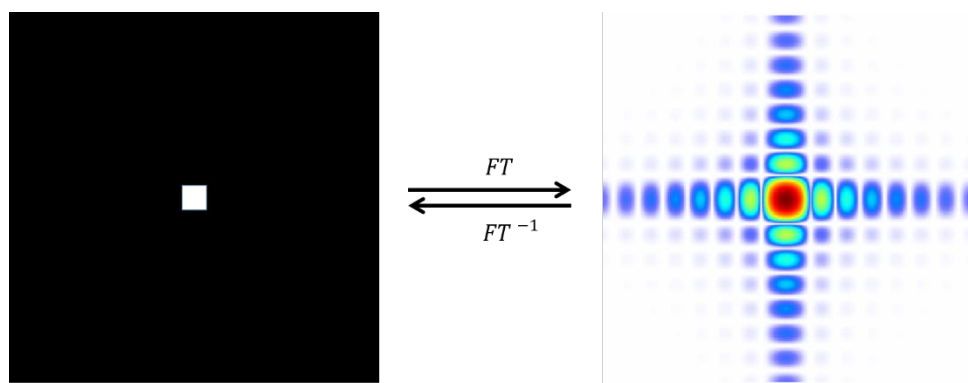


Fig. A. 2. Real space and equivalent in the reciprocal space (FT) at high frequencies

Fourier transform of a light wave passing through a sample describes the observed interference pattern in the far field (the object is at a distance, from screen, much larger than the aperture size). This complex (amplitude and phase) mathematical function replace the uses of the basic lens used in optical microscope to form the image.

A.1.1 Interference

Interference can be observed through the superposition of two or more waves in space that pass through the same region at the same moment in time.¹³⁶ Suppose we are given two monochromatic waves with equal frequencies and wavelengths. The waves should have the same polarization direction. The complex amplitudes of the two waves are described by:

$$A_1(x, y, z) = a_1 \exp(i\varphi_1)$$

$$A_2(x, y, z) = a_2 \exp(i\varphi_2)$$

The resulting wave of complex amplitude is the sum of the individual amplitudes:

$$A = A_1 + A_2$$

The idea of the superposition principle is illustrated in Fig. A. 3.

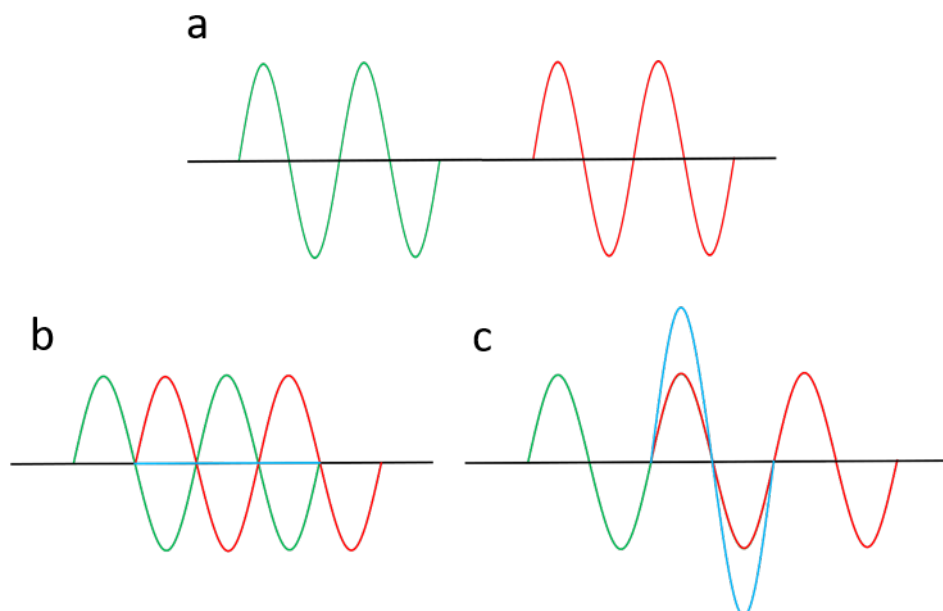


Fig. A. 3. Representation of the superposition of two waves b) constructive interference and c) destructive interference

The interference is constructive if the amplitude of A is greater than the individual ones (Fig. A. 3-c), and destructive if smaller than the individual ones (Fig. A. 3-b). In other words an interference pattern is describe by a series of dark and light lines, “fringes”, across the field-of-view as a result of this constructive and destructive interferences. All lensless microscope are working on the principle of coherent diffraction.

A.1.2 Coherence

In order to look at interference fringes, the phases of the individual waves should be maintained constant. Once two light point sources are directed to a same target, a uniform brightness shows, given by the sum of their individual intensities. Though this additive intensity is the most typical result, some correlation properties between the phases of the two implied waves, can lead, instead, to a sequence of dark and bright fringes. The property of light to make interference patterns is named coherence..

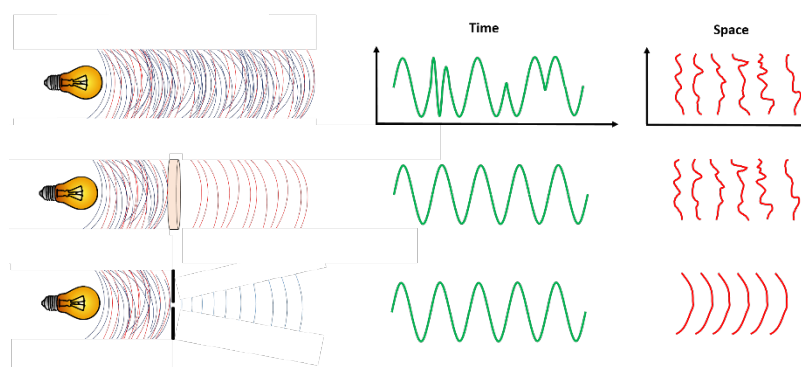


Fig. A. 4. Representation of spatial and temporal coherence. Adapted from A. Schawlow¹³⁷

Coherence property of a light source can be characterized by its temporal coherence and spatial coherence values, respectively (see Fig. A. 4). The temporal coherence depends on the correlation of a wave with itself at different points along the direction of propagation (longitudinal coherence). Within the temporal coherence we know how monochromatic a source is. The spatial coherence is based on the correlation between the phases of the light waves at different points transverse to the direction of propagation (transverse coherence).

Light emitted from an incandescent lightbulb is incoherent because the light consists waves of different wavelengths and they do not maintain a constant phase relationship. Thus, no interference pattern is observed. That is why in any lensless method it is crucial to use at least a partially coherent source. A simple way to make an incoherent light source into a coherent can be made by propagation.

The coherence can be further improved by spatially filtering with a small aperture. Many experiments were performed to show the importance of the coherence, and you could find more details in the literature^{138 139}.

A.1.3 Diffraction

When a wave encounters small object or a small aperture (that is, small compared with the wavelength of the wave), the wave can bend around the object (or pass through the aperture) then spread out. This bending or spreading out is called diffraction. In addition to interference, one of the most important property used in a lensless imaging configuration is the diffraction properties. The diffraction properties can be qualitatively explained with Huygens' principle, that all points of a wave front of light (traveling in vacuum or transparent medium) may be consider as new sources of waves that expand in every direction. A schematic representation is shown in Fig. A. 5.

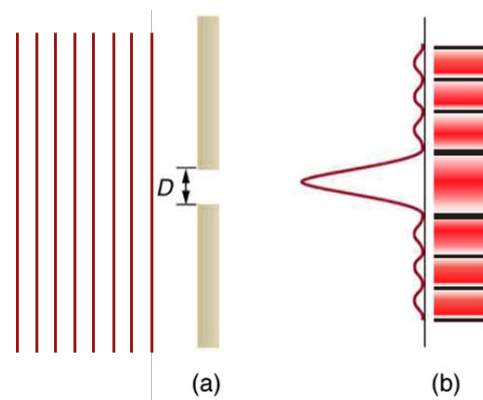


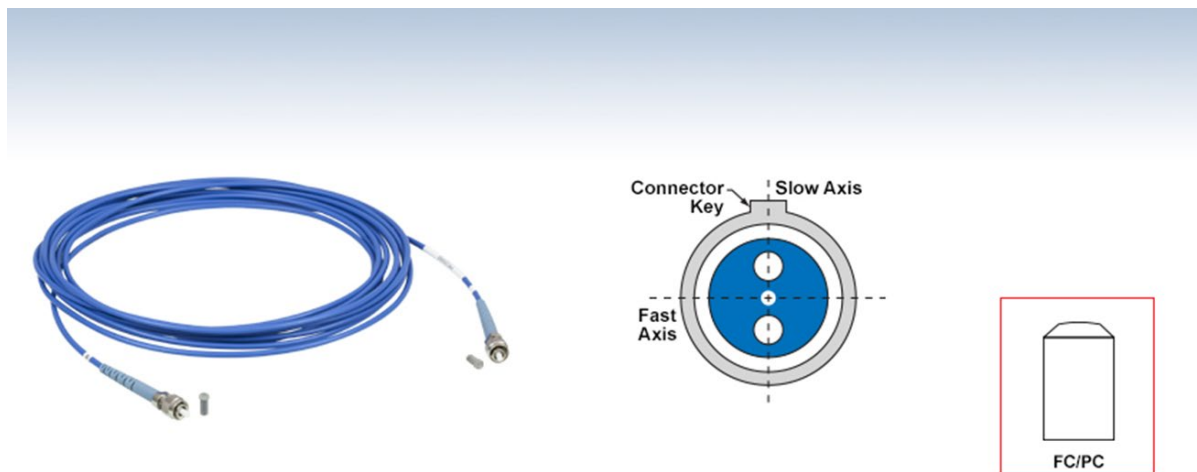
Fig. A. 5. Young's single-slit experiment: a) Monochromatic light passing through a slit of diameter D ; b) the diffraction pattern (dark and light fringes)¹⁴⁰

In Fig. A. 5, the Young's single-slit experiment is presented. Light passing through a single slit is diffracted in all directions and may interfere constructively or destructively, depending on the angle. The light waves emerging from the slit then interfere and form an interference pattern on the imaging screen, the so called diffraction pattern. The bright bands (fringes) correspond to interference maxima, and the dark band interference minima. The diffraction pattern encodes the complex optical field scattered (the phase part carry information about individual scattering events) from an object within a single image. The impediment is that the detector 'sees' only the intensity, i.e. the square of the amplitude of the scattered wave. The consequent is the phase is lost and we cannot recover the object' structure. Until today the phase retrieval problem is still under

investigation and lot of solutions are proposed^{141 142}. Diffraction has been discussed in theory by a large number of authors, such as E. Wolf and J. R. Shewell¹⁴³.

Annex B

Diode Specifications-405nm

***P1-405BPM-FC-2 - PM Patch Cable, PANDA, 405 nm, FC/PC, 2 m***

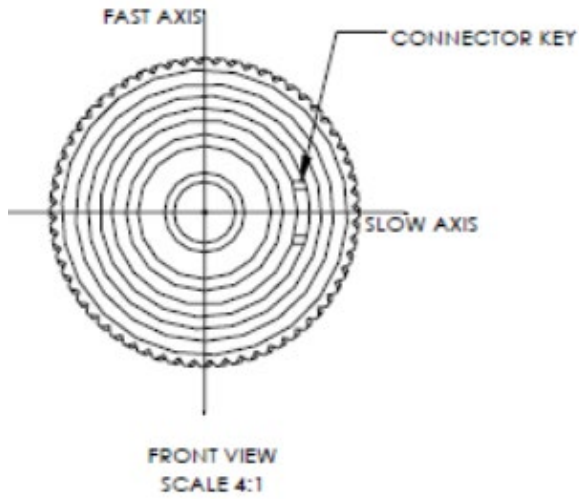
FIBER SPECIFICATIONS	
ITEM	PM-S405-XP
OPERATING WAVELENGTH	400 - 680 nm
MODE FIELD DIAMETER*	3.3 ± 0.5 μm @ 405 nm 4.6 ± 0.5 μm @ 630 nm
CLADDING	125 ± 2 μm
COATING	245 μm ± 15 μm
CUTOFF WAVELENGTH	380 ± 20 nm
NA**	0.12

* MODE FIELD DIAMETER (MFD) IS SPECIFIED AS A NOMINAL VALUE. IT IS THE DIAMETER AT THE 1/e² POWER LEVEL IN THE NEAR FIELD.

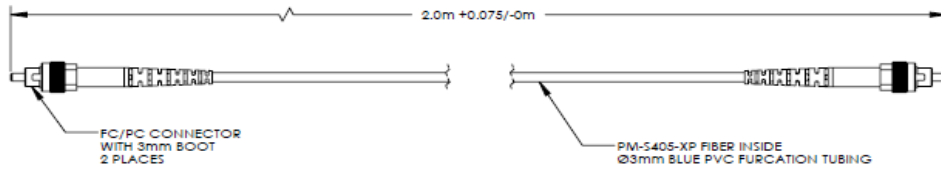
** NUMERICAL APERTURE (NA) IS SPECIFIED AS A NOMINAL VALUE.

CABLE SPECIFICATIONS	
ALIGNMENT WAVELENGTH	405 nm
MAX INSERTION LOSS*	1.5 dB
MIN EXTINCTION RATIO*	15 dB
RETURN LOSS (TYPICAL)	50 dB
CONNECTOR TYPE	FC/PC
KEY WIDTH NARROW	(2.0 mm)
KEY ALIGNMENT	SLOW AXIS
OPERATING TEMPERATURE]C	0 to 70 C
STORAGE TEMPERATURE C	-45 to 85 C

*EACH CABLE INCLUDES INDIVIDUAL TEST DATA INCLUDED BUT NOT SHOWN: • PLASTIC DUST CAPS



DRAWING PROJECTION				THORLABS www.thorlabs.com	
DRAWN	NAME	DATE	2m, 405nm, FC/PC PM CABLE		
APPROVAL	BAG	25/JUL/18	MATERIAL	N/A	REV E
COPYRIGHT © 2018 BY THORLABS			ITEM #	P1-405BPM-FC-2	APPROX WEIGHT
VALUES IN PARENTHESIS ARE CALCULATED AND MAY CONTAIN ROUND OFF ERRORS					0.08kg



Annex C

Diode Specifications-637nm

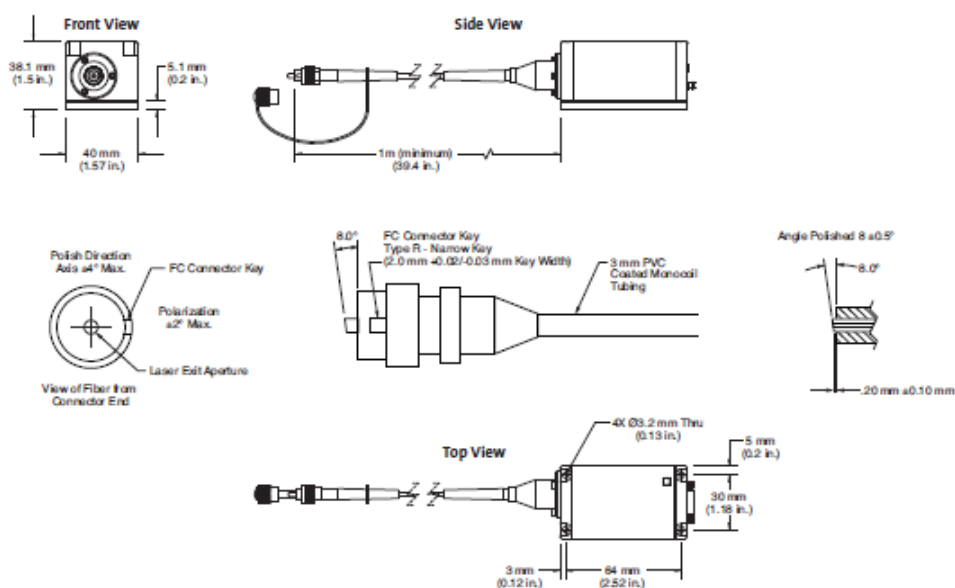


OBIS FP

Fiber Pigtailed Lasers for Plug-and-Play Simplicity Across the Spectrum

Features

- Compact and identical footprint across the spectrum
- Integrated control electronics
- OEM and end user versions
- Superior beam quality from single mode polarization maintaining fiber
- Analog and digital modulation
- USB with complete I/O and controls
- Superior reliability
- FC/APC connector

Mechanical Specifications
OBIS FP LX

Superior Reliability & Performance

System Specifications

OBIS FP Fibre Pigtailed Lasers for Plug-and-Play Simplicity Across the Spectrum	637LX
Wavelength ¹ (nm)	637
Output Power ² (mW)	100
Output from Fibre	FC/APC; 8° angled ⁸
Fibre Cable Type	3 mm Mono-Coil
Fibre Cable Length (m)(minimum)	1
Fibre Numerical Aperture (NA)(1/e ²)	0.09
Fibre Core Diameter (µm)(typical)	4.5
Spatial Mode	TEM00
M2 (Beam Quality) ³	<1:1.1
Beam Asymmetry	<1.1
RMS Noise (%) (20 Hz to 20 MHz)	<0.2
Peak-to-Peak Noise (%) (20 Hz to 20 MHz)	<2
Long-Term Power Stability (%) (8 hrs., ±3°C)	<2
Long-Term Output Power Average (%/hrs.)	<3/1000
Warm-Up Time (minutes)(from Cold Start) ⁴	<5
Polarization Ratio	Minimum 100:1
Laser Drive Modes	CW, Analog Modulation, Digital Modulation and Computer Control
Digital Modulation	
Maximum Bandwidth (MHz)	150
Rise Time (10% to 90%)(nsec)	<2
Fall Time (90% to 10%)(nsec)	<2
Modulation Depth (extinction ratio)	>1,000,000:1 at 0 Hz, >250:1 at 150 MHz
Analog Modulation	
Maximum Bandwidth (kHz)	300
Rise Time (10% to 90%)(nsec)	<1200
Fall Time (10% to 90%)(nsec)	<800
Modulation Depth (extinction ratio)	>1,000,000:1
Laser Safety Classification	3b 3b
ESD Protection ⁵	Level 4 Level 4
Power Consumption (W)	Typical 5, Max. 13
Laser Head Baseplate Temperature (Max., °C)	40 40
Heat Dissipation of Laser Head ⁶ (W)	Typical 5, Max. 13
Ambient Temperature ⁷	
Operating Condition (°C)	10 to 40
Non-Operating Condition (°C)	-20 to +60
Shock Tolerance (g)(6 ms)	30 30

¹ Laser-to-laser tolerance. All LS versions ±2 nm. All LX versions with ±5 nm except 520LX with a 510 to 530 nm range, 640LX with 635 to 644 nm

range and 660LX with 652 to 665 nm range.

² Output power is variable in CW Mode from 1 mW (1% for LX Models) to 110% of rated power. Specifications are valid for 100% power.

³ M2 and Beam Asymmetry measured with ModeMaster with 90/10 clip levels.

⁴ Typical power-on delay 0.1 minutes.

⁵ Electro-Static Discharge Standard IEC 1000-4-2, 1995.

⁶ Typically 85% of heat load through the base plate. See Users Manual for more detail.

⁷ Non-Condensing. See User Manual for more detail.

⁸ Fibre FC/APC connector output not compatible for patchcord-to-patchcord connection.

* Preliminary version.

OBIS FP**Fibre Pigtailed Lasers for Plug-and-Play Simplicity Across the Spectrum****Utility and Environmental Requirements**

Operating Voltage: (VDC)

12 ±2

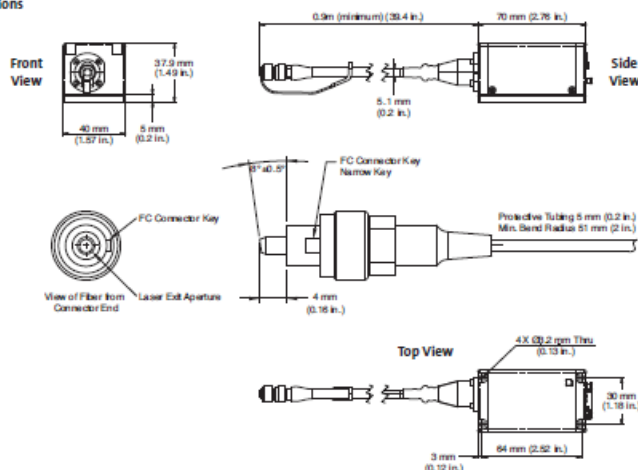
Dimensions (L x W x H)

Laser	70 x 40 x 38 mm (2.75 x 1.57 x 1.5 in.)
OBIS Remote (optional)	105 x 68 x 36 mm (4.13 x 2.68 x 1.42 in.)
DC Power Supply (optional)	105 x 42 x 33 mm (4.13 x 1.65 x 1.3 in.)
Cable, laser to OBIS Remote (optional)	1 m (3.28 ft.) (3 meter and 0.3 meter sold separately)
Fibre Minimum Bend Radius	51 mm (2.0 in.)

Weights

Laser	0.23 kg (0.51 lbs.)
OBIS Remote (optional)	0.24 kg (0.53 lbs.)
DC Power Supply (optional)	0.36 kg (0.79 lbs.)
Cable, laser to OBIS Remote (optional)	0.1 kg (0.22 lbs.) for 1 meter
Fibre Tensile Load (max.)	1 kg (2.2 lbs.)

¹ If user supplied, the DC power supply has to meet the following requirements: power >20W; ripple <5% peak-to-peak; line regulation <0.5%.

**Mechanical Specifications
OBIS FP LS**

Coherent follows a policy of continuous product improvement. Specifications are subject to change without notice.

Coherent's scientific and industrial lasers are certified to comply with the Federal Regulations (21 CFR Subchapter J) as administered by the Center for Devices and Radiological Health on all systems ordered for shipment after August 2, 1976.

Coherent offers a limited warranty for all OBIS lasers. For full details of this warranty coverage, please refer to the Service section at www.Coherent.com or contact your local Sales or Service Representative.



Coherent, Inc.
5100 Patrick Henry Drive
Santa Clara, CA 95054
phone (800) 527-3786
(408) 764-4983
fax (408) 764-4646
e-mail tech.sales@Coherent.com

Benelux +31 (30) 280 6060
China +86 (0) 825 3600
France +33 (0) 8038 1000
Germany +49 (607) 968 333
Italy +39 (02) 31 03 951
Japan +81 (3) 5635 8000
Korea +82 (2) 460 7900
UK +44 (1353) 658 833

Printed in the U.S.A. MC-008-12-01May13revD
Copyright ©2013 Coherent, Inc.



Annex D

CCD Specifications



Sensor Type	CCD Color Image Sensor
Active Pixels	3296(H)×2472(V)
Active Imager Size	18.13(H)×13.60(V)mm 4/3"
Scan Mode	Progressive Scan
Pixel Size	5.5(H)×5.5(V)μm
Shutter Type	Global Shutter
Color Filter Array	RGB Bayer Pattern
Frame Rate	6.6fps
Shutter Speed	1/116788~1/6.64s
Interface	USB3.0 Bulk Transfer
Synchronization System	Internal Synchronization
Lens Mount	F Mount
Power	DC5V(AC adapter)
Power Consumption	Under Approx.20W
AC Adapter	Input : AC100V Output : DC5V 4A
Ambient Conditions	Operating Temperature/Humidity : 0~35°C /10~80%(Non condensing) Storage Temperature/Humidity : 0~60°C /10~95%(Non condensing)
External Dimensions	71.6(W)×61.5(H)×84.7(D)mm *Lens, tripod and cable not included
Weight	Approx.440g *Lens, tripod and cable not included
810KAI-USB3 Series	Range : 1~2523(Exposure Time : 1/116788~1/6.64 sec) Exposure Time= ((2523 – Shutter Value)×1911+274)×0.03125 [μsec]

*at 32MHz

System Requirements

1 Recommended System Requirements

- Intel chip set, Southbridge above ICH6
- CPU: Intel Core2duo 2.4GHz or higher
- Memory: Above 512MB
- OS: Windows XP or above

2 Minimum System Requirements

- USB3.0 Enhanced Host Controller
- CPU: Intel Pentium4 1.7GHz or higher
- Memory: Above 256MB
- OS: Windows XP or above

■Please refer the restrictions below when you use ARTCAM.

(1)Recommended System requirements

If the system specifications are below the recommended requirements, it is possible that the camera may not reach the maximum speed.

(2) Use of other USB3.0 hardware

The data on our camera/converter is transferred in bulk mode. For this reason, when using our camera/converter, please avoid using other bulk transferred USB3.0 hardware such as Memory stick, External HDD, External DVD, CDROM and etc.

As a solution, we recommend to install a PCI USB host card to the PC and connect external USB hardware to this port only.

(3) USB3.0 cable Extension

We cannot guarantee the functionality of the USB3 camera if the user adopts USB3.0 extension cables or repeaters which are not confirmed by us. With the extension cables or repeaters, the bandwidth of transfer may differ, and thus caused malfunctions such as a low frame rate or recognition failure on the camera.

What may cause the problem is that the regulation of the power lines becomes not enough, and so causes impedance mismatch on data signals.

*For the recommended extension cable, please contact our sales department. (TEL: +81-3-3389-5488)



ARTRAY CO., LTD.

1-17-5 Kouenjikita, Suginami-ku, Tokyo 166-0002 Japan

Tel : +81-3-3389-5488 Fax : +81-3-3389-5486

Email : sales@artray.us URL : www.artray.us

Annex E

CCD Specifications



Prosilica GT

6600

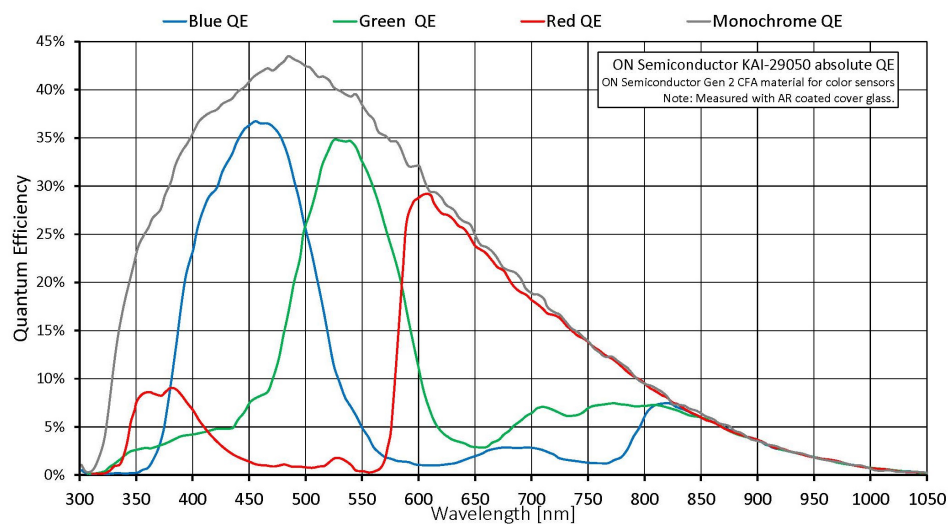
- Versatile temperature range for extreme environments
- IEEE 1588 PTP
- Power over Ethernet
- 4 fps at full resolution

Specifications

Prosilica GT	6600
Interface	IEEE 802.3 1000BASE-T, IEEE 802.3af (PoE)
Resolution	6576 (H) × 4384 (V)
Sensor	ON Semi KAI-29050
Sensor type	CCD Progressive
Shutter mode	Global shutter
Sensor size	Type 35 mm
Pixel size	5.5 μm × 5.5 μm
Lens mounts (available)	F-Mount, F-Mount PA, M58-Mount, M58-Mount PA, EF-Mount PA, M42-Mount, M42-Mount PA
Max. frame rate at full resolution	4 fps
ADC	14 Bit
Image buffer (RAM)	128 MByte
Imaging performance	
Imaging performance data is based on the evaluation methods in the EMVA 1288 Release 3.1 standard for characterization of image sensors and cameras. Measurements are typical values for monochrome models measured at full resolution without optical filter. Contact Sales or AE for more information.	
Quantum efficiency at 529 nm	40 %
Temporal dark noise	14.7 e ⁻
Saturation capacity	18400 e ⁻
Dynamic range	60.0 dB
Absolute sensitivity threshold	18.3 e ⁻
Output	
Bit depth	12/14 Bit
Monochrome pixel formats	Mono8, Mono12, Mono12Packed, Mono14
YUV color pixel formats	YUV411Packed, YUV422Packed, YUV444Packed
RGB color pixel formats	RGB8Packed, BGR8Packed, RGBA8Packed, BGRA8Packed
Raw pixel formats	BayerGR8, BayerGR12, BayerRG12Packed
General purpose inputs/outputs (GPIOs)	
TTL I/Os	1 input, 2 outputs
Opto-isolated I/Os	1 input, 2 outputs
RS232	1

Prosilica GT	6600
Operating conditions/dimensions	
Operating temperature	-20 °C to +50 °C ambient (without condensation)
Power requirements (DC)	7 to 25 VDC AUX or IEEE 802.3at Type 1 PoE
Power consumption	External power: 6.6 W at 12 VDC Power over Ethernet: 8.1 W
Mass	372 g
Body dimensions (L × W × H in mm)	96 × 66 × 53.3 (including connectors)
Regulations	CE: 2014/30/EU (EMC), 2011/65/EU, including amendment 2015/863/EU (RoHS); FCC Class A; CAN ICES-003 Issue 4/5

Quantum efficiency



Features

Image optimization features:

- Auto gain (manual gain control: 0 to 32 dB)
- Auto exposure (manual exposure control: 30 μs to 33.5 s)
- Auto white balance (GT6600C model only)
- Binning (horizontal and vertical)
- Color correction, hue, saturation (GT6600C only)
 - Defect pixel masking (user defined with Defect Mask Loader tool)

Annex F

Simulation of the electric field for the second design

The simulation of the electric field distribution inside the chamber and consequently the DEP force are presented in the following images.

C1 - negative DEP

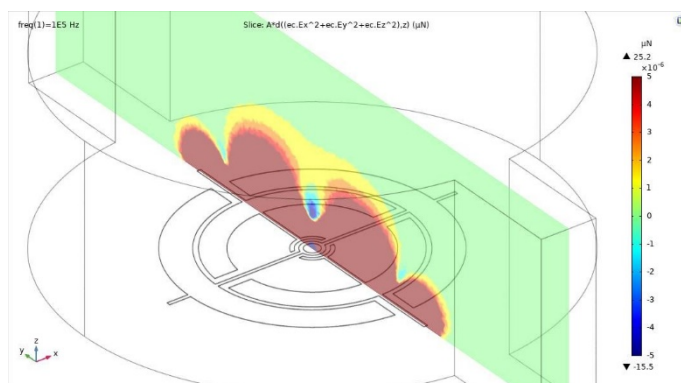


Fig. F.1. Negative F_{DEP} (z component magnitude). Cross-section view along the input-output channels.

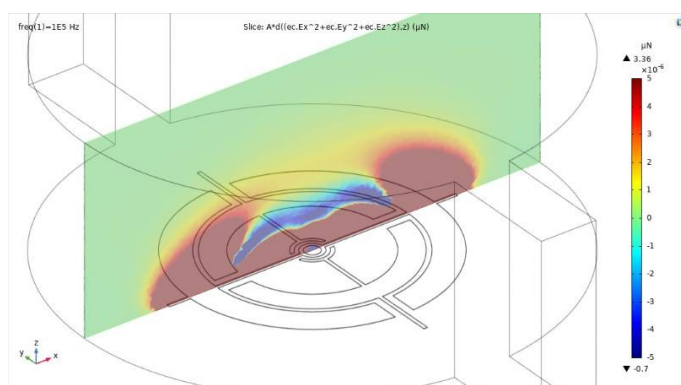


Fig. F.2 Negative F_{DEP} (z component magnitude). Cross-section view across the input-output channels.

C1 - positive DEP

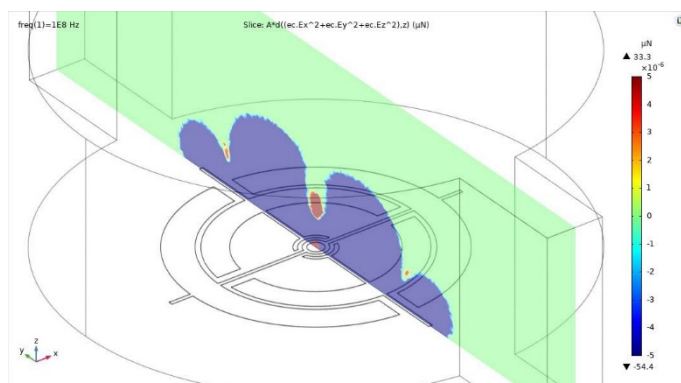


Fig. F.3 Positive F_{DEP} (z component magnitude). Cross-section view along the input-output channels.

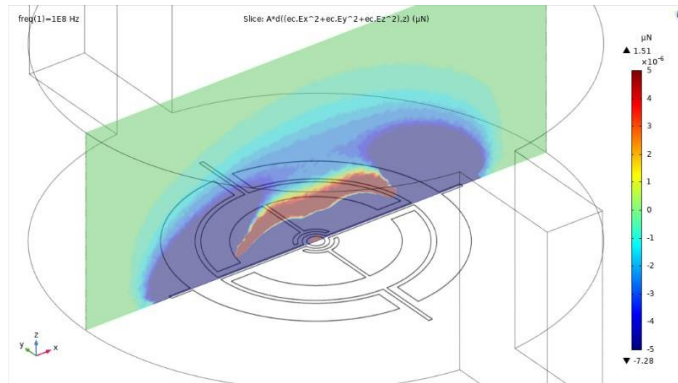


Fig. F.4 Positive F_{DEP} (z component magnitude). Cross-section view across the input-output channels

C2 - negative DEP

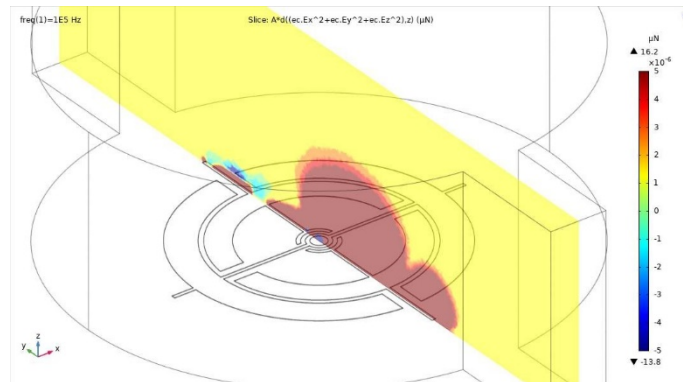


Fig. F.5 Negative F_{DEP} (z component magnitude). Cross-section view along the input-output channels

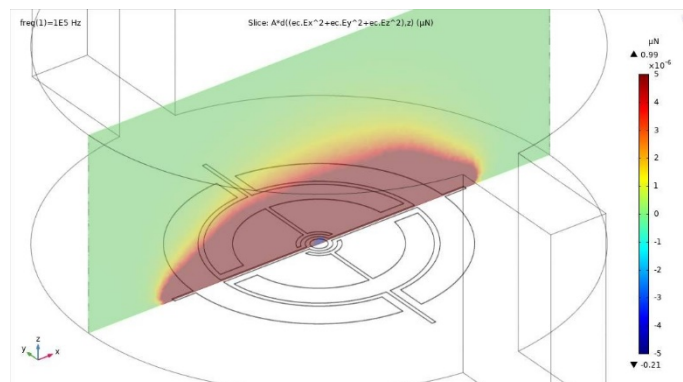


Fig. F.6 Negative F_{DEP} (z component magnitude). Cross-section view across the input-output channels

C2- positive DEP

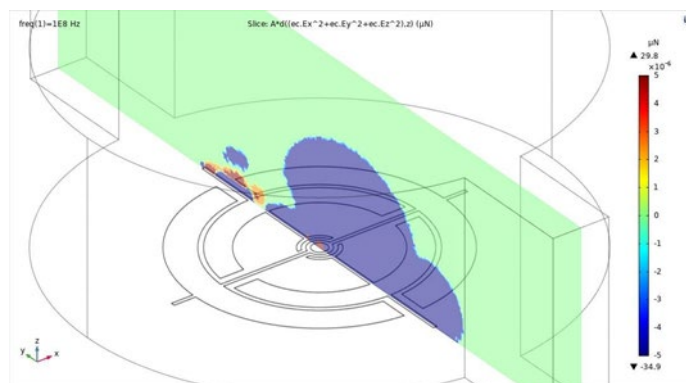


Fig. F.7 Positive F_{DEP} (z component magnitude). Cross-section view along the input-output channels.

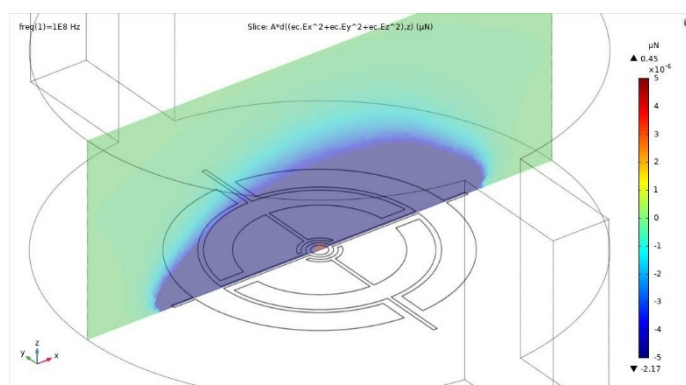


Fig. F.8 Positive F_{DEP} (z component magnitude). Cross-section view across the input-output channels.

C4 - negative DEP

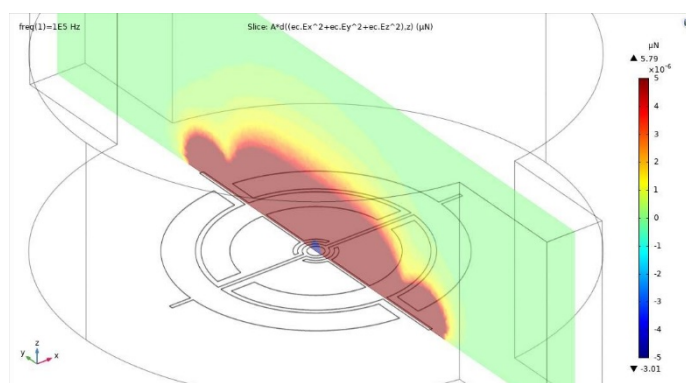


Fig. F.9 Negative F_{DEP} (z component magnitude). Cross-section view along the input-output channels.

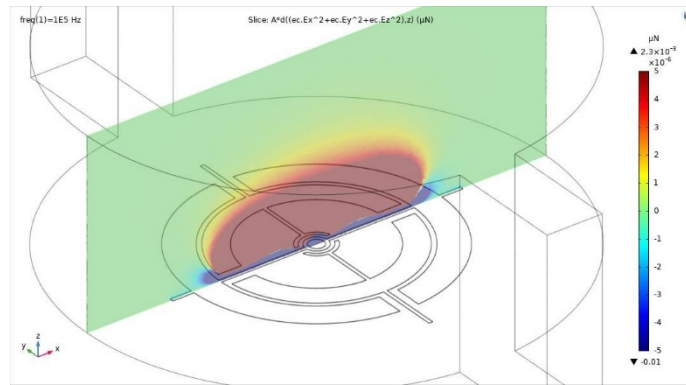


Fig. F.10 Negative F_{DEP} (z component magnitude). Cross-section view across the input-output channels.

C4- positive DEP

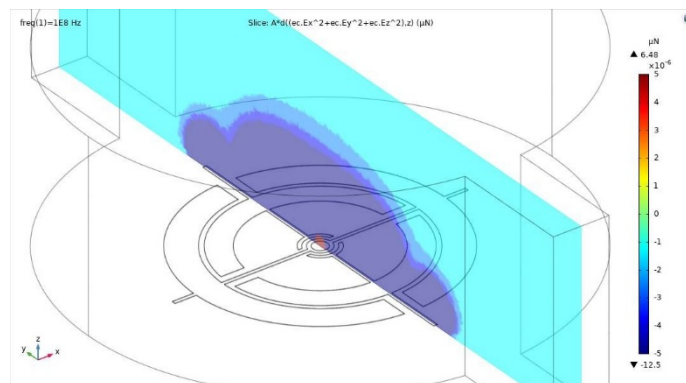


Fig. F.11 Positive F_{DEP} (z component magnitude). Cross-section view along the input-output channels.

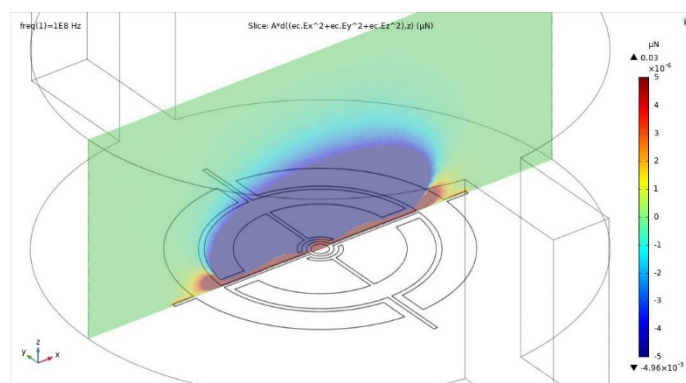


Fig. F.12 Positive F_{DEP} (z component magnitude). Cross-section view across the input-output channels.

Annex G

Function Generator

Model Enertec - Schlumberger 4433



Generator Specifications:

Output Generator → System Input Specification

Voltage: 2-30 V

Signal type: Sinusoidal

Frequency: 100 kHz – 20 MHz

Articles

Lensless microscopy platform for single cell and tissue visualization

R. Corman, W. Boutu, A. Campalans, P. Radicella, J. Duarte, M. Kholodtsova, L. Bally-Cuif, N. Dray, F. Harms, G. Dovillaire, S. Bucourt, and H. Merdji

Biomed. Opt. Express 11, 2806-2817 (2020)

<https://doi.org/10.1364/BOE.380193>

Bibliography

- ¹ P. Mazzarello, “A Unifying Concept: The History of Cell Theory,” *Nature Cell Biology* 1, no. 1 (May 1, 1999): E13–15, <https://doi.org/10.1038/8964>.
- ² O. Shimomura, “The Discovery of Aequorin and Green Fluorescent Protein,” *Journal of Microscopy* 217, no. 1 (2005): 3–15, <https://doi.org/10.1111/j.0022-2720.2005.01441.x>.
- ³ R.Y. Tsien, “Building and Breeding Molecules to Spy on Cells and Tumors,” *FEBS Letters*, Molecular Mechanisms of Biological Systems. 130th Nobel Symposium, 579, no. 4 (February 7, 2005): 927–32, <https://doi.org/10.1016/j.febslet.2004.11.025>.
- ⁴ C. Cremer and BR. Masters, “Resolution Enhancement Techniques in Microscopy,” *The European Physical Journal H* 38, no. 3 (April 1, 2013): 281–344, <https://doi.org/10.1140/epjh/e2012-20060-1>.
- ⁵ L. Rayleigh F.R.S, “XXXI. Investigations in Optics, with Special Reference to the Spectroscope,” *The London, Edinburgh, and Dublin Philosophical Magazine and Journal of Science* 8, no. 49 (October 1, 1879): 261–74, <https://doi.org/10.1080/14786447908639684>.
- ⁶ “Introductory Confocal Concepts,” Nikon’s MicroscopyU, accessed June 27, 2019, <https://www.microscopyu.com/techniques/confocal/introductory-confocal-concepts>.
- ⁷ A.H. J. Kim *et al.*, “New Approaches in Renal Microscopy: Volumetric Imaging and Superresolution Microscopy.,” *Current Opinion in Nephrology and Hypertension* 25, no. 3 (2016): 159–67, <https://doi.org/10.1097/MNH.0000000000000220>.
- ⁸ J. Jonkman *et al.*, “Chapter 7 - Quantitative Confocal Microscopy: Beyond a Pretty Picture,” in *Methods in Cell Biology*, ed. Jennifer C. Waters and Torsten Wittman, vol. 123, Quantitative Imaging in Cell Biology (Academic Press, 2014), 113–34, <https://doi.org/10.1016/B978-0-12-420138-5.00007-0>.
- ⁹ F. Göttfert *et al.*, “Strong Signal Increase in STED Fluorescence Microscopy by Imaging Regions of Subdiffraction Extent,” *Proceedings of the National Academy of Sciences* 114, no. 9 (February 28, 2017): 2125–30, <https://doi.org/10.1073/pnas.1621495114>.
- ¹⁰ H. Blom and H. Brismar, “STED Microscopy: Increased Resolution for Medical Research?,” *Journal of Internal Medicine* 276, no. 6 (2014): 560–78, <https://doi.org/10.1111/joim.12278>.
- ¹¹ G. Vicidomini *et al.* “STED Super-Resolved Microscopy,” *Nature Methods* 15, no. 3 (March 2018): 173–82, <https://doi.org/10.1038/nmeth.4593>.
- ¹² L. Schermelleh *et al.*, “A Guide to Super-Resolution Fluorescence Microscopy,” *The Journal of Cell Biology* 190, no. 2 (July 26, 2010): 165–75, <https://doi.org/10.1083/jcb.201002018>.
-

-
- ¹³ T. Warwick *et al.*, “Soft X-Ray Spectromicroscopy Development for Materials Science at the Advanced Light Source,” *Journal of Electron Spectroscopy and Related Phenomena* 84, no. 1 (March 1, 1997): 85–98, [https://doi.org/10.1016/S0368-2048\(97\)00026-1](https://doi.org/10.1016/S0368-2048(97)00026-1).
- ¹⁴ R. Belkhou *et al.*, “HERMES: A Soft X-Ray Beamline Dedicated to X-Ray Microscopy,” *Journal of Synchrotron Radiation* 22, no. 4 (July 1, 2015): 968–79, <https://doi.org/10.1107/S1600577515007778>.
- ¹⁵ E. Fogelqvist *et al.*, “Laboratory Cryo X-Ray Microscopy for 3D Cell Imaging,” *Scientific Reports* 7, no. 1 (October 18, 2017): 1–8, <https://doi.org/10.1038/s41598-017-13538-2>.
- ¹⁶ R.W. Langhans and T.W. Tibbitts, “Radiation,” in *Plant Growth Chamber Handbook*, vol. 138, 340 (Iowa Agriculture and Home Economics Experiment Station Special Report No. 99, 1997), <https://www.controlledenvironments.org/growth-chamber-handbook/>.
- ¹⁷ “Lensless Coherence Diffraction Imaging – Application Note | LOT-QuantumDesign,” accessed July 11, 2019, <https://lot-qd.be/en/news/product-application-news-spectrum/international-spectrum-e21/lensless-coherence-diffraction-imaging-application-note/>.
- ¹⁸ K. Wakonig *et al.*, “X-Ray Fourier Ptychography,” *Science Advances* 5, no. 2 (February 1, 2019): eaav0282, <https://doi.org/10.1126/sciadv.aav0282>.
- ¹⁹ Y. S. G. Nashed *et al.*, “Distributed Automatic Differentiation for Ptychography,” *Procedia Computer Science*, International Conference on Computational Science, ICCS 2017, 12-14 June 2017, Zurich, Switzerland, 108 (January 1, 2017): 404–14, <https://doi.org/10.1016/j.procs.2017.05.101>.
- ²⁰ J. Miao *et al.*, “Imaging Whole Escherichia Coli Bacteria by Using Single-Particle x-Ray Diffraction,” *Proceedings of the National Academy of Sciences* 100, no. 1 (January 7, 2003): 110–12, <https://doi.org/10.1073/pnas.232691299>.
- ²¹ “Three-Dimensional Mass Density Mapping of Cellular Ultrastructure by Ptychographic X-Ray Nanotomography | Elsevier Enhanced Reader,” accessed September 2, 2019, <https://doi.org/10.1016/j.jsb.2015.10.008>.
- ²² J. Miao *et al.*, “Extending the Methodology of X-Ray Crystallography to Allow Imaging of Micrometre-Sized Non-Crystalline Specimens,” *Nature* 400, no. 6742 (July 1999): 342–44, <https://doi.org/10.1038/22498>.
- ²³ H. N. Chapman *et al.*, “Femtosecond Diffractive Imaging with a Soft-X-Ray Free-Electron Laser,” *Nature Physics* 2, no. 12 (December 2006): 839–43, <https://doi.org/10.1038/nphys461>.
- ²⁴ R. L. Sandberg *et al.*, “Lensless Diffractive Imaging Using Tabletop Coherent High-Harmonic Soft-X-Ray Beams,” *Physical Review Letters* 99, no. 9 (August 29, 2007): 098103, <https://doi.org/10.1103/PhysRevLett.99.098103>.
-

-
- ²⁵ A. Ravasio *et al.*, “Single-Shot Diffractive Imaging with a Table-Top Femtosecond Soft X-Ray Laser-Harmonics Source,” *Physical Review Letters* 103, no. 2 (July 8, 2009): 028104, <https://doi.org/10.1103/PhysRevLett.103.028104>.
- ²⁶ D. Gauthier *et al.*, “Single-Shot Femtosecond X-Ray Holography Using Extended References,” *Physical Review Letters* 105, no. 9 (August 24, 2010): 093901, <https://doi.org/10.1103/PhysRevLett.105.093901>.
- ²⁷ X. Ge *et al.*, “Impact of Wave Front and Coherence Optimization in Coherent Diffractive Imaging,” *Optics Express* 21, no. 9 (May 6, 2013): 11441–47, <https://doi.org/10.1364/OE.21.011441>.
- ²⁸ B. Vodungbo *et al.*, “Laser-Induced Ultrafast Demagnetization in the Presence of a Nanoscale Magnetic Domain Network,” *Nature Communications* 3, no. 1 (August 14, 2012): 1–6, <https://doi.org/10.1038/ncomms2007>.
- ²⁹ X. Ge *et al.*, “Sub-100 Nanometer Lensless Probing of Co/Pd Magnetic Nanodomains Using a Table-Top Femtosecond Soft X-Ray Harmonic Source,” *Journal of Modern Optics* 60, no. 17 (October 7, 2013): 1475–83, <https://doi.org/10.1080/09500340.2013.839058>.
- ³⁰ M. Ducouso *et al.*, “Single-Shot Studies of a Co/Pd Thin Film’s Magnetic Nano-Domain Structure Using Ultrafast x-Ray Scattering,” *Laser Physics* 24, no. 2 (January 2014): 025301, <https://doi.org/10.1088/1054-660X/24/2/025301>.
- ³¹ M. Zürch *et al.*, “Real-Time and Sub-Wavelength Ultrafast Coherent Diffraction Imaging in the Extreme Ultraviolet,” *Scientific Reports* 4, no. 1 (December 8, 2014): 1–5, <https://doi.org/10.1038/srep07356>.
- ³² G. O. Williams *et al.*, “Fourier Transform Holography with High Harmonic Spectra for Attosecond Imaging Applications,” *Optics Letters* 40, no. 13 (July 1, 2015): 3205–8, <https://doi.org/10.1364/OL.40.003205>.
- ³³ J. Huijts *et al.*, “Broadband Coherent Diffraction for Single-Shot Attosecond Imaging,” *ArXiv:1909.11345 [Physics]*, September 25, 2019, <http://arxiv.org/abs/1909.11345>.
- ³⁴ J. Duarte *et al.*, “Computed Stereo Lensless X-Ray Imaging,” *Nature Photonics* 13, no. 7 (July 2019): 449–53, <https://doi.org/10.1038/s41566-019-0419-1>.
- ³⁵ E. N. Leith and J. Upatnieks, “Reconstructed Wavefronts and Communication Theory,” *JOSA* 52, A, 1123-1130(1962). <https://doi.org/10.1364/JOSA.52.001123>
- ³⁶ M. Bartels *et al.*, “Low-Dose Three-Dimensional Hard x-Ray Imaging of Bacterial Cells,” *Optical Nanoscopy* 1, no. 1 (November 30, 2012): 10, <https://doi.org/10.1186/2192-2853-1-10>.
- ³⁷ T. Gorkhovor *et al.*, “Femtosecond X-Ray Fourier Holography Imaging of Free-Flying Nanoparticles,” *Nature Photonics* 12, no. 3 (March 2018): 150–53, <https://doi.org/10.1038/s41566-018-0110-y>.
-

-
- ³⁸ A. Ozcan and E. McLeod, “Lensless Imaging and Sensing,” *Annual Review of Biomedical Engineering* 18, no. 1 (July 11, 2016): 77–102, <https://doi.org/10.1146/annurev-bioeng-092515-010849>.
- ³⁹ D. Donnarumma *et al.*, “4D Holographic Microscopy of Zebrafish Larvae Microcirculation,” *Optics Express* 24, no. 23 (November 2016): 26887–900, <https://doi.org/10.1364/OE.24.026887>.
- ⁴⁰ A. Berdeu *et al.*, “Lens-Free Microscopy for 3D + Time Acquisitions of 3D Cell Culture,” *Scientific Reports* 8, no. 1 (October 31, 2018): 16135, <https://doi.org/10.1038/s41598-018-34253-6>.
- ⁴¹ R. Delacroix *et al.*, “Cerebrospinal Fluid Lens-Free Microscopy: A New Tool for the Laboratory Diagnosis of Meningitis,” *Scientific Reports* 7 (January 3, 2017): 39893, <https://doi.org/10.1038/srep39893>.
- ⁴² N. Anthony *et al.*, “Ptychographic Imaging of NaD1 Induced Yeast Cell Death,” *Biomedical Optics Express* 10, no. 10 (October 1, 2019): 4964–74, <https://doi.org/10.1364/BOE.10.004964>.
- ⁴³ A. Ali *et al.*, “Quantitative Live Single-Cell Mass Spectrometry with Spatial Evaluation by Three-Dimensional Holographic and Tomographic Laser Microscopy,” *Analytical Sciences* 32, no. 2 (2016): 125–27, <https://doi.org/10.2116/analsci.32.125>.
- ⁴⁴ A. Yakimovich *et al.*, “Label-Free Digital Holo-Tomographic Microscopy Reveals Virus-Induced Cytopathic Effects in Live Cells,” *MSphere* 3, no. 6 (December 26, 2018): e00599-18, <https://doi.org/10.1128/mSphereDirect.00599-18>.
- ⁴⁵ G. Pinget *et al.*, “Impact of the Food Additive Titanium Dioxide (E171) on Gut Microbiota-Host Interaction,” *Frontiers in Nutrition* 6 (2019), <https://doi.org/10.3389/fnut.2019.00057>.
- ⁴⁶ L.M.R. Silva *et al.*, “Besnoitia Besnoiti Infection Alters Both Endogenous Cholesterol de Novo Synthesis and Exogenous LDL Uptake in Host Endothelial Cells | Scientific Reports,” accessed September 6, 2019, <https://www.nature.com/articles/s41598-019-43153-2>.
- ⁴⁷ D. Gabor, “A New Microscopic Principle,” *Nature* 161, no. 4098 (May 1948): 777–78, <https://doi.org/10.1038/161777a0>.
- ⁴⁸ E.N. Leith and J. Upatnieks, “Wavefront Reconstruction with Continuous-Tone Objects*,” *JOSA* 53, no. 12 (December 1, 1963): 1377–81, <https://doi.org/10.1364/JOSA.53.001377>.
- ⁴⁹ H. J. Kreuzer and R. A. Pawlitzek, “Digital In-Line Holography,” *Europhysics News* 34, no. 2: 62–65, accessed January 10, 2018, <https://doi.org/10.1051/epn:2003206>.
- ⁵⁰ C.B. Giuliano *et al.*, “Digital Inline Holographic Microscopy (DIH) of Weakly-Scattering Subjects,” *Journal of Visualized Experiments: JoVE*, no. 84 (February 8, 2014), <https://doi.org/10.3791/50488>.
-

-
- ⁵¹ W. Xu *et al.*, “Digital In-Line Holography for Biological Applications,” *Proceedings of the National Academy of Sciences of the United States of America* 98, no. 20 (September 25, 2001): 11301–5, <https://doi.org/10.1073/pnas.191361398>.
- ⁵² T.M. Kreis and W.P. O. Jueptner, “Suppression of the Dc Term in Digital Holography,” *Optical Engineering* 36, no. 8 (August 1, 1997): 2357–60, <https://doi.org/10.1117/1.601426>.
- ⁵³ D. Kim and B. Javidi, “Distortion-Tolerant 3-D Object Recognition by Using Single Exposure on-Axis Digital Holography,” *Optics Express* 12, no. 22 (November 1, 2004): 5539–48, <https://doi.org/10.1364/OPEX.12.005539>.
- ⁵⁴ U. Schnars and W. Jüptner, “Direct Recording of Holograms by a CCD Target and Numerical Reconstruction,” *Applied Optics* 33, no. 2 (January 10, 1994): 179–81, <https://doi.org/10.1364/AO.33.000179>.
- ⁵⁵ Y. Zhang *et al.*, “Elimination of Zero-Order Diffraction in Digital off-Axis Holography,” *Optics Communications* 240, no. 4 (October 15, 2004): 261–67, <https://doi.org/10.1016/j.optcom.2004.06.040>.
- ⁵⁶ L. Xu *et al.*, “Properties of Digital Holography Based on In-Line Configuration,” *Optical Engineering* 39, no. 12 (December 1, 2000): 3214–19, <https://doi.org/10.1117/1.1327503>.
- ⁵⁷ J. Samaan, “Étude et applications de l’imagerie sans lentille par diffraction cohérente” (Ph.D. Thesis, Université Paris-Saclay, 2016), <https://www.theses.fr/2016SACLS557>.
- ⁵⁸ T. E. Agbana *et al.*, “Aliasing, Coherence, and Resolution in a Lensless Holographic Microscope,” *Optics Letters* 42, no. 12 (June 15, 2017): 2271–74, <https://doi.org/10.1364/OL.42.002271>.
- ⁵⁹ A. Pogany *et al.*, “Contrast and Resolution in Imaging with a Microfocus X-Ray Source,” *Review of Scientific Instruments* 68, no. 7 (July 1, 1997): 2774–82, <https://doi.org/10.1063/1.1148194>.
- ⁶⁰ Joseph W. Goodman, *Introduction to Fourier Optics* (Roberts and Company Publishers, 2005).
- ⁶¹ S. K. Jericho *et al.*, “Submersible Digital In-Line Holographic Microscope,” *Review of Scientific Instruments* 77, no. 4 (April 1, 2006): 043706, <https://doi.org/10.1063/1.2193827>.
- ⁶² T. Latychevskaia and H.-W. Fink, “Practical Algorithms for Simulation and Reconstruction of Digital In-Line Holograms,” *Applied Optics* 59, no. 9 (2015): 2424–2434.
- ⁶³ T. Latychevskaia and H.-W. Fink, “Inverted Gabor Holography Principle for Tailoring Arbitrary Shaped Three-Dimensional Beams,” *Scientific Reports* 6 (May 20, 2016): 26312, <https://doi.org/10.1038/srep26312>.
- ⁶⁴ H. Zhang *et al.*, “Object Plane Detection and Phase Retrieval from Single-Shot Holograms Using Multi-Wavelength in-Line Holography,” *Applied Optics* 57, no. 33 (November 20, 2018): 9855–62, <https://doi.org/10.1364/AO.57.009855>.
-

-
- ⁶⁵ T.-C. Poon *et al.*, “Twin-Image Elimination Experiments for Three-Dimensional Images in Optical Scanning Holography,” *Optics Letters* 25, no. 4 (February 15, 2000): 215–17, <https://doi.org/10.1364/OL.25.000215>.
- ⁶⁶ D. Attwood, *Soft X-Rays and Extreme Ultraviolet Radiation: Principles and Applications* (Cambridge: Cambridge University Press, 1999), <https://doi.org/10.1017/CBO9781139164429>.
- ⁶⁷ D. Loerke *et al.*, “Quantitative Imaging of Epithelial Cell Scattering Identifies Specific Inhibitors of Cell Motility and Cell-Cell Dissociation,” *Science Signaling* 5, no. 231 (July 3, 2012): rs5–rs5, <https://doi.org/10.1126/scisignal.2002677>.
- ⁶⁸ M. Burute *et al.*, “Polarity Reversal by Centrosome Repositioning Primes Cell Scattering during Epithelial-to-Mesenchymal Transition,” *Developmental Cell* 40, no. 2 (January 23, 2017): 168–84, <https://doi.org/10.1016/j.devcel.2016.12.004>.
- ⁶⁹ “Zebrafish Development - Embryology,” accessed October 17, 2019, https://embryology.med.unsw.edu.au/embryology/index.php/Zebrafish_Development.
- ⁷⁰ J. Gao *et al.*, “In Vivo Imaging and Quantitative Analysis of Zebrafish Embryos by Digital Holographic Microscopy,” *Biomedical Optics Express* 3, no. 10 (October 1, 2012): 2623–35, <https://doi.org/10.1364/BOE.3.002623>.
- ⁷¹ W. Choi *et al.*, “Tomographic Phase Microscopy,” *Nature Methods* 4, no. 9 (September 2007): 717–19, <https://doi.org/10.1038/nmeth1078>.
- ⁷² K. Haseda *et al.*, “Significant Correlation between Refractive Index and Activity of Mitochondria: Single Mitochondrion Study,” *Biomedical Optics Express* 6, no. 3 (March 1, 2015): 859–69, <https://doi.org/10.1364/BOE.6.000859>.
- ⁷³ J. D. Wilson *et al.*, “Index-of-Refraction-Dependent Subcellular Light Scattering Observed with Organelle-Specific Dyes,” *Journal of Biomedical Optics* 12, no. 1 (January 2007): 014010, <https://doi.org/10.1117/1.2437765>.
- ⁷⁴ M. Kohl *et al.*, “Influence of Glucose Concentration on Light Scattering in Tissue-Simulating Phantoms,” *Optics Letters* 19, no. 24 (December 15, 1994): 2170–72, <https://doi.org/10.1364/OL.19.002170>.
- ⁷⁵ J. Vörös, “The Density and Refractive Index of Adsorbing Protein Layers,” *Biophysical Journal* 87, no. 1 (July 2004): 553–61, <https://doi.org/10.1529/biophysj.103.030072>.
- ⁷⁶ V. Backman *et al.*, “Detection of Preinvasive Cancer Cells,” *Nature* 406, no. 6791 (July 2000): 35–36, <https://doi.org/10.1038/35017638>.
- ⁷⁷ B. Koch *et al.*, “Confinement and Deformation of Single Cells and Their Nuclei Inside Size-Adapted Microtubes,” *Advanced Healthcare Materials* 3, no. 11 (November 2014): 1753–58, <https://doi.org/10.1002/adhm.201300678>.
-

-
- ⁷⁸ N. Schuergers *et al.*, “Cyanobacteria Use Micro-Optics to Sense Light Direction,” *ELife* 5, accessed September 25, 2018, <https://doi.org/10.7554/eLife.12620>.
- ⁷⁹ D. A. Hodgson, “The Ecology of Cyanobacteria: Their Diversity in Time and Space, Edited by B. A. Whitton and M. Potts,” *Journal of Paleolimnology* 28, no. 3 (September 1, 2002): 383–84, <https://doi.org/10.1023/A:1021694308518>.
- ⁸⁰ H. Čelešnik *et al.*, “Biosafety of Biotechnologically Important Microalgae: Intrinsic Suicide Switch Implementation in Cyanobacterium *Synechocystis* PCC 6803,” *Biology Open* 5, no. 4 (April 15, 2016): 519, <https://doi.org/10.1242/bio.017129>.
- ⁸¹ M. Herdman, S. F. Delaney, and N. G. Carr, “A New Medium for the Isolation and Growth of Auxotrophic Mutants of the Blue-Green Alga *Anacystis Nidulans*,” *Microbiology*, 79, no. 2 (1973): 233–37, <https://doi.org/10.1099/00221287-79-2-233>.
- ⁸² D.-P. Häder, “Signal Perception and Amplification in Photoresponses of Cyanobacteria,” *Biophysical Chemistry* 29, no. 1 (February 1, 1988): 155–59, [https://doi.org/10.1016/0301-4622\(88\)87035-2](https://doi.org/10.1016/0301-4622(88)87035-2).
- ⁸³ A. Wilde and C. W. Mullineaux, “Motility in Cyanobacteria: Polysaccharide Tracks and Type IV Pilus Motors,” *Molecular Microbiology* 98, no. 6 (December 1, 2015): 998–1001, <https://doi.org/10.1111/mmi.13242>.
- ⁸⁴ M. Guizar-Sicairos *et al.*, “Phase Tomography from X-Ray Coherent Diffractive Imaging Projections,” *Optics Express* 19, no. 22 (October 24, 2011): 21345–57, <https://doi.org/10.1364/OE.19.021345>.
- ⁸⁵ Y. Yang and Bo-Seon Kang, “Determination of Depth-of-Focus in Lensless in-Line Digital Particle Holography,” *Optik* 122, no. 17 (September 1, 2011): 1552–57, <https://doi.org/10.1016/j.ijleo.2010.05.038>.
- ⁸⁶ C. Demant *et al.*, *Industrial Image Processing: Visual Quality Control in Manufacturing* (Berlin Heidelberg: Springer-Verlag, 1999), <https://www.springer.com/gp/book/9783642636424>.
- ⁸⁷ Y. Zhang *et al.*, “3D Imaging of Optically Cleared Tissue Using a Simplified CLARITY Method and On-Chip Microscopy,” *Science Advances* 3, no. 8 (August 1, 2017): e1700553, <https://doi.org/10.1126/sciadv.1700553>.
- ⁸⁸ Y. Wu *et al.*, “Extended Depth-of-Field in Holographic Imaging Using Deep-Learning-Based Autofocusing and Phase Recovery,” *Optica* 5, no. 6 (June 20, 2018): 704–10, <https://doi.org/10.1364/OPTICA.5.000704>.
- ⁸⁹ W.F. Schlotter, “Lensless Fourier Transform Holography with Soft X-Rays” (Ph.D. Thesis, Stanford University, 2007), <https://www-ssrl.slac.stanford.edu/stohr/Schlotter-Thesis.pdf>.
- ⁹⁰ S. Movahed and D. Li, “Microfluidics Cell Electroporation,” *Microfluidics and Nanofluidics* 10, no. 4 (April 1, 2011): 703–34, <https://doi.org/10.1007/s10404-010-0716-y>.
-

-
- ⁹¹ W.-C. Yang *et al.*, “Detection of Prion Protein Using a Capillary Electrophoresis-Based Competitive Immunoassay with Laser-Induced Fluorescence Detection and Cyclodextrin-Aided Separation,” *Electrophoresis* 26, no. 9 (May 2005): 1751–59, <https://doi.org/10.1002/elps.200410202>.
- ⁹² W. Cheng *et al.*, “Microfluidic Cell Arrays for Metabolic Monitoring of Stimulated Cardiomyocytes,” *Electrophoresis* 31, no. 8 (2010): 1405–13, <https://doi.org/10.1002/elps.200900579>.
- ⁹³ N. Bao *et al.*, “Microfluidic Electroporation of Tumor and Blood Cells: Observation of Nucleus Expansion and Implications on Selective Analysis and Purging of Circulating Tumor Cells,” *Integrative Biology: Quantitative Biosciences from Nano to Macro* 2, no. 2–3 (March 2010): 113–20, <https://doi.org/10.1039/b919820b>.
- ⁹⁴ Y. Kang and D. Li, “Electrokinetic Motion of Particles and Cells in Microchannels,” *Microfluidics and Nanofluidics* 6, no. 4 (April 1, 2009): 431–60, <https://doi.org/10.1007/s10404-009-0408-7>.
- ⁹⁵ J. Park *et al.*, “An Efficient Cell Separation System Using 3D-Asymmetric Microelectrodes,” *Lab on a Chip - Miniaturisation for Chemistry and Biology* 5, no. 11 (November 1, 2005): 1264–70, <https://doi.org/10.1039/b506803g>.
- ⁹⁶ D. Li, ed., *Encyclopedia of Microfluidics and Nanofluidics*, 2nd ed. (New York: Springer-Verlag, 2015), <https://www.springer.com/gp/book/9781461454885>.
- ⁹⁷ Z. Zou, S. Lee, and C. H. Ahn, “A Polymer Microfluidic Chip With Interdigitated Electrode Arrays for Simultaneous Dielectrophoretic Manipulation and Impedimetric Detection of Microparticles,” *IEEE Sensors Journal* 8, no. 5 (May 2008): 527–35, <https://doi.org/10.1109/JSEN.2008.918907>.
- ⁹⁸ M. Borgatti *et al.*, “Dielectrophoresis-Based ‘Lab-on-a-Chip’ Devices for Programmable Binding of Microspheres to Target Cells,” *International Journal of Oncology* 27, no. 6 (December 2005): 1559–66.
- ⁹⁹ S. Park and A. Beskok, “Alternating Current Electrokinetic Motion of Colloidal Particles on Interdigitated Microelectrodes,” *Analytical Chemistry* 80, no. 8 (April 15, 2008): 2832–41, <https://doi.org/10.1021/ac7024859>.
- ¹⁰⁰ V. Gauthier *et al.*, “Analytical Formulation of the Electric Field Induced by Electrode Arrays: Towards Automated Dielectrophoretic Cell Sorting,” *Micromachines* 8, no. 8 (August 17, 2017), <https://doi.org/10.3390/mi8080253>.
- ¹⁰¹ J. Kentsch *et al.*, “Microdevices for Separation, Accumulation, and Analysis of Biological Micro- and Nanoparticles,” *IEE Proceedings. Nanobiotechnology* 150, no. 2 (November 2003): 82–89, <https://doi.org/10.1049/ip-nbt:20031127>.
- ¹⁰² M. Dürr *et al.*, “Microdevices for Manipulation and Accumulation of Micro- and Nanoparticles by Dielectrophoresis,” *Electrophoresis* 24, no. 4 (February 2003): 722–31, <https://doi.org/10.1002/elps.200390087>.

-
- ¹⁰³ H.-Y. Huang, *et al.*, “Dielectrophoretic Microfluidic Device for in Vitro Fertilization,” *Micromachines* 9, no. 3 (March 20, 2018), <https://doi.org/10.3390/mi9030135>.
- ¹⁰⁴ A. Valero *et al.*, “Gene Transfer and Protein Dynamics in Stem Cells Using Single Cell Electroporation in a Microfluidic Device,” *Lab on a Chip* 8, no. 1 (December 19, 2007): 62–67, <https://doi.org/10.1039/B713420G>.
- ¹⁰⁵ T. Suzuki *et al.*, “High Throughput Cell Electroporation Array Fabricated by Single-Mask Inclined UV Lithography Exposure and Oxygen Plasma Etching,” in *TRANSDUCERS 2007 - 2007 International Solid-State Sensors, Actuators and Microsystems Conference*, 2007, 687–90, <https://doi.org/10.1109/SENSOR.2007.4300223>.
- ¹⁰⁶ HY. Wang, *et al.*, “A Microfluidic Flow-through Device for High Throughput Electrical Lysis of Bacterial Cells Based on Continuous Dc Voltage,” *Biosensors & Bioelectronics* 22, no. 5 (December 15, 2006): 582–88, <https://doi.org/10.1016/j.bios.2006.01.032>.
- ¹⁰⁷ Z. Fei *et al.*, “Micronozzle Array Enhanced Sandwich Electroporation of Embryonic Stem Cells,” *Analytical Chemistry* 82, no. 1 (January 1, 2010): 353–58, <https://doi.org/10.1021/ac902041h>.
- ¹⁰⁸ N. G. Green, A. Ramos, and H. Morgan, “Ac Electrokinetics: A Survey of Sub-Micrometre Particle Dynamics,” *Journal of Physics D: Applied Physics* 33, no. 6 (March 2000): 632–641, <https://doi.org/10.1088/0022-3727/33/6/308>.
- ¹⁰⁹ D. Cukjati *et al.*, “Real Time Electroporation Control for Accurate and Safe in Vivo Non-Viral Gene Therapy,” *Bioelectrochemistry (Amsterdam, Netherlands)* 70, no. 2 (May 2007): 501–7, <https://doi.org/10.1016/j.bioelechem.2006.11.001>.
- ¹¹⁰ T. Geng *et al.*, “Flow-through Electroporation Based on Constant Voltage for Large-Volume Transfection of Cells,” *Journal of Controlled Release: Official Journal of the Controlled Release Society* 144, no. 1 (May 21, 2010): 91–100, <https://doi.org/10.1016/j.jconrel.2010.01.030>.
- ¹¹¹ N. Ikeda *et al.*, “On-Chip Single-Cell Lysis for Extracting Intracellular Material,” *Japanese Journal of Applied Physics* 46, no. 9S (September 20, 2007): 6410, <https://doi.org/10.1143/JJAP.46.6410>.
- ¹¹² T. Geng and C. Lu, “Microfluidic Electroporation for Cellular Analysis and Delivery,” *Lab on a Chip* 13, no. 19 (2013): 3803–21, <https://doi.org/10.1039/C3LC50566A>.
- ¹¹³ H. Lu *et al.*, “A Microfluidic Electroporation Device for Cell Lysis,” *Lab on a Chip* 5, no. 1 (January 2005): 23–29, <https://doi.org/10.1039/b406205a>.
- ¹¹⁴ N. Bao *et al.*, “Microfluidic Electroporation of Tumor and Blood Cells: Observation of Nucleus Expansion and Implications on Selective Analysis and Purging of Circulating Tumor Cells,” *Integrative Biology* 2, no. 2–3 (March 5, 2010): 113–20, <https://doi.org/10.1039/B919820B>.
-

¹¹⁵ Z. Fei *et al.*, “Gene Transfection of Mammalian Cells Using Membrane Sandwich Electroporation,” *Analytical Chemistry* 79, no. 15 (August 1, 2007): 5719–22, <https://doi.org/10.1021/ac070482y>.

¹¹⁶ D. Malleo *et al.*, “Continuous Differential Impedance Spectroscopy of Single Cells,” *Microfluidics and Nanofluidics* 9, no. 2–3 (August 2010): 191–98, <https://doi.org/10.1007/s10404-009-0534-2>.

¹¹⁷ M.G. Moisescu *et al.*, “Changes of Cell Electrical Parameters Induced by Electroporation. A Dielectrophoresis Study,” *Biochimica et Biophysica Acta (BBA) - Biomembranes* 1828, no. 2 (February 1, 2013): 365–72, <https://doi.org/10.1016/j.bbamem.2012.08.030>.

¹¹⁸ Fei *et al.*, “Micronozzle Array Enhanced Sandwich Electroporation of Embryonic Stem Cells.”

¹¹⁹ S. Lakshmanan *et al.*, “Physical Energy for Drug Delivery; Poration, Concentration and Activation,” *Advanced Drug Delivery Reviews* 0 (May 2014): 98–114, <https://doi.org/10.1016/j.addr.2013.05.010>.

¹²⁰ Y.Huang and B. Rubinsky, “Flow-through Micro-Electroporation Chip for High Efficiency Single-Cell Genetic Manipulation,” *Sensors and Actuators A: Physical*, Selected papers based on contributions revised from the Technical Digest of the 2002 Solid-State Sensors, Actuators and Microsystems workshop, 104, no. 3 (May 15, 2003), [https://doi.org/10.1016/S0924-4247\(03\)00050-5](https://doi.org/10.1016/S0924-4247(03)00050-5).

¹²¹ S. Moon *et al.*, “Integrating Microfluidics and Lensless Imaging for Point-of-Care Testing,” *Biosensors & Bioelectronics* 24, no. 11 (July 15, 2009): 3208–14, <https://doi.org/10.1016/j.bios.2009.03.037>.

¹²² M. Rothbauer *et al.*, “Recent Advances in Microfluidic Technologies for Cell-to-Cell Interaction Studies,” *Lab on a Chip* 18, no. 2 (January 16, 2018): 249–70, <https://doi.org/10.1039/C7LC00815E>.

¹²³ Tao Luo *et al.*, “Microfluidic Single-Cell Manipulation and Analysis: Methods and Applications,” *Micromachines* 10, no. 2 (February 1, 2019), <https://doi.org/10.3390/mi10020104>.

¹²⁴ M. L. Coluccio *et al.*, “Microfluidic Platforms for Cell Cultures and Investigations,” *Microelectronic Engineering* 208 (March 1, 2019): 14–28, <https://doi.org/10.1016/j.mee.2019.01.004>.

¹²⁵ PR. C. Gascoyne and J. Vykoukal, “Particle Separation by Dielectrophoresis,” *Electrophoresis* 23, no. 13 (July 2002): 1973–83, [https://doi.org/10.1002/1522-2683\(200207\)23:13<1973:AID-ELPS1973>3.0.CO;2-1](https://doi.org/10.1002/1522-2683(200207)23:13<1973:AID-ELPS1973>3.0.CO;2-1).

¹²⁶ H. Shafiee *et al.*, “Selective Isolation of Live/Dead Cells Using Contactless Dielectrophoresis (CDEP),” *Lab on a Chip* 10, no. 4 (February 21, 2010): 438–45, <https://doi.org/10.1039/b920590j>.

¹²⁷ FY. Chang *et al.*, “Electrical Properties of HeLa Cells Based on Scalable 3D Interdigital Electrode Array,” *Electroanalysis* 28, no. 5 (2016): 962–69, <https://doi.org/10.1002/elan.201500624>.

-
- ¹²⁸ S. Kinio and J. K. Mills, “Design of Electrode Topologies for Dielectrophoresis through the Use of Genetic Optimization with COMSOL Multiphysics,” in *2015 IEEE International Conference on Mechatronics and Automation (ICMA)*, 2015, 1019–24, <https://doi.org/10.1109/ICMA.2015.7237625>.
- ¹²⁹ K.-C. Lan and L.-S. Jang, “Integration of Single-Cell Trapping and Impedance Measurement Utilizing Microwell Electrodes,” *Biosensors and Bioelectronics* 26, no. 5 (January 15, 2011): 2025–31, <https://doi.org/10.1016/j.bios.2010.08.080>.
- ¹³⁰ M.-H. Wang and W.-H. Chang, “Effect of Electrode Shape on Impedance of Single HeLa Cell: A COMSOL Simulation,” *BioMed Research International* 2015 (2015), <https://doi.org/10.1155/2015/871603>.
- ¹³¹ R. Dulbecco and M. Vogt, “Plaque Formation and Isolation of Pure Lines with Poliomyelitis Viruses,” *The Journal of Experimental Medicine* 99, no. 2 (February 1954): 167–82, <https://doi.org/10.1084/jem.99.2.167>.
- ¹³² L.-S. Jang and M.-H. Wang, “Microfluidic Device for Cell Capture and Impedance Measurement,” *Biomedical Microdevices* 9, no. 5 (October 2007): 737–43, <https://doi.org/10.1007/s10544-007-9084-0>.
- ¹³³ C. M. Kurz *et al.*, “Chip-Based Impedance Measurement on Single Cells for Monitoring Sub-Toxic Effects on Cell Membranes,” *Biosensors & Bioelectronics* 26, no. 8 (April 15, 2011): 3405–12, <https://doi.org/10.1016/j.bios.2011.01.012>.
- ¹³⁴ S. Park *et al.*, “Individually Addressable Multi-Chamber Electroporation Platform with Dielectrophoresis and Alternating-Current-Electro-Osmosis Assisted Cell Positioning,” *Biomicrofluidics* 8, no. 2 (April 24, 2014), <https://doi.org/10.1063/1.4873439>.
- ¹³⁵ M. Molaei and J. Sheng, “Imaging Bacterial 3D Motion Using Digital In-Line Holographic Microscopy and Correlation-Based de-Noiseing Algorithm,” *Optics Express* 22, no. 26 (December 19, 2014): 32119–37, <https://doi.org/10.1364/OE.22.032119>.
- ¹³⁶ A. Robinson, *The Last Man Who Knew Everything: Thomas Young, the Anonymous Polymath Who Proved Newton Wrong, Explained How We See, Cured the Sick, and Deciphered the Rosetta Stone, among Other Feats of Genius* (New York: Pi Press, 2006), <http://archive.org/details/lastmanwhoknewev00robi>.
- ¹³⁷ A.L. Schawlow, “Laser Light,” *Scientific American* 219, no. 3 (1968): 120–39, <http://www.jstor.org/stable/24927508>.
- ¹³⁸ Y. Deng and D. Chu, “Coherence Properties of Different Light Sources and Their Effect on the Image Sharpness and Speckle of Holographic Displays,” *Scientific Reports* 7, no. 1 (July 19, 2017): 5893, <https://doi.org/10.1038/s41598-017-06215-x>.
- ¹³⁹ J. Hagemann and T. Salditt, “Coherence-Resolution Relationship in Holographic and Coherent Diffractive Imaging,” *Optics Express* 26, no. 1 (January 8, 2018): 242–53, <https://doi.org/10.1364/OE.26.000242>.
-

¹⁴⁰ “Single Slit Diffraction – College Physics,” accessed October 14, 2019, <https://opentextbc.ca/physicstestbook2/chapter/single-slit-diffraction/>.

¹⁴¹ H. M. L. Faulkner and J. M. Rodenburg, “Movable Aperture Lensless Transmission Microscopy: A Novel Phase Retrieval Algorithm,” *Physical Review Letters* 93, no. 2 (July 9, 2004): 023903, <https://doi.org/10.1103/PhysRevLett.93.023903>.

¹⁴² Daniel W. E. Noom *et al.*, “Lensless Phase Contrast Microscopy Based on Multiwavelength Fresnel Diffraction,” *Optics Letters* 39, no. 2 (January 15, 2014): 193–96, <https://doi.org/10.1364/OL.39.000193>.

¹⁴³ E. Wolf and J. R. Shewell, “Diffraction Theory of Holography,” *Journal of Mathematical Physics* 11, no. 8 (August 1, 1970): 2254–67, <https://doi.org/10.1063/1.1665390>.

Titre : Imagerie sans lentille 2D / 3D: Prototype et applications

Mots clés : holographie, imagerie sans lentille, microscopie, microfluidique, lab-on-a-chip

Résumé : L'imagerie biologique a réalisé des progrès significatifs durant les dernières décennies. Les récentes innovations portent sur la manipulation et la visualisation de cellules uniques avec une résolution spatiale de l'ordre du nanomètre. Une technologie d'imagerie récente, l'imagerie «sans lentille», est particulièrement prometteuse car elle combine une bonne résolution spatiale, un champ de vision étendu, une simplicité d'utilisation, un coût abordable et la possibilité de travailler sur des échantillons exempts de marqueurs spécifiques. En imagerie sans lentille, le système optique classiquement utilisé pour constituer l'image de l'échantillon est remplacé par des algorithmes informatiques qui s'appuient sur les propriétés de cohérence spatiale de la lumière. Dans cette thèse, deux approches différentes de microscopie sans lentille sont considérées : l'holographie numérique en ligne et l'holographie par transformée de Fourier. Deux prototypes d'imagerie, construits selon ces principes, sont présentés. Ils offrent une résolution de l'ordre du micron, ainsi que la possibilité de retrouver les informations relatives à l'amplitude spatiale et à la phase du champ optique. Cela permet la réalisation de reconstructions pseudo-3D d'objets volumétriques à partir d'un unique hologramme. Les deux dispositifs ont d'abord été caractérisés avec des échantillons de référence. Par la suite, des expériences d'applications ont été testées pour estimer la capacité des dispositifs à répondre à des problématiques concrètes dans le domaine de la biologie, grâce à la haute résolution, l'imagerie en temps réel et la reconstruction 3D. L'objectif de cette thèse est également de développer une nouvelle plateforme qui intègre, dans une puce microfluidique, d'une part un système

permettant la manipulation de cellules par diélectrophorèse, et d'autre part un masque optique pour la visualisation des cellules par imagerie sans lentille.

Le principe de fonctionnement est basé sur le déplacement des cellules en milieu liquide et la séparation des cellules dans le champ de vision du microscope en utilisant un champ électrique induit par des électrodes spécifiques. Le masque optique permet de définir le champ de vision du microscope et de créer les faisceaux de référence nécessaires pour l'imagerie par holographie par transformée de Fourier. Le principal avantage de ce système électro-optique pour l'imagerie cellulaire réside dans sa capacité à fournir une plateforme d'imagerie compacte qui regroupe précision et sensibilité. Les champs d'applications de cette plateforme sont variés. Une application concrète qui découle immédiatement des premières expériences présentées dans ce manuscrit serait l'analyse du comportement des cellules et de leurs modifications morphologiques lors d'un processus électrochimique de diélectrophorèse.

L'un des challenges majeurs dans le domaine de la microscopie est de réduire les coûts de fabrication. Les deux types de microscopes sans lentille présentés dans cette thèse visent à introduire dans le monde scientifique des outils d'imagerie permettant d'obtenir une haute résolution à un faible coût et sans marquage. Par ailleurs, la puce microfluidique est une première démonstration de plateforme intégrée pour l'analyse des cellules en temps réel dans un dispositif de type « Lab-on-a-chip ».

Title : 2D/3D lensless imaging: Prototype and applications

Keywords : holography, lensless, microscopy, microfluidics, lab-on-a-chip

Abstract : Biological imaging has made tremendous progresses these last decades. The latest developments concern manipulating and imaging single cells with nanometer spatial resolutions. A recent category of imaging techniques, called lensless microscopy, is very promising because they combine very good spatial resolutions in a large field-of-view, with simplicity of use and low cost, while operating on label free samples. In this thesis, two different lensless approaches are considered: digital in-line holography (DIH) and Fourier transform holography (FTH). In lensless imaging, the usual optical system used to form the sample's image are removed and replaced by numerical algorithms using the light spatial coherence properties.

Two imaging prototypes, built on these principles, are presented. They offer (sub-) micrometer scale resolutions, and offer the possibility to retrieve both spatial amplitude and phase information of the optical field. This allows to achieve pseudo-3D reconstructions of volumetric objects from a single 2D hologram. Both devices were first characterized with reference samples. In a second step, real applications, relevant to selected biological problems, were performed to assess the device's performances towards high resolution, real time imaging and 3D.

This thesis objective is also to develop a new platform directly integrating in a single chip a microfluidics system for biological cell handling by dielectrophoresis and an optical mask for cell visualization by lensless microscopy. Its working principle is based on cell transport in a liquid media by microfluidics, cell separation in the microscope field of view by the electric field induced by specific electrodes, and simultaneous cell imaging by Fourier Transform Holography. The main advantage of such coupled electro-optical system for cell imaging and analysis are the improved control, the precision and sensitivity regarding cell morphology all together merged in a compact imaging platform. The capability of the platform can be extended to analysis of cells' behavior and morphologic deviation during the electrochemical processes of DEP.

A major challenge in microscopy field is to reduce the production costs. The two types of lensless microscopy presented in this thesis aims to introduce new imaging tools that allows scientists to obtain low-cost high-resolution images in label-free conditions. Additionally, the microfluidics chip is a first demonstration of a new integrated platform for cell live analysis into a single Lab-on-a-chip device.